

**Search for Composite Signatures at the  $Z^0$   
Resonance**

by

Soo J. Chung

Bachelor of Arts, The Colorado College

(1988)

Submitted to the Department of Physics  
in partial fulfillment of the requirements for the degree of

Doctor of Philosophy

at the

MASSACHUSETTS INSTITUTE OF TECHNOLOGY

September, 1994

© Massachusetts Institute of Technology 1994. All rights reserved.



Author .....  
Department of Physics  
July 12, 1994

Certified by .....  
Min Chen  
Professor Of Physics  
Thesis Supervisor

Accepted by .....  
George F. Koster  
Chairman, Departmental Committee on Graduate Students  
Department of Physics

MASSACHUSETTS INSTITUTE  
OF TECHNOLOGY

OCT 14 1994

LIBRARIES

Science



# Search for Composite Signatures at the $Z^0$ Resonance

by  
Soo J. Chung

Submitted to the Department of Physics  
on July 12, 1994, in partial fulfillment of the  
requirements for the degree of  
Doctor of Philosophy

## Abstract

Data collected in the L3 detector at LEP during 1991 through 1993, corresponding to approximately  $65.1 \text{ pb}^{-1}$  of luminosity, is used to search for evidence of composite particles via their coupling strengths to ordinary fermions and bosons. Evidence for compositeness can manifest itself in the bosonic sector via anomalous couplings of the  $Z^0$  to photons or through an excess of low-mass di-lepton pairs due to a  $Z^0\gamma\gamma$  vertex interaction. Fermionic compositeness would be most evident with the existence of excited leptons. Direct searches are performed for singly produced electrons, muons and taus. The  $\tau^*$  analysis also yields information on the directly unmeasurable static electromagnetic properties of the tau lepton. For pair produced excited leptons, direct searches are performed in the electron and muon channels along with an indirect search independent of final state kinematics based on  $Z^0$  lineshape measurements.

In the absence of evidence of substructure, depending on the nature of the search, either mass regions are excluded or upper limits are placed on branching ratios and coupling strengths.

Thesis Supervisor: Min Chen  
Title: Professor Of Physics



## Acknowledgments

My first thanks goes to my thesis supervisor, Professor Min Chen. I also wish to thank the L3 spokesman, Professor S.C.C. Ting for the opportunity to work in his Collaboration. My gratitude to Dr. Y. Karyotakis, Dr. S. Shevchenko, for their leadership; Prof. F. Pauss for the L3P experience and for her continued support in many ways; Prof. G. Herten for his great course in particle physics and to Prof. M. Bardadin-Otwinowska for her most useful discussions and willingness to help.

Thank you Dr. B. Clare for your answers to my many questions and I. Clare for the fun conversations.

Mme Y. Bernard and Ms. G. Guidess must be acknowledged for their kindness and willingness to help with so many different tasks.

I thank Dr. S. Ting, Dr. F. Epling and J. Donahue for taking care of us at MIT.

Thank you to all my friends and colleagues at MIT and CERN who made it bearable. Thank you P. Berkovitz for everything you did to keep everything going between MIT and CERN.

To my physics professors of C.C., I thank you all for the wonderful training and the encouragement to study physics in the first place.

I want to thank my Father for doing his best to make sure that I had a chance to study. I thank my Aunt, Uncle, cousins and my dear Grandmother for all their continued support throughout my life. And thank you Lan for listening to me and putting up with my craziness all your life. I wish to convey my gratitude to my dearly departed Mother, who gave everything so that her children could study and succeed.

Last but most importantly I give my deepest gratitude to André, whose endless knowledge of all aspects of physics never ceases to amaze me; for having been all to me, and also for having taught me everything I know about particle physics and L3. Without him and his continuous, unwavering support, I never would have gotten here. Also I thank his wonderful family for their support and kindness, to his Mother Mme Rubbia, his Father Professor Rubbia, his sister Laura, her husband Alain and their adorable little one, Nicolas.

And thank you Kiidi and Coco for your endless affections.



# Table of Contents

<b>Acknowledgments</b>	<b>5</b>
<b>Chapter 1 Introduction</b>	<b>13</b>
<b>Chapter 2 Theory</b>	<b>15</b>
2.1 QED . . . . .	15
2.2 Standard Model . . . . .	16
2.2.1 Particles and interactions . . . . .	16
2.2.2 The processes $e^+e^- \rightarrow \mu^+\mu^-, \tau^+\tau^-$ . . . . .	18
2.2.3 The process $e^+e^- \rightarrow e^+e^-$ . . . . .	19
2.2.4 Radiative Corrections . . . . .	19
2.2.5 The $Z^0$ width . . . . .	21
2.2.6 The process $e^+e^- \rightarrow \gamma\gamma\gamma$ . . . . .	22
2.3 Composite Fermions . . . . .	24
2.3.1 g-2 constraints . . . . .	24
2.3.2 The process $e^+e^- \rightarrow l^*\bar{l}^*$ . . . . .	27
2.3.3 The process $e^+e^- \rightarrow l^{*+}l^-, l^{*-}l^+$ . . . . .	29
2.3.4 Decays of excited states $l^* \rightarrow lV$ . . . . .	32
2.3.5 The electromagnetic properties of the $\tau$ . . . . .	35
2.4 Composite Gauge Bosons . . . . .	36
2.4.1 Composite models . . . . .	37
2.4.2 The process $Z^0 \rightarrow \gamma\gamma\gamma$ . . . . .	38
2.4.3 The process $Z^0 \rightarrow \gamma l^+l^-$ . . . . .	39
<b>Chapter 3 Experiment</b>	<b>41</b>
3.1 LEP . . . . .	41
3.2 The L3 Detector . . . . .	42
3.2.1 TEC Central Tracking Chamber . . . . .	43
3.2.2 BGO Electromagnetic Calorimeter . . . . .	43
3.2.3 The Hadron Calorimeter . . . . .	44
3.2.4 The Muon Chambers . . . . .	45
3.2.5 Scintillation Counters . . . . .	47
3.2.6 Luminosity Monitor . . . . .	47
3.2.7 Forward Tracking Chambers . . . . .	48
3.2.8 Trigger . . . . .	48

<b>Chapter 4 Simulation and Reconstruction</b>	<b>59</b>
4.1 Introduction . . . . .	59
4.2 Physics processes generation . . . . .	59
4.3 Detector simulation . . . . .	60
4.4 Event reconstruction . . . . .	62
4.4.1 Electromagnetic clusters . . . . .	62
4.4.2 Tracks . . . . .	62
4.4.3 Hadronic clusters . . . . .	63
4.4.4 Muon tracks . . . . .	63
<b>Chapter 5 Composite Fermions Indirect Search</b>	<b>69</b>
5.1 Introduction . . . . .	69
5.2 Indirect searches . . . . .	69
<b>Chapter 6 Composite Fermions Direct Searches</b>	<b>75</b>
6.1 Decay topologies . . . . .	75
6.2 Data quality requirements . . . . .	76
6.3 $e^+e^- \rightarrow ee\gamma$ . . . . .	81
6.3.1 Electron identification . . . . .	81
6.3.2 Event selection . . . . .	83
6.3.3 $e^+e^- \rightarrow ee\gamma\gamma$ . . . . .	86
6.4 $e^+e^- \rightarrow e(e)\gamma$ . . . . .	103
6.4.1 Event selection . . . . .	103
6.5 $e^+e^- \rightarrow \mu\mu\gamma$ . . . . .	114
6.5.1 Muon momentum resolution . . . . .	114
6.5.2 Event selection . . . . .	115
6.5.3 $e^+e^- \rightarrow \mu\mu\gamma\gamma$ . . . . .	118
6.6 $e^+e^- \rightarrow \tau\tau\gamma$ . . . . .	136
6.6.1 Tau identification . . . . .	136
6.6.2 Event selection . . . . .	137
6.6.3 Invariant mass reconstruction . . . . .	140
6.6.4 The $\tau$ moments . . . . .	141
6.7 Results . . . . .	164
<b>Chapter 7 Composite Gauge Boson</b>	<b>167</b>
7.1 Decay topologies . . . . .	167
7.2 $Z^0 \rightarrow \gamma\gamma\gamma$ . . . . .	167
7.2.1 Data sample . . . . .	168
7.2.2 $e^+e^- \rightarrow e^+e^-\gamma$ background . . . . .	168
7.2.3 Event selection . . . . .	169
7.2.4 Branching ratio limit . . . . .	171
7.3 $Z^0 \rightarrow \mu^+\mu^-\gamma, e^+e^-\gamma$ . . . . .	171

<b>Chapter 8 Conclusion and Remarks</b>	<b>187</b>
8.1 Summary . . . . .	187
8.2 Other searches for compositeness . . . . .	189
8.2.1 $e^*$ from $e^+e^- \rightarrow \gamma\gamma(\gamma)$ . . . . .	189
8.2.2 $\nu^*$ . . . . .	189
8.2.3 $q^*$ . . . . .	190
8.2.4 Contact terms . . . . .	190
8.2.5 Electric dipole transition of the $Z^0$ . . . . .	192
8.2.6 Leptoquarks . . . . .	192
8.3 Future prospects . . . . .	193
8.4 Concluding remarks . . . . .	194
<b>Appendix A Cross-section involving excited leptons <math>l^*</math></b>	<b>197</b>
<b>Appendix B Decay width and lifetime of the <math>l^*</math></b>	<b>199</b>
<b>Bibliography</b>	<b>201</b>



*“No one has found structure inside the electron or quark. For all we know, there may be ancient civilizations buried in there...”*

*L.M. Lederman, DPF '92.*



# Chapter 1

## Introduction

In the 1950's and 60's, the theory of strong interactions was realized with the partial wave scattering method of pions and nucleons. This theory was renormalizable [1], the pion-nucleon couplings were calculated [2], the dominant pion-nucleon  $\Delta$  resonance was successfully implemented into the theory [3], low energy theorems were proven with the inclusion of light scattering [4, 5] and the lifetime of the  $\pi^0$  was calculated [6]. For over twenty years this was considered to be the fundamental theory of strong interactions. However, it is now known that the pseudoscalar theory of pion-nucleon interactions is just an effective theory valid in energy regions studied at the time; it was a phenomenological theory which dealt with the composite states of the quarks at low energies.

Historically, many of the particles which were initially thought to be fundamental, have revealed substructure when probed at larger energy scales, and this has been central to our understanding of matter. It is therefore natural to explore the possibility that some or all of the particles which we consider today to be *elementary* may be composite. The existence of excited states is the most unambiguous and characterizing signal for substructure in the fermionic sector. Indeed, if the known quarks and leptons are composite, they should be regarded as the ground states of a rich spectrum of excited states. In the bosonic sector, anomalous gauge couplings could indicate non-elementarity.

Now in the 90's with the advent of LEP 100, the energy scale in question has been pushed up to the order of 100 GeV. Consequently, a new regime of fundamentality in the 'elementary' particles can be tested. The Standard Model [7], with its intrinsic assumptions that the leptons and gauge bosons are pointlike, has been confirmed and so far no evidence is in contradiction with it, but this behavior could again be the result of an effective approximation of a more fundamental interaction manifested in the present energy scale. Also, since there still remain unanswered questions in the Standard Model such as the 'family problem,' and the origin of mass, it is quite possible that there is more to be understood. Compositeness is an attractive solution since it contains the potential to answer these questions. Although there does not yet exist a composite theory with absolute predictive power, there are nonetheless effective theories which predict phenomenological anomalies from Standard Model results which would be unambiguous signs of underlying structure in the fermions

and gauge bosons, and it is in this manner we search for evidence for composite structure.

Data collected in the L3 detector at LEP during 1991, 1992 and 1993, corresponding to approximately  $65 \text{ pb}^{-1}$  of luminosity, is used to search for evidence of composite particles via their coupling strengths to ordinary fermions and bosons.

# Chapter 2

## Theory

Presently, our best knowledge of the theory of particle physics is based on the Standard Model (SM) and Quantum Chromodynamics (QCD). These theories whose precursor was the Quantum Electrodynamics (QED) are gauge field theories. The electroweak interactions are described by the Standard Model and the strong interactions by QCD. In this chapter, a short summary of QED, the Standard Model and possible extensions within composite scenarios are presented.

### 2.1 QED

Quantum Electrodynamics [8] is the interaction of light with matter. It assumes the existence of point-like particles (electron, muon, etc.) interacting with the electromagnetic field via the Lagrangian:

$$\mathcal{L}_{int,QED} = e\bar{\Psi}\gamma^\mu A_\mu\Psi \quad (2.1)$$

where  $e$  is the electric charge, related to the fine structure constant by

$$e = \sqrt{4\pi\alpha} \quad (2.2)$$

$\Psi$  is the particle spinor,  $\gamma^\mu$  are the Dirac matrices and  $A_\mu$  is the electromagnetic field. The QED Lagrangian is by construction invariant under local gauge transformation of the fields  $\Psi(x)$  and  $A_\mu(x)$ . This gauge transformation belongs to unitary group  $U(1)$  and the Lagrangian has the symmetry  $U(1)_Q$  where  $Q$  is the charge.

The success of QED stemmed from the remarkable agreement between its predictions and experiment. Historically, deviations from the theory were expressed in terms of a fictitious “cut-off” up to which the theory had been found to hold. In this language, the confirmations of the prediction of a theory are expressed in terms of upper limits to the coupling strengths and/or lower limits to the masses of hypothetical new particles and interactions. This suggests that experiments should search both directly and indirectly for these new particles.

First attempts to formalize in a gauge invariant way possible deviations from QED led to the possibility of a new interaction of the electron to a new heavy excited

electron by a magnetic coupling of the form [9]:

$$\mathcal{L}_{magn} = \frac{e}{\Lambda} \bar{\Psi}_e \cdot \sigma^{\mu\nu} \Psi_e F_{\mu\nu} + h.c. \quad (2.3)$$

where  $\Lambda$  is the cut-off parameter and  $F_{\mu\nu} = \partial_\mu A_\nu - \partial_\nu A_\mu$ . The cut-off  $\Lambda$  is in units of energy and can be expressed as

$$\frac{1}{\Lambda} \equiv \frac{\text{coupling}}{m_e} \quad (2.4)$$

where the coupling constant is unitless and  $m_e$  is the mass of the excited electron. As noted in [9], the Lagrangian 2.3 is not renormalizable and should be considered as the effective Lagrangian which describes the low energy manifestation of a more complete theory.

## 2.2 Standard Model

### 2.2.1 Particles and interactions

The building blocks of the Standard Model are the point-like particles sub-divided into two classes: the *fermions* and the *bosons*. The fermions come in three families, or generations, each composed of a charged and neutral lepton and of an up-type and down-type quark. The three families are identical in structure but differ in the mass of their constituents. The gauge bosons are the intermediators of the forces. In the minimal version, the Higgs mechanism responsible for the generation of mass, leaves one physical state called the Higgs boson. The main properties of the twelve fermions and twelve intermediate bosons and the Higgs boson are listed in Tables 2.1, 2.2.

Fermion $f$	Masses (MeV)	$Q_f/e$	color	$\frac{1}{2}I_3^f L$	$\frac{1}{2}Y_L^f$	$I_3^f R$	$\frac{1}{2}Y_R^f$
$e, \mu, \tau$	0.511, 105, 1780	-1	singlet	$-\frac{1}{2}$	$-\frac{1}{2}$	0	-1
$\nu_e, \nu_\mu, \nu_\tau$	$< 13 \times 10^{-6}, < 0.27, < 35$	0	singlet	$+\frac{1}{2}$	$-\frac{1}{2}$	?	?
$u, c, t$	2 - 8, 1300 - 1700, > 131000	+2/3	triplet	$+\frac{1}{2}$	$+\frac{1}{6}$	0	$-\frac{2}{3}$
$d, s, b$	5 - 15, 100 - 300, 4700 - 5300	-1/3	triplet	$-\frac{1}{2}$	$+\frac{1}{6}$	0	$-\frac{1}{3}$

Table 2.1: List of fundamental spin-1/2 fermions and associated charge  $Q_f$ , weak isospin  $I_3^f$  and hypercharge  $Y^f$  quantum numbers in the representation of  $SU(3)_{Color} \times SU(2)_L \times U(1)_Y$ .

The Standard Model is a non-Abelian gauge theory or a Yang-Mills theory [10]. Its Lagrangian is constructed under invariance of the  $SU(2)_L \times U(1)_Y$  symmetry where  $L$  is the weak isospin and  $Y$  the weak hypercharge. Specifically its interaction is:

$$\mathcal{L}_{int,SM} = g \bar{\Psi}_L \vec{\tau} \gamma^\mu \vec{W}_\mu \Psi_L + g' \bar{\Psi} \frac{Y}{2} \gamma^\mu B_\mu \Psi \quad (2.5)$$

where  $g, g'$  are weak coupling constants,  $\vec{\tau}$  are the Pauli matrices for the weak isospin,  $\vec{W}_\mu$  and  $B_\mu$  are the electroweak fields and  $\Psi_L = (1/2)(1 - \gamma_5)\Psi$ .

Name	Mass (GeV)	$J^{PC}$	Q/e	color
$\gamma$ (photon)	$< 3 \times 10^{-36}$	$1^{--}$	$< 2 \times 10^{-32}$	singlet
$Z^0$ (weak boson)	$91.187 \pm 0.007$	1	0	singlet
$W^\pm$ (weak boson)	$80.22 \pm 0.26$	1	$\pm 1$	singlet
$g_i, i = 1, \dots, 8$ (gluons)	0 (theo.)	$1^-$	0	octet
H (Higgs boson)	$> 63.5$	0	0	singlet

Table 2.2: *Intermediate Gauge bosons and Higgs boson*

The electromagnetic interaction  $\mathcal{L}_{int,QED}$  (Eq. 2.1) must be contained in the neutral term of the Standard Model Lagrangian. The third component of  $\overline{W}_\mu$  and the  $B$  fields are therefore linear combinations of the electromagnetic field  $A_\mu$  and a new field  $Z_\mu$  written as:

$$\begin{pmatrix} W_3 \\ B \end{pmatrix} = \begin{pmatrix} \cos \theta_W & \sin \theta_W \\ -\sin \theta_W & \cos \theta_W \end{pmatrix} \begin{pmatrix} Z \\ A \end{pmatrix} \quad (2.6)$$

where  $\theta_W$  is a free mixing parameter of the theory. With this constraint, one has

$$g = \frac{e}{\sin \theta_W}, \quad g' = \frac{e}{\cos \theta_W}. \quad (2.7)$$

The physical states of the  $Z_\mu$  and  $A_\mu$  fields are respectively the intermediate vector gauge boson  $Z^0$  and the massless photon  $\gamma$ . To the charge raising and lowering operators  $\tau^\pm = (\tau_1 \pm i\tau_2)/2$  correspond the charged intermediate vector bosons  $W^+$  and  $W^-$  defined as  $W_\mu^\pm = (W_\mu^1 \mp iW_\mu^2)$ . To account for the strength of the weak forces relative to the electromagnetic force, the  $W^\pm$  and  $Z^0$  gauge bosons must be massive. The theory of Spontaneous Symmetry Breaking [11, 12] is used within the Standard Model for the generation of mass. In its minimal version, an  $SU(2)_L$  doublet  $\Phi$  is introduced with a potential  $V(\Phi) = \mu^2|\Phi|^2 + \lambda|\Phi|^4$ . The vacuum expectation value for  $\mu^2 < 0$  and  $\lambda > 0$  is given by:

$$v = \sqrt{2}(-\mu^2/2\lambda)^{1/2} \quad (2.8)$$

The symmetry is explicitly broken when the field is expanded along a particular minimum. The four degrees of freedom of the field give rise to the masses of the gauge bosons and the Higgs boson is created. The mass relations are  $m_H = \sqrt{2\lambda}v$ ,  $m_W = (1/2)gv$ ,  $m_Z = (1/2)v\sqrt{g^2 + g'^2}$  and  $m_\gamma = 0$ . Given the relation  $v = (\sqrt{2}G_F)^{-(1/2)}$ , the vector boson masses can be calculated from the measurement of the Fermi coupling constant  $G_F$  (including radiative corrections).

The lowest order Feynman diagram rules for the couplings between the physical intermediate bosons  $W^\pm$ ,  $Z^0$  and  $\gamma$  with fermions are:

$$\gamma f \bar{f} : -ieQ_f \gamma_\mu \quad (2.9)$$

$$W^\pm f \bar{f}' : -\frac{ig}{\sqrt{2}} \frac{1}{2} (1 - \gamma_5) \gamma_\mu \quad (2.10)$$

$$Z^0 f \bar{f} : -\frac{ig}{\cos \theta_W} \frac{1}{2} (g_V^f - g_A^f \gamma_5) \gamma_\mu \quad (2.11)$$

where the vector coupling  $g_V^f$  and axial-vector coupling  $g_A^f$  are given by (see Table 2.1):

$$g_V^f = \frac{1}{2}I_3^f L - 2Q_f \sin^2 \theta_W, \quad g_A^f = \frac{1}{2}I_3^f L \quad (2.12)$$

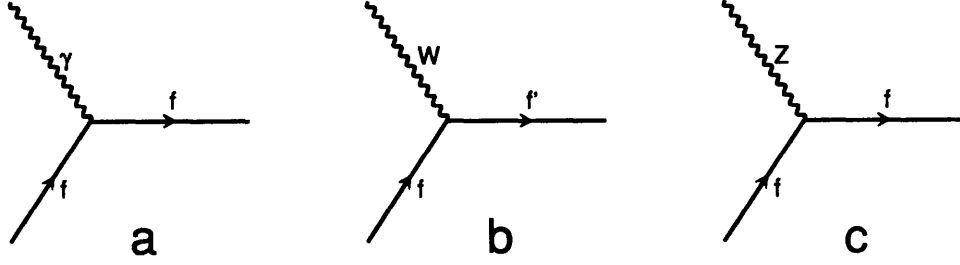


Figure 2-1: The lowest order Feynman diagrams for the couplings a)  $-ieQ_f\gamma_\mu$ ; b)  $(-ig/\sqrt{2})((1 - \gamma_5)\gamma_\mu)/2$  and c)  $(-ig/\cos\theta_W)((g_V^f - g_A^f\gamma_5)\gamma_\mu)/2$ .

### 2.2.2 The processes $e^+e^- \rightarrow \mu^+\mu^-, \tau^+\tau^-$

The process  $e^+e^- \rightarrow l^+l^- (l \neq e)$  is given by  $Z^0$  and photon exchange in the s-channel. The tree-level differential cross section is (neglecting  $m_l$ ):

$$\frac{d\sigma^0}{d\Omega} = \left(\frac{d\sigma^0}{d\Omega}\right)_{Z^0} + \left(\frac{d\sigma^0}{d\Omega}\right)_\gamma + \left(\frac{d\sigma^0}{d\Omega}\right)_{\gamma Z^0} \quad (2.13)$$

where

$$\begin{aligned} \left(\frac{d\sigma^0}{d\Omega}\right)_{Z^0} &= \frac{G_F^2 M_Z^4}{(4\pi)^2 4s} |\chi(s)|^2 \times \\ &\quad \left( (g_V^e{}^2 + g_A^e{}^2)(g_V^l{}^2 + g_A^l{}^2)(1 + \cos^2 \theta) + 8g_V^e g_A^e g_V^l g_A^l \cos \theta \right) \end{aligned} \quad (2.14)$$

$$\left(\frac{d\sigma^0}{d\Omega}\right)_\gamma = \frac{\alpha^2}{4s} (1 + \cos^2 \theta) \quad (2.15)$$

$$\left(\frac{d\sigma^0}{d\Omega}\right)_{\gamma Z^0} = \frac{\sqrt{2}\alpha G_F M_Z^2}{16\pi s} \Re e(\chi(s)) (g_V^e g_V^l (1 + \cos^2 \theta) + 2g_A^e g_A^l \cos \theta) \quad (2.16)$$

The angle  $\theta$  is defined between the incoming electron and the outgoing negatively charged lepton and  $\chi(s)$  is the  $Z^0$  propagator:

$$\chi(s) = \frac{s}{s - M_Z^2 + iM_Z\Gamma_Z} \quad (2.17)$$

Numerically, the value of  $g_V^l$  is very close to zero because  $\sin^2 \theta_W \approx 1/4$ . The differential cross section is therefore dominated by the  $(1 + \cos^2 \theta)$  distribution such that large scattering angles are frequent.

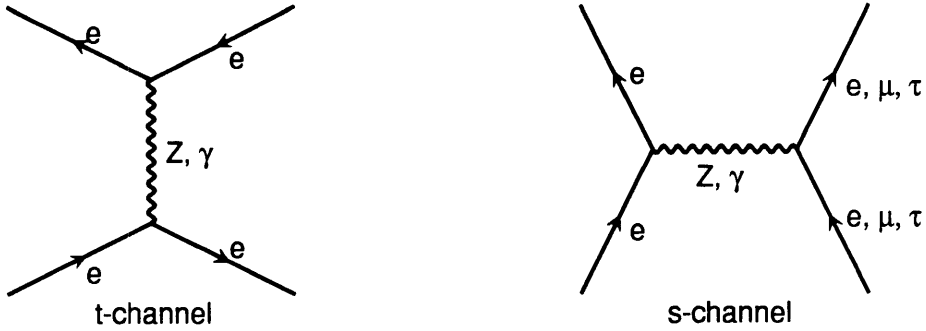


Figure 2-2: The lowest order Feynman diagrams for the processes  $e^+e^- \rightarrow l^+l^-$  where  $l = e, \mu, \tau$ .

### 2.2.3 The process $e^+e^- \rightarrow e^+e^-$

The Bhabha process  $e^+e^- \rightarrow e^+e^-$  has contributions from the s-channel and t-channel diagrams. The t-channel is dominated by photon exchange and exhibits divergent behavior in the limit  $\theta \rightarrow 0$ . Taking into account the four tree-level diagrams ( $\gamma$ ,  $Z^0$  exchange in s-,t-channels) and their interference, the differential cross section using the notation of [13] is written as:

$$\frac{d\sigma^0}{d\Omega} = \sum_{i=1}^{10} \frac{d\sigma^{0(i)}}{d\Omega}. \quad (2.18)$$

The s-channel  $Z^0$  exchange,  $\frac{d\sigma^{0(10)}}{d\Omega}$ , and  $\gamma$  exchange,  $\frac{d\sigma^{0(1)}}{d\Omega}$ , contributions are identical to Eqs. 2.14 and 2.15. The t-channel  $\gamma$  exchange is:

$$\frac{d\sigma^{0(3)}}{d\Omega} = \frac{2}{(1 - \cos \theta)^2} [(1 + \cos \theta)^2 + 4] \quad (2.19)$$

The t-channel  $Z^0$  exchange and the interference terms can be found in Ref. [13].

### 2.2.4 Radiative Corrections

The relations given in the previous sections are modified by the inclusion of higher order corrections. These effects can be classified in electromagnetic corrections (QED) which include initial and final state radiation of photons and virtual photon loops. The weak corrections come from non-photon propagator vertex and box diagrams involving massive bosons and unknown parameters  $m_t$  and  $m_H$ , the top and Higgs mass respectively. Weak corrections are usually absorbed in a re-definition of the coupling constants and mixing angle such that the tree-level relations remain almost intact. Using these effective couplings, the weak corrections are included in our calculations.

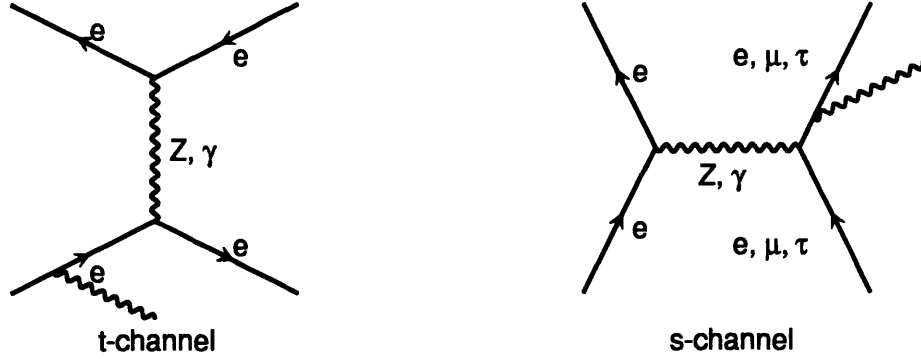


Figure 2-3: *Example of Feynman diagrams for initial state radiation in the t-channel process  $e^+e^- \rightarrow e^+e^-\gamma$  and final-state radiation in the process  $e^+e^- \rightarrow l^+l^-\gamma$  where  $l = e, \mu, \tau$ .*

QED corrections have a significant effect at LEP energies and are usually calculated to first order. The process  $e^+e^- \rightarrow l^+l^-$  never strictly occurs as it is always accompanied by the emission of electromagnetic radiation:

$$e^+e^- \rightarrow l^+l^-n(\gamma) \quad (2.20)$$

The number of photons detected depends on the experimental setup and the selection criteria. One distinguishes three steps:

- emission of radiation from initial state particles;
- the hard elastic scattering  $e^+e^- \rightarrow l^+l^-$ ;
- emission of radiation from final state particles.

Initial state radiation effectively reduces the center-of-mass energy of the hard collision. Let  $\sigma^0(s')$  be the total cross section at center-of-mass energy  $s'$ . To find the cross section with initial state radiation, the convolution of  $\sigma^0(s')$  with the probability distribution function  $G(z)$  where  $z = s'/s$  to emit a photon of total energy  $\sqrt{s} - \sqrt{s'}$  is used.

$$\sigma(s) = \int_{z_0}^1 \sigma^0(sz)G(z)dz \quad (2.21)$$

A possible form of the radiator is[14]:

$$G(z) = - \left[ 1 + \frac{3\beta}{4} \right] \beta(1-z)^{\beta-1} + \beta \left[ 1 - \frac{1-z}{2} \right] \quad (2.22)$$

where  $\beta = (2\alpha/\pi)(\ln(s/m_e^2) - 1)$ . The distributions of the photon energy and of its polar angle for  $E_{beam} = 45.6$  GeV are shown in Figure 2-4. A large fraction of the photons emitted by initial state radiation are along the direction of the initial electron

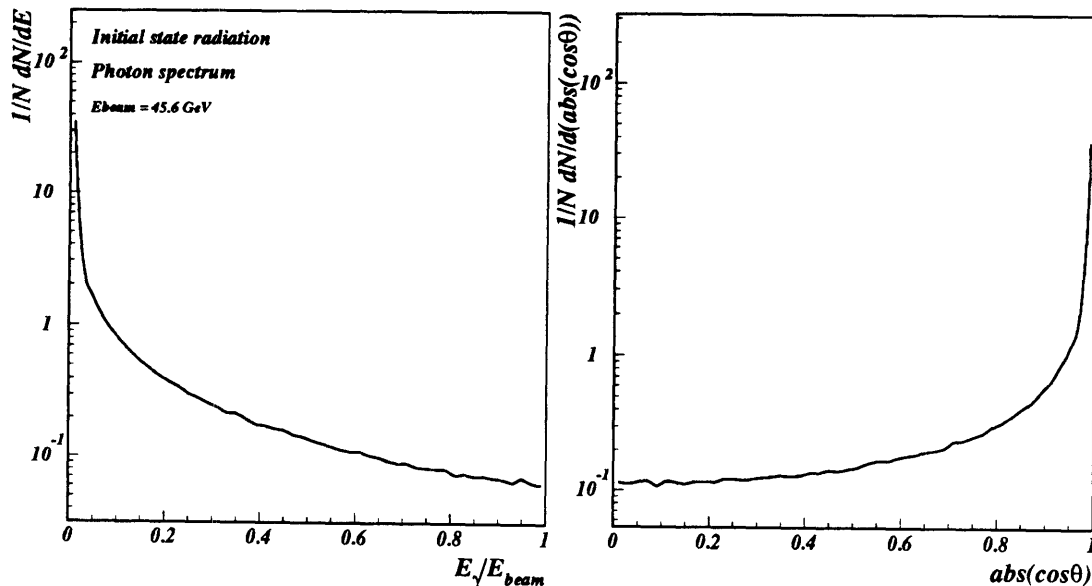


Figure 2-4: *The photon energy spectrum  $(1/N)(dN/dE)$  and polar angle distribution  $(1/N)(dN/d|\cos \theta_\gamma|)$  from initial state radiation.*

and will therefore not be visible in the detector. After inclusion of the initial state radiation, the Born cross section at the  $Z^0$  peak is typically reduced by 25%.

Final state radiation affects the cross section by a multiplicative factor  $1 + \delta_{QED}$ . In the calculations one distinguishes energetic and non-collinear (hard) photons from collinear and/or low energy (soft) photons. The hard photons appear in the detector as distinguishable, separate final state particles.

### 2.2.5 The $Z^0$ width

The  $Z^0$  boson decays to all kinematically allowed fermion pairs. For a massive fermion with vector and axial-vector coupling to the  $Z^0$ , the decay  $Z^0 \rightarrow f\bar{f}$  width is

$$\Gamma_{f\bar{f}} = \frac{G_F M_Z^3 N_C}{6\sqrt{2}\pi} (1 - 4\eta)^{1/2} \left[ (1 - \eta)(g_V^f{}^2 + g_A^f{}^2) + 3\eta(g_V^f{}^2 - g_A^f{}^2) \right] \quad (2.23)$$

where  $\eta = m_f^2/M_Z^2$ ,  $N_C$  is the number of colors, and  $g_V^f(g_A^f)$  are the vector (axial-vector) coupling constants. The predicted widths and branching ratios  $Br(Z^0 \rightarrow f\bar{f}) = \Gamma_{f\bar{f}}/\Gamma_Z$  where  $\Gamma_Z$  are completely predicted at tree-level from  $M_Z$ , the  $Z^0$  mass,  $\alpha$ , the electromagnetic fine structure constant, and  $G_F$ , the Fermi constant. Three other parameters  $\alpha_s$ , the strong interaction coupling constant,  $m_t$ , the top mass and  $m_H$ , the Higgs mass, which enter in the radiative corrections must be included as well due to precision of the LEP measurements. The total  $Z^0$  width and the partial widths

	$\nu\bar{\nu}$	$e^+e^-$	$\mu^+\mu^-$	$\tau^+\tau^-$	$q\bar{q}$	total
$m_t = 131 \text{ GeV}, m_H = 63 \text{ GeV}, \alpha_s = 0.118$						
$\Gamma \text{ (MeV)}$	500.43	83.70	83.70	83.51	1741.9	2493
$Br \text{ (%)}$	20.07	3.36	3.36	3.35	69.87	
$m_t = 225 \text{ GeV}, m_H = 63 \text{ GeV}, \alpha_s = 0.118$						
$\Gamma \text{ (MeV)}$	505.59	84.75	84.75	84.56	1762.2	2522
$Br \text{ (%)}$	20.05	3.36	3.36	3.35	69.89	
$m_t = 131 \text{ GeV}, m_H = 1 \text{ TeV}, \alpha_s = 0.118$						
$\Gamma \text{ (MeV)}$	499.5	83.50	83.50	83.31	1734.9	2484
$Br \text{ (%)}$	20.11	3.36	3.36	3.35	69.84	
$m_t = 225 \text{ GeV}, m_H = 1 \text{ TeV}, \alpha_s = 0.118$						
$\Gamma \text{ (MeV)}$	504.72	84.53	84.53	84.33	1755.5	2513
$Br \text{ (%)}$	20.08	3.36	3.36	3.35	69.85	

Table 2.3: *The Standard Model values for the leptonic and hadronic widths and branching ratios for the input parameters:  $m_t = 131 \text{ GeV}$  and  $205 \text{ GeV}$ ,  $m_H = 63 \text{ GeV}$  and  $1 \text{ TeV}$  and the  $L3$  values of  $M_Z = 91.198 \text{ GeV}$ ,  $\alpha_s = 0.118$ .*

are listed in Table 2.3 for the input parameters  $M_Z = 91.198 \text{ GeV}$ ,  $m_t = 131 \text{ GeV}$ ,  $m_H = 63 \text{ GeV}$  and  $\alpha_s = 0.118$ . The top and Higgs masses are at their excluded lower bounds. The values obtained for their “upper” bounds are listed in Table 2.3 to show the magnitude of their contributions. These values will be used in Chapter 5 to place a limit on non-Standard Model contributions to the widths.

The total width is related to the Born-level cross section  $e^+e^- \rightarrow f\bar{f}$  at the peak by:

$$\sigma_{peak}^0 = \frac{12\pi\Gamma_{ee}\Gamma_{f\bar{f}}}{M_Z^2\Gamma_Z^2} \quad (2.24)$$

## 2.2.6 The process $e^+e^- \rightarrow \gamma\gamma\gamma$

The decay  $Z^0 \rightarrow \gamma\gamma\gamma$  has contributions from triangle loops with fermions and  $W$ -boson loops. The triple gauge boson vertices  $Z^0WW$  and  $\gamma WW$  as well as the quadrupole vertices  $Z^0\gamma WW$  and  $\gamma\gamma WW$  also participate. Assuming standard boson couplings, the dominant contribution comes from the fermion loop[15]. It is given by[16]:

$$\Gamma(Z^0 \rightarrow \gamma\gamma\gamma) = \alpha(M_Z^2)\alpha^3(0)\frac{M_Z}{12\pi^3}X\frac{1}{6}\left(3\sum_q e_q^3 g_V^q + \sum_l e_l^3 g_V^l\right)^2 \quad (2.25)$$

where  $X \approx 14.954$  results from the integral of matrix elements and  $g_V$  are the vector couplings to quarks and leptons. This width is very small, i.e.:

$$\Gamma(Z^0 \rightarrow \gamma\gamma\gamma) \approx 0.7 \times 10^{-9} \text{ GeV} \quad (2.26)$$

	$\nu\bar{\nu}$	$e^+e^-$	$\mu^+\mu^-$	$\tau^+\tau^-$	$q\bar{q}$	total
$m_t = 131 \text{ GeV}, m_H = 63 \text{ GeV}, \alpha_s = 0.130$						
$\Gamma \text{ (MeV)}$	500.43	83.70	83.70	83.51	1749.3	2500
$Br \text{ (\%)}$	20.02	3.36	3.36	3.35	69.96	
$m_t = 225 \text{ GeV}, m_H = 63 \text{ GeV}, \alpha_s = 0.130$						
$\Gamma \text{ (MeV)}$	505.59	84.75	84.75	84.56	1769.9	2529
$Br \text{ (\%)}$	20.02	3.36	3.36	3.35	69.98	
$m_t = 131 \text{ GeV}, m_H = 1 \text{ TeV}, \alpha_s = 0.130$						
$\Gamma \text{ (MeV)}$	499.5	83.50	83.50	83.31	1742.2	2492
$Br \text{ (\%)}$	20.02	3.36	3.36	3.35	69.92	
$m_t = 225 \text{ GeV}, m_H = 1 \text{ TeV}, \alpha_s = 0.130$						
$\Gamma \text{ (MeV)}$	504.72	84.53	84.53	84.33	1763.1	2521
$Br \text{ (\%)}$	20.02	3.36	3.36	3.35	69.94	

Table 2.4: *ibid* for  $\alpha_s = 0.130$ .

yielding a branching ratio of approximately  $3 \times 10^{-10}$ . It is clear that within the Standard Model, the rate for this decay will be negligible at LEP even after inclusion of the  $W$ -boson loop contributions.

The dominant source of three photon events is therefore the QED process  $e^+e^- \rightarrow \gamma\gamma(\gamma)$ . The integrated cross section  $\sigma(|\cos\theta| < 0.97)$  as a function of  $\sqrt{s}$  was measured in L3[17]:

$$\sigma_{\gamma\gamma(\gamma)}(\sqrt{s} = 91.2 \text{ GeV}, |\cos\theta| < 0.97) = 58.0 \pm 3.5 \text{ pb} \quad (2.27)$$

Because of the nature of the QED process, one of the three photons tends to have small energy and be collinear with another photon. In the process we are interested in, signatures with three separate energetic photons will be searched for (see Chapter 7). These events are effectively suppressed by a factor  $\alpha$  compared to the cross section (2.27) such that we expect a QED “3-photons” cross section of about half a pb.

## 2.3 Composite Fermions

Leptons and quarks are presently viewed as point-like constituents of matter. However, in view of their proliferation and their eminent regularities like those in charge, flavor, and color, it is tempting to suppose the existence of more fundamental particles which are building blocks of leptons and quarks. (See Table 2.1). The mass spectra and the mixing patterns could be explained in composite models. Theoretically, a unification of quarks and leptons in terms of a small number of common constituents is very attractive.

If the electron, the muon and the tau are in fact composite systems, they must be simultaneously light in mass and small in spatial extension. The non-relativistic size  $R$  of an atom is given by

$$R \approx \frac{1}{\sqrt{ME_B}} \quad (2.28)$$

where  $M$  is the mass,  $E_B$  is the binding energy. For the electron we know that the intrinsic size is limited by  $R < 10^{-16}$  cm. It is the challenge of composite models to explain why the electron mass is so light compared to the scale of its size  $1/R > 200$  GeV. The electron must be then thought of as having a very small spatial extension because it is made of very tightly bound sub-constituents of a much larger mass  $M \gg m_e$ . Should the leptons have spatial extension, then it is clear that they could acquire anomalous moments like the anomalous magnetic and the electric dipole moments. The natural scale for these is  $eR \approx e/M$ . The implication in terms of a lower bound on  $M$  given by the extremely stringent experimental limits of  $g-2$  and electric dipole moment measurements will be discussed below.

The most natural consequence of composite models is the existence of *excited states* of leptons,  $l^*$  ( $l = e, \mu, \tau$ ). For simplicity, the excited states are assumed to be fermions with spin-1/2. Higher spin assignments are possible and have been investigated in the literature[18]. Their effects are to alter the angular distributions of production and decays of the excited states but from a phenomenological point of view, the experimental signatures that are searched for are identical to the ones of spin-1/2 particles. We will therefore limit ourselves to spin-1/2 excited leptons keeping in mind that the results could be reinterpreted for higher spin states.

When searching for excited leptons, one should remember that even if the compositeness scale is very large (i.e. a few hundred GeV or even TeV region), that the mass of the excited states can be in a much lower energy domain since the dynamics at the subconstituent level are completely unspecified. This motivates the searches for excited states within all the kinematical range reachable at LEP I.

### 2.3.1 $g-2$ constraints

The  $g$ -factor is a dimensionless number which relates the magnetic dipole of a particle to its intrinsic angular momentum. The magnetic moment is written

$$\mu = \frac{g}{2} \frac{e\hbar}{2m} \quad (2.29)$$

and if a particle obeys the Dirac equation[19] then it is expected that  $g = 2$  exactly for that particle. Departure from this value would imply a deviation from the point-like nature as for example was the case of the proton with a g-factor of 5.586. In fact, however, higher order QED corrections alter the g-factor even in the absence of intrinsic structure. These corrections are nevertheless small and it is conventional to define the magnetic moment anomaly  $a$  such that

$$g = 2(1 + a) \quad (2.30)$$

Precise calculations within QED lead to the following theoretical predictions for the anomalous magnetic moment of the electron and of the muon:

$$a_e^{QED} = (1159652.4 \pm 0.4) \times 10^{-9} \quad (2.31)$$

$$a_\mu^{QED} = (1165921 \pm 8.3) \times 10^{-9} \quad (2.32)$$

For the muon value, the error is dominated by weak and QCD correction uncertainties.

A non point-like nature could lead to a non-zero electric dipole moment. The existence of such a static property would imply that the electromagnetic interaction violates P and T symmetries and very stringent limits have been therefore placed on it.

The latest experimental measurements and limits on the magnetic moment and the electric dipole moment for the leptons are listed in Table 2.5.

	Electric dipole moment (e-cm)	Magnetic moment $(g - 2)/2$
$e$	$(-0.27 \pm 0.83) \times 10^{-26}$	$(1159.652193 \pm 0.000010) \times 10^{-6}$
$\mu$	$(3.7 \pm 3.4) \times 10^{-19}$	$(1165.9230 \pm 0.0084) \times 10^{-6}$
$\tau$	$< 1.6 \times 10^{-16}$ (90%C.L.)	$< 0.12$ (90%C.L.)

Table 2.5: *The experimental measurements of electric dipole and magnetic moments of leptons [20]. The measurements for the electron and the muon moments come from  $g - 2$  experiments.*

Let us now see what would be the effect of excited leptons on the anomalous magnetic moment and electric dipole moment. By generalizing Eq. 2.3 to include vector and axial-vector contributions, the general form of the magnetic interaction  $l^*l\gamma$  between excited leptons, ordinary leptons and a photon is written as:

$$\mathcal{L}_{l^*l\gamma} = \frac{e\lambda_\gamma^l}{2m_{l^*}} \bar{\Psi}_{l^*} \sigma^{\mu\nu} (a_\gamma - b_\gamma \gamma_5) \Psi_l A_{\mu\nu} + h.c. \quad (2.33)$$

where  $\lambda_\gamma^l$  is the unitless coupling constant,  $m_{l^*}$  the mass of the excited lepton,  $a_\gamma$ ,  $b_\gamma$  are the vector and axial-vector couplings and  $A_{\mu\nu} = \partial_\mu A_\nu - \partial_\nu A_\mu$ . The following approximate relation holds in this context

$$\frac{1}{M} \approx \frac{f}{\Lambda} \equiv \frac{\lambda_\gamma^l}{m_{l^*}} \quad (2.34)$$

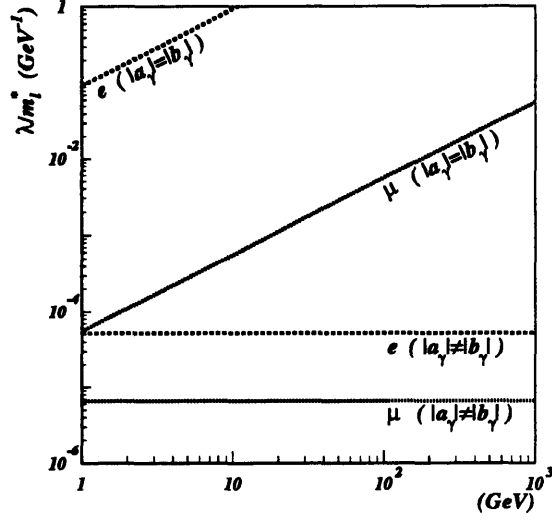


Figure 2-5: The limits on  $(\lambda \equiv \lambda_\gamma^{l^2} (|a_\gamma|^2 \pm |b_\gamma|^2))/m_{l^*}$  as a function of  $m_{l^*}$  from  $g-2$  experiments.

where  $f$  is a factor of order unity. The extra anomalous magnetic moment  $\chi_l^B$  and the electric dipole moment  $\chi_l^E$  of the ordinary leptons calculated with the inclusion of the  $ll^*\gamma$  contributions are[21]:

$$\chi_l^B \simeq \frac{16\alpha}{\pi} \lambda_\gamma^{l^2} (|a_\gamma|^2 - |b_\gamma|^2) \frac{m_l}{m_{l^*}} + \frac{18\alpha}{\pi} \lambda_\gamma^{l^2} (|a_\gamma|^2 + |b_\gamma|^2) \frac{m_l^2}{m_{l^*}^2} \quad (2.35)$$

$$\chi_l^E \simeq \frac{32\alpha}{\pi} \lambda_\gamma^{l^2} \Re e(a_\gamma b_\gamma^*) \left( \frac{m_l}{m_{l^*}} \right) \quad (2.36)$$

Comparing the measured values with the expected theoretical calculations of the anomalous magnetic moment, the 95% C.L. limits for an extra anomalous moment of the electron and muon are derived to be :  $\delta a_e < 10^{-9}$  and  $\delta a_\mu < 26 \times 10^{-9}$ . For the previous limits, the experimental and theoretical errors have been added in quadrature. To interpret the results in terms of limits on the mass of excited leptons, we note that the expression for  $\chi_l^B$  is actually composed of two parts, one proportional to  $m_l/m_{l^*}$  and a second proportional to  $(m_l/m_{l^*})^2$ . Two cases are distinguished:

- $a_\gamma$  or  $b_\gamma$  is sizable, i.e.  $|a_\gamma|/|b_\gamma| \gg 1$  or  $|a_\gamma|/|b_\gamma| \ll 1$  : this leads to an anomalous magnetic moment at order  $m_l/m_{l^*}$ . The limits are:

$$\lambda_\gamma^{e^2} (|a_\gamma|^2 - |b_\gamma|^2) / m_{e^*} < \frac{1}{19 \text{ TeV}} \quad (2.37)$$

$$\lambda_\gamma^{\mu^2} (|a_\gamma|^2 - |b_\gamma|^2) / m_{\mu^*} < \frac{1}{151 \text{ TeV}} \quad (2.38)$$

- $|a| \approx |b|$  : this leads to a vanishing of the order  $m_l/m_{l^*}$  and leaves only the contribution  $(m_l/m_{l^*})^2$ . This case exhibits chiral symmetry, i.e. the left(right)-handed ordinary fermions couple to the left(right)-handed excited leptons similarly. The limits are:

$$\lambda_\gamma^{e^2} (|a_\gamma|^2 + |b_\gamma|^2) / m_{e^*}^2 < \frac{1}{(3.3 \text{ GeV})^2} \quad (2.39)$$

$$\lambda_\gamma^{\mu^2} (|a_\gamma|^2 + |b_\gamma|^2) / m_{\mu^*}^2 < \frac{1}{(134 \text{ GeV})^2} \quad (2.40)$$

In Figure 2-5 the 95% C.L. exclusion regions are shown as a function of the excited lepton mass. It is obvious from the figure that the chiral symmetric scenario is less strongly constrained than the first case due to the cancellation of the term at order  $m_l/m_{l^*}$ . In the direct searches that we will undertake below, we will always consider the case where  $|a| = |b|$ .

Using the expression  $d_l = \chi_l^E / 2m_l$  where  $d_l$  is the electric dipole moment, similar limits on the coupling constants can be derived. Specifically, one finds:

$$\lambda_\gamma^{e^2} \Re(a_\gamma b_\gamma^*) / m_{e^*} < \frac{1}{5 \times 10^{10} \text{ GeV}} \quad (2.41)$$

$$\lambda_\gamma^{\mu^2} \Re(a_\gamma b_\gamma^*) / m_{\mu^*} < \frac{1}{700 \text{ GeV}} \quad (2.42)$$

It is more difficult to extract limits on the mass of the excited lepton via these constraints since the relative phase of  $a_\gamma$  and  $b_\gamma$  are not known.

### 2.3.2 The process $e^+e^- \rightarrow l^*\bar{l}^*$

Spin-1/2 excited states have been assumed. For simplicity, the excited states are also imposed to have weak isospin 1/2 keeping in mind that higher isospin assignments are also possible[18] but that the experimental signatures are not affected by these. We have seen in Section 2.3.1 that the  $g - 2$  measurements impose strict limits on excited leptons but that these limits are weakened in the presence of chiral symmetry, that was expressed as  $|a| = |b|$  in the Lagrangian 2.33.

Unlike the case of ordinary leptons where the left-handed states form a weak isodoublet and the right-handed states form a weak singlet, the existence of chiral symmetry imposes that both the left-handed and right-handed states of excited leptons are in weak isodoublets:

$$l_L = \begin{pmatrix} \nu_l \\ l \end{pmatrix}; \quad l_R; \quad L_L = \begin{pmatrix} \nu_l^* \\ l^* \end{pmatrix}_L; \quad L_R = \begin{pmatrix} \nu_l^* \\ l^* \end{pmatrix}_R$$

The excited leptons are ‘homodoublets’ since their left and right components have the same quantum numbers. In analogy to the electroweak interactions of ordinary leptons (see Eq. 2.5), the  $SU(2) \times U(1)$  interaction Lagrangian for the couplings of

excited leptons to ordinary gauge bosons is given by [22]:

$$\begin{aligned} \mathcal{L}_{l^* \bar{l}^*} &= \bar{L} \gamma^\mu \left[ g \frac{\vec{\tau}}{2} \vec{W}_\mu + g' \frac{Y}{2} B_\mu \right] L \\ &+ g \frac{\kappa}{2m_{l^*}} \bar{L} \frac{\vec{\tau}}{2} \sigma^{\mu\nu} \partial_\mu \vec{W}_\nu L + g' \frac{\kappa'}{2m_{l^*}} \bar{L} \frac{Y}{2} \sigma^{\mu\nu} \partial_\mu B_\nu L \end{aligned} \quad (2.43)$$

where  $L = L_R + L_L$  and  $\kappa, \kappa'$  are anomalous magnetic moments included because of the composite nature of the particles. Because both right and left handed excited leptons contribute in  $L$ , the pair production of excited leptons from a gauge boson is necessarily vector-like. In addition to this gauge interaction, there is a possibility to have 'contact' interactions [23] that could arise from the interchange of the more elementary constituents. The latter forces are not considered here. Equation 2.43 can be expressed as an effective Lagrangian of the form[22]:

$$\mathcal{L}_{l^* \bar{l}^*, eff} = \sum_{V=\gamma, Z} e \bar{F} \left[ (A_{VF} + B_{VF} \gamma_5) \gamma^\mu V_\mu + \frac{\kappa_{VF}}{2m_F} \sigma^{\mu\nu} \partial_{\mu\nu} V_\nu \right] F \quad (2.44)$$

where  $B_{VF}$  vanishes since excited leptons are homodoublets.  $A_{VF}, B_{VF}$  and  $\kappa_{VF}$  for excited charged leptons and excited neutrinos, expressed in terms of the previous variables, have the following values:

	$V = \gamma$	$V = Z^0$
$\kappa_{Vl^*}$	$-\frac{1}{2}(\kappa + \kappa')$	$\frac{1}{2}(\kappa' \tan \theta_W - \kappa \cot \theta_W)$
$A_{Vl^*}$	-1	$\frac{2 \sin^2 \theta_W - 1}{2 \sin \theta_W \cos \theta_W}$
$B_{Vl^*}$	0	0
$\kappa_{V\nu^*}$	$\frac{1}{2}(\kappa - \kappa')$	$\frac{1}{2}(\kappa' \tan \theta_W + \kappa \cot \theta_W)$
$A_{V\nu^*}$	0	$\frac{1}{2 \sin \theta_W \cos \theta_W}$
$B_{V\nu^*}$	0	0

With this notation, the couplings of the excited leptons to the physical state gauge bosons are clear.

In  $e^+e^-$  collisions, excited fermions can be pair produced through the s-channel gauge boson exchange (see Figure 2-6) if their masses are smaller than the beam energy. For the pair of charged fermions, the process can proceed through  $\gamma$  or  $Z^0$  exchange. For the excited electron, pair production is also possible through t-channel exchanges of a  $\gamma$  or a  $Z^0$  because of the existence of the coupling  $l^*V$  (see Sections 2.3.1 and 2.3.3) but these can be safely neglected as their contributions are much smaller than the s-channel diagrams since suppressed by a power  $(\lambda/m_{e^*})^4$ . In any case, if the t-channel were of any significance for the double production mechanism, then excited fermions would be much more copiously produced singly (see Section 2.3.3).

If the excited fermions have the 'standard' vectorial couplings, that is, if  $\kappa_{\gamma F} = \kappa_{ZF} = 0$  in Eq. 2.44, the differential cross section exhibits a behavior of the type  $1 + (1 - 4\eta) \cos^2 \theta$  where  $\theta$  is the scattering angle of the excited lepton with respect

to the beam axis and  $\eta = m_{i^*}^2/M_Z^2$ . In particular, there is no forward-backward asymmetry because of the vectorial nature of the couplings contrary to the production of a sequential family lepton.

In the presence of possibly large magnetic moments, the angular distribution can be distorted. The differential cross section is then[22]<sup>1</sup>:

$$\frac{d\sigma}{d\cos\theta} = \pi\alpha^2\beta s \sum_{V,V'} \chi_V(s)\chi_{V'}^*(s)(B_0 + B_1 \cos\theta + B_2 \cos^2\theta) \quad (2.45)$$

where  $\beta = \sqrt{1 - 4\eta}$ ,  $\eta = m_{i^*}^2/M_Z^2$  and

$$B_0(V, V') = ((v_V^e)(v_{V'}^e)^* + (a_V^e)(a_{V'}^e)^*) [(A_V + \kappa_V)(A_{V'}^* + \kappa_{V'}^*) - \frac{\beta^2}{2}(A_V A_{V'}^* - B_V B_{V'}^*) - \frac{1}{4\eta}\kappa_V \kappa_{V'}^*] \quad (2.46)$$

$$B_1(V, V') = \beta ((v_V^e)(a_{V'}^e)^* + (a_V^e)(v_{V'}^e)^*) [(B_V + \kappa_V)A_{V'}^* + A_V(B_{V'}^* + \kappa_{V'}^*)] \quad (2.47)$$

$$B_2(V, V') = \frac{\beta^2}{2} ((v_V^e)(v_{V'}^e)^* + (a_V^e)(a_{V'}^e)^*) \left[ A_V A_{V'}^* + B_V B_{V'}^* - \frac{1}{4\eta}\kappa_V \kappa_{V'}^* \right] \quad (2.48)$$

where  $v_V^e$  and  $a_V^e$  are the coupling of the ordinary electron to the gauge boson V and  $\chi_V(s) = (s - M_V^2 + iM_V\Gamma_V)^{-1}$ . In our case  $B_{VF} = 0$  and a non-vanishing forward-backward asymmetry  $A_{FB} \propto B_1$  implies non-zero magnetic moments. The total cross section can be readily integrated:

$$\sigma = 2\pi\alpha^2 s\beta \sum_{V,V'} \chi_V(s)\chi_{V'}^*(s)(B_0 + \frac{1}{3}B_2) \quad (2.49)$$

### 2.3.3 The process $e^+e^- \rightarrow l^{*+}l^-, l^{*-}l^+$

The Lagrangian describing the transition between excited leptons and ordinary leptons should respect the chiral symmetry to protect the light leptons from radiatively acquiring large anomalous magnetic moments that are incompatible with the strong  $g - 2$  experiments' measurements (see Section 2.3.1). This implies that only the right-handed parts of the excited leptons take part in the interaction.

The form of the  $l^*lV$  interaction can be generalized from Eq. 2.33 within the Standard Model framework and expressed in a  $SU(2) \times U(1)$  invariant form as:

$$\mathcal{L}_{ff^*} = \frac{gf}{2\Lambda} \bar{L}\sigma^{\mu\nu}\vec{\tau} l_L \partial_\mu \vec{W}_\nu + \frac{g'f'}{2\Lambda} \bar{L}\sigma^{\mu\nu} Y l_L \partial_\mu B_\nu + h.c. \quad (2.50)$$

$\Lambda$  is the interaction scale and the  $f, f'$  parameters allow for different scales associated to the  $SU(2)$  and  $U(1)$  groups.  $g, g'$  are the Standard Model  $SU(2) \times U(1)$  coupling constants,  $\vec{\tau}$  are the Pauli matrices and  $Y = -\frac{1}{2}$  is the hypercharge.

<sup>1</sup>Note that there is an error in the definition of  $B_1$  of Ref. [22], page 118

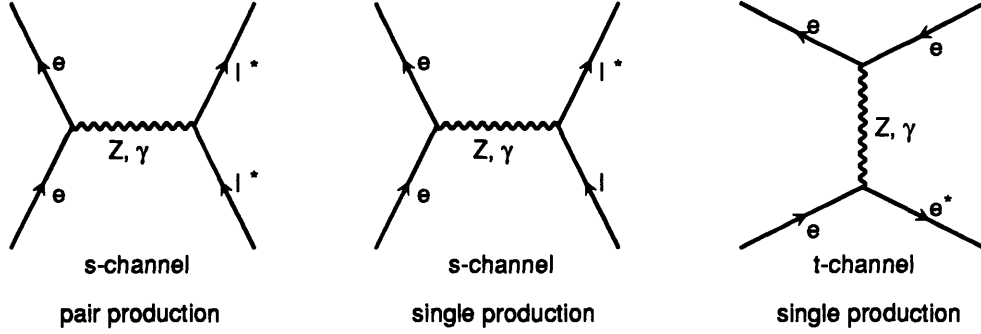


Figure 2-6: *The lowest order Feynman diagrams for (left to right) pair production s-channel, single production s-channel and single production t-channel.*

In a similar way as in the standard couplings, the interaction can be rewritten as an effective Lagrangian in terms of the physical gauge bosons:

$$\mathcal{L}_{l^*l,eff} = \sum_{V=\gamma,Z,W} \frac{e}{2\Lambda} \bar{L} [(C_{Vll^*} - D_{Vll^*} \gamma_5) \sigma^{\mu\nu} \partial_\mu V_\nu] l_L + h.c. \quad (2.51)$$

The chiral symmetry imposes that  $|C_{Vll^*}| = |D_{Vll^*}|$  and in terms of the previous parameters, the coupling constants are:

$$\begin{aligned} C_{\gamma ll^*} &= -\frac{1}{2}(f + f') \\ C_{Z ll^*} &= -\frac{1}{2}(f \cot \theta_W - f' \tan \theta_W) \\ C_{W \nu l^*} &= -\frac{f}{\sqrt{2} \sin \theta_W} \\ C_{\gamma \nu \nu^*} &= -\frac{1}{2}(f - f') \\ C_{Z \nu \nu^*} &= -\frac{1}{2}(f \cot \theta_W + f' \tan \theta_W) \\ C_{W l \nu^*} &= -\frac{f}{\sqrt{2} \sin \theta_W} \end{aligned} \quad (2.52)$$

A natural choice where  $f = f'$  leads to the absence of tree-level coupling between the excited neutrino and the photon, i.e., the decay  $\nu^* \rightarrow \nu \gamma$  is highly suppressed. The decay through the weak bosons,  $\nu^* \rightarrow \nu Z^0$  and  $\nu^* \rightarrow l W$  remain allowed.

Under this assumption which we will make in the following, the parameter  $f$  is the only free coupling in the Lagrangian and for charged leptons and it is related to the coupling strength by:

$$\frac{f}{\Lambda} \equiv \frac{\lambda_\gamma}{m_{l^*}} \quad (2.53)$$

$$\frac{f}{\Lambda} \equiv \frac{\lambda_Z}{m_{l^*}} \times \frac{2}{\cot \theta_W - \tan \theta_W} \quad (2.54)$$

$$\frac{f}{\Lambda} \equiv \frac{\lambda_W}{m_{l^*}} \times \sqrt{2} \sin \theta_W \quad (2.55)$$

Our results will be expressed in terms of  $\lambda_V/m_{l^*}$  which are model independent.

In  $e^+e^-$  annihilation, excited leptons can be produced *singly* in association with their ordinary partners in the reactions

$$e^+e^- \rightarrow Z^0 \rightarrow l^*l \quad (2.56)$$

$$e^+e^- \rightarrow \gamma^* \rightarrow l^*l \quad (2.57)$$

where  $l^*l \equiv l\bar{l}^* + \bar{l}l^*$ . The lowest order Feynman diagrams contributing to  $e^+e^- \rightarrow e^*e^-$  and  $e^+e^- \rightarrow l^*l^-$  ( $l \neq e$ ) are shown in Figure 2-6. In principle, masses up to the total energy of the collision may be probed. The production rate depends on the parameter  $\lambda_V^l/m_{l^*}$  which measures the strength of the transition. While all production mechanisms at the  $Z^0$  peak proceed through s-channel  $Z^0$  exchange, for the first generation there is the additional t-channel  $\gamma$  exchange contribution which should be taken into account.

The differential cross sections for the processes via photon exchange are calculated using the formula in Ref. [22] (Eq. 3.1) which includes the s,t channels and their interference term:

$$\begin{aligned} \left( \frac{d\sigma^{e^*e}}{dt} \right)_\gamma &= \frac{2\pi\alpha^2\lambda_\gamma^{e^2}}{m_e^2 s} \left[ \frac{(m_e^2(s - m_e^2) + 2t(m_e^2 - s - t))}{s} + \right. \\ &\quad \left. \frac{(m_e^2(t - m_e^2) + 2s(m_e^2 - s - t))}{t} + \right. \\ &\quad \left. 2(m_e^2 - s - t) - \frac{2m_e^4 m_e^2}{t^2} \right] \quad (2.58) \end{aligned}$$

$$\left( \frac{d\sigma^{l^*l}}{dt} \right)_\gamma = \frac{2\pi\alpha^2\lambda_\gamma^{l^2}}{m_e^2 s^3} [m_{l^*}^2(s - m_{l^*}^2) - 2t(s + t - m_{l^*}^2)] \quad (2.59)$$

where  $s$  and  $t$  are the Mandelstam variables  $s = (p_1^\mu + p_2^\mu)^2$  and  $t = (p_1^\mu - p_3^\mu)^2$ . The terms proportional to the ordinary electron mass have been neglected except for the term proportional to  $m_e^2$  in Eq. 2.58 which is important for the t-channel exchange[22]. For the s-channel  $Z^0$  exchange, the differential cross section for all three leptons is:

$$\begin{aligned} \left( \frac{d\sigma^{l^*l}}{dt} \right)_{Z^0} &= \frac{2\pi\alpha^2\lambda_Z^{l^2}}{m_{l^*}^2 s |\chi(s)|^2} \left[ 2(A^2 + B^2) (m_{l^*}^2(s - m_{l^*}^2) + 2tm_{l^*}^2 - 2ts - 2t^2) \right. \\ &\quad \left. + 4ABm_{l^*}^2 (2t + s - m_{l^*}^2) \right] \quad (2.60) \end{aligned}$$

where  $A$  and  $B$  are the Standard Model couplings to the electron:

$$A = \frac{1 - 4 \sin^2 \theta_W}{4 \sin \theta_W \cos \theta_W}, \quad B = \frac{1}{4 \sin \theta_W \cos \theta_W}. \quad (2.61)$$

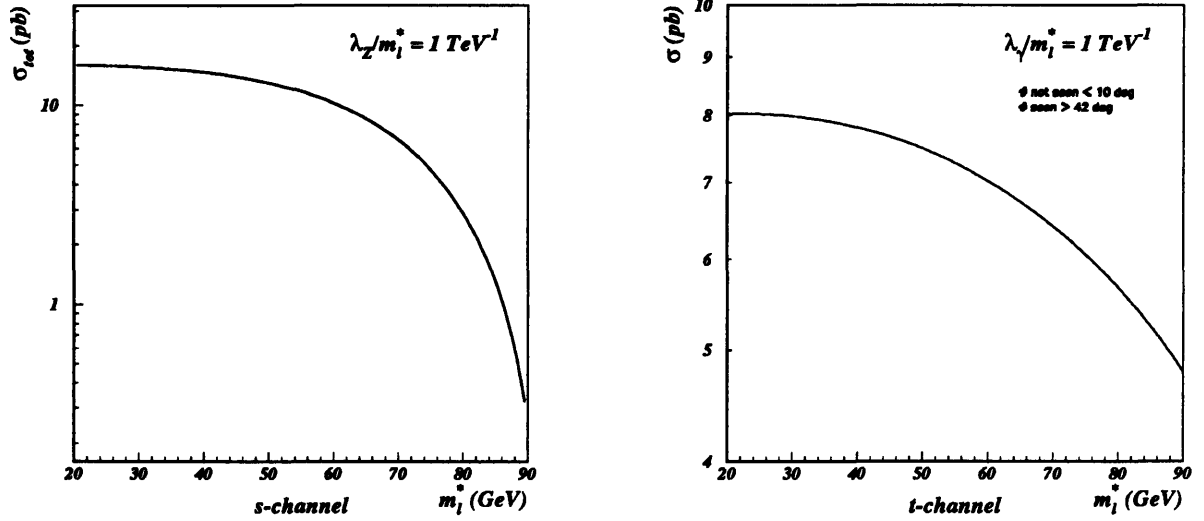


Figure 2-7: The  $s$  and  $t$ -channel cross sections for the single production of excited leptons with  $\lambda/m_{l^*} = 1 \text{ TeV}^{-1}$ . Without angular restrictions, the total  $e^*$   $t$ -channel cross section is approximately a factor 2 higher.

The differential cross section can be integrated to yield the total cross section. For the  $t$ -channel exchange, care must be taken to avoid divergences. The details of the integrations are shown in Appendix A. The results are:

$$(\sigma^{l^*l})_{\gamma} = \frac{2\pi\alpha^2\lambda_{\gamma}^{l^*2}}{3m_{e^*}^2s^3}(m_{e^*}^2 - s)^2(2m_{e^*}^2 + s) \quad (2.62)$$

$$(\sigma^{l^*l})_{Z^0} = \frac{4\pi\alpha^2\lambda_Z^{l^*2}}{3m_{l^*}^2s|\chi(s)|^2}(A^2 + B^2)(m_{l^*}^2 - s)^2(2m_{l^*}^2 + s) \quad (2.63)$$

$$(\sigma^{e^*e})_{\gamma} = \frac{2\pi\alpha^2\lambda_{\gamma}^{e^*2}}{3m_{e^*}^2s^3} \left( 3s \ln \left[ \frac{t_{min}}{m_{e^*}^2 - s} \right] (-m_{e^*}^4 + 2m_{e^*}^2s - 2s^2) - (m_{e^*}^2 - s)(2m_{e^*}^4 - 7m_{e^*}^2s + 8s^2) \right) \quad (2.64)$$

where  $t_{min} = t(\theta = 0)$  (see Appendix). For a given value of  $\lambda/m_{l^*} = 1 \text{ TeV}^{-1}$ , the  $s$  and  $t$ -channel cross sections are respectively shown in Figures 2-7.

### 2.3.4 Decays of excited states $l^* \rightarrow lV$

Excited leptons decay into light ordinary leptons and a virtual or real gauge boson. The heavy gauge boson subsequently decays into a pair of fermions yielding the final states  $l^* \rightarrow lf\bar{f}$  and  $l^* \rightarrow \nu ff'$ . The Feynman diagrams for these decays are shown in Figure 2-8.

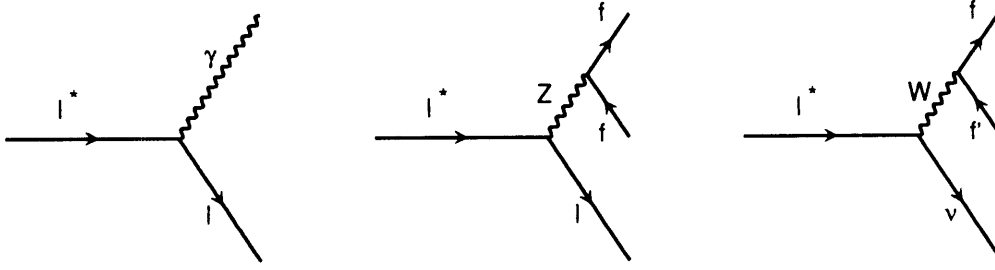


Figure 2-8: *The lowest order Feynman diagrams for the decays of excited leptons into an ordinary lepton and a gauge boson.*

The decay width for  $l^* \rightarrow l\gamma$  is:

$$\Gamma(l^* \rightarrow l\gamma) = \frac{\alpha}{4} \left( \frac{\lambda_\gamma}{m_{l^*}} \right)^2 m_{l^*}^3 \quad (2.65)$$

The details of its derivation are given in Appendix B. The decay width into a real massive gauge boson  $l^* \rightarrow lV$  where  $V = Z^0, W$  is[24]:

$$\Gamma(l^* \rightarrow lV) = \frac{\alpha}{4} \left( \frac{\lambda_V}{m_{l^*}} \right)^2 m_{l^*}^3 \left( 1 - \frac{M_V^2}{m_{l^*}^2} \right)^2 \left( 1 + \frac{M_V^2}{2m_{l^*}^2} \right) \quad (2.66)$$

The decay into a virtual gauge boson occurs for  $m_{l^*} < M_V$  even though it is suppressed by the virtual boson propagator. This latter width is:

$$\Gamma(l^* \rightarrow lV^*) = \Gamma(l^* \rightarrow lV) \frac{M_{V^*}^4}{(M_{V^*}^2 - M_V^2)^2 + (M_V \Gamma_V)^2} \quad (2.67)$$

The branching ratios  $Br(l^* \rightarrow l\gamma)$ ,  $Br(l^* \rightarrow lZ^0)$  and  $Br(l^* \rightarrow \nu W)$  as a function of the  $l^*$  mass are shown in Figure 2-9. The relation between the coupling constants of the photon and electroweak gauge bosons to the  $l^*$  has been assumed in these plots (see Eqs. 2.52).

The photonic decay mode is dominant for masses below  $M_W$  and decreases above  $M_W$  due to the decay  $l^* \rightarrow \nu W^*$ . The decay involving a  $Z^0$  boson is always suppressed.

The mean decay paths of the excited leptons are very small (see Appendix B). This means that the produced particles always decay very close to the interaction point and we will assume that their lifetimes are negligible.

We will consider only photonic decays of excited leptons which as we have shown are expected to be dominant. If desired, our results can be reinterpreted in terms of a general branching ratio by the following substitution

$$\frac{\lambda}{m_{l^*}} \rightarrow \frac{\lambda}{m_{l^*}} \times \frac{1}{Br(l^* \rightarrow l\gamma)} \quad (2.68)$$

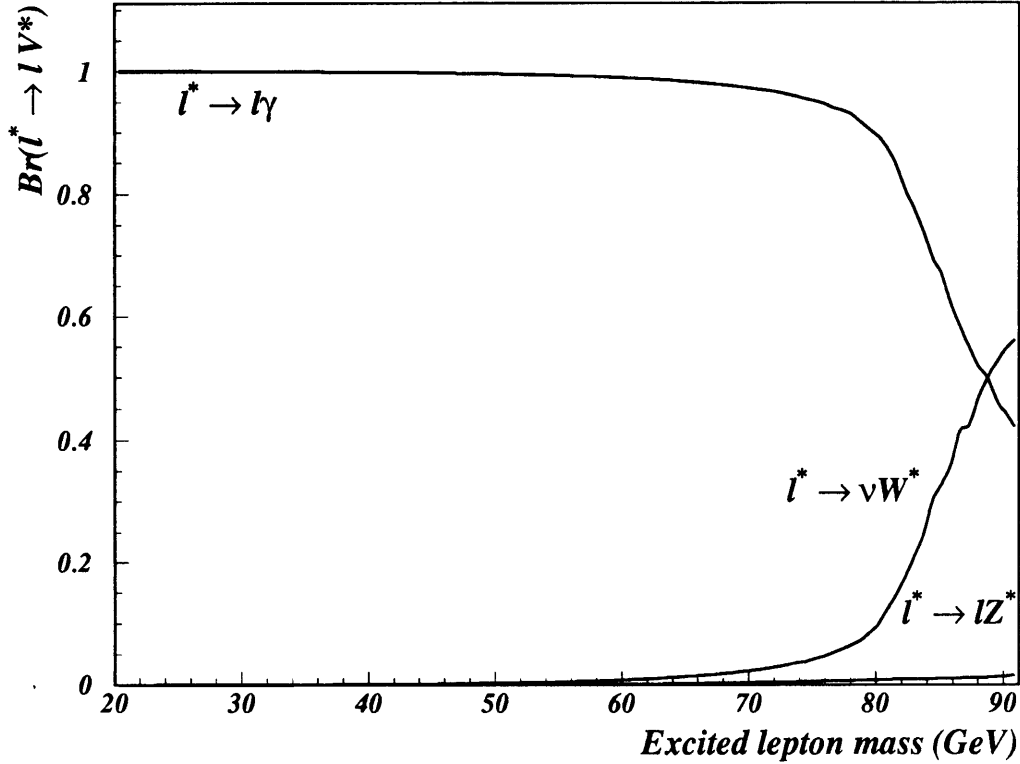


Figure 2-9: The predicted branching ratios  $Br(l^* \rightarrow l\gamma)$ ,  $Br(l^* \rightarrow lZ^0)$  and  $Br(l^* \rightarrow \nu W)$  as a function of the  $l^*$  mass. The relation between the coupling constants of the photon and electroweak gauge bosons to the  $l^*$  has been assumed.

where  $Br(l^* \rightarrow l\gamma)$  is the photonic branching ratio. It should be also noted that for masses above  $M_W$  one could in principle improve the results by including the decay mode involving the  $W$  boson, i.e.  $l^* \rightarrow \nu W \rightarrow \nu ff'$ . In  $e^+e^-$  collisions, the signature is  $e^+e^- \rightarrow ll^* \rightarrow l\nu ff'$ . For the interesting masses, the  $W$  boson is almost at rest in the laboratory frame and also the neutrino is kinematically restrained from taking much energy. Unless the leptonic decay modes of the  $W$  are considered, the search for the signal will be largely hampered by the hadronic  $Z^0$  decays with an inclusive lepton (the biggest background is expected to be  $Z^0 \rightarrow b\bar{b}, c\bar{c}$  where the heavy flavor decays leptonically).

### 2.3.5 The electromagnetic properties of the $\tau$

The electromagnetic properties of the  $\tau$  lepton, i.e. the magnetic and electric dipole moments, cannot be readily probed in a g-2 type of experiment since the life-time of the tau is too short ( $c\tau = 91.4 \mu\text{m}$ ).

In [25], it is suggested that the study of the process  $Z^0 \rightarrow \tau^+\tau^-\gamma$  gives information on the electromagnetic properties of the tau. The current for photon emission with an anomalous term is

$$e\bar{u}(p') \left( \gamma^\mu + i \frac{F_2(q^2)}{2m_\tau} \sigma^{\mu\nu} q_\nu \right) u(p) \quad (2.69)$$

where  $p$  and  $p'$  are the four-momenta of the tau and  $q$  the one of the photon. For a real photon, one has  $q^2 = 0$ , such that  $F_2(0)$  is probed, i.e. the static anomalous magnetic moment. The term proportional to  $\gamma^\mu$  yields the “standard” bremsstrahlung emission of photons, infrared divergent. The anomalous contribution to the partial width  $\Gamma_{ano}(Z^0 \rightarrow \tau^+\tau^-\gamma)$  evaluates as[25]:

$$\Gamma_{ano} = \frac{\alpha^2 F_2(0)^2 M_Z^3}{64\pi \sin^2 \theta_W \cos^2 \theta_W m_\tau^2} \frac{1}{4} \left[ (g_V^2 + g_A^2) - \frac{1}{9}(g_V^2 - g_A^2) \right] \quad (2.70)$$

The energy distribution of the photons from the anomalous term is uniform, in striking contrast to standard term where soft photons are favored.

The existence of an electric dipole moment of the tau results in the anomalous current term

$$e\bar{u}(p') \left( iF_{EDM}(q^2) \sigma^{\mu\nu} \gamma_5 q_\nu \right) u(p). \quad (2.71)$$

which yields an anomalous partial width

$$\Gamma_{EDM} = \frac{\alpha^2 F_{EDM}^2 M_Z^3}{32\pi \sin^2 \theta_W \cos^2 \theta_W} \frac{1}{4} \left[ (g_V^2 + g_A^2) - \frac{1}{9}(g_V^2 - g_A^2) \right]. \quad (2.72)$$

## 2.4 Composite Gauge Bosons

The discovery of the  $W^\pm$  and  $Z^0$  bosons[26] at the masses predicted by the Standard Model and the agreements between theory and the experiments that have been undertaken since then, seem to indicate that there is not much room left for alternative gauge boson models. The perfect agreements of the  $Z^0$  lineshape precisely measured at LEP[27] with the predicted values make us confident that we understand the nature of the  $Z^0$  intermediate gauge boson. Though less precise, the results on the  $W^\pm$  boson at  $p\bar{p}$  machines also confirm the Standard Model predictions with good accuracy[26].

There are still, however, at least two essential missing ingredients that need verification:

- a mechanism for acquiring mass
- couplings between gauge bosons  $W^+W^-Z^0$ ,  $W^+W^-\gamma$

Within the Standard Model, the gauge bosons  $W^\pm$  and  $Z^0$  are point-like particles which acquire mass when the symmetry  $SU(2)_L \times U(1)_Y$  is spontaneously broken (see Section 2.2.1). Since there is at the moment no experimental evidence for a scalar Higgs boson, models where masses are acquired differently must be tested.

The non-Abelian structure of the  $SU(2)_L \times U(1)_Y$  theory predicts the tri-linear weak boson couplings  $WW\gamma$  and  $WWZ^0$ . At the  $Z^0$  pole, it is not possible to test these tri-linear couplings directly. The decays  $Z^0 \rightarrow W + X \rightarrow e\nu + X$  have branching ratios of the order of  $10^{-8}$ [16], well below the observable rates. The tri-linear couplings will be probed in  $e^+e^-$  collisions during the second phase of LEP (LEP 200) where the center-of-mass energy will be sufficient to produce pairs of gauge bosons. Until then, the actual constraints on possible anomalous contributions to the tri-linear couplings are expressed quantitatively through the magnetic moment  $\mu_W$  and quadrupole moment  $Q_W$  of the  $W$ , which are given by:

$$\mu_W = \frac{e(1 + \kappa + \lambda)}{2M_W} \quad (2.73)$$

and

$$Q_W = \frac{-e(\kappa - \lambda)}{M_W^2} \quad (2.74)$$

At tree level, the Standard Model values are  $\kappa = 1$  and  $\lambda = 0$ . The present limits [28]:

$$-3.5 < \kappa < 5.9 \quad (2.75)$$

and

$$-3.6 < \lambda < 3.5 \quad (2.76)$$

remain rather weak. At the moment no deviations are seen.

Since the mechanism that induces mass to the gauge bosons is not understood and that their gauge nature has not been directly tested via the tri-linear couplings, a solution where the gauge bosons are composite particles cannot be ruled out.

## 2.4.1 Composite models

In this section, we review some of ideas behind the many phenomenological models for composite gauge bosons[29, 30, 31]. In general, the composite scenarios are motivated by the wish to decouple the massless, elementary photon from the massive, composite weak gauge bosons. The  $W^\pm$  and  $Z^0$  are postulated as the lowest states of fermionic constituents bound together by a new strong force called “hypercolor” which only manifests itself at a large energy scale  $\Lambda_H$ . The subconstituents  $\alpha$  and  $\beta$  carrying hypercolor are the “haplons”[29].

The dynamics of subconstituents can be described by the gauge group  $U(1)_{EM} \times SU(3)_{Color} \times G_H$  where  $G_H$  is the hypercolor gauge group which is responsible for the binding of the subconstituents. In most models, the gauge bosons are composed of two subconstituents in haplon and anti-haplon bound states[29, 31]:

$$W^+ = \alpha\bar{\beta}; \quad W^0 = \frac{1}{\sqrt{2}}(\alpha\bar{\alpha} - \beta\bar{\beta}); \quad W^- = \beta\bar{\alpha} \quad (2.77)$$

With this notation, the analogy with the  $\rho$ -meson in QCD is apparent. At tree level the masses are all identical and the mass splitting between the  $W^\pm$  and the  $Z^0$  bosons arises in these models as a perturbation when the electromagnetic interaction is turned on. The mixing of the weak interaction with the photon is explained via annihilation of the subconstituents like in the Vector Meson Dominance[32] of the  $\rho$  meson (see Figure 2-10). Note that just as in QCD where each loop contains three colors, the haplon loop can contain a large number of hypercolors and/or colors. It is one of the problems of these composite models to explain the observed mass ratio between the gauge bosons, or in other terms, to correctly predict the value of  $\sin \theta_W$ . Here, authors give different possibilities[29, 31] and the results are specific model dependent. The general idea is that the relatively large value of  $\sin \theta_W$  can be accommodated by the proper choice of hypercolors and colors even though the responsible force is electromagnetic in strength. As an example, we quote[33]:

$$\sin^2 \theta_W = \frac{e^2 F_W}{g M_W}$$

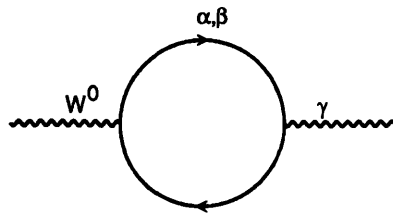


Figure 2-10: *The mixing between the neutral weak boson and the photon in a composite model[31]. The fermion  $\alpha$  and  $\beta$  are the haplon subconstituents. In QCD, the  $\rho\gamma$  mixing occur through a similar loop composed of  $u$  and  $d$  quarks.*

$$= \frac{e^2}{g} (N_H N_C)^{1/2} \left( \frac{2}{M_W^3} \right)^{1/2} \frac{\phi(0)}{(4\pi)^{1/2}} \quad (2.78)$$

where  $g$  is the weak coupling constant,  $F_W$  is the  $W$  decay constant,  $\phi(0)$  is its wave function at the origin,  $N_C$  the number of colors and  $N_H$  the number of hypercolors. It should be stressed that the charged  $Q_H$  of the haplons does not appear in the expression of  $\sin^2\theta_W$  and that they can be therefore large, with the sole constraint that  $|Q_\alpha - Q_\beta| = 1$  to recover the charge of the  $W^\pm$  bosons.

The observability of the gauge boson substructure will clearly depend on the scale  $\Lambda_H$ . At LEP I, we expect to be able to study the compositeness of the  $Z^0$  and therefore limit ourselves to this case. Possible signatures were investigated [33, 31] and led to the predictions that anomalies were most promisingly to be searched in final states involving one or many photons[34].

We shall investigate the decays  $Z^0 \rightarrow \gamma\gamma\gamma$  and  $Z^0 \rightarrow l^+l^-\gamma$  within composite scenarios.

### 2.4.2 The process $Z^0 \rightarrow \gamma\gamma\gamma$

Because the rate within the Standard Model is so low (see Section 2.2.6), the observation of such a decay could only be explained through new physics. It is therefore considered as the 'gold-plated' signal to look for compositeness at LEP I.

In composite models, the decay to three photons, as illustrated in Figure 2-11, can be large due to the direct coupling of the photons with the haplons  $\alpha, \beta$  of charge  $Q_\alpha, Q_\beta$ . The decay width is [33]:

$$\Gamma_{Z^0 \rightarrow \gamma\gamma\gamma} \approx \left( \frac{64\alpha^3 \langle Q^3 \rangle^2}{9M_Z^2} \right) \frac{(\pi^2 - 9) N_H N_C |\phi(0)|^2}{4\pi} \quad (2.79)$$

where  $\langle Q \rangle$  is the average charge of the subconstituents inside the composite  $Z^0$  and  $N_H(N_C)$  is the number of hypercolors(colors).

Using the expression Eq. 2.78, the decay width is [33]:

$$Br(Z^0 \rightarrow \gamma\gamma\gamma) \simeq \mathcal{O}(0.3 \times 10^{-4}) \quad (2.80)$$

which is many orders of magnitude larger than the Standard Model expectation. Although this number is an order of magnitude estimate, it is clear that should the

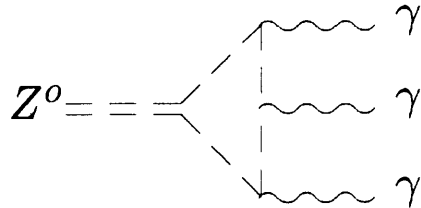


Figure 2-11: The diagram  $Z^0 \rightarrow \gamma\gamma\gamma$  in the composite model.

$Z^0$  have substructure, the decay rate of  $Z^0 \rightarrow \gamma\gamma\gamma$  will nonetheless be enhanced from the Standard Model value. Thus this decay is an excellent probe for radically new physics, as it would be an unambiguous sign of compositeness. As mentioned in Section 2.2.6, the QED process  $e^+e^- \rightarrow \gamma\gamma(\gamma)$  is a source of three photon final states but as we will see with a very different kinematical distribution of the photons.

### 2.4.3 The process $Z^0 \rightarrow \gamma l^+ l^-$

The process  $Z^0 \rightarrow \gamma l^+ l^-$  where the photon is emitted directly by the haplons (internal line radiation) can occur provided that a parity breaking leads to a mixing between possible internal states of angular momentum  $^3S_1 - ^3P_1$  because only the spin-parity  $1^{++}$  can decay directly to what is effectively a two-photon final state.

The differential photon branching ratio for this process is [33]:

$$\frac{dB}{dz} \approx \left( \frac{256\alpha^3 \langle Q^3 \rangle^2 M_Z}{2\Gamma_Z} \right) \frac{N_H N_C |\phi'(0)|^2}{4\pi M_Z^5} \quad (2.81)$$

where  $z = (k^2/m_Z^2)$  and  $k^2$  is the lepton pair invariant mass. The expression is aimed at and valid for  $z \ll 1$ , i.e., where the Standard Model background is smallest. With some assumptions on the value of the derivative of  $\phi$  at the origin, the *flat* photon spectrum is predicted to be at the level of:

$$\frac{dB}{dz} \simeq \mathcal{O}(10^{-3}) \quad (2.82)$$

for  $z \ll 1$ .

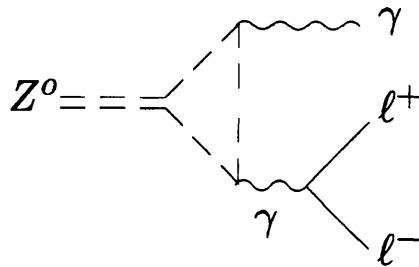


Figure 2-12: The diagram  $Z^0 \rightarrow \gamma l^+ l^-$  in the composite model.



# Chapter 3

## Experiment

### 3.1 LEP

LEP is the Large Electron Positron collider located at CERN on the French/Swiss border near Geneva, Switzerland. It is currently the largest storage ring in the world with a circumference of 26.7 km, capable of accelerating electrons and positrons up to center-of-mass energies of 120 GeV (phase I) and  $\geq 2M_W$  GeV (phase II). The tunnel is 50-70 m underground, with a 3.8 m bore. See Figure 3-2. The electron and positron beams are controlled with approximately 3400 dipole bending magnets and over 1300 focusing quadrupole and hexapole magnets. The main LEP parameters for Phase I are given in Table 3.1.

The injection chain begins with a linear accelerator which produces a 200 MeV, 100 Hz beam of electrons which is shot onto a tungsten target to produce positrons. The electrons and the outcoming positrons are accelerated to 600 MeV with another linac and are then injected into the Electron Positron Accumulation ring, where they are stored until approximately  $2 \times 10^{11}$  electrons and positrons are collected. These are then injected into the PS, (Proton Synchrotron) where they are accelerated to 3.5 GeV, and then into SPS, (Super Proton Synchrotron) where they are further accelerated to 20 GeV. At this point, they are injected into the LEP ring. The layout is given in Figure 3-3.

The 45 GeV electron and positron bunches circulate in the tunnel with an accuracy of  $\sigma_x = 250 \mu\text{m}$ ,  $\sigma_y = 15 \mu\text{m}$ , and  $\sigma_{beam} = 250 \text{ mm}$ . At this energy, the synchrotron radiation loss is approximately 120 MeV per turn. In order to compensate this loss 128 RF cavities give 1.6 MW of power at 350 MHz to accelerate the beams. The beam intensity eventually decreases due to beam-beam bremsstrahlung and after  $\sim 7$ -20 hours the beam is dumped and refilled.

The LEP beam energy is measured via a reference magnet which provides information on the integral field in the bending magnets yielding the particle momentum at central orbit. The reference magnet contains a flip-coil for field measurement. The dipole magnets contain a flux loop and a change in the flux is measured by applying a symmetric current cycle and integrating the induced voltage. Another method of energy calibration is the measurement of the revolution frequency of 20 GeV protons. Since protons are non-relativistic at this energy, a measurement of their revolution

circumference	26658.883 m
average radius	4242.893 m
revolution time	88.9245 $\mu s$
accelerating frequency	352.2 MHz
accelerating gradient	1.47 MV/m
nominal beam current	3 mA
injection energy	20 GeV
maximum beam energy	$\sim 60$ GeV
nominal luminosity	$1.7 \times 10^{31} \text{ cm}^{-2} \text{ s}^{-1}$
synchrotron radiation power	1.6 MW
horizontal betatron	70.44
vertical betatron	78.37
dipole bending radius	3096.175 m
dipole magnet field	0.06 T
bunches per beam	4 or 8
number of interaction points	4

Table 3.1: *LEP parameters (Phase I).*

frequency gives their momentum, which is the same for electrons and protons for a fixed magnet setting and orbit. These measurements yield a relative error at 45 GeV beam energy of  $3 \times 10^{-4}$ , thus the absolute beam energy is known to 20 MeV precision with an energy spread of  $\approx 10$  MeV. (For full details on LEP design and energy calibration see Refs. [35]). During the 1991 energy scan, improvements were made in the energy calibration which took into consideration temperature effects, tidal movements and local modifications to collision energies in individual interaction points. The result is an uncertainty of  $2\sigma = 5.3$  MeV at  $2E_{beam} = 93$  GeV for a systematic uncertainty in the  $Z^0$  mass of  $\approx 6.3$  MeV in its width of  $\approx 4.9$  MeV [36].

## 3.2 The L3 Detector

The L3 experiment is one of the four large detectors at LEP. It is the only detector that concentrates its efforts on limited goals of measuring electrons, muons and photons. By not attempting to identify hadrons, L3 has been able to provide an order of magnitude better resolution for electrons, muons and photons. The construction of L3 has involved much state of the art technology in a new principle of vertex detection, in new crystals for large scale electromagnetic shower detection and ultra precise muon detection. See Figures 3-4 through 3-6. Full details on the construction of the L3 detector can be found in [37].

### 3.2.1 TEC Central Tracking Chamber

The central tracking chamber is the first subdetector from the interaction region and is comprised of two concentric cylindrical drift chambers on common endplates that operate in the Time Expansion mode. Surrounding this are two cylindrical proportional chambers with cathode strip readout, the Z detector and a plastic scintillating fiber system (see Fig. 3-7). The TEC is a new type of precision drift chamber designed to optimally function in the limited space available within the electromagnetic calorimeter and was designed with the following goals:

- measure precisely the location and direction of charged particles to  $40\ \mu\text{m}$  precision;
- determine the sign of charged particles and its transverse momentum up to energies of 50 GeV;
- provide track multiplicity at the trigger level;
- reconstruct the interaction point and secondary vertices for particles with lifetimes greater than  $10^{-13}\ \text{s}$ .

The TEC is 1 meter in length, extends from 9 cm to 49 cm in the radial direction, covers  $|\cos\theta| \leq 0.8$  in the polar region and is composed of three regions: the inner, outer, and Z chambers. The inner TEC is fitted around the beam pipe and separates  $r - \phi$  in 12 segments, each segment having 8 signal and 8 charge division wires. The outer sector radially extends from 15 cm to 46 cm and is divided in 24 segments, each with 54 wires. The Z chamber is two layers of drift chambers located on the outer shell of the outer chamber. It has a cathode strip readout to enhance the precision of the z-coordinate. The inner and outer segments contain a gas mixture of 80%  $\text{CO}_2$ , and 20%  $\text{C}_4\text{H}_{10}$  and the Z chamber contains 80% Argon and 20%  $\text{CO}_2$ .

There are three types of signal wires with sensitive length of 982 mm. The standard sense wires measure precisely the  $r - \phi$  coordinate. The charge division wires determine the z-coordinate by measuring the charge asymmetry at both ends of the wire. Groups of five grid wires on each side of the amplification region help solve the left-right ambiguity. See Figure 3-8.

The PSF (plastic scintillating fibers) surrounds the outer TEC with 143 fibers/per segment running parallel to the beam pipe. These fibers yield information on whether a minimum ionizing particle traversed the TEC and are an independent measurement used to calibrate the TEC in order to measure the drift velocity to 0.1% accuracy, the necessary precision needed to distinguish charge at 45 GeV.

### 3.2.2 BGO Electromagnetic Calorimeter

The electromagnetic calorimeter located between the tracking chamber and the hadron calorimeter is comprised of nearly 11,000 Bismuth Germanate (BGO) crystals pointing to the interaction region as depicted in Figure 3-9. Each crystal is 24 cm long (about 22 radiation lengths) and is  $2 \times 2\ \text{cm}^2$  at the inner end and  $3 \times 3\ \text{cm}^2$  at the outer end. BGO crystals were chosen for the following reasons:

- to provide excellent energy resolution for electrons and photons over the entire energy range between 100 MeV ( $\approx 5\%$ ) and 50 GeV ( $< 1\%$  for  $E \geq 2$  GeV);
- short radiation length, large nuclear interaction length;
- serves as both showering and detection medium with high radiation hardness;
- excellent position resolution (2 mm) using center-of-gravity method to localize the shower peak.

The calorimeter is comprised of two half barrels with a total of 7680 crystals and two endcaps each with 1536 crystals. The total polar angular coverage is from  $12^\circ$  to  $168^\circ$ . Each crystal is mounted in a carbon fiber structure which serves to fix their locations, support the weight and minimize the space between crystals. Since the entire calorimeter is located inside a 0.5 T magnetic field, photomultiplier tubes cannot be implemented and thus two photodiodes/per crystal are used to collect the light. The crystals were calibrated in the CERN SPS X3 beam where electron beams of 2, 20 and 50 GeV momenta were used to measure the calibration constants. In addition, the effects of different impact points and variations of temperature were measured. The overall resolution achieved in the test beam was 1.6% at 2 GeV and 0.62% at 50 GeV [38].

### 3.2.3 The Hadron Calorimeter

The hadron calorimeter measures the energy of hadrons via total absorption calorimetry with a uranium hadron calorimeter and the BGO crystals. It consists of two parts, the barrel and forward-backward regions and is located between the electromagnetic calorimeter and the support tube, extending from 88 to 213 cm in radius. The barrel covers the full azimuthal range and a polar region between  $35^\circ$  and  $145^\circ$ . It is a fine sampling calorimeter made of depleted uranium absorber plates interspersed with proportional wire chambers. Uranium is used because it has the following properties:

- it has a short absorption length (the BGO and HCAL comprise 6-7 absorption lengths for particles originating at the interaction region);
- it acts as a filter so that only non-showering particles reach the muon detector;
- the uranium radioactivity provides a gamma source to aid in calibration of the wire chamber.

The chambers are planes of brass tubes oriented alternatively perpendicular to each other for determination of the  $z$  and  $\phi$  coordinate. The polar angle is measured by stretching the endcap wires azimuthally. The signal wires are grouped into readout towers to avoid separate readout channels without significant loss of granularity.

The barrel is 4.725 m long and is modular in structure consisting of 9 rings of 16 modules each. Table 3.2 lists some parameters of the barrel. In total there are 7968 chambers and 371,764 wires and 3960 readout towers. The gas mixture used in the proportional chambers is 80% Argon and 20%  $\text{CO}_2$ .

	3 Central Rings	6 Outer Rings
Number of wire chambers	60	53
Number of uranium plates	58	51
Outer radius	1.795 m	1.795 m
Inner radius	0.885 m	0.979 m
Readout towers in $\phi - z$	9	9
Readout towers in r	10	8

Table 3.2: *Parameters of L3 barrel calorimeter.*

The forward-backward calorimeter is made of three rings, each of which is split vertically into half rings for a total of 12 modules. It has full azimuthal coverage and extends polarly from  $5.5^\circ$  to  $35^\circ$  on either side. Each module consists of alternating layers of proportional chambers and depleted uranium absorber plates. The overall resolution for jets vs. energy is obtained from test beam and experimental data [39]:

$$\frac{\sigma}{E} \approx \left( \frac{55}{\sqrt{E}} \oplus 5 \right) \% \quad (3.1)$$

Outside the hadron calorimeter is a muon filter designed to reduce punchthroughs necessary for muon identification. It consists of 8 octants each of which have 6 brass absorber plates interleaved with 5 layers of proportional chambers and 1.5 cm thick absorber plate. In total it adds 1.03 absorption lengths to the hadron calorimeter.

### 3.2.4 The Muon Chambers

The design goal of the muon chambers was to precisely measure muon momenta with  $\frac{\Delta p}{p} \approx 2\%$  at  $E_\mu = 45$  GeV. This precision corresponds to a mass resolution of 1.4% on the  $Z^0$  peak.

The muon spectrometer is made of 3 layers of high precision drift chambers which measure the curvature of the muon track between the support tube and magnet coil. The inner radius is 2.5 m, the outer radius is 5.4 m and it covers the angular range  $44^\circ \leq \theta \leq 136^\circ$ . It is made of 2 ferris wheels each having 8 octants all within a 0.5 T solenoidal field along the beam direction. Each octant has a special mechanical structure which supports 5 drift chambers which measure the muon momentum and thus are called P-chambers. There are one inner (MI), two middle (MM), and two outer (MO) chambers. The chambers are divided into individual cells designed to have a very uniform electric field. The MO, MI, and MM chambers have 21, 19 and 15 cells respectively. Each MO and MI cell contains 16 sense wires and the MM cell contain 24 sense wires. On the tops and bottoms of the inner and outer chambers are the Z-chambers. These measure the z-coordinate using two layers of drift chambers with wires perpendicular to the beam direction and offset by  $\frac{1}{2}$  cell relative to each other in order to solve the left-right ambiguity. The middle chambers are closed by honeycomb panels of 0.9% radiation lengths to minimize resolution degradation. The

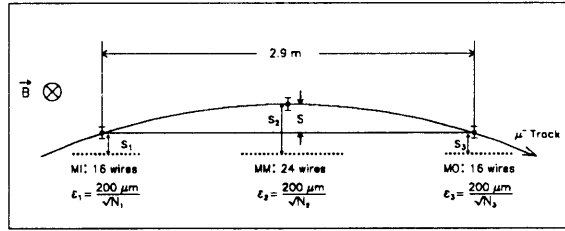


Figure 3-1: *The sagitta of a muon track.*

single wire resolution is less than  $220 \mu\text{m}$  in the P-chambers and  $500 \mu\text{m}$  in the Z-chambers. The gas composition for the P-chambers is 61.5% Argon and 38.5% Ethane and the Z-chambers contain 91.5% Argon and 8.5% Methane.

In the polar region  $44^\circ \leq \theta \leq 136^\circ$ , muons originating from the interaction region are measured by all three layers. The momentum is known by measuring how much the muon trajectory deviates from a straight path, which can be given in terms of the sagitta  $s$ , defined as:

$$s = X_{MM} - \frac{X_{MI} - X_{MO}}{2} \quad (3.2)$$

where  $X$  is the measured position in the respective chamber. The relation between the sagitta  $s$  and the transverse momentum is:

$$p_T(\text{ GeV}) = \frac{0.3B(T)L^2(m^2)}{8s(m)} \quad (3.3)$$

For a 45 GeV muon,  $s = 3.7 \text{ mm}$ .

In the angular region  $35^\circ \leq \theta \leq 44^\circ$  and  $136^\circ \leq \theta \leq 145^\circ$  muons are measured in two out of the three chambers, MI and MM covering  $\approx 12 \%$  of the solid angle. The resolution for the 'doublets' is  $\sim 21 \%$ . The uncertainty of the muon energy loss in the calorimeter is  $\sim 350 \text{ MeV}$ . The muon resolutions can be written in the general form:

$$\frac{\Delta p_\mu}{p_\mu} = \frac{(2.79 \times 10^{-7} p_\mu^4 + 0.1225)^{1/2}}{p_\mu} \quad (3.4)$$

for triplets and

$$\frac{\Delta p_\mu}{p_\mu} = \frac{(1.11 \times 10^{-5} p_\mu^4 + 0.1225)^{1/2}}{p_\mu} \quad (3.5)$$

for doublets.

In order to achieve a momentum resolution of 2% the accuracy necessary in the sagitta measurement is  $\Delta s = 2 \% \times 3700 \mu\text{m} = 74 \mu\text{m}$ . There are three sources of systematic errors in the sagitta measurement:

- intrinsic drift chamber resolution which is dependent on the single wire resolution ( $200 \mu\text{m}$ ) and on the number of wires used for reconstruction of the track. This leads to a sagitta uncertainty of  $\sim 54 \mu\text{m}$ ;

- multiple scattering inside chambers adds  $31 \mu\text{m}$  of uncertainty;
- accuracy of alignment of the three different layers and knowledge of wire positions. This adds  $33 \mu\text{m}$  to uncertainty.

Adding these errors in quadrature yields  $\Delta s = 69.8 \mu\text{m}$ .

The determination of the sagitta to high precision requires critical alignment between chambers in a given octant. (For muons with energy greater than 3 GeV the trajectory will be confined to one octant). An alignment system consisting of LED's, lenses and quadrant photodiodes is built into each octant to define the octant central line and the positions of the wires are measured relative to it. This method yields the wire positions to an accuracy of  $10 \mu\text{m}$ . To assure two octant center lines are parallel to each other, a laser beacon is used to measure the angle between the two octant center lines to a precision of  $25 \mu\text{m}$  corresponding to an error in the sagitta of less than  $10 \mu\text{m}$ . Laser events are used to test the overall alignment and measured sagittas were within  $30 \mu\text{m}$  for all octants. The muon chambers are shown in Figures 3-11 and 3-12.

### 3.2.5 Scintillation Counters

The scintillator counter system consists of 30 plastic counters situated between the electromagnetic and hadronic calorimeters. They have two primary purposes:

- measure the time-of-flight between two opposite counters in order to reject cosmic events;
- the hit multiplicity is used as a trigger on hadronic events.

The counters are divided into 32  $\phi$  sectors positioned along the beam line following the shape of the hadron calorimeter. (Two sectors at  $\phi = 0, \pi$  are taken up by the BGO rail). Phototubes at both ends of each scintillator are read by high precision TDC's and the time resolution is measured from dimuon events is  $\approx 0.5 \text{ ns}$ . The overall coverage is within  $|\cos \theta| \leq 0.83$  and 93 % of  $\phi$ .

### 3.2.6 Luminosity Monitor

The luminosity monitors are located at  $z = \pm 2765 \text{ mm}$  with respect to the interaction region and consist of two cylindrical BGO detectors and charged particle tracking chambers with good position resolution. They measure the integrated luminosity to 1% precision by counting the low angle Bhabha events and comparing this with the theoretical Bhabha cross section in the appropriate angular region. The coverage in the forward angular region is from  $24.7 \text{ mrad} \leq \theta \leq 69.3 \text{ mrad}$  with 100 % efficiency which corresponds to an effective Bhabha cross section of  $\approx 100 \text{ nb}$ .

### 3.2.7 Forward Tracking Chambers

The Forward Tracking Chambers (FTC) are located between the TEC endflange and the BGO endcaps. They cover the polar angular range between  $12^\circ$  to  $32^\circ$  and between  $148^\circ$  to  $168^\circ$ . They were designed to perform the following:

- veto charged particles when looking for low angle photons;
- to improve tracking in the forward-backward regions;
- provide the impact point of charged particles when they enter they BGO endcaps.

Each chamber consists of two perpendicular layers of 20 drift tubes, one measuring the x-coordinate, the other the y-coordinate. Each drift tube has 4 sense wires with a single wire resolution of  $200\ \mu\text{m}$ . The gas is 61.5% Argon and 38.5% Ethane.

### 3.2.8 Trigger

The trigger system determines if an  $e^+e^-$  interaction occurred and if so, whether or not it should be recorded. This is achieved through a tri-level trigger system of increasing complexity. Each trigger level has redundant selection criteria which are logically OR'd. The 45 kHz beam crossing rate (4 by 4 bunch mode) is reduced to a few Hz tape writing rate. During data taking the quality of the data, the detector calibration, and safety are monitored. All rates noted are "typical" and apply for the 4 by 4 bunch mode.

#### Level 1

The level 1 trigger operates at 45 kHz so within  $22\ \mu\text{s}$  it must decide whether to start data digitization or clear the front end electronics. Negative level 1 decisions do not contribute to the dead time. The expected trigger rate is 100 Hz with  $\sim 5\%$  deadtime. Level 1 functions as a logical OR of trigger conditions from 4 different sources: the calorimetric, muon, scintillator and TEC triggers.

- Calorimeter Trigger

This trigger processes information from the electromagnetic and hadronic calorimeters and the luminosity monitor and reaches a decision in  $16.8\ \mu\text{s}$ . The threshold of every channel is  $\sim 1\ \text{GeV}$ . There are several sub-triggers and a trigger is given if the following conditions are satisfied:

- Total Energy Trigger ( $\sim 0.2\ \text{Hz}$ ): a trigger is given if the total energy is above a pre-defined threshold, which can be different if the energy is localized in the central part of the detector and can also depend on the ratio of the electromagnetic to hadronic energy.
  - \* the energy in all calorimeters  $> 20\ \text{GeV}$
  - \* the energy in the electromagnetic calorimeter is  $> 20\ \text{GeV}$

- \* sum of energy in the electromagnetic and hadronic calorimeters  $>15$  GeV
- \* energy in the hadronic barrel  $>10$  GeV
- Cluster Trigger ( $\sim 1.2$  Hz): a cluster is a localized deposit of energy in different detector layers at the same  $\phi, \theta$  coordinates. A trigger is given if there is at least one cluster with energy of more than 7 GeV.
- Single Photon Trigger ( $\sim 2.1$  Hz): A cluster in the BGO is accepted even if the energy is very low if the ratio of this energy to the total BGO energy is greater than 0.8.
- Hit Counting Trigger ( $\sim 0.2$  Hz): the energy in one or more trigger cells is above a certain value.
- Luminosity Trigger ( $\sim 0.6$  Hz): energy greater than 15 GeV in both monitors or with an energy greater than 25 GeV in one monitor while there is more than 5 GeV in the other monitor.
- Single Tag Trigger ( $\sim 0.2$  Hz): energy of more than 30 GeV in one luminosity monitor while some energy is deposited in the central part of the detector

The overall calorimeter trigger rate is typically  $\sim 3.0$  Hz.

#### • Muon Trigger

The muon trigger uses information from the muon chambers and looks for tracks pointing to the interaction region. It accepts events with  $p_T > 2$  GeV in the chambers and has three subtriggers which accept events on the following criteria:

- Single Muon Trigger ( $\sim 2.2$  Hz): a muon track with at least 2 out of 3 possible hits in the P-chambers and any 3 out of 4 possible hits in the Z-chambers. This trigger is effective in the polar region  $44^\circ \geq \theta \geq 136^\circ$ .
- Di-muon Trigger ( $\sim 6.0$  Hz): a muon track identified in at least two octants with the same hit conditions as in the single muon trigger. In addition an acoplanarity criteria must be satisfied. This trigger covers the polar region  $36^\circ \geq \theta \geq 144^\circ$ .
- Small Angle Muon Trigger ( $\sim 4.2$  Hz): a muon track with 1 P-chamber hit and 2 hits in the inner Z-chamber with a coincident hit of similar activity in the opposite hemisphere. This trigger covers the forward-backward regions  $35^\circ \geq \theta \geq 44^\circ$  and  $136^\circ \geq \theta \geq 144^\circ$  where there is only one layer of P-chambers available.

The total muon trigger rate is  $\sim 9.5$  Hz. When at least one scintillator counter is required the rate is reduced to  $\sim 1.5$  Hz, mainly due to cosmic rejection.

#### • Scintillator Trigger

The scintillator trigger is based on the signals of the 30 barrel counters and are used for the following purposes:

- veto cosmic events by requiring 2 counters in coincidence with the beam gate of  $\Delta t \sim 30$  ns. This trigger is efficient for events with two muons or two hadronic jets so it serves as a backup trigger for the dimuon and cluster triggers and is useful to monitor their efficiencies.
- coincidence pattern conditions allow the selection of pre-defined pattern of hits. It can ask for 6/30 barrel counters with a trigger rate of 0.2 Hz.

The scintillator signals are also sent to the calorimetric trigger to contribute to the decision of the cluster trigger.

- **TEC Trigger**

The TEC trigger uses 14/54 wires for each of the 24 outer segments. The  $r$ - $\phi$  plane is then subdivided into 96  $\phi$  bins, for each of which a Track Finder module searches for tracks that originate at the beam line. The module performs the track search including inefficiency effects and additional hits in less than 1  $\mu$ s. Due to drift times, the search for forward tracks begins 5  $\mu$ s after the beam crossing and after another 5  $\mu$ s the central tracks are located. In total, the track search is completed in 11  $\mu$ s. Then a Track Adder module adds the total number of tracks found, the number of clusters, and the number of pairs of tracks with some pre-defined acoplanarity. The results are sent to Level 1 for a trigger decision as well as to the calorimetric trigger and Level 2.

- **Trigger Control**

The trigger control synchronizes the data acquisition and the Level 1 trigger and implements the final Level 1 decision. If the event is accepted then a signal is sent to the subdetectors to start data conversion and buffering, otherwise the system is reset and readied for the next event.

- **Level 2**

The Level 2 trigger implements all the Level 1 data which is further analyzed by four programmable processors (XOP's). Level 2 also receives information that was not available on time for a Level 1 decision, specifically the charge and drift time information from the charge division wires of the TEC. The main purpose of the Level 2 computation is to reduce the event rate by analyzing the following:

- detecting clustered energy in the electromagnetic and hadronic calorimeters
- the longitudinal and transverse energy imbalance of the clustered energy
- the recognition of the vertex by the charge division wires of the TEC.

Overall, Level 2 reduces the rate of about a factor 10.

- **Level 3**

Unlike the Level 1 and Level 2 triggers, Level 3 has access to the complete digitized data with finer granularity and higher resolution. A selection of good events is based on:

- the correlation of the energy deposited in the electromagnetic and hadronic calorimeters;
- the reconstruction of the muon track in the Z-chambers;
- the reconstruction of the vertex in the TEC chamber.

If the Level 3 decision is affirmative, a FASTBUS computer interface transfers the data from the emulator memory to the main data acquisition computer for tape writing.

For the data acquisition, FASTBUS is used and a VAX 8800 along with small VAX stations for each subdetector take the data. The overall system includes buffering capacity to allow asynchronous operation while maximizing the lifetime.

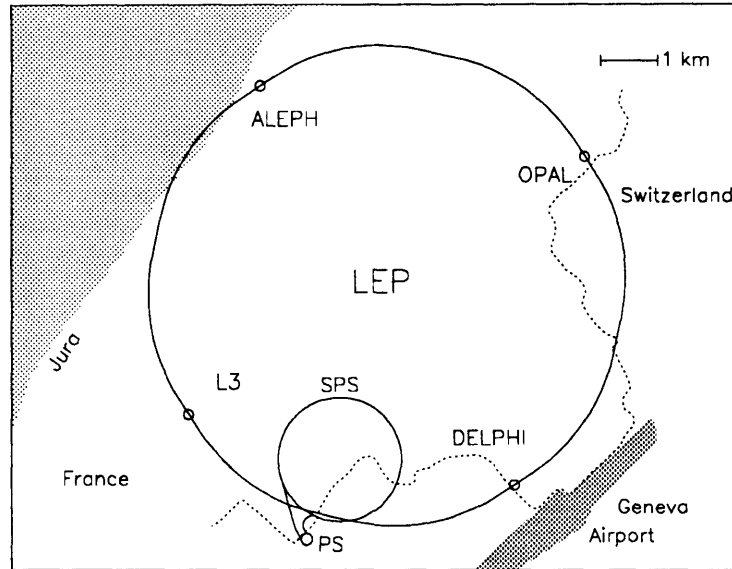


Figure 3-2: *The LEP ring.*

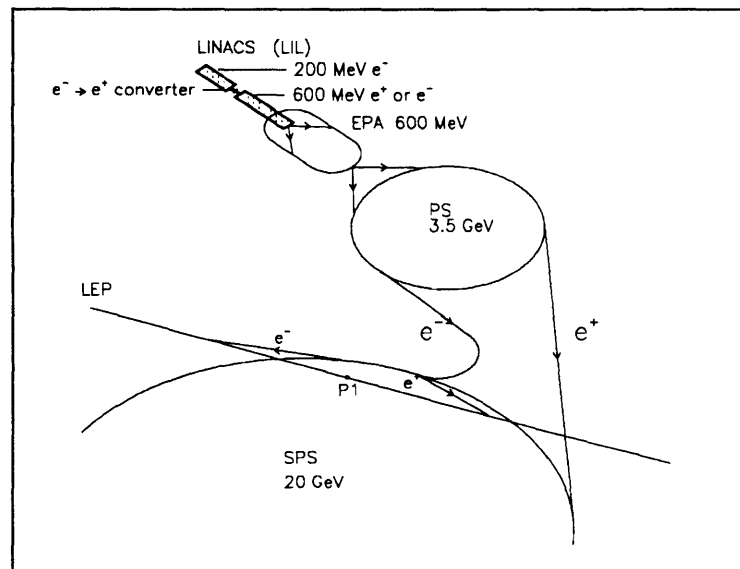


Figure 3-3: *LEP injection chain.*

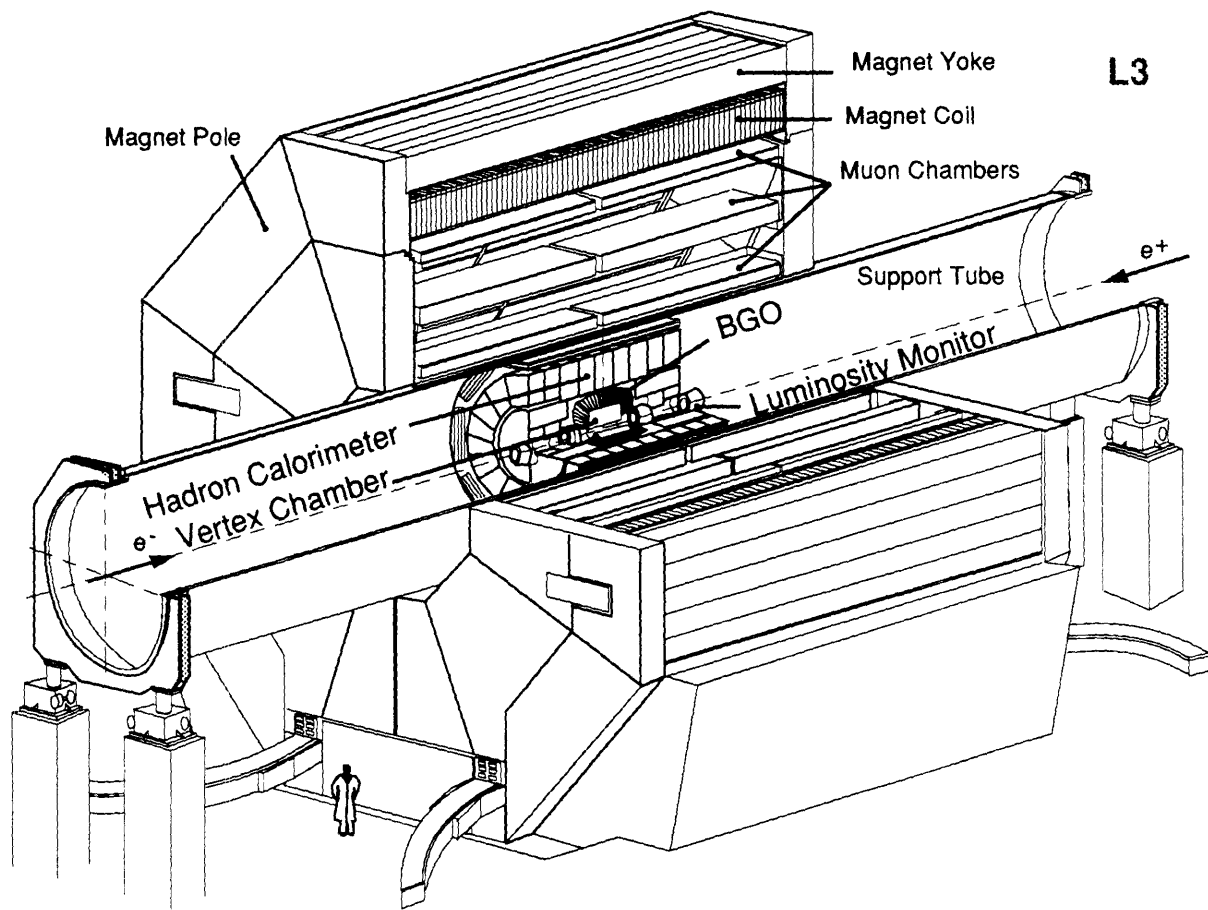


Figure 3-4: *The L3 Detector.*

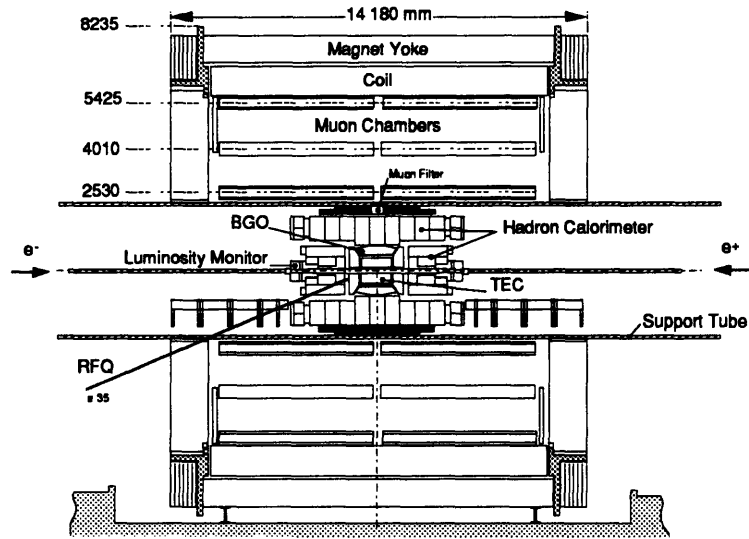


Figure 3-5: *The L3 detector interior view.*

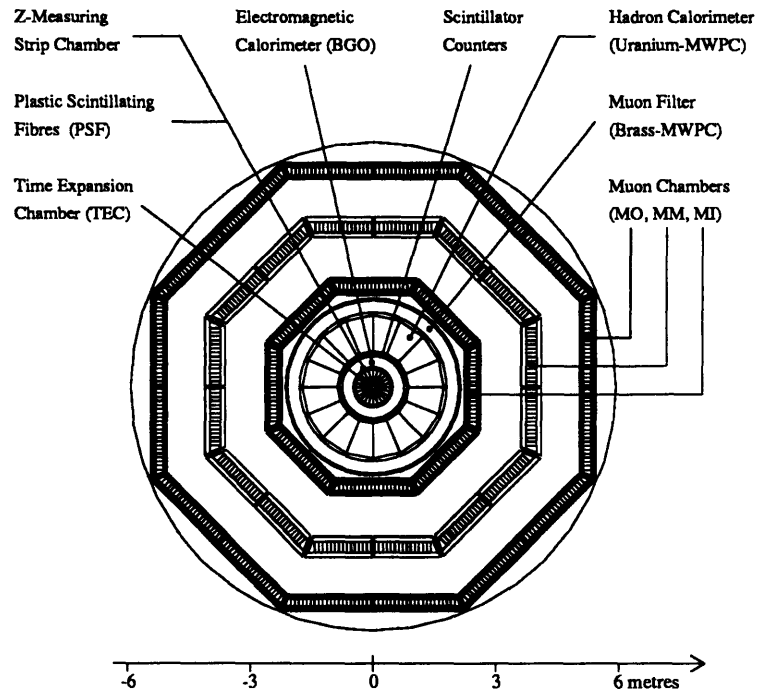


Figure 3-6: *The L3 detector  $r - \phi$  view.*

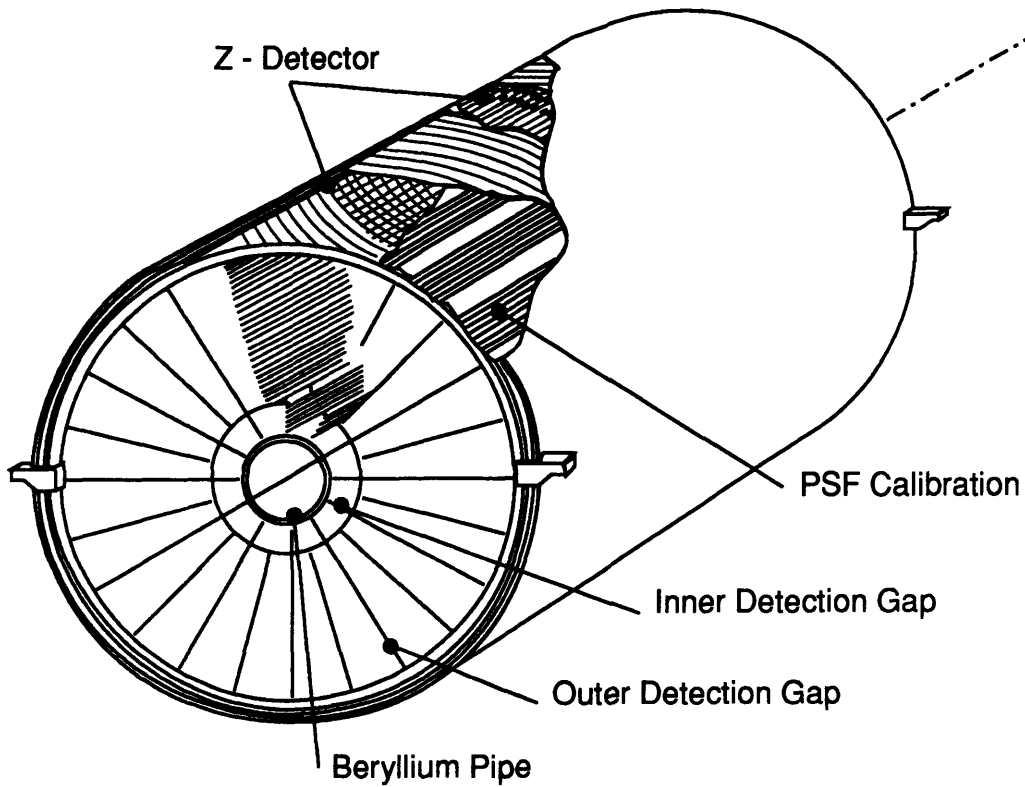


Figure 3-7: *The Central Track Detector and its wire configuration.*

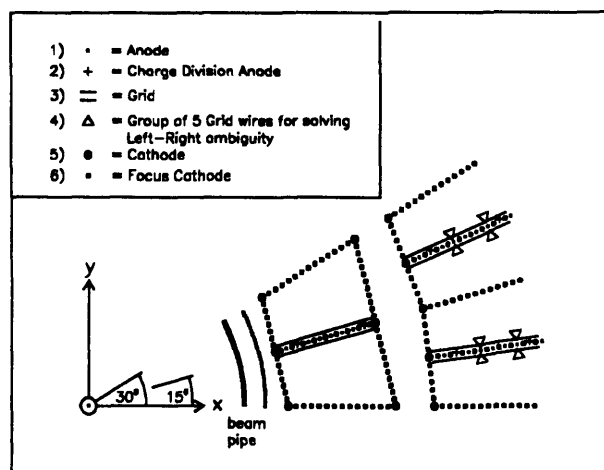


Figure 3-8: *An  $r - \phi$  view of an inner and two outer TEC sectors.*

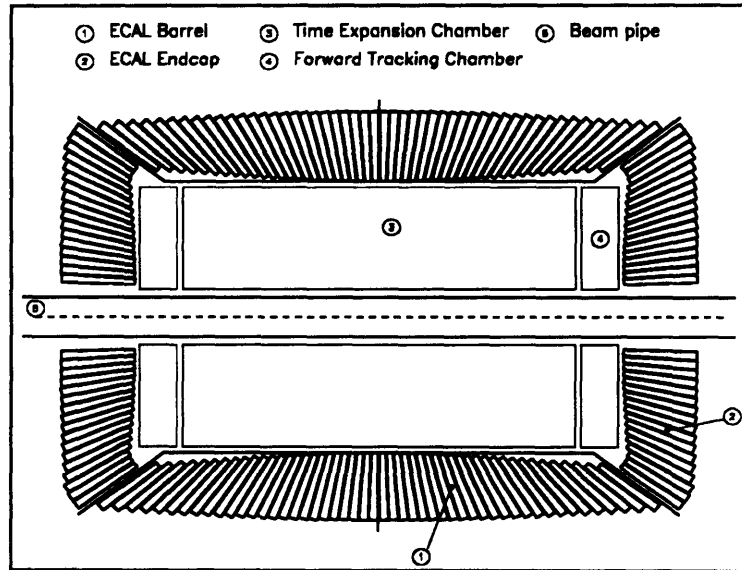


Figure 3-9: *The BGO electromagnetic calorimeter.*

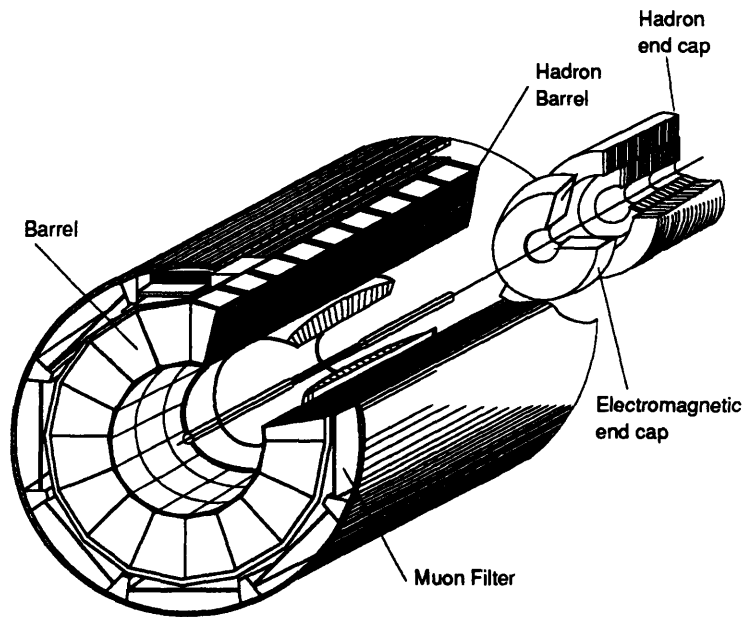


Figure 3-10: *The hadron calorimeter.*

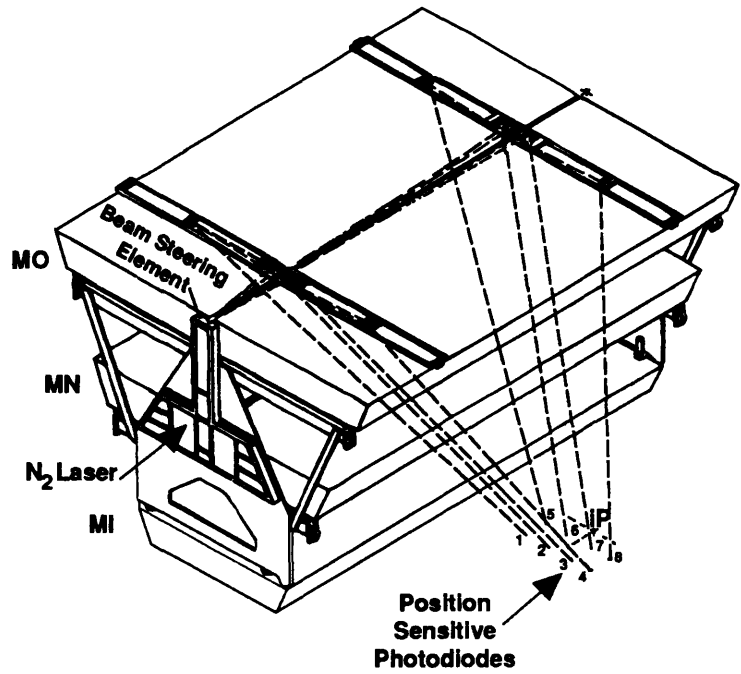


Figure 3-11: *The Muon chamber octant.*

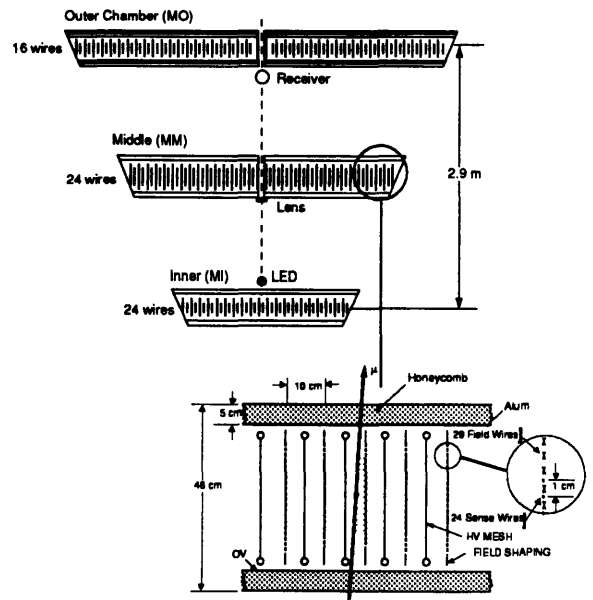


Figure 3-12: *Side view of the muon chamber octant.*



# Chapter 4

## Simulation and Reconstruction

### 4.1 Introduction

A summary of the methods used in the simulation and reconstruction of the physics processes of signal and background for our searches will be discussed.

### 4.2 Physics processes generation

In the direct searches for compositeness that are undertaken in the next chapters, a small fraction of the large number of events accumulated during the periods of data taking are selected in order to improve the signal-to-background ratio. To do so, selection algorithms composed of cuts on appropriate variables are developed. Most of the time, these variables describe the kinematical configuration of the events. In order to test the performance of the selection algorithms, we will need unweighted samples of signal and background events.

The samples of events are generated using a Monte-Carlo integration technique[40]. This method, based on random sampling, provides a unique way of calculating the integrals of the differential cross section of the processes of interest. For instance the process  $e^+e^- \rightarrow e^+e^-\gamma$  contains five independent variables which would be very difficult to integrate analytically. The connection between integration and statistics is made possible via the relation

$$\int_0^1 dx_1 \dots \int_0^1 dx_n f(x_1, \dots, x_n) \approx \frac{1}{N} \sum_{i=1}^N f(x_1(i), \dots, x_n(i)) \quad (4.1)$$

where  $x_j(i)$  is the  $i$ th sample of a random variable  $x_j$  *uniformly* distributed over the range  $(0, 1)$ . Since the r.h.s. of Eq. 4.1 is based on a random sampling, the larger the sample the more precise the result will be. This has the drawback that in order to compare our Monte-Carlo predictions with the data sample, a very large sample of simulated events has to be generated. In principle the Monte-Carlo sample of events should always be a few times larger than the data sample but this is not always feasible due to limited computing power.

The large number of events in the data sample also implies that the background processes must be described precisely, that is, the theoretical errors must not exceed a few percent. From a physics point of view, higher order corrections (i.e. radiative corrections) must be included in the Monte-Carlo programs. In the programs, the numerical imprecisions of the calculations could be relevant. In view of the complexity of the physics simulation programs, a set of standard generators have been developed for the entire high-energy physics community. The programs that have been used for the background estimations are BABAMC 2.5[41] ( $e^+e^- \rightarrow e^+e^-(\gamma)$ ), TEEGG 7.1[42] ( $e^+e^- \rightarrow e(e)\gamma$ ), KORALZ 4.0[43] ( $e^+e^- \rightarrow \mu^+\mu^-(\gamma), \tau^+\tau^-(\gamma)$ ), JETSET 7.3[44] ( $e^+e^- \rightarrow qq(\gamma)$ ), and GGG[45] ( $e^+e^- \rightarrow \gamma\gamma(\gamma)$ ).

Process	Program	Sample size
$e^+e^-(\gamma)$	BABAMC	30,000
$e(e)\gamma$	TEEGG	10,000
$\mu^+\mu^-(\gamma)$	KORALZ	170,000
$\tau^+\tau^-(\gamma)$	KORALZ	252,000
$\gamma\gamma(\gamma)$	GGG	80,000

Table 4.1: *The list of generators used for background estimations.*

### 4.3 Detector simulation

In order to compare the prediction of the Standard Model processes with the ones actually observed in the detector, events simulated with the previously mentioned event generators are processed by a particle tracking program called SIL3. SIL3 is based on the GEANT 3.15 package[46] which by a Monte-Carlo technique propagates particles through detector volumes taking into account the following effects related to the passage of particles through matter and fields:

- bending of a charged particle in a magnetic field;
- multiple scattering (Molière scattering) in materials;
- energy loss due to Bremsstrahlung (with Landau fluctuations);
- energy loss due to ionization;
- energy loss due to Bremsstrahlung of a hard photon;
- positron annihilation;
- photon conversions;
- Compton and Rayleigh scattering;

- photoelectric effect;
- electron pair production by muons;
- nuclear interactions (by the GHEISHA[47] package).

The precision of the descriptions of the different processes is typically at a level better than 10% and is improved by a tuning of the parameters to best describe the kinematical regions of interest. The electromagnetic showers produced by electrons or photons in the BGO calorimeter are completely simulated yielding a very large number of secondary particles. The nuclear interactions simulate the development of hadronic showers.

The entire L3 detector is described by a series of layered volumes in space. Each subdetector is designated by a mother volume that delimits its extent. Inside the mother, smaller volumes are used to model as precisely as possible the different materials of the subdetector.

Each simulated event is processed sequentially by the program. All the particles are tracked one after the other through each volume of the detector until their energy is either below a predefined threshold (typically on the order of 10 MeV), they are absorbed or decay. Secondary particles produced during Bremsstrahlung, photon conversions, decays and nuclear interactions are also tracked similarly.

The energy deposited in each volume is recorded. For example, in the case of the electromagnetic calorimeter, the total energy deposited in each BGO crystal is saved. For tracking chambers, hits recorded in the detector wires are simulated by a digitization process which takes into account the fluctuations and the resolution of the reconstructed hit in space.

For each event, the SIL3 program produces a list of detector hits and deposited energies in the same format as that which is read in from the detector during data taking. The simulated events can therefore be reconstructed in the same way as the data events.

The description of the detector in SIL3 is in principle so precise as to allow direct comparison between simulated and data events. The simulation includes detector uninstrumented regions which affect the acceptance, the energy and angular resolution of the calorimeters, the momentum and position resolution of the tracking chambers, as well as the efficiencies for reconstructing event quantities (see Section 4.4). It is clear, however, that the time dependent status of the detector is not reflected in the simulation. In other terms, the detector's description corresponds to a 'perfect' detector with design resolutions and acceptances. The acceptance of the simulation must be corrected for dead channels that are present in the actual detector. The resolution parameters that are always functions of changing physical parameters like temperature, pressure, gas mixtures, calibrations, etc. which are in fact time dependent are included at the stage of analysis instead of simulation because it is not possible to fully simulate events with a large set of time-dependent detector parameters.

The simulated event samples described in Section 4.2 have been fully simulated through a 'perfect' detector description.

## 4.4 Event reconstruction

The L3 reconstruction program REL3 is an essential part of the analysis of the data. The goal is to try to identify particle trajectories and to estimate their parameters like energy, momentum and direction. The reconstruction of an event is split into two steps. In the first step, objects are reconstructed within subdetectors. In the second step, information from each of the subdetectors is combined to reconstruct trajectories through the entire detector.

### 4.4.1 Electromagnetic clusters

The light collected in each BGO crystal is converted to an energy from the set of calibration constants. Neighboring crystals are merged into electromagnetic clusters. Starting with the crystal with the largest energy deposition, the cluster is constructed by adding all the contiguous crystals with energy above a given threshold. Each cluster is subsequently split into electromagnetic bumps by identifying local energy maximas. A local maxima is defined by the crystal in which the energy deposition is larger than in any of the eight surrounding crystals. The crystals are assigned to the bumps based on their distance to the local maxima. If crystals are equally close to more than one bump, they get assigned to the most energetic bump. The coordinates of the electromagnetic bumps are found by the energy weighted mean of its crystals position. A correction is applied to account for the non-uniformity due to the discrete positioning of the crystals.

The energy and the position of the incident particle is calculated from the  $3 \times 3$  matrix around the most energetic crystal of a bump. In this way, the results are less sensitive to fluctuations that appear in the transverse tails of the electromagnetic showers.

### 4.4.2 Tracks

The central tracking chamber algorithm tries to reconstruct charged particle trajectories starting from the hits recorded in the wires of the TEC. In the  $r - \phi$  plane, the drift-time information recorded by each wire is translated into an  $x, y$  position with a two-fold ambiguity. For the simulation, the generated hits are smeared with a resolution dependent on the distance of the point to the wire. Collecting neighboring hits, a track is constructed and a fit is accomplished to find the transverse momentum  $p_T$ , the  $\phi$  direction and the impact parameters (distance of closest approach) of the track. The two-fold ambiguity of a track is resolved by matching the inner and outer TEC sectors. To obtain the slope of the tracks, the wires with charge division are used to provide information along the  $z$  direction. The Z chambers hits are then matched to the tracks in the  $r - \phi$  plane to provide precise points along  $z$ . These hits and the information from the charge division wires are merged to find the slopes and the  $z$ -intercepts at the vertex of the tracks.

At the detector level, tracks are improved by combining the  $z$  information from the electromagnetic bumps. The subsample of these reconstructed tracks that passed

the quality cuts described below have been consistently used for the analyses. A good track must have:

- transverse momentum  $p_T > 0.1$  GeV;
- impact parameter DCA  $< 10$  mm;
- the span,  $s$ , defined as the length of the track from the vertex until it exits the central tracker volume in units of wire spacing, must satisfy  $s > 30$  (the maximum is 62);
- at least 20 hits;
- a ratio hits to span greater than 0.75.

### 4.4.3 Hadronic clusters

The hadronic energy clusters are reconstructed by grouping in space the hits recorded in the proportional chambers of the hadronic calorimeter. Unlike the electromagnetic cluster in the BGO, the hadron calorimeter hits provide a position in space, i.e. in  $\theta$ ,  $\phi$  and  $r$  due to lateral and longitudinal segmentations. The  $\phi$  and the  $z$  towers are matched to avoid double-counting. The energy of the cluster is determined by summing the energy deposited in matched towers only. A special algorithm identifies tracks in the hadronic calorimeters, typical of the energy deposition of muons.

### 4.4.4 Muon tracks

The reconstruction of a muon track is composed of three steps. The drift-time of the hits recorded in the muon chamber P-cells are transformed via a cell-map to the  $x, y$  coordinates which are used to fit track segments within the cells. For tracks that do not cross the mesh plane, there is a two-fold ambiguity. Muon tracks composed of three segments in the same octant, one in each chamber MI, MM, and MO are tentatively fitted across the entire octant. By matching the local slope of the track segment with the muon track segment, most of the ambiguities can be resolved in these track ‘triplets’. In case one chamber is missing (typically in the forward direction), pairs of segments are matched yielding track ‘doublets’. The transverse momentum of triplets is fit by calculating the sagitta found with the three points in the middle in each segment. For the doublets, the local segment slopes are used to fit the track.

The tracks identified in the transverse plane are matched in the  $z$ -direction with the segments reconstructed in the Z-chambers. The parameters  $(1/p, \theta, \phi)$  of the tracks are then fitted. These values correspond to the trajectories of muons in the muon chambers. The tracks are then extrapolated to the vertex with an algorithm which takes into account the propagation of error matrices due to energy loss and multiple scattering inside materials. During the back-tracing of the muon from the muon chambers to the interaction point, the geometry of the detector as described in SIL3 is used to calculate in approximate steps the most probable energy loss and the average multiple scattering that a muon undergoes. The GEANE algorithm allows

the fitting of the tracks with many constrained points and adds to the fit information on the position provided by the hadronic clusters, the electromagnetic bumps and the constraints on the momentum and position from the central tracking chamber. The new parameters  $(1/p, \theta, \phi)$  at the vertex are the values used in the following analyses. The subsample of these reconstructed tracks that passed the quality cuts described below have been consistently used. A good muon track must have:

- at least 2 P-segments;
- at least 1 Z-segment;
- distance of closest approach in  $r < 20$  mm;
- distance of closest approach in  $z < 50$  mm;
- transverse momentum  $> 3$  GeV.

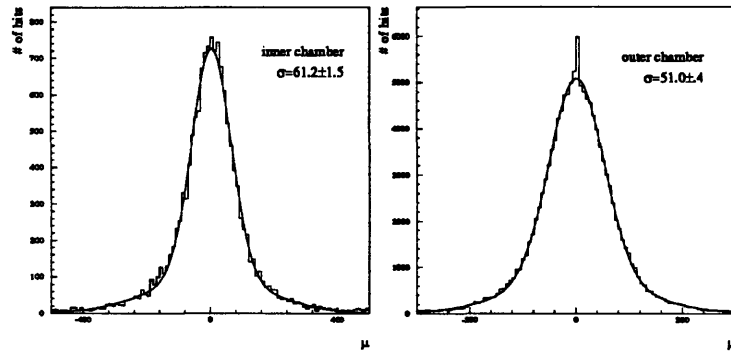


Figure 4-1: *The single wire resolutions for the central tracking chamber.*

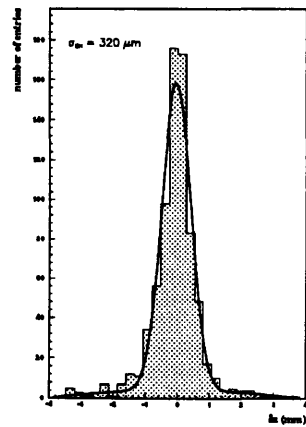


Figure 4-2: *The measured Z chamber position resolution.*

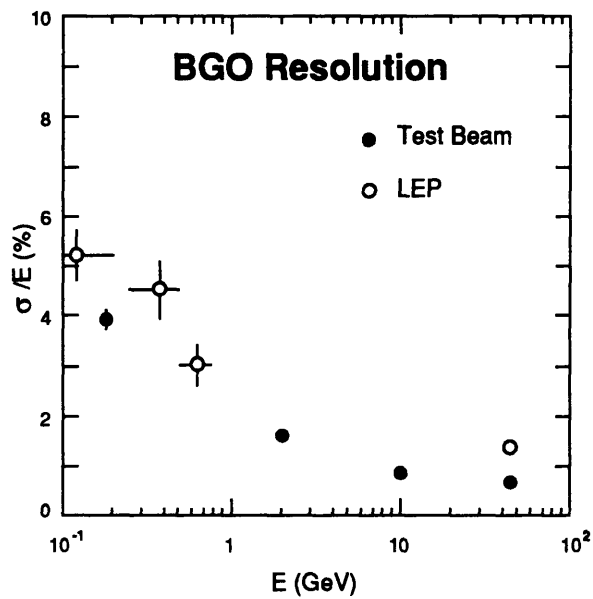


Figure 4-3: *The barrel ECAL resolution.*

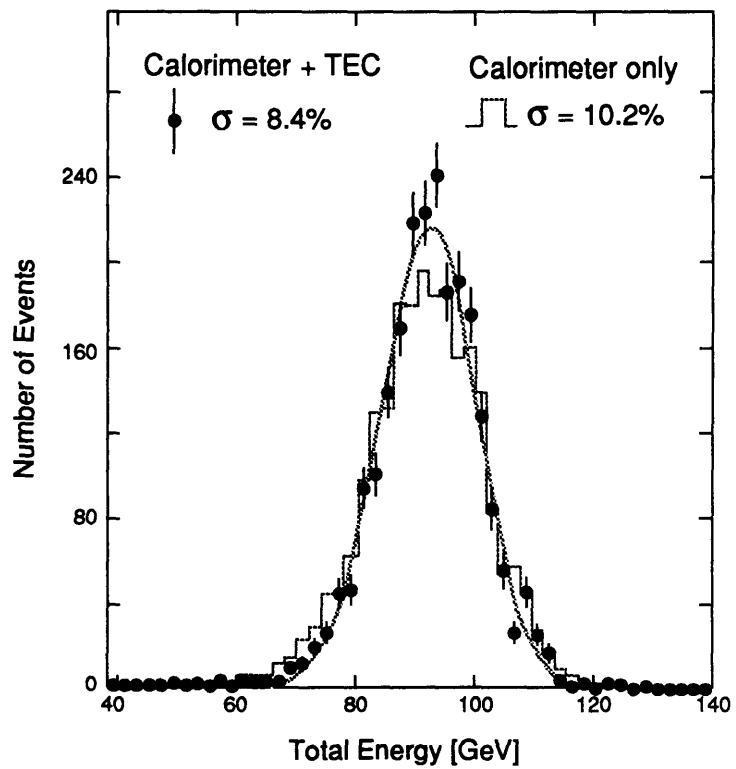


Figure 4-4: *The energy resolution for the calorimeters with the improvement of 8.4% with the inclusion of the TEC.*

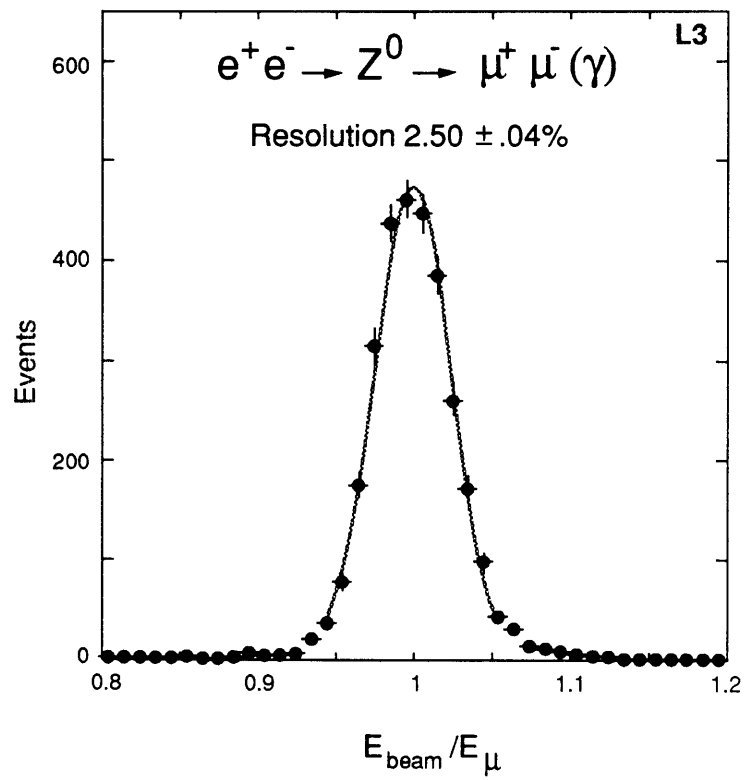


Figure 4-5: *The resolution for muon track triplets.*



# Chapter 5

## Composite Fermions Indirect Search

### 5.1 Introduction

Searches for new particles is an important process in the realm of high energy physics. The types of particles searched for here are those which could be produced should the fermions be composite states rather than fundamental particles. Evidence for new physics can be found either directly, through a discovery of a resonant invariant mass peak, or indirectly, via deviations from Standard Model predictions for various parameters, including branching ratios or total decay widths. In the absence of new physics, *exclusion regions* are placed. Depending on the nature of the search, mass regions can be excluded, or upper limits can be placed on coupling strengths and branching ratios.

### 5.2 Indirect searches

An indirect search for pair produced excited leptons up to masses of  $\approx \sqrt{s}/2$  can be carried out from the measurement of the total  $Z^0$  width  $\Gamma_Z$ . Since all decays of the  $Z^0$  contribute to its total width, a comparison between the measured and the value  $\Gamma_Z$  predicted by the Standard Model constrains the allowed possible width coming from any non-Standard decay modes. A coupling-dependent lower limit on the masses of excited pair produced leptons can be placed once it is determined what is the maximum width allowed for this process.

The total width  $\Gamma_Z$  can be experimentally divided into three separate categories:

- $\Gamma_h$  the hadronic width;
- $\Gamma_l$  the leptonic width;
- $\Gamma_{inv}$  the invisible width.

The first two are measured from final states with back-to-back structures and momentum conservation with high and low multiplicities, and any decay not falling into

these two categories are considered to be part of the invisible width since  $\Gamma_Z$  will be affected whereas the other widths will not be. Within the framework of the Standard Model, all the widths  $\Gamma_Z$ ,  $\Gamma_h$ ,  $\Gamma_l$  and  $\Gamma_{inv}$  can be calculated at tree-level from  $M_Z$  ( $Z^0$  mass),  $\alpha$  (electromagnetic fine structure constant) and  $G_F$  (Fermi constant). The not well known parameter  $\alpha_s$  (strong coupling constant) and two other unknown parameters  $m_t$  (top mass), and  $m_H$  (Higgs mass) enter as radiative corrections. In order to find an upper limit on the differences:

$$\Gamma'_Z \equiv \Gamma_Z^{measured} - \Gamma_Z^{SM} \quad (5.1)$$

and

$$\Gamma'_{inv} \equiv \Gamma_{inv}^{measured} - \Gamma_{inv}^{SM} \quad (5.2)$$

the values of  $M_Z$ ,  $\alpha$ , and  $G_F$  are taken at their precisely measured central values and the parameters  $\alpha_s$ ,  $m_t$ , and  $m_H$  are varied over reasonable ranges since these are less precisely known[48]:

$$\begin{aligned} \alpha_s &= 0.117 - 0.129 \\ m_t &= 131 - 225 \text{ GeV} \\ m_H &= 63 - 1000 \text{ GeV} \end{aligned}$$

The lower and upper bounds for the top mass are experimental results. The lower bound for the Higgs mass is experimental while the upper bound is theoretical. The most conservative (i.e. largest) values of  $\Gamma'_Z$  and  $\Gamma'_{inv}$  are kept (this corresponds to a small  $\alpha_s$ , small  $m_t$  and a large  $m_H$ ):

$$\begin{aligned} \Gamma_Z \text{ (SM)} &= 2482.9 \text{ MeV} \\ \Gamma_{inv} \text{ (SM)} &= 166.46 \text{ MeV} \end{aligned}$$

The measured values for the respective widths and their errors are taken from recent LEP cumulative data [27] and are:

$$\begin{aligned} \Gamma_Z \text{ (measured)} &= 2489 \text{ MeV} \\ \Gamma_{inv} \text{ (measured)} &= 165.9 \text{ MeV} \\ \sigma_Z \text{ (measured)} &= 7 \text{ MeV} \\ \sigma_{inv} \text{ (measured)} &= 1.4 \text{ MeV} \end{aligned}$$

These measured values are then compared to their Standard Model values for a one-sided confidence limit assuming Gaussian errors in the following manner (see Fig. 5-1): for example in the case of the total width, the Gaussian distribution is centered at the *measured* value  $\Gamma_Z = 2489 \text{ MeV}$  with a  $\sigma_Z$  equivalent to the measured error 7 MeV. The region on the left side of the predicted Standard Model value  $\Gamma_Z^{SM} = 2482.9 \text{ MeV}$  is considered to be unphysical. The region to the right-hand side is normalized to 1. The 95% confidence level upper limit  $\Gamma'_Z$  is found such that the area under the Gaussian from the value  $\Gamma_Z^{SM}$  is 0.95. The same method is used to determine the limit in the case of the invisible width from its values given above. In this manner, the values of  $\Gamma'_Z$  and  $\Gamma'_{inv}$  at the 95% C.L. are found to be:

$$\begin{aligned} \Gamma'_Z &< 12.2 \text{ MeV} \\ \Gamma'_{inv} &< 9.0 \text{ MeV} \end{aligned}$$

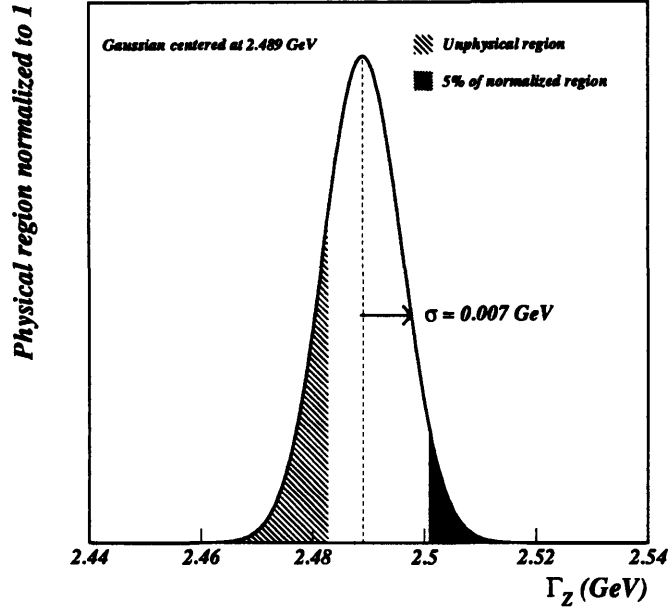


Figure 5-1: *The Gaussian distribution for limit extraction from the total  $Z^0$  width.*

To interpret these results, the  $Z^0$  width into fermion pairs as a function of the mass and coupling is examined. The general form for the decay width of the  $Z^0$  into a fermion-anti-fermion pair is given in Eq. 2.23.

For a homodoublet heavy lepton,

$$\begin{aligned} g_V &= -1 + 2 \sin \theta_W \\ g_A &= 0 \\ N_C &= 2 \end{aligned}$$

For a sequential heavy lepton, we have the Standard values of:

$$\begin{aligned} g_V &= -1/2 + 2 \sin \theta_W \\ g_A &= -1/2 \\ N_C &= 1 \end{aligned}$$

The width as a function of mass and couplings is shown in Fig. 5-2 along with the limits of  $\Gamma'_Z$  and  $\Gamma'_{inv}$  found above.

One obtains a topology dependent limit from the value of  $\Gamma'_{inv}$  where it is assumed that the decay mode of the excited lepton will not fall within the topologies required for the hadronic or leptonic width measurements. This is inclusive of the decays

$$l^* \rightarrow \nu W \quad (5.3)$$

$$l^* \rightarrow l Z^0 \quad (5.4)$$

The process in Eq. 5.3 would not display back to back structure so it might not be seen except indirectly in  $\Gamma_{inv}$ . The decay shown in Eq. 5.4 could be missed by the hadronic and leptonic selections as it would not fall into either categorical multiplicity.

The more conservative limit is topology independent in that it stems from the total width of the  $Z^0$  and thus is inclusive of all possible decay modes of the  $l^*$  which includes its decay into  $\nu W$ ,  $lZ^0$  as well as into  $l\gamma$  and in fact is completely independent of the decay mode.

From Fig. 5-2 we conclude that the masses are constrained at the 95% confidence level to lie above:

	Homodoublet	Sequential
	(GeV)	
Topology dependent	45.6	40.1
Topology independent	45.6	38.7

It is clear that if sequential family couplings are assumed, the mass limits are less stringent. However, the homodoublet pair produced excited leptons are excluded to the kinematical limit. The next step are direct searches. A direct search can still be performed for pair produced excited leptons which is model independent, yet is based on the decay  $Z^0 \rightarrow l^* \bar{l}^* \rightarrow l\gamma l\gamma$ . This shall be done in the future sections for  $l = e, \mu$  but primarily we shall be concerned with the search for the single production of  $l^*$  for masses between  $M_Z/2$  up to  $M_Z$ .

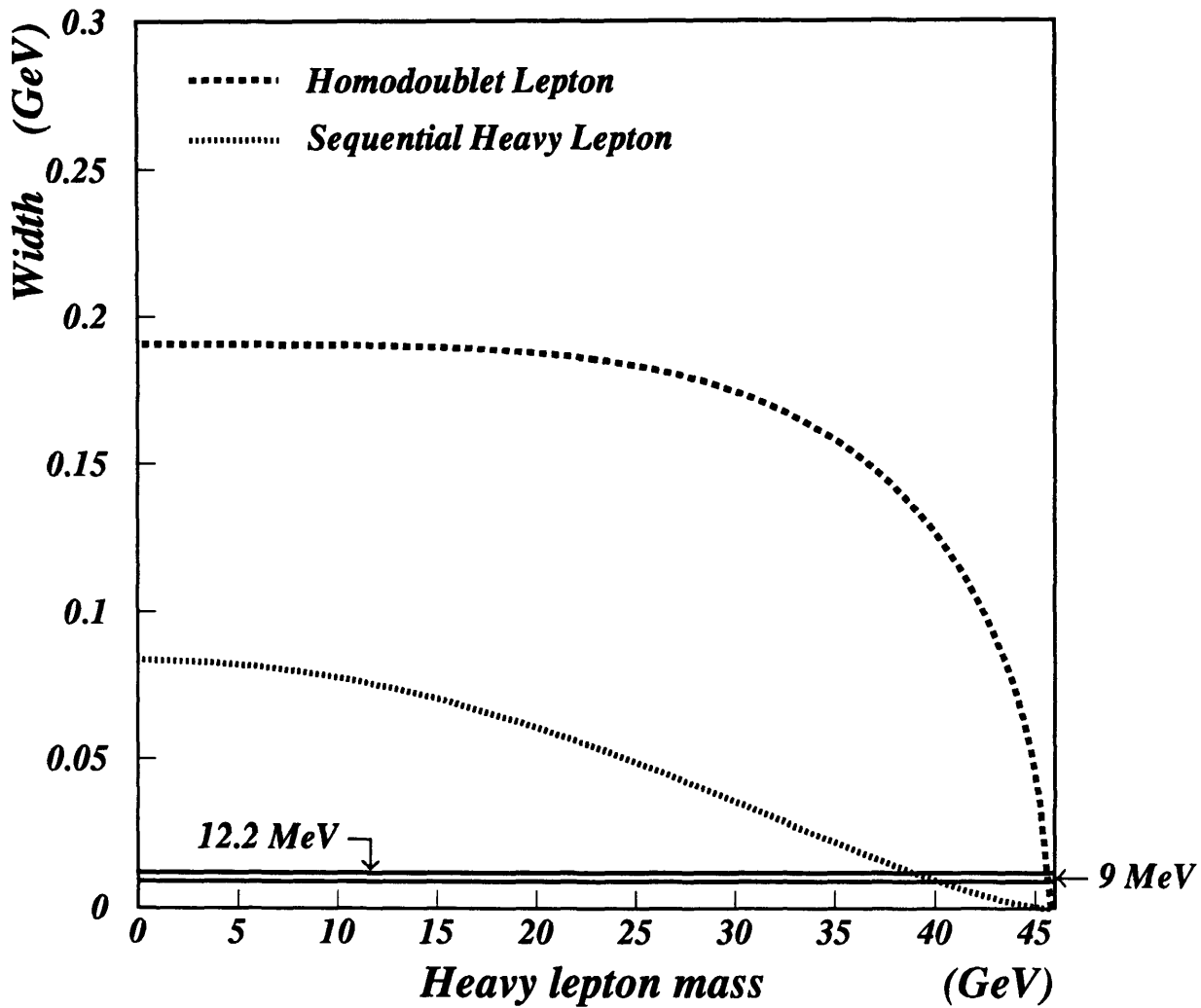


Figure 5-2: Limits extracted at the 95% C.L. for pair produced excited leptons. Shown are the widths for the homodoublet and sequential heavy leptons. The two horizontal lines are the allowed widths from  $\Gamma_{inv}$  and  $\Gamma_Z$ .





The signal searched for is an  $l\gamma$  invariant mass peak above the respective Standard Model distribution. For the s-channel two combinations are taken for each event, one for each of the two lepton candidates, (without explicit determination of the charge) whereas for the t-channel we search for only one electron and a photon.

## 6.2 Data quality requirements

In all analyses where track information is used for photon/electron identification or veto, the status of the TEC central tracking chamber must be known, and events associated with an unacceptable TEC condition must be discarded. The status of the TEC is defined by the track reconstruction efficiency which is directly related to the operating conditions (level of high voltage, for example) in the central tracking chamber. During moments of data taking, it is sometimes necessary that the high voltage of the TEC be lowered in certain sectors ultimately resulting in a lower track reconstruction efficiency. A method must be realized which will select data events for which the TEC status was 'acceptable.' In order to do this, two things must be determined: first, what is acceptable must be defined, and secondly, the corresponding total luminosity must be known.

As was described in Section 3.2.1, the TEC central tracking chamber is composed of three regions, of which, the inner and outer sectors will be used to determine its status. There are 12 inner sectors, each spanning  $30^\circ$  in  $\phi$  and outside these are 24 outer sectors, each spanning  $15^\circ$ . In one azimuthal region of  $30^\circ$  there are two outer sectors and one inner sector as shown in Figure 6-1.

The status of each sector is defined in the following manner: a list is made for all the data in  $\Delta t$  minute segments and in this list is a record of how many tracks there were in each of the 36 sectors. A sector is declared 'on' at time  $t$  if there is at least a track in that sector within the time interval  $t, t + \Delta t$ .

To retain a period of time  $t, t + \Delta t$ , the track reconstruction efficiency must be ensured in the entire azimuthal region. To require all TEC sectors to be operational at all times is too stringent a requirement that would result in a large loss of luminosity. For the data sample from 1991 to 1993, this would result in a loss of  $21 \text{ pb}^{-1}$  of luminosity. On the other hand, an *a posteriori* event-by-event check of the TEC status of selected candidates cannot be done without biasing the sample and leads to an overestimate of the usable luminosity. In the analysis presented below, we will be concerned with the identification of a charged particle and not with the measurement of its momentum. For track identification, it is not required to have a large number of hits (the maximum number of hits of a track is given by the number of wires of the inner and outer sectors totalling to 62). It suffices to ask that either the inner or the outer sector be operational and has recorded some hits. The condition for retainment of a time period  $t, t + \Delta t$  shall then be that in each of the 24  $15^\circ \phi$  sectors, either the outer sector *or* the corresponding inner sector must have a reconstructed track to be considered 'on.' The TEC condition is considered unusable during the period  $t, t + \Delta t$  whenever at least one of the 24  $\phi$  sectors is 'off.'

With the instantaneous luminosity of  $\mathcal{L} = 10^{31} \text{ cm}^{-2}\text{s}^{-1}$ , the hadronic rate is

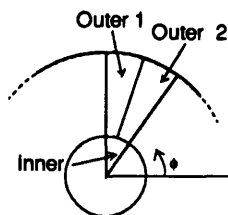


Figure 6-1: One azimuthal region of  $30^\circ$  of the TEC central tracking chamber.

approximately one event/3 seconds on the  $Z^0$  peak. In order to reduce statistical fluctuations, i.e. that there is sufficient time for all 24 outer and 12 inner sectors to be covered by the high cross section of hadronic decays, it is determined that the time slot of  $\Delta t = 4$  minutes is optimal. Indeed, in 4 minutes, the average number of hadronic events is:

$$\langle N_{had} \rangle = \mathcal{L}\sigma\Delta t \approx 72, \quad (6.1)$$

i.e.,  $\approx 1500$  tracks or  $\approx 60$  tracks per outer sector. (For the years of 1991 and part of 1992, LEP was running at an instantaneous luminosity of about  $10^{30} \text{ cm}^{-2}\text{s}^{-1}$ , which still yields about 6 tracks per outer sector in the time period  $\Delta t = 4$  min).

Although the TEC high voltage status is checked in four-minute intervals, data is kept according to *run number*. A separate run is given to all data which is taken uninterrupted in time, and can last anywhere from a few minutes to several hours. An entire run is discarded when the TEC criterion is not met in any of its 4 minute time intervals. The reason for this strong rejection is that the smallest period of time for which the integrated luminosity is precisely known is given by the run length.

A complete subsample of acceptable data is selected from the entire data sample of 1991 to 1993. It is determined that for all center-of-mass energies, the total integrated luminosity of usable data is  $57.3 \text{ pb}^{-1}$  out of a total  $65.1 \text{ pb}^{-1}$  collected. Table 6.1 shows the total and usable luminosities for the different center-of-mass energies.

By disregarding runs previous to data analysis, this method unbiasedly yields the correct luminosity for the data sample. When dealing with processes which exhibit the  $Z^0$  resonance in their cross sections, it is often more practical to work with effective luminosities to normalize the distributions of the simulated events. These Monte-Carlo events which are most often generated at the energy  $\sqrt{s} = M_Z$  can be directly normalized neglecting the  $\sqrt{s}$  dependence of initial state radiation. We have for the number of events  $N$ :

$$N = \sum_i \mathcal{L}_i(\sqrt{s_i})\sigma(\sqrt{s_i}) = \sum_i \mathcal{L}_i(\sqrt{s_i}) \frac{\sigma^{had}(\sqrt{s_i})}{\sigma^{had}(M_Z)}\sigma(M_Z) = \mathcal{L}_{eff}\sigma(M_Z) \quad (6.2)$$

for processes that exhibit the  $Z^0$  resonance shape. The effective luminosities are shown in Table 6.2.

Runs are disregarded when at least one sector is not fully operational. To see if this strong requirement could be relaxed, it is relevant to study on how many of the

24 sectors was the run rejection based on. In Figure 6-2 the number of sectors which were bad or 'off' for each run is shown weighted by the luminosity for that run. It is seen that in most cases the runs are not rejected due to one bad sector; on the contrary, in almost  $1.8 \text{ pb}^{-1}$  all sectors were off and only in  $0.63 \text{ pb}^{-1}$  one sector was off. Thus it is not feasible to consider the TEC loss in terms of an overall efficiency.

Therefore, for the following searches, we use a data sample with a total luminosity of  $57.3 \text{ pb}^{-1}$  out of which  $40.0 \text{ pb}^{-1}$  is taken on the  $Z^0$  peak. In the case of the excited muon search which does not require track information from the TEC (details follow in Section 6.5), we have a total luminosity of  $65.1 \text{ pb}^{-1}$ .

$\sqrt{s}$ ( GeV)	1991	1992	1993	Usable	Lost	Total
				$\mathcal{L}$ (nb <sup>-1</sup> )		
88.47	100.53	–	–	100.53	680.13	780.66
89.47	433.93	–	6818.74	7252.67	1313.73	8566.40
90.22	675.44	–	–	675.44	117.85	793.29
91.22	6140.61	19989.10	13901.25	40030.91	4776.20	44807.12
91.96	478.65	–	–	478.65	102.65	581.30
93.08	633.02	–	7685.71	8318.74	376.55	8695.29
93.72	460.86	–	–	460.86	370.50	831.36
Totals:	8923.0	19989.1	28405.7	57317.8	7737.6	65055.4

Table 6.1: *The usable and total luminosities summed for each year and for the different center-of-mass energies.*

$\sqrt{s}$ ( GeV)	1991	1992	1993	Usable	Lost	Total
				$\mathcal{L}$ (nb <sup>-1</sup> )		
88.47	17.09	–	–	17.09	115.62	132.71
89.47	154.91	–	2434.29	2589.20	469.00	3058.21
90.22	404.59	–	–	404.59	70.59	475.18
91.22	6140.61	19989.10	13901.25	40030.91	4776.20	44807.12
91.96	387.71	–	–	387.71	83.15	470.85
93.08	278.53	–	3381.71	3660.24	165.68	3825.92
93.72	152.54	–	–	152.54	122.64	275.18
Totals:	7536.0	19989.1	19717.4	47242.3	5802.9	53045.2

Table 6.2: *The effective usable and total luminosities summed for each year and for the different center-of-mass energies. They are scaled with the hadron cross sections. These values are used for the Monte-Carlo normalization.*

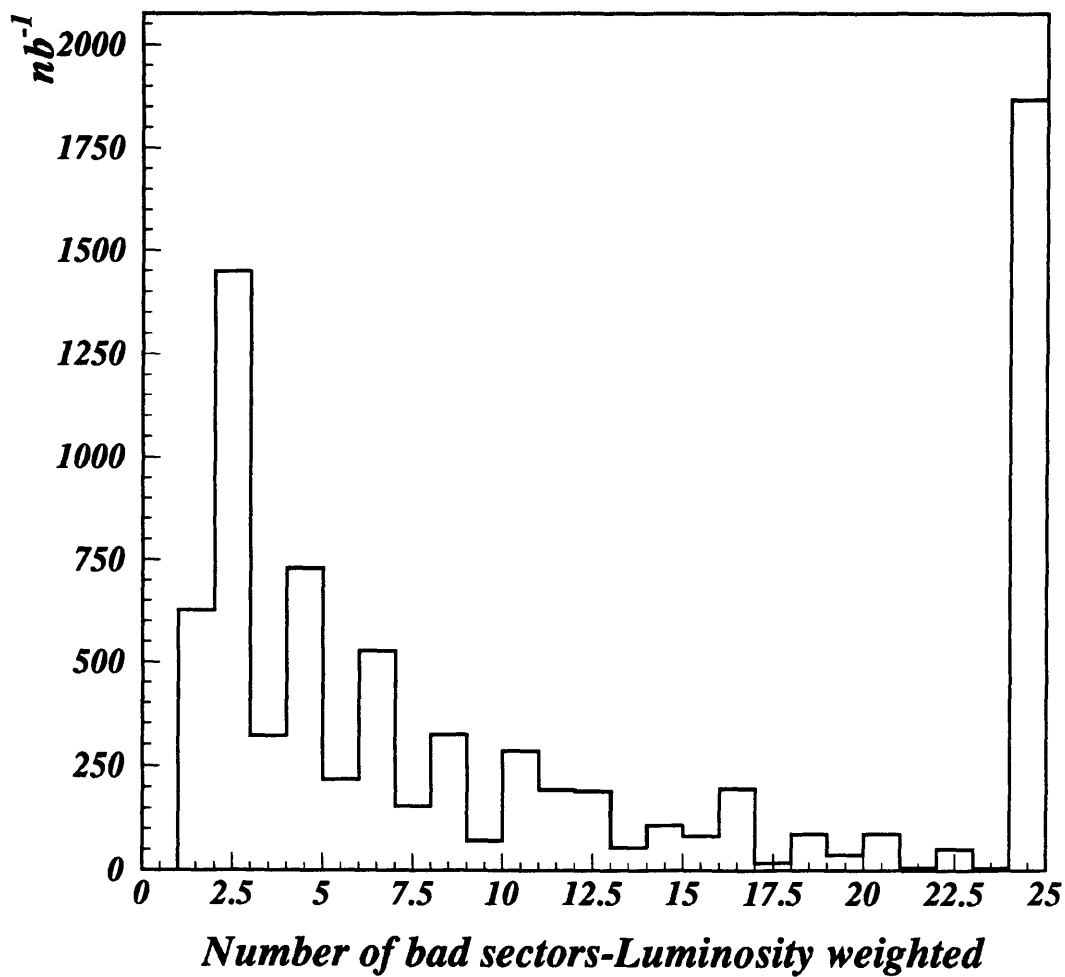


Figure 6-2: *The number of bad sectors for each run considered unusable. In almost  $1.8 \text{ pb}^{-1}$  all the sectors are off. But only in  $0.63 \text{ pb}^{-1}$  is only one sector off.*

## 6.3 $e^+e^- \rightarrow ee\gamma$

The search for excited electrons requires looking for possible signals in excess of radiative Bhabha events. This analysis requires selecting two electrons and a photon; these particles are identified in the BGO electromagnetic calorimeter and distinguished from each other using the TEC central tracker information.

### 6.3.1 Electron identification

Electromagnetic energy is deposited and identified in the BGO crystals. Both photons and electrons are identically absorbed in the BGO, their distinction realized with the presence of a matched track in the TEC chamber. A photon is distinguished from an electron by requiring that the nearest track in the  $r - \phi$  plane be farther than a determined distance.

In order to qualify as an electromagnetic cluster, the energy deposition in the BGO must satisfy the following requirements:

- $\frac{\sum_{9corr}}{\sum_{25corr}} \geq 0.95$

$\Sigma_9 / \Sigma_{25}$  is the ratio of the energy deposited in the  $3 \times 3$  crystal matrix centered at the most energetic crystal divided by the energy in the total  $5 \times 5$  crystals surrounding the most energetic crystal. The GEANT-based Monte-Carlo predictions for the fraction of energy deposited in the  $\Sigma_1$ ,  $\Sigma_9$  and  $\Sigma_{25}$  are listed in Table 6.3[49]. For electrons (or photons), the fraction of deposited energies are well determined and suffer little fluctuations. This is well verified in the data for instance by studying Bhabha events  $e^+e^- \rightarrow e^+e^-$ . The small fluctuations in energy deposition is in strong contrast with for example charged pions where the average fractional energy deposited is small and suffers from very large fluctuations (the largest deposition occurs in the case where the pion undergoes a charge exchange with a nucleon and is converted into a neutral pion. This latter decays into two photons which can carry a large fraction of the original charged pion energy).

The reduced sums  $\Sigma_9$  and  $\Sigma_{25}$  are used to estimate the energy of the incoming electrons/photons. The corrected sums are defined as:

$$\sum_{9corr} = \frac{\Sigma_9}{0.1231(\Sigma_1 / \Sigma_9) + 0.8222} \quad (6.3)$$

$$\sum_{25corr} = \frac{\Sigma_{25}}{0.1241(\Sigma_1 / \Sigma_{25}) + 0.8713} \quad (6.4)$$

These sums are used as estimators for the incoming electron/photon energy. The ratio of the two sums is used to identify the shape of the electromagnetic shower that developed in the BGO calorimeter. For an isolated electromagnetic cluster,  $\sum_{9corr} / \sum_{25corr}$  is approximately Gaussian in distribution, with the mean at 1.01 after position-dependent energy leakage corrections are applied. It is independent of the actual cluster energy for energies above 1 GeV. The situation is very different for

50 GeV electrons	Mean	Sigma
/E(incident)	%	%
$\Sigma_1$	$76.76 \pm 0.03$	$0.59 \pm 0.05$
$\Sigma_9$	$92.29 \pm 0.05$	$0.58 \pm 0.05$
$\Sigma_{25}$	$96.10 \pm 0.07$	$0.89 \pm 0.11$
30 GeV pions	Mean	RMS
/E(incident)	%	%
$\Sigma_1$	10.1	12.2
$\Sigma_9$	16.6	18.4
$\Sigma_{25}$	18.8	20.4

Table 6.3: *The Monte-Carlo predicted values for the mean and sigma(RMS) for the fraction of energy deposited in the reduced sums for 50 GeV electrons(30 GeV pions).*

the charged pions. In this case, the shower shape is not ruled by the Molière radius but rather by the rare nuclear interactions that can enlarge the nuclear showers to neighboring crystals. In this case, the ratio  $\Sigma_{9corr} / \Sigma_{25corr}$  is close to one only in a few percent of the cases. A good charged pion rejection is therefore achievable.

The Monte-Carlo distributions for the electrons produced in BABAMC[41] and for taus from KORALZ[43] are shown in Figure 6-3. For the taus, all the possible decay modes have been included which explains the long tail that is observed below 0.95. The tail is not shown completely on the plot but extends down to  $\Sigma_{9corr} / \Sigma_{25corr} \approx 0.5$ . With a cut at 0.95, the rejection for tau events is about 2 while the efficiency for Bhabha events is nearly 100%.

- $\chi^2 \leq 20$

The  $\chi^2$  function is defined as:

$$\chi^2 = \sum_{i=1}^9 \frac{(Fr_i - Fr_i^{TB}(x, y, E))^2}{\sigma_i^2(x, y, E)}$$

where  $Fr_i = E_i/E$ , the fraction of energy deposited in crystal  $i$ , and  $x, y$  is the impact point on the front face of the central crystal and  $E$  is the energy in the 9 crystals.  $Fr_i^{TB}$  is the fraction of energy for the  $i^{th}$  crystal and  $\sigma_i$  is its variance measured in the test beam with electrons.

The  $\chi^2$  is a statistical measure which gives an estimate of the authenticity of an electromagnetic cluster as having originated from a photon or electron by comparing in each crystal the observed energy to the expected energy depositions for electromagnetic showers. Because it takes into account the fraction deposited in each crystal, the  $\chi^2$  improves the background rejection provided by the  $\Sigma_9 / \Sigma_{25}$  criterion. In particular, the chi-square cut can reduce the fraction of electromagnetic clusters formed

E (GeV)	e efficiency (%)	$\pi^0$ rejection (%)
8	$92.3 \pm 1.2$	$83 \pm 1.7$
10	$92.6 \pm 1.2$	$80 \pm 1.8$
15	$94.3 \pm 1.2$	$60 \pm 2.2$
20	$91.3 \pm 1.2$	$38 \pm 2.2$
25	$93.4 \pm 1.2$	$20 \pm 1.8$
30	$92.3 \pm 1.2$	$10 \pm 1.3$
35	$93.7 \pm 1.2$	$3.1 \pm 0.8$

Table 6.4: *Efficiency for isolated electrons and rejection for  $\pi^0$  with the condition  $\chi^2 < 12$ . The errors are statistical only.*

by two very neighboring photons, such as the ones originating from the decay of a neutral pion  $\pi^0$ . To illustrate this, Table 6.4 shows the  $\pi^0$  rejection of the cut  $\chi^2 < 12$  as a function of the neutral pion energy[50]. Figure 6-4 shows the distribution for electrons from BABAMC and for tau events produced with the KORALZ Monte-Carlo. All the decay modes of the tau have been included. The rejection of the cut  $\chi^2 < 20$  for tau events is about 3.

The  $\sum_9 / \sum_{25}$  and  $\chi^2$  cuts are very effective at reducing the backgrounds to electrons and photons. These cuts will be used in the next sections to identify these particles. The presence of a TEC track within a given distance of an electromagnetic cluster candidate will define it to be an electron. The distance is analysis-dependent and must be determined based on event dynamics.

### 6.3.2 Event selection

This analysis is restricted to the polar angular range of  $38^\circ$ - $142^\circ$  which is covered by the barrel electromagnetic calorimeter. The main source of background to the signal comes from radiative Bhabha events. The forward and backward regions suffer even more from this background due to the divergent cross section at small scattering angles and the signal to background ratio is not as favorable as in the barrel region. The forward region is therefore not used.

The second source of background arises from the  $Z^0$  decays into a pair of tau leptons. The cross section of  $Z^0 \rightarrow \tau^+\tau^-$  is comparable to that of the Bhabha events pertinent to the angular region in question and is of the order of  $\sim 1$  nb on the peak. This background enters in two distinct ways: 1) via the leptonic decay of the tau into an electron and neutrinos

$$\tau^- \rightarrow e\bar{\nu}_e\nu_\tau \quad (6.5)$$

This background is suppressed due to the branching ratio of  $\approx 18\%$  and also because of the kinematics of the  $\tau$  decay which involves invisible energy taken away by the neutrinos.

2) in relation to the identification of electrons. The decay

$$\tau^- \rightarrow \pi^- \pi^0 \nu_\tau \quad (6.6)$$

is a background if the charged pions enter the electromagnetic calorimeter close to the two photon decay products of the  $\pi^0$ . This results in a charge particle trajectory pointing to a BGO cluster which have the characteristics of a photon interaction. The selections cuts on the  $\Sigma_9/\Sigma_{25}$  and  $\chi^2$  mentioned above reduce this contamination.

The very small background coming from  $Z^0 \rightarrow \gamma\gamma(\gamma)$  is negligible since this process has a cross section of the order of  $\sim 50 - 60$  pb, and the presence of two tracks would imply two photon conversions.

The selection of  $e^*$  candidates are as follows:

- (1)  $\text{NASRC} < 12$ ; This is the number of Simple Reconstructed Clusters found in the detector. In general the distinction between hadronic  $Z^0$  decays and leptonic ones occur at  $\text{NASRC} \approx 16$ .
- (2) At least 3 good electromagnetic clusters in the barrel region with energy greater than 0.5 GeV and all must satisfy the electromagnetic criteria  $\Sigma_9 / \Sigma_{25} > 0.95$  and  $\chi^2 < 20$ ;
- (3) All 3 clusters within polar region  $|\cos \theta| < 0.78$ ;
- (4)  $E_3 \geq 3$  GeV; this is a first-pass cut to reduce radiative Bhabha events.
- (5) Energy in the hadron calorimeter  $\leq 10$  GeV.
- (6) Exactly two good tracks in the TEC passing the quality cuts described in Section 4.4.2 and pointing to a good electromagnetic cluster. (From hereon all mentioned tracks must satisfy the same condition).

These select radiative Bhabha events in the barrel region. Figures 6-5 through 6-10 show the distributions for the three energies of the electromagnetic clusters in the BGO along with the distributions for the  $e^*$  signals of 60, 80 and 85 GeV. The energies are normalized to the center-of-mass energy and the overall normalization of the Monte-Carlo is made to the effective usable luminosity of  $47.2 \text{ pb}^{-1}$ . Figure 6-5 shows the energy of the most energetic electromagnetic cluster for the data and the two Monte-Carlo event samples. The Bhabha peak is clearly seen at the normalized energy of 1 and the distribution from 0.6 to about 0.8 is due almost exclusively to taus. These clusters are lower in energy due to the energy taken by the neutrinos. In Figure 6-6 is the same distribution for the  $e^*$  signal of different masses. The 60 GeV signal is relatively dispersed while the two higher mass signals show a peak nearer the center-of-mass energy. This is due to the boosting of the  $e^*$  in the laboratory frame for lower masses. The emitted photon can have a low energy in the laboratory if emitted in the backward direction. It should be noted that for the signal either the first or second most energetic electromagnetic cluster can be the photon; this is mass dependent and the two cases have not yet been distinguished.

The second most energetic cluster is seen in Figures 6-7, 6-8. The peak produced by the Bhabha events is seen near 1. The tau events are distributed at lower energies. For the signal, the same energy peaks are seen for the high mass  $e^*$  events while the 60 GeV one is still dispersed as it must be, since in this case the photon and electron of the  $e^*$  will alternate in which is more energetic. The energy distribution of the third electromagnetic cluster is quite different in that the QED shows the expected radiative spectrum whereas the signal exhibits monoenergetic behavior for heavy  $e^*$  masses. This is due to the fact that in these cases the third cluster is the ordinary electron recoiling off the  $e^*$ . For the light  $e^*$  mass, the energy is more dispersed but a slight monoenergetic behavior is still apparent. These are shown in Figures 6-9 and 6-10.

The QED background is suppressed with the following requirements:

- (7) Normalized energy of the first cluster  $\geq 0.7$ ;
- (8) Normalized energy of the second cluster  $\leq 0.96$ ;
- (9) Normalized energy of the third cluster  $\geq 0.1$ .

The normalized total BGO energy distribution after the previous cuts is shown in Figure 6-11. The data exhibits the expected Bhabha peak and the flat spectrum at energies lower than about 0.9 are due to tau decay. Contrary to this is the signal distribution, which shows a narrow peak around 1. Since the signals leave nearly the total center-of-mass energy in the BGO one can place a lower cut on this parameter in order to reject tau events. Therefore we require:

- (10) Normalized total BGO energy  $\geq 0.91$ .

Now it is possible to use the tracks in the TEC to choose a photon candidate out of the three electromagnetic clusters. Since our data sample is required to contain exactly two tracks, the photon is chosen as being the cluster with the farthest distance in  $\phi$  to any track. The distribution of the distances given in radians is shown in Figures 6-13 for the electron candidates and 6-15 for the photon candidate. The signal distributions are shown respectively in Figures 6-14 and 6-16. For the photon candidate, it is seen in the data that although there are some tracks which are very close to the center-of-gravity of the electromagnetic clusters, the distribution is relatively flat in comparison to that of the electron candidate. Note the different horizontal scales for the two cases. For the electron candidate, most tracks are within 0.01 radians of the cluster. In the signal distributions, the photon spectrum is almost entirely flat whereas that of the electron candidate is almost entirely peaked at distances closer than 0.01 radians. From these it is clear that one can safely put a restriction on the electron-track distance. In order to allow any left-right track reconstruction ambiguities, the distance criterion is relaxed and it is required that the electron candidates must satisfy:

- (11) Distance in  $\phi$  from the track to the electron candidates must be less than 50 mrad

$e^*(\text{s-channel})$	60 GeV	$33.4 \pm 2.1\%$
$e^*(\text{s-channel})$	80 GeV	$32.2 \pm 2.1\%$
$e^*(\text{s-channel})$	85 GeV	$26.3 \pm 2.0\%$
BABAMC $e^+e^-$ Monte-Carlo		$0.29 \pm 0.03\%$
KORALZ $\tau^+\tau^-$ Monte-Carlo		$< 3.2 \times 10^{-3}\%$

Table 6.5: The  $e^*$  signal detection efficiencies are based on 500 generated and fully simulated events and the selection efficiencies on the background Monte-Carlo events.

and no track requirement is made on the photon candidate. The energy distribution of the photon candidate is shown in Figures 6-17 and 6-18. The expected monoenergetic behavior is seen for the higher mass signals. The data exhibits the expected radiative behavior. No additional energy requirement is placed at this point.

Once the two electrons are identified one can put a requirement in their acollinearity since QED events are dominantly back-to-back. Figures 6-19 and 6-20 show respectively the distribution for the data, the Monte-Carlo events and the signals. It is now a trade-off between keeping as much signal as possible while rejecting the QED background. The following cut is chosen:

$$(12) \theta_{e(1)e(2)} < 140^\circ.$$

After these cuts the invariant mass is made between the photon and each electron which in the relativistic case is:

$$\mathcal{M}_{e\gamma} = \sqrt{2E_\gamma E_e(1 - \cos \theta_{e\gamma})} \quad (6.7)$$

There are two entries per event and the resulting distribution is shown in Figure 6-21. This distribution will be used to find a limit on the coupling as a function of mass. There are 108 entries in the data while  $92.4 \pm 10.6$  in total are expected from the background sources.

We restrict ourselves to invariant mass combinations above 45 GeV. Below this energy pair production of excited leptons should dominate as discussed in Section 5.2. However, a model independent search is carried out and explained in Section 6.3.3 which looks for invariant mass peaks up to  $\sim \sqrt{s}/2$ .

The efficiencies for the selection of  $e^*$  events are mass dependent since one set of selection cuts were used for each analysis. After all cuts, all the signal events falling underneath a fitted Gaussian on the mass peak but *above* the peak background are counted. The  $e^*$  signal detection efficiencies are based on 500 events simulated through the detector and are listed in Table 6.5.

An example of an  $e^*$  candidate is shown in Figure 6-23. The photon energy is 36.0 GeV and the two electrons have 33.9 and 19.3 GeV.

### 6.3.3 $e^+e^- \rightarrow ee\gamma\gamma$

It is possible to execute a model independent search for an excited electron by looking for pairs of  $e^*$  with similar invariant masses. This exploits the excellent resolution

of the L3 detector (At 45 GeV the resolution is of the order of 1% for electrons and photons). A very narrow photon-electron invariant mass peak could be readily identified should this peak exist. We impose no limitation on the mass region looked at; any invariant mass up to the beam energy is accessible.

All the events that have at least four electromagnetic clusters with  $\sum_9 / \sum_{25} > 0.95$  and  $\chi^2 < 20$  and with energy above 5 GeV are considered. Only twelve events pass these cuts in the entire data sample. Two invariant mass combinations are produced for each event by matching the first electron  $e_1$  with the closest photon  $\gamma_1$  and the two other ones  $e_2$  and  $\gamma_2$ . The opposite combination is calculated as well. A scatter plot of the invariant masses  $\mathcal{M}_{e_1\gamma_1}$  vs.  $\mathcal{M}_{e_2\gamma_2}$  and  $\mathcal{M}_{e_1\gamma_2}$  vs.  $\mathcal{M}_{e_2\gamma_1}$  is shown in Figure 6-24. To test the hypothesis that these events are produced by the reaction

$$e^+e^- \rightarrow e^*e^{\bar{*}} \rightarrow e\gamma e\gamma \quad (6.8)$$

we select the events that satisfy one of the following criteria:

$$|\mathcal{M}_{e_1\gamma_1} - \mathcal{M}_{e_2\gamma_2}| < 3 \text{ GeV}$$

or

$$|\mathcal{M}_{e_1\gamma_2} - \mathcal{M}_{e_2\gamma_1}| < 3 \text{ GeV}.$$

The 3 GeV window corresponds to a  $2\sigma$  level since the expected resolution is  $\sigma = 1.2$  GeV. Three events survive this last requirement. To better estimate the possible invariant mass of the candidates, the average invariant mass is calculated. It is shown for the events which fall within the allowed mass window in Figure 6-25. There does not exist a reliable Monte-Carlo generator which accurately describes hard, multiple radiative Bhabha events, therefore the three events are taken as signal. It is clear however that the invariant mass distribution does not exhibit a significant peak which would be an unambiguous signal for a resonant  $e^*$  state. In terms of branching ratios, the previous result can be interpreted as a limit at the 95% C.L. assuming a 50% detection efficiency:

$$Br(e^+e^- \rightarrow e^*e^{\bar{*}}) \times Br(e^* \rightarrow e\gamma)^2 < 4.6 \times 10^{-6} \quad (6.9)$$

for  $m_{e^*} < 45$  GeV.

In addition, one can look for a  $\gamma\gamma$  resonance and Figure 6-26 shows the  $\gamma\gamma$  invariant mass vs. the  $ee$  invariant mass.

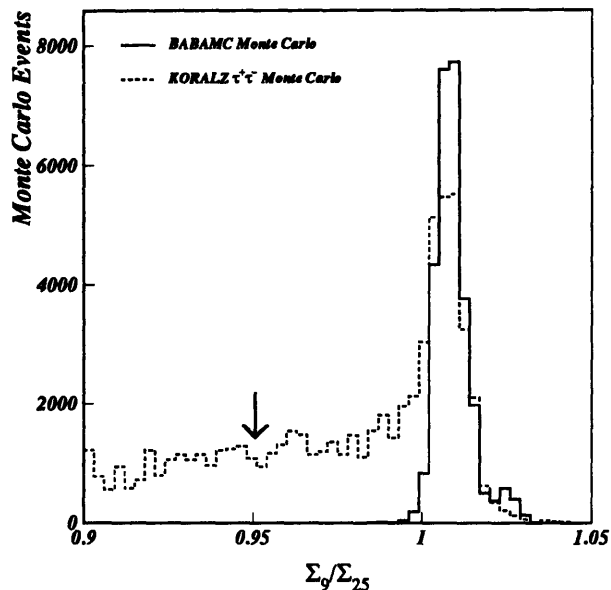


Figure 6-3: *The ratio of the energy deposited in the central 9 crystals to that of the energy deposited in the surrounding 25 crystals for KORALZ tau Monte-Carlo events compared to that of BABAMC Monte-Carlo events. A cut is placed at 0.95 to help distinguish between charged pions and photons.*

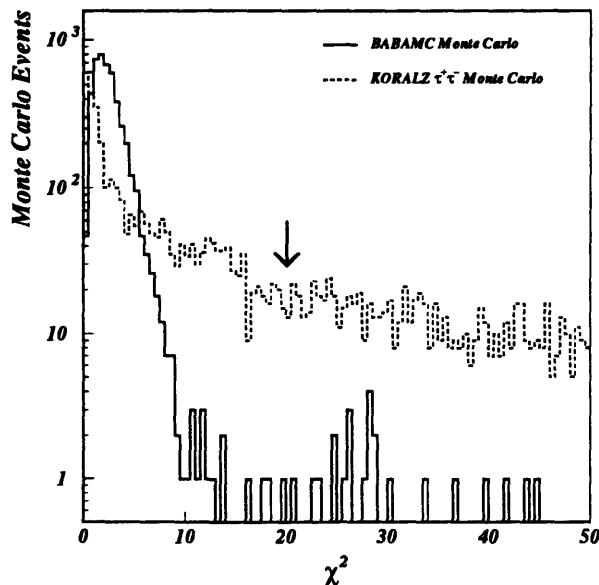


Figure 6-4: *The chi-square distribution for KORALZ tau Monte Carlo events compared to that of Bhabha Monte-Carlo events. A cut is placed at  $\chi^2 = 20$ .*

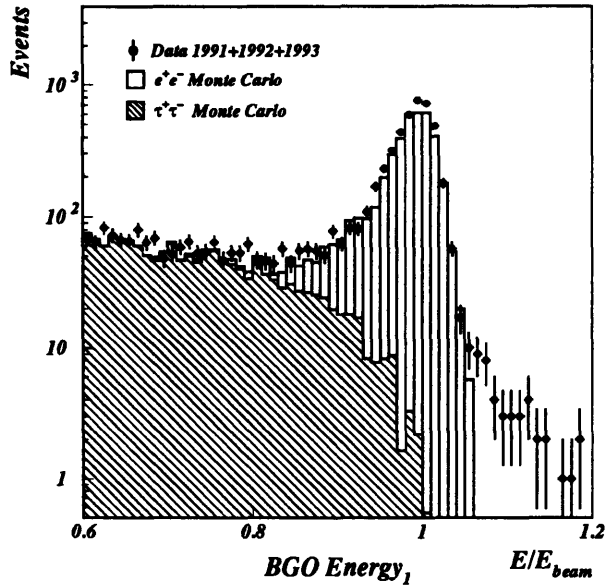


Figure 6-5: The total energy of the most energetic electromagnetic cluster. It is normalized to the beam energy.

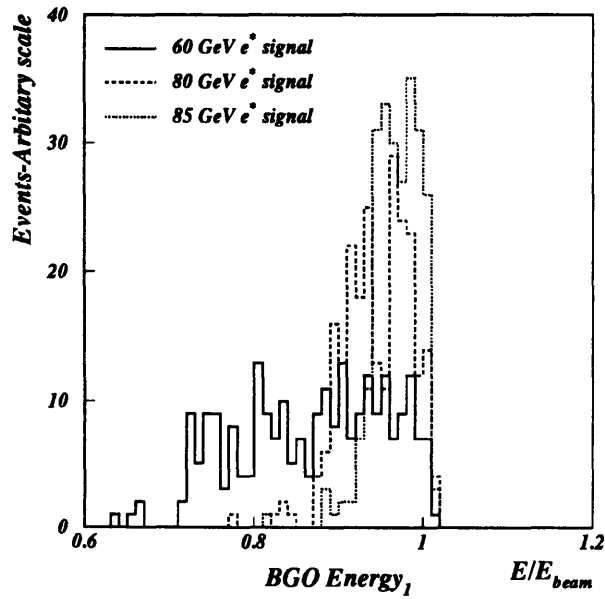


Figure 6-6: The corresponding distributions for the three different mass signals. A cut is placed at 0.7.

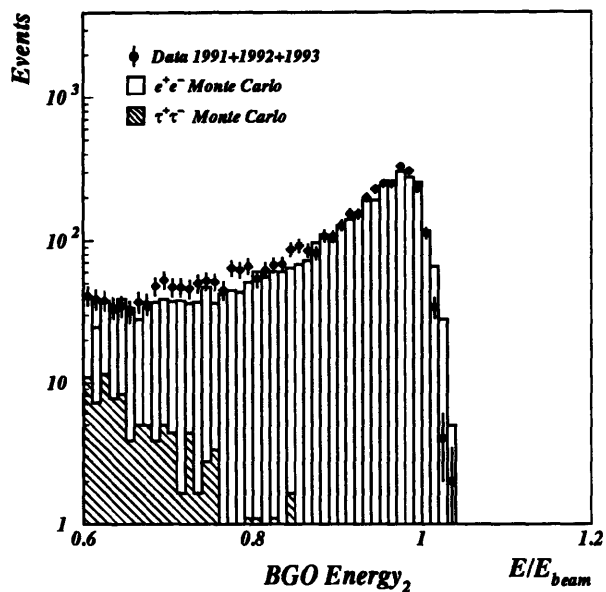


Figure 6-7: The total energy of the second most energetic electromagnetic cluster. It is normalized to the beam energy.

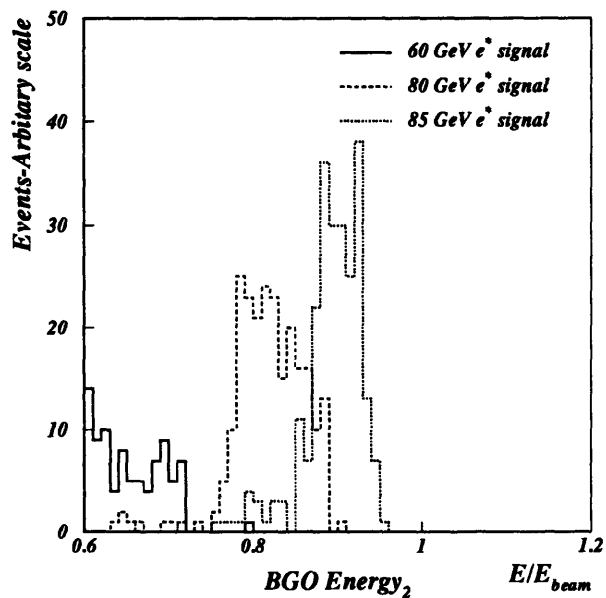


Figure 6-8: The corresponding distributions for the three different mass signals. A cut is placed at 0.96.

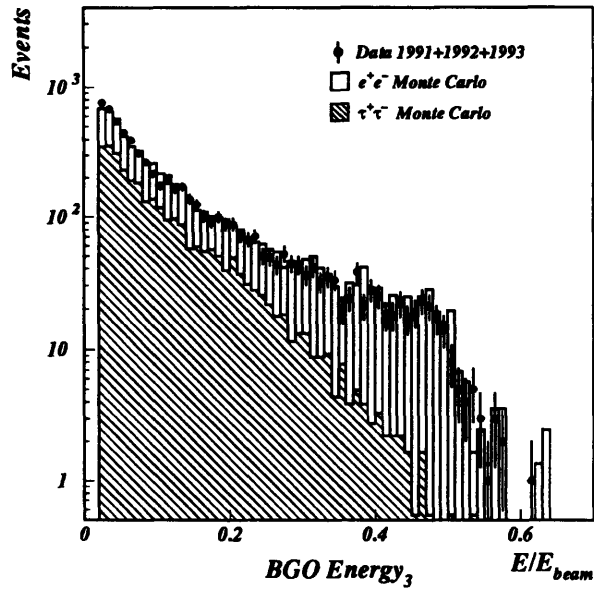


Figure 6-9: The total energy of the third most energetic electromagnetic cluster. It is normalized to the beam energy.

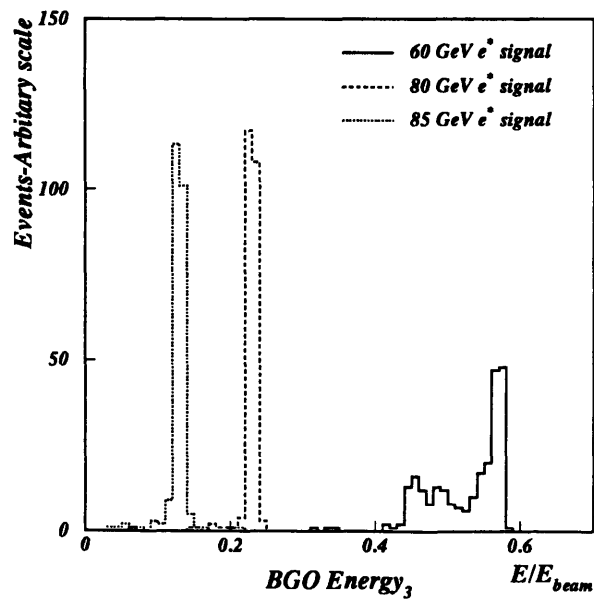


Figure 6-10: The corresponding distributions for the three different mass signals. A cut is placed at 0.1.

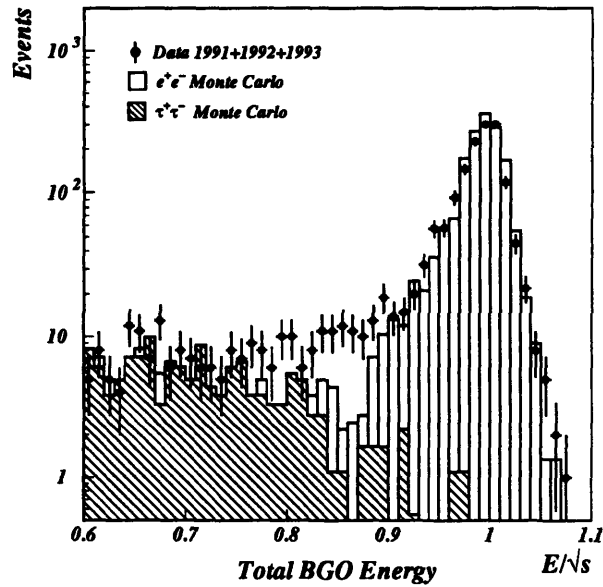


Figure 6-11: The total normalized energy deposited in the electromagnetic calorimeter.

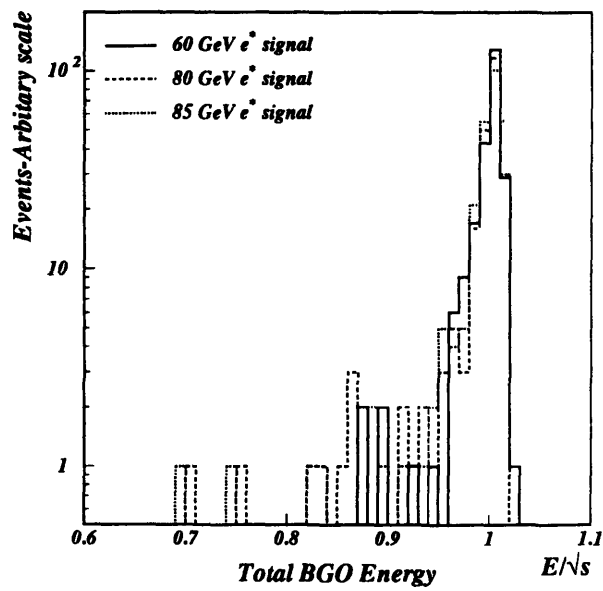


Figure 6-12: The corresponding distributions for the three different mass signals. A cut is placed at 0.91.

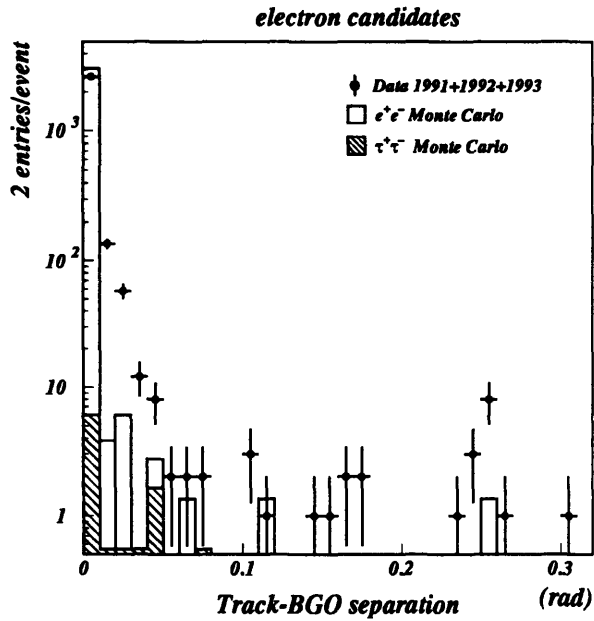


Figure 6-13: The distance in radians from the track in the TEC to the center-of-gravity of the BGO cluster for the electron candidates. There are two entries per event.

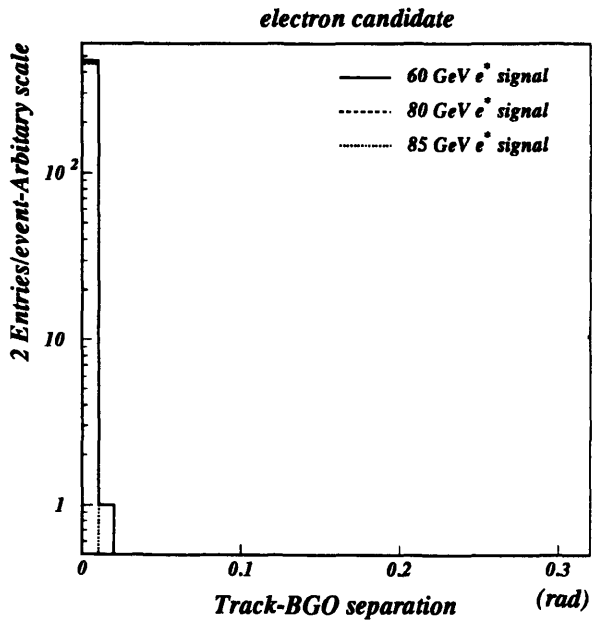


Figure 6-14: The corresponding distributions for the three different mass signals. A cut is placed at 0.05 radians to qualify as an electron.

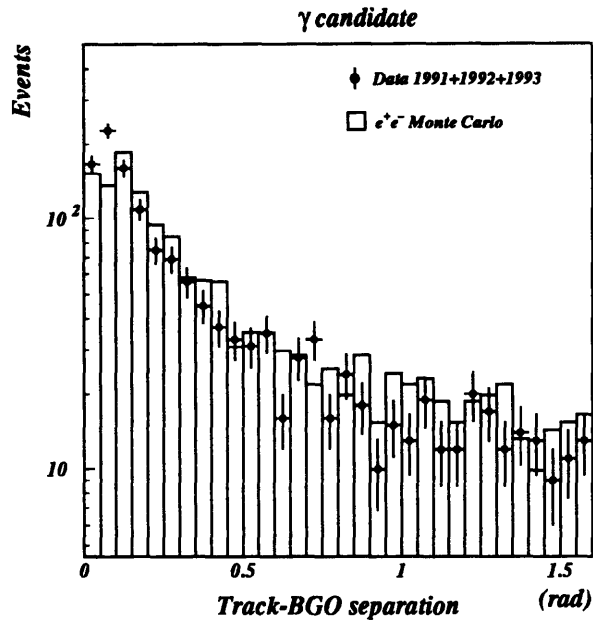


Figure 6-15: The distance in radians from the track in the TEC to the center-of-gravity of the BGO cluster for the photon candidate.

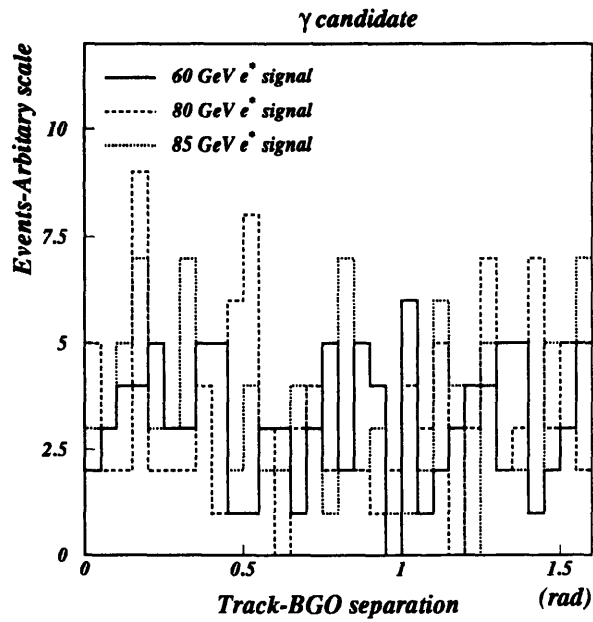


Figure 6-16: The corresponding distributions for the three different mass signals.

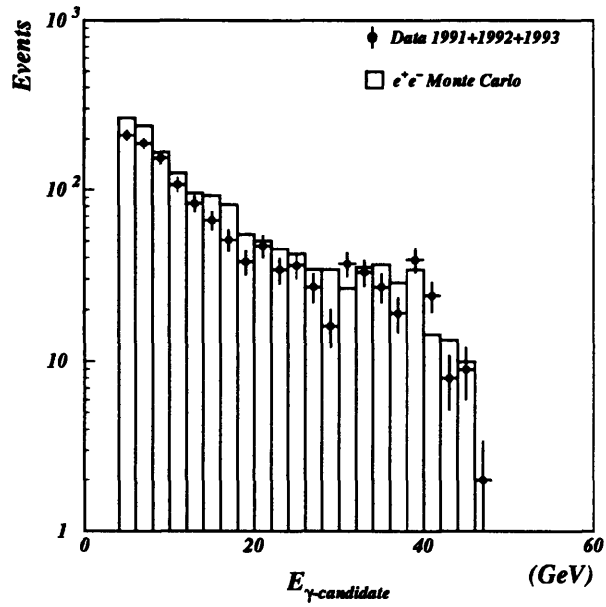


Figure 6-17: *The energy of the photon candidate.*

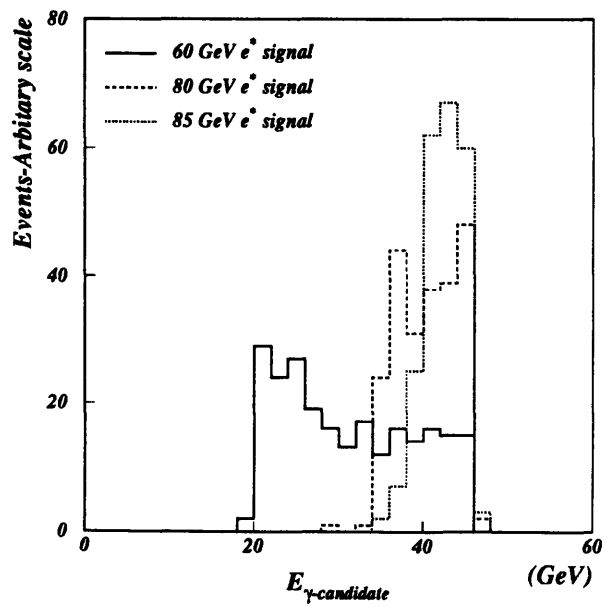


Figure 6-18: *The corresponding distributions for the three different mass signals.*

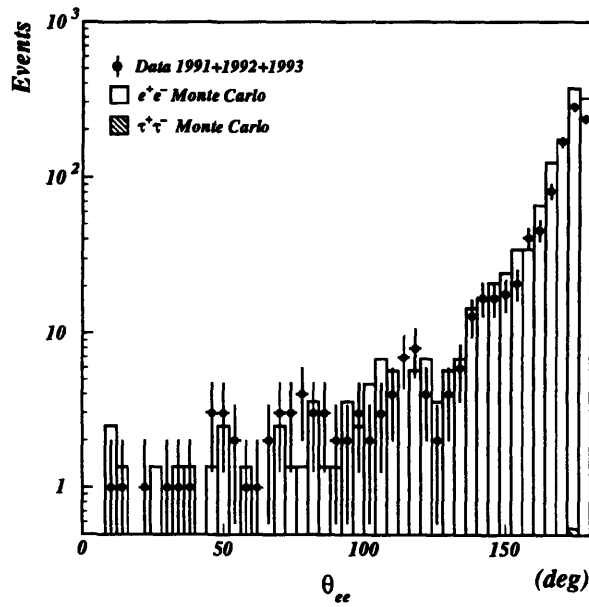


Figure 6-19: *The distance in degrees between the two electron candidates.*

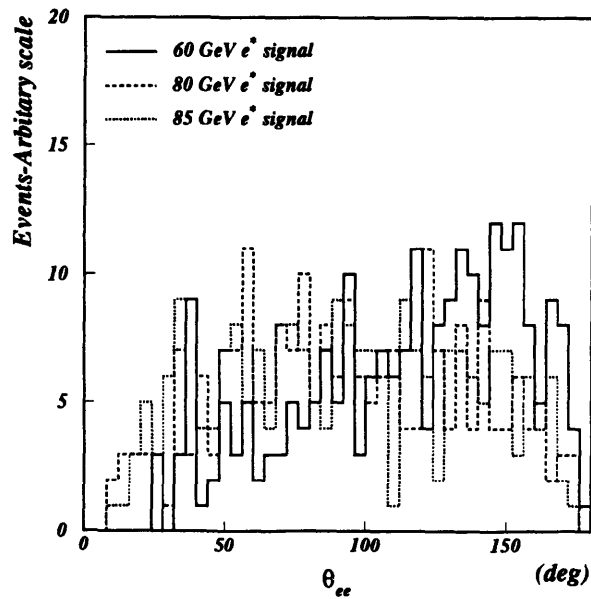


Figure 6-20: *The corresponding distributions for the three different mass signals. A cut is placed at  $140^\circ$ .*

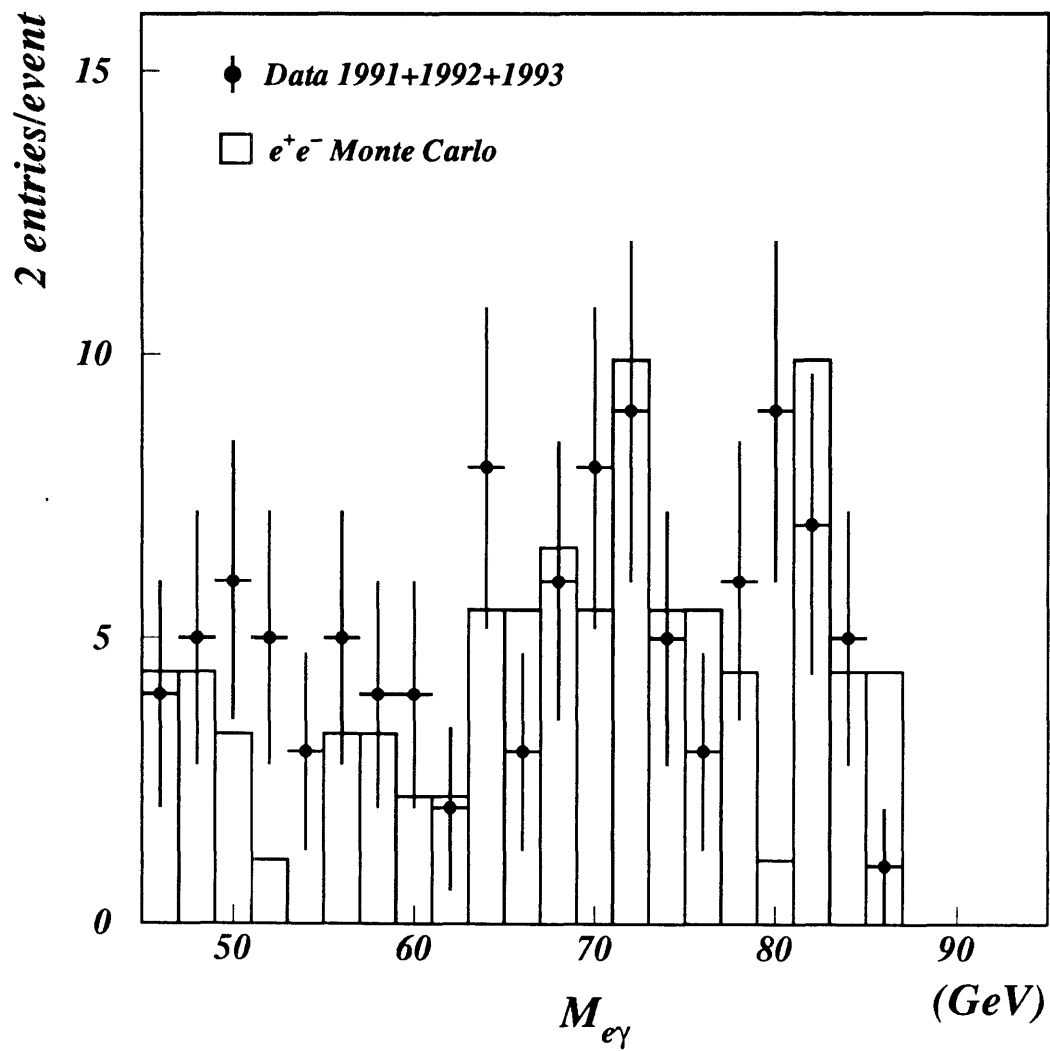


Figure 6-21: The invariant mass distribution for  $e\gamma$  pairs. There are 108 events in the data while  $92.4 \pm 10.6$  are expected from the background Monte-Carlo.

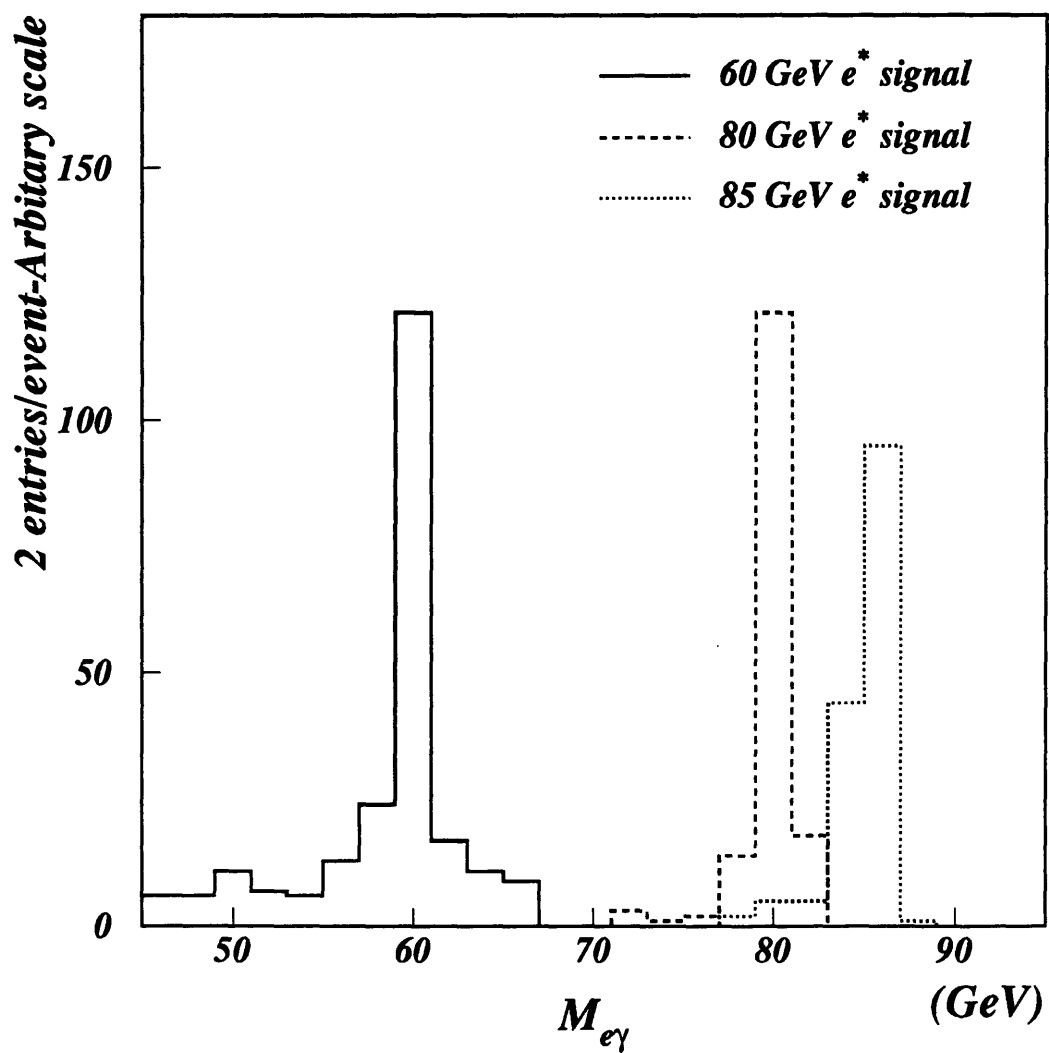


Figure 6-22: The invariant mass distribution for  $e\gamma$  pairs in three different signal masses. The relative weights are due to selection efficiencies; 500 events of each mass were generated and fully simulated.

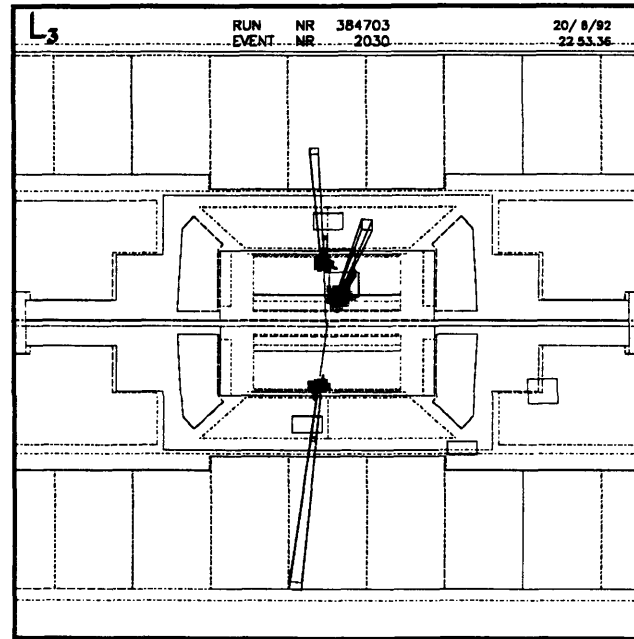
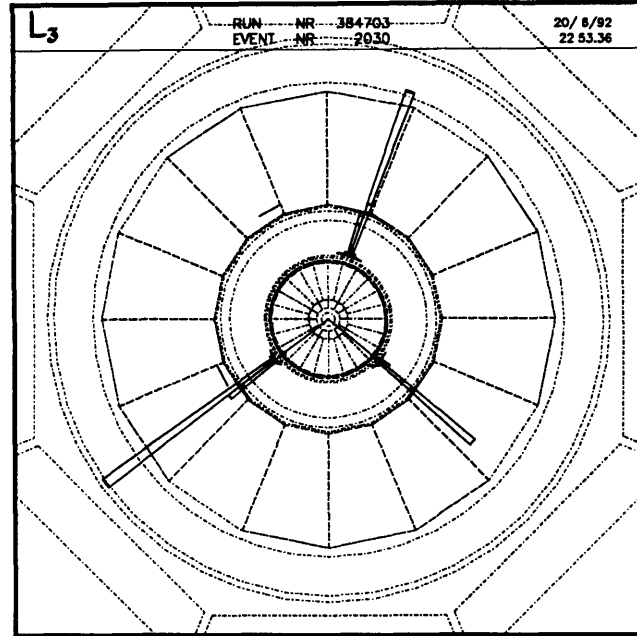


Figure 6-23: An example of a radiative Bhabha event from 1992. The energy of the photon is 36.0 GeV and the electrons have 33.9 and 19.8 GeV.

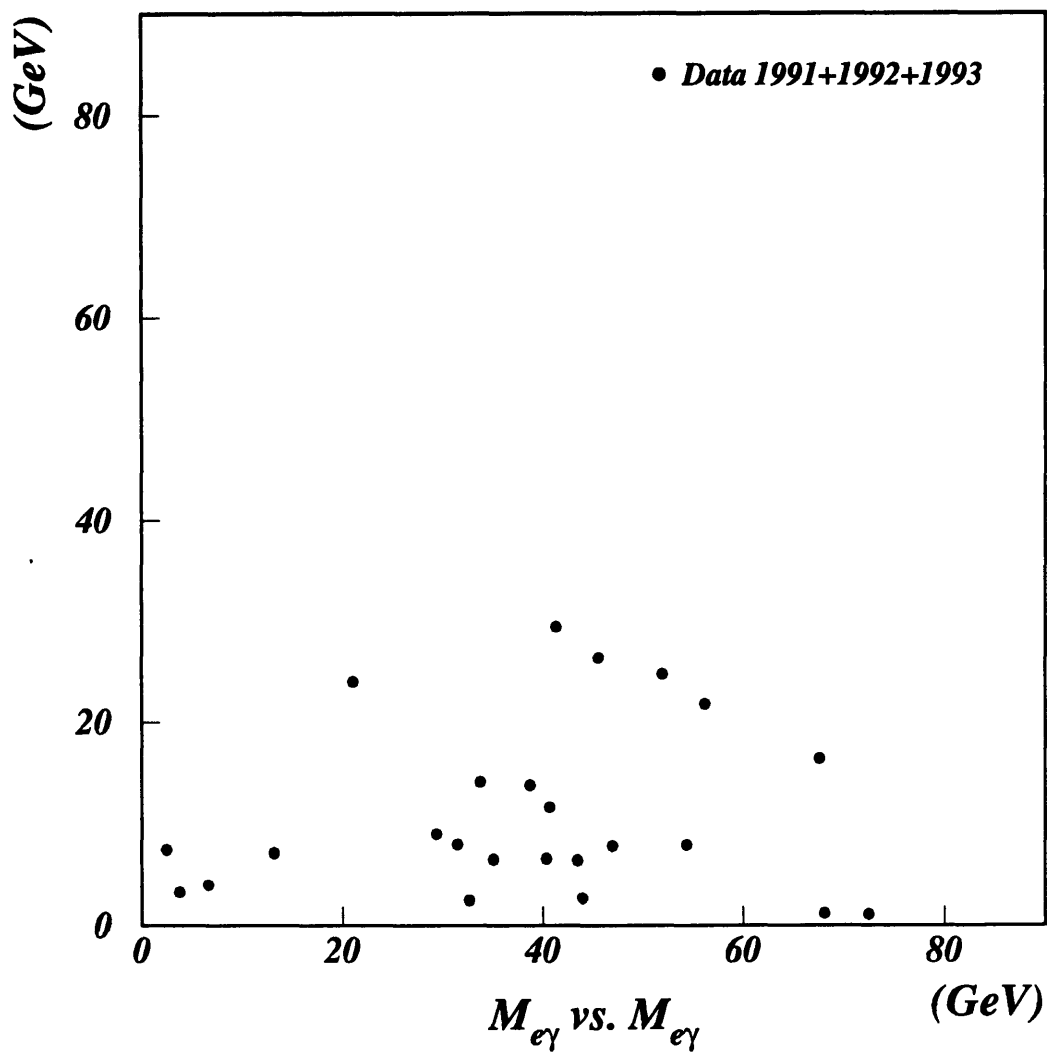


Figure 6-24: The 2-dimensional spectrum of the  $e-\gamma$  invariant masses in the context of pair production. Plotted are  $M_{e_1\gamma_1}$  vs.  $M_{e_2\gamma_2}$  and  $M_{e_1\gamma_2}$  vs.  $M_{e_2\gamma_1}$  for each event. The average invariant mass of any events lying within 3 GeV of the diagonal are shown in Figure 6-25.

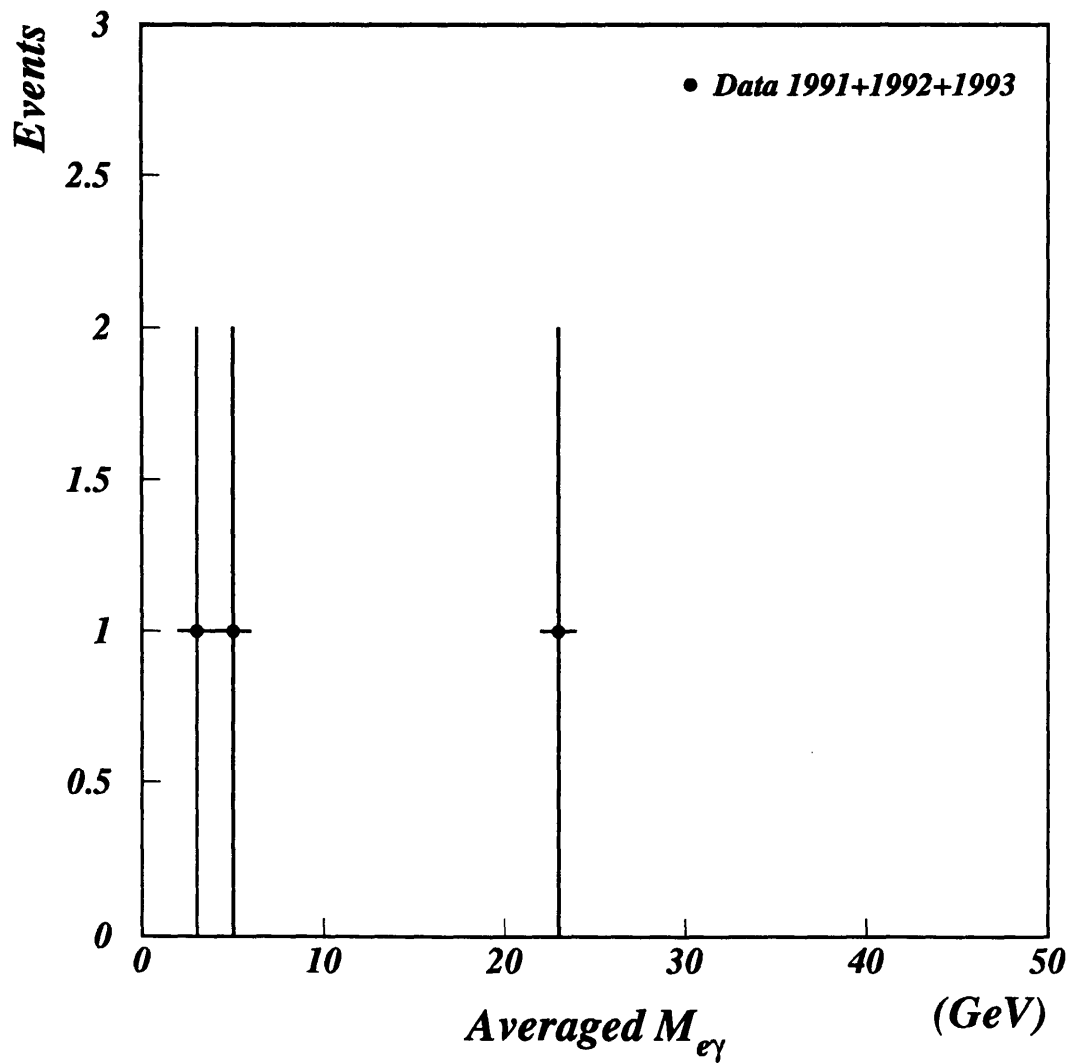


Figure 6-25: The average invariant mass of any pair-produced  $e^*$  candidates. The two invariant masses must lie within  $2\sigma$  of the resolution, which is conservatively set at 3 GeV. No peak is seen.

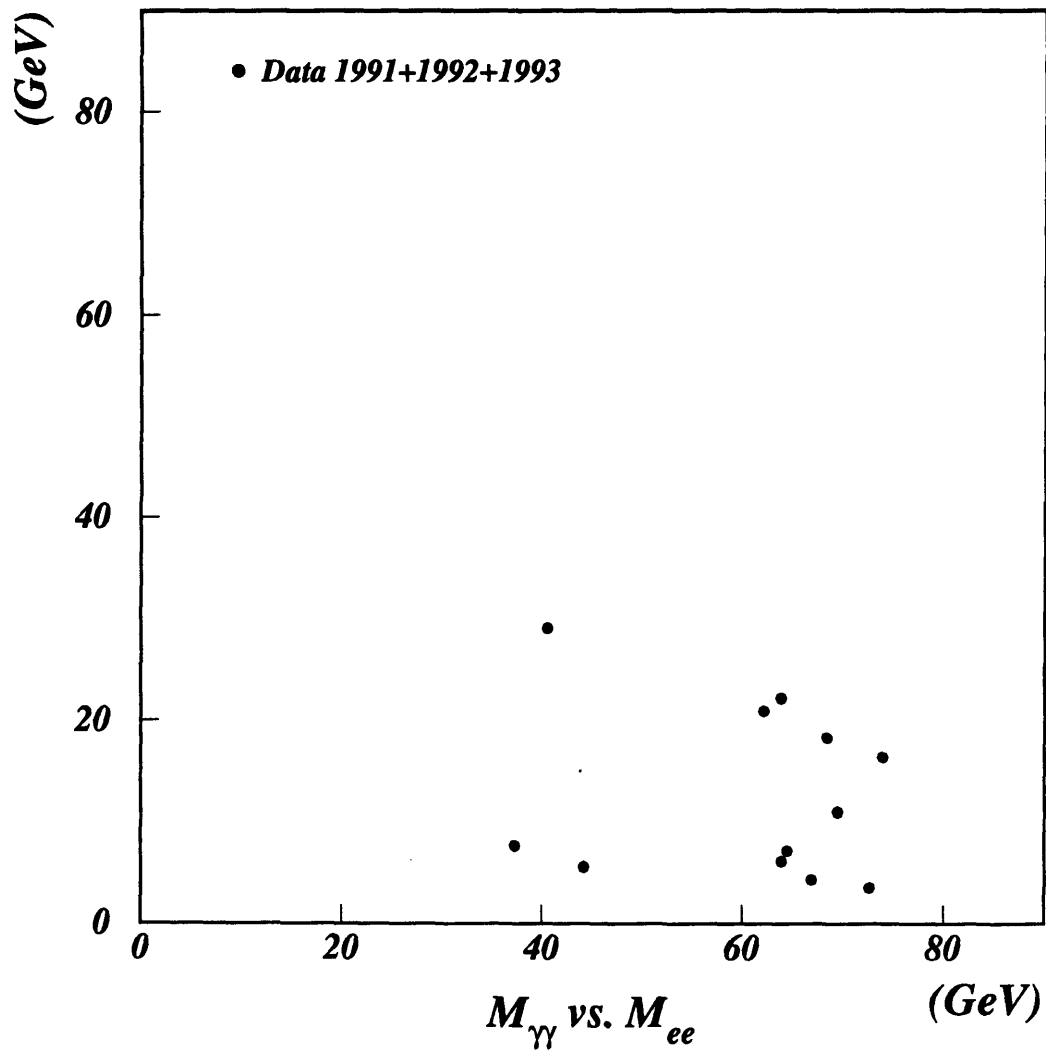


Figure 6-26: The distribution of the  $\gamma\gamma$  vs. the  $ee$  invariant mass for the three years of data. The least energetic electromagnetic cluster must have at least 5 GeV of energy.

## 6.4 $e^+e^- \rightarrow e(e)\gamma$

This physics process is unique in that the  $\lambda_\gamma$  coupling of the photon can be examined. The t-channel diagram is shown in Figure 2-6. Its cross section as derived in Chapter 2 is dominant over those of the s-channel excited leptons and it is not expected to scale as the hadronic one. Thus, we normalize to the full luminosity of  $57.3 \text{ pb}^{-1}$ .

This process is dominant when the scattered ordinary electron is in the extreme forward-backward regions. Therefore we impose that the ordinary electron might be missing as it scatters into the beampipe. In the calculation of the cross section, the scattered lepton was constrained to lie within  $10^\circ$  of the beam pipe. The heavy excited lepton is almost at rest in the laboratory frame. It decays into a well separated electron and photon pair with large scattering angles.

In this analysis, radiative Bhabha events with missing energy and momentum in the very forward-backward regions are examined. Events with one photon and one electron are searched for in the electromagnetic calorimeter and the TEC central tracking chamber is used to require at most one electron necessary to veto the large  $e^+e^-$  contamination where one track was not reconstructed. Due to the even higher level of contamination from Bhabha events in the forward regions, the photon and electron are required to be seen inside the barrel region of the electromagnetic calorimeter, or  $|\cos\theta| < 0.78$ . The only expected background comes from the QED Bhabha events and from other sources like cosmics and beam losses.

### 6.4.1 Event selection

The selection of  $e^+$  t-channel candidates are as follows:

- (1)  $\text{NASRC} < 10$ ;
- (2) Number of good tracks  $\leq 4$ ;
- (3) Energy in the BGO at least 30 GeV;
- (4) Exactly two good electromagnetic clusters;
- (5) Energy in the hadron calorimeter  $< 5 \text{ GeV}$ ;
- (6) Energy in the luminosity monitor  $< 1 \text{ GeV}$ ;
- (7) Fiducial volume is restricted to  $|\cos\theta| < 0.78$ ;

These pre-select all kinematically suitable events. The distribution of the number of tracks is shown in Figure 6-27. In this sample, we have an excess of data events with one track. There are two sources of single charge events:

- $(e)e\gamma$  events, the standard source for these is low angle radiative Bhabha events where one of the leptons is lost in the beam pipe; missing energy/momentum is expected.

- $e^+e^-$  Bhabha events where only one track was reconstructed; no missing energy and momentum imbalance are expected.

Before continuing, we must evaluate the single track reconstruction efficiency and ensure that this is properly included in the Monte-Carlo simulation. This is done using the data sample to calculate the track reconstruction efficiency by counting the number of events with 1 and 2 tracks. (Details of this are given in Section 7.2.2). In the data sample, the single track reconstruction efficiency is  $\epsilon = 99.46 \pm .02\%$  while in the simulation it is  $99.80 \pm .02\%$ . The efficiency is calculated using a large sample of events with no missing energy, i.e. radiative Bhabha events with no back-to-back structure. This limits the correlation in the estimation of the efficiency. After the Monte-Carlo sample is corrected for the efficiency, the better agreement is seen in Figure 6-28. It is now possible to put a track number constraint:

- (8) Exactly one good track in the TEC pointing to one of the two good electromagnetic clusters;

After these cuts, 351 data events survive while  $362.0 \pm 36.1$  are expected from the background Monte-Carlo samples. Two different Monte-Carlo generators are implemented to simulate the sources of backgrounds expected:

- BABAMC[41] simulates the  $e^+e^-$  Bhabha events where one track is not reconstructed;
- TEEGG[42] is used to simulate the events where one electron is not seen while leaving a hard photon in the detector. This is a higher order process ( $\alpha^3$ ) when demanding a hard photon in the calorimetric barrel.

When discussing the expected Monte-Carlo background events, both processes are implicitly included.

The distribution of the magnitude of the missing momentum is shown in Figure 6-30 for the data and Monte-Carlo and in Figure 6-31 for three different mass  $e^*$  signals. For the data and Monte-Carlo the magnitude of the missing momentum is peaked near low energies, which is dominated by the Bhabha process. For higher values, near 20 and 30 GeV, the missing momentum is due to the loss of an electron at low polar angles. In the signal, the loss of the ordinary electron implies that there is missing momentum along these low angular regions. Upon comparison with the signal distributions, since it is evident that an  $e^*$  signal would leave a monoenergetic missing momentum, a cut is placed at:

- (9)  $p_{missing} > 3$  GeV;

After this criterion, there remains 186 events in the data and  $188.9 \pm 25.1$  for the Monte-Carlo, in perfect agreement.

The distribution of the polar angle of the missing momentum vector is shown in Figures 6-32 for the data and Monte-Carlo and 6-33 for the signals. In the former, it is seen that the distribution again falls into two classes. The first is that of Bhabha

$e^*(t\text{-channel})$	48 GeV	$26.2 \pm 2.0\%$
$e^*(t\text{-channel})$	60 GeV	$44.4 \pm 2.2\%$
$e^*(t\text{-channel})$	80 GeV	$50.1 \pm 2.2\%$
$e^*(t\text{-channel})$	85 GeV	$53.4 \pm 2.2\%$

Table 6.6: *The  $e^*$  signal detection efficiencies are based on 500 generated and fully simulated events and the selection efficiencies on the background Monte-Carlo events. All errors are statistical.*

events where the missing momentum vector points randomly, hence is flat in distribution. This is as expected, for it is a consequence of the resolution of the BGO energy and cannot be spatially dependent. The distribution is however dominated with events having a missing momentum vector pointing low in the polar region, below  $10^\circ$ , and these events are due to the  $e(e)\gamma$  process. Figure 6-33 shows the corresponding distribution for the signals. In order to better isolate the signal, imposing a cut at

$$(10) \theta_{miss} < 20^\circ;$$

leaves 148 events in the data and  $137.9 \pm 21.6$  Monte-Carlo events.

Let us study the kinematical configuration of the remaining events. After all cuts, the acollinearity between the electron and photon of the surviving events is plotted in Figures 6-34 and 6-35. Since at this point the signal events possess the same kinematics, no further cuts are placed in order to maintain a good selection efficiency for the higher mass signals. It is noted that the distribution of the acollinearity is fixed for a given  $e^*$  mass since the ordinary electron recoils off the very massive excited electron, while the data and Monte-Carlo show a broad distribution.

A class of events with missing energy and missing momentum vector pointing toward the beam pipe has been isolated. However, these events do not give any evidence of a signal since the missing momentum is not monoenergetic and the angle between the electron and photon is not fixed. The remaining task is to search for an electron-photon invariant mass peak. Keeping only those events whose mass is 45 GeV or more, the resulting distribution is shown in Figure 6-36 for the data and background Monte-Carlo and in Figure 6-37 for the signals. After all cuts, there are 119 events in the data where  $115.8 \pm 19.8$  are expected in total from the background Monte-Carlo. No invariant mass peak is significantly seen.

The mass dependent efficiencies for the selection of  $e^*$  t-channel events are listed in Table 6.6. After all cuts, all the signal events falling underneath a fitted Gaussian on the mass peak but *above* the peak background are counted. The signal detection efficiencies are based on 500 events simulated through the detector.

An example of an  $e^*$  candidate is shown in Figure 6-38. The photon energy is 37.0 GeV and the electron energy is 33.1 GeV. The direction of the missing momentum is shown in the side view which clearly points into the beam-pipe.

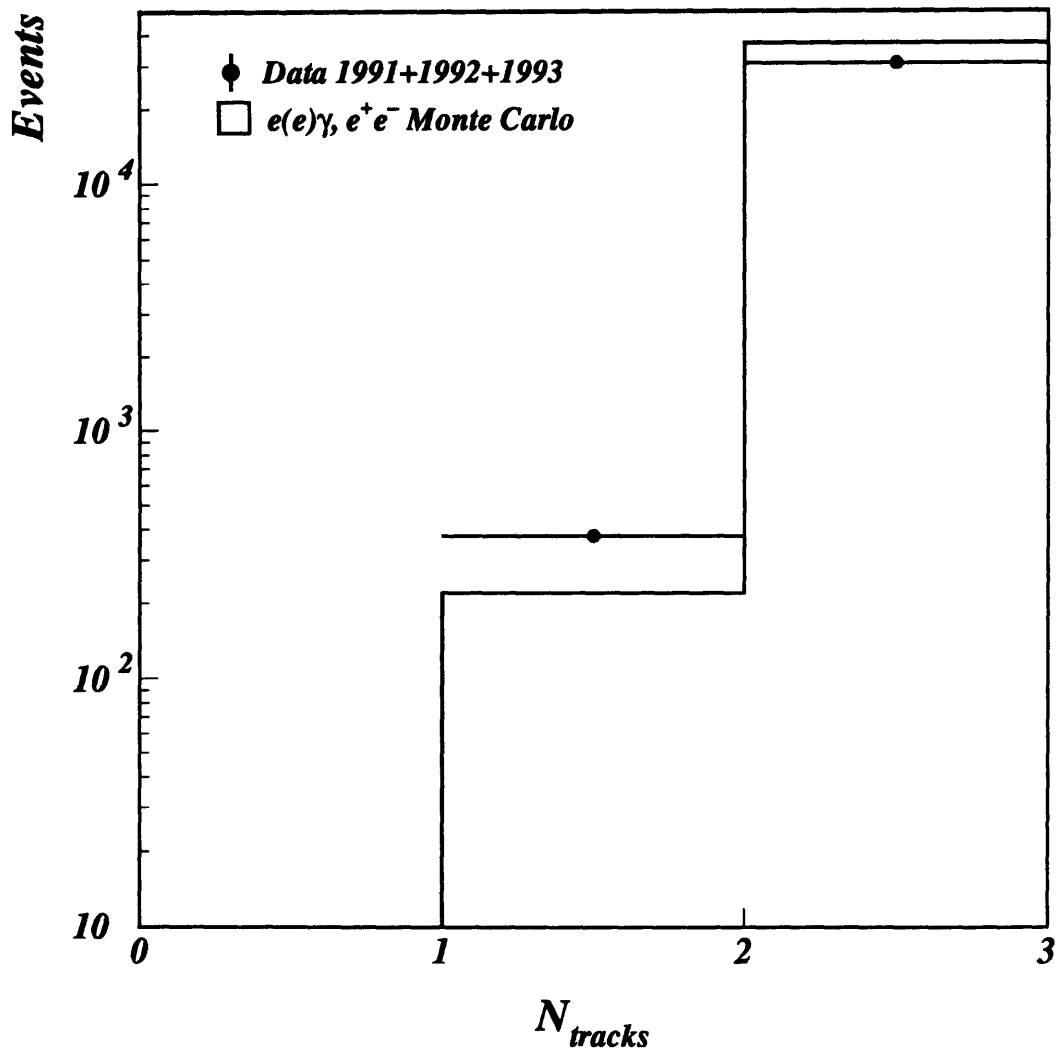


Figure 6-27: The number of tracks in the data and Monte-Carlo. It is seen that the Monte-Carlo does not correctly reproduce the track reconstruction efficiency of the data. The single track reconstruction efficiency must be rescaled. See Figure 6-28.

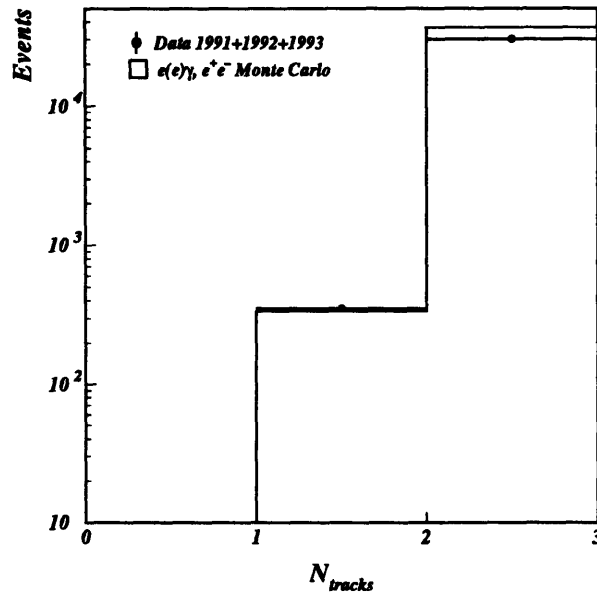


Figure 6-28: The number of tracks seen in the data and Monte-Carlo events after rescaling the single reconstruction track efficiency to that of the data sample. A much better agreement is seen.

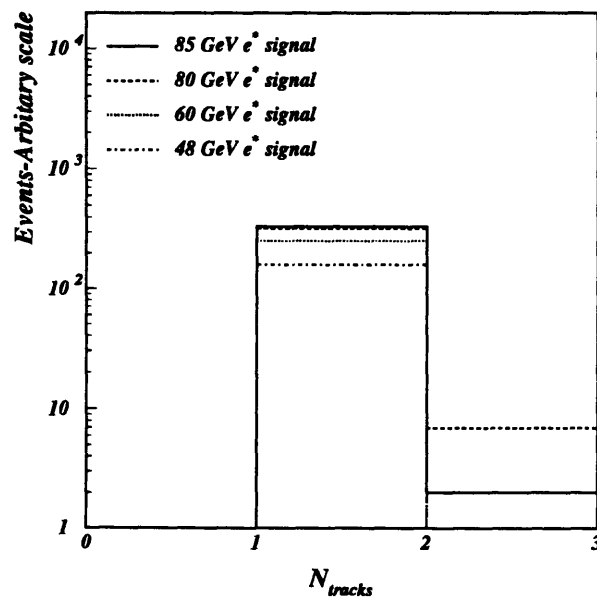


Figure 6-29: The number of tracks in the signal Monte-Carlo events after rescaling with the single track reconstruction efficiency.

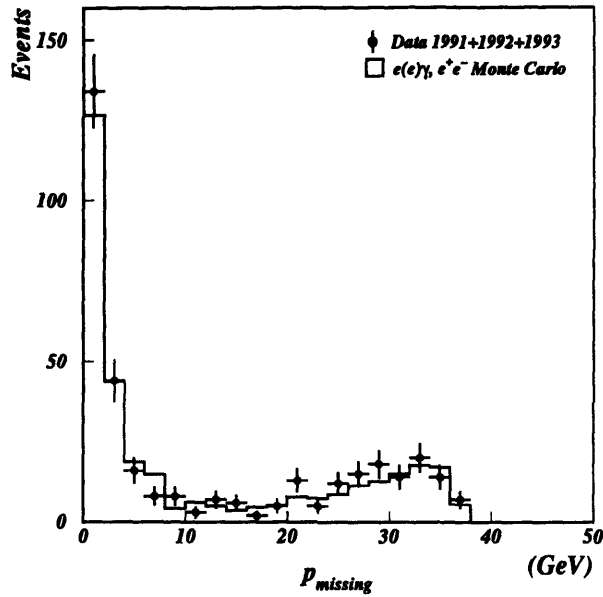


Figure 6-30: The magnitude of the missing momentum for the data and Bhabha Monte-Carlo. The distribution is dominated by events with little missing momentum as is expected from the Bhabha process. Events with higher missing momentum are the result of one electron escaping undetected.

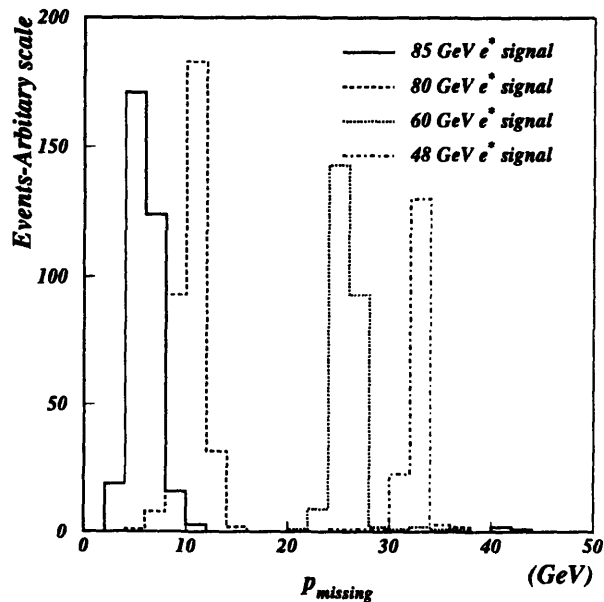


Figure 6-31: The magnitude of the missing momentum for the  $e^*$  signals events. The value is fixed for a given  $e^*$  mass since the ordinary electron recoils off of it and is lost.

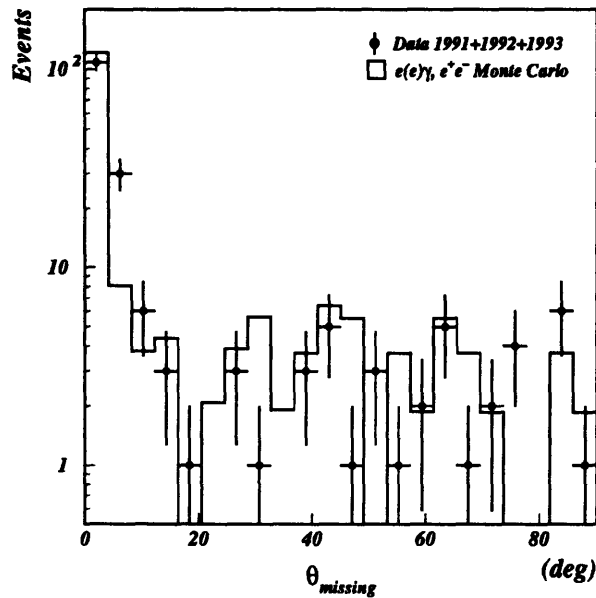


Figure 6-32: The direction of the missing momentum for the data and Bhabha Monte-Carlo. The kinematics of the  $e^*$  signal is better isolated as seen below if a cut is placed to require that  $\theta_{miss} < 20^\circ$ .

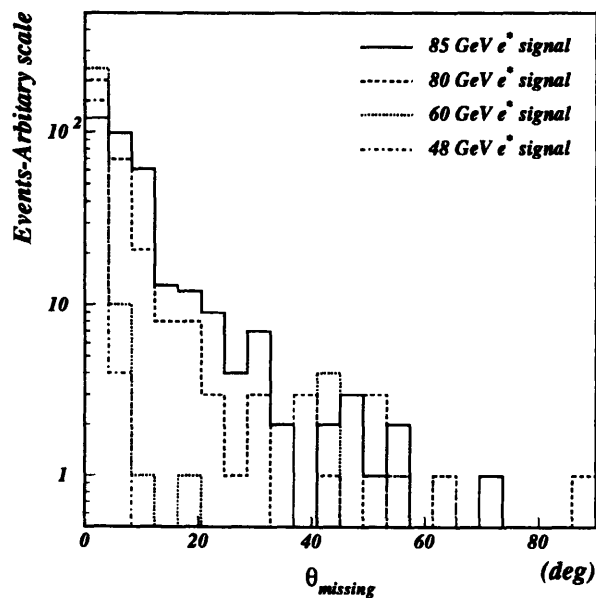


Figure 6-33: The direction of the missing momentum in  $\theta$  for the  $e^*$  signals. It is seen that most of the time it is in low polar regions.

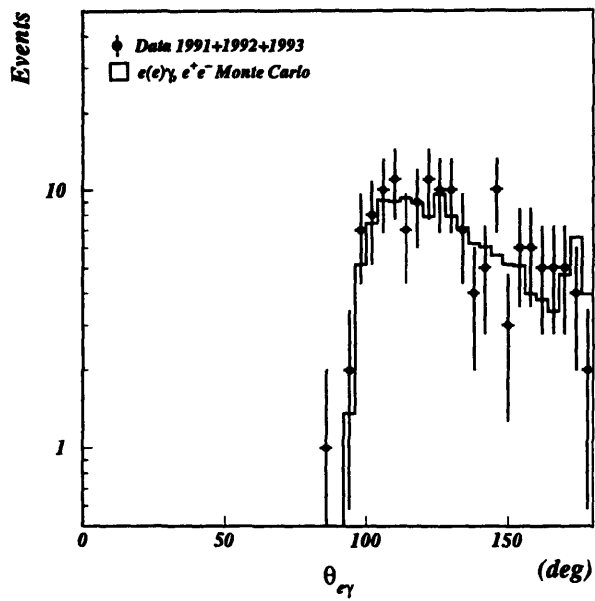


Figure 6-34: The acollinearity between the electron and photon. Since the distribution of the data is similar to those of the possible signal, no cut is placed on this parameter.

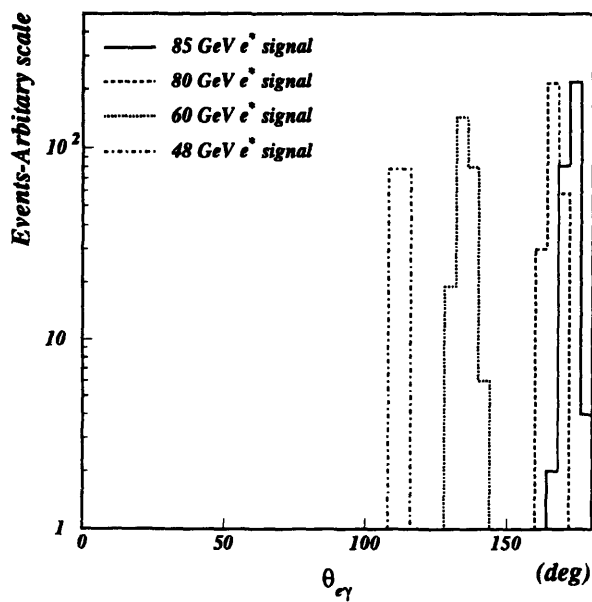


Figure 6-35: The acollinearity for the  $e^+$  signals. For a given mass, in the laboratory frame, the angle between the electron and photon is fixed.

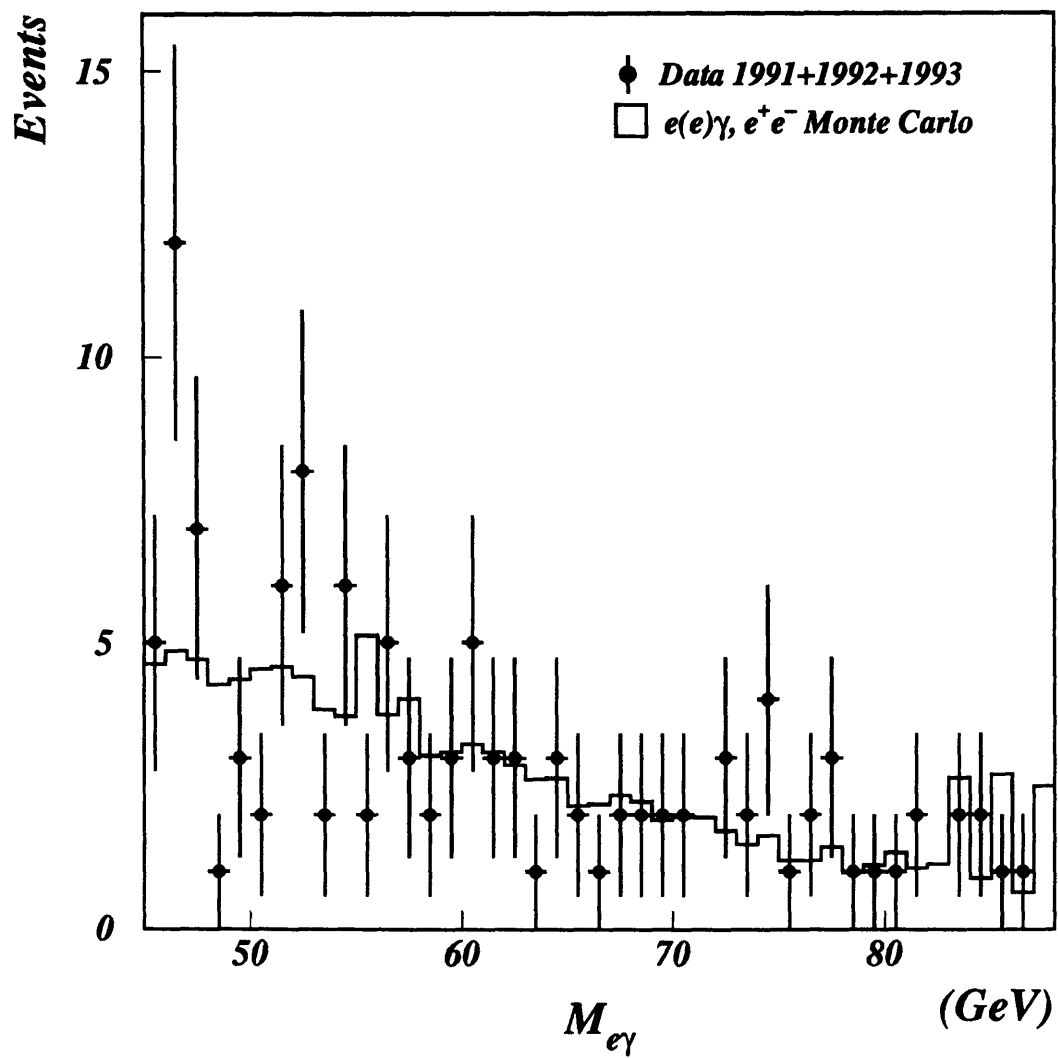


Figure 6-36: The invariant mass distribution for  $e\gamma$  pairs. There are 119 data events while  $115.8 \pm 19.8$  are expected from the background Monte-Carlo processes.

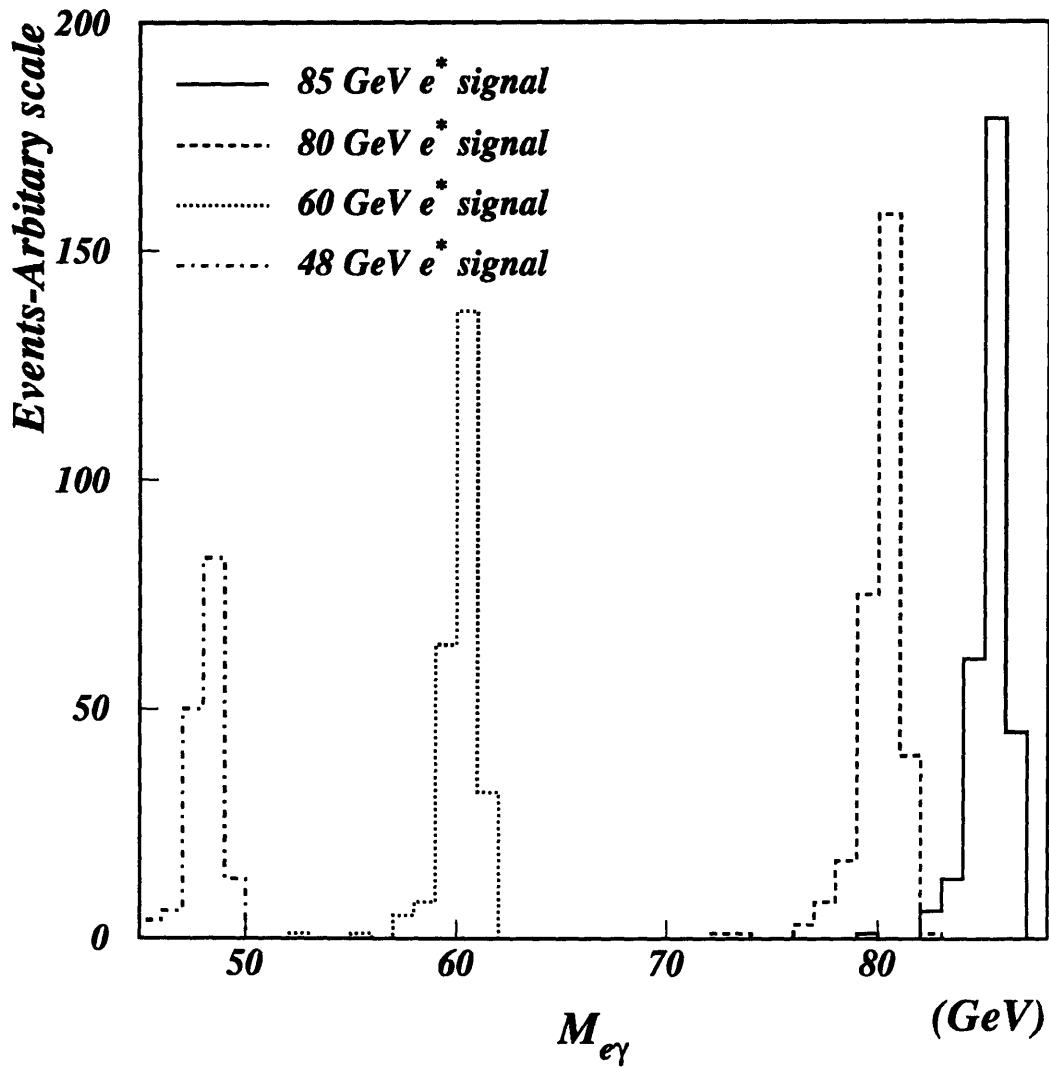


Figure 6-37: The invariant mass distribution for  $e\gamma$  pairs of the signal Monte-Carlo for different  $e^*$  masses. The relative number of entries is due to the mass-dependent selection efficiency. For each mass, 500 events were generated and simulated.

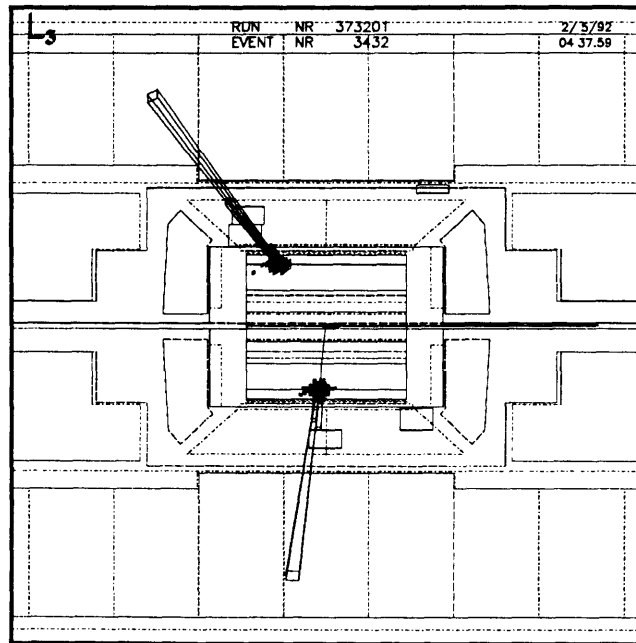
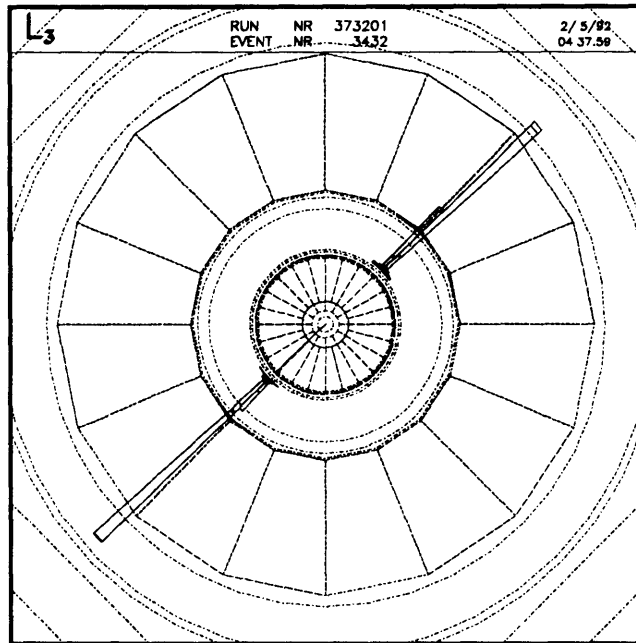


Figure 6-38: An example of an  $t$ -channel  $e^*$  candidate. Shown is a Bhabha event where one electron is missing. The photon and electron energies are 37.0 and 33.1 GeV respectively. The direction of missing momentum points exactly into the beampipe as shown in the side view.

## 6.5 $e^+e^- \rightarrow \mu\mu\gamma$

This analysis is restricted to the central region covered by the muon chambers. Since the muons are identified and measured by the muon chambers, the TEC chamber tracks are not necessary for their identification. In this direct search it is then possible to use the full effective luminosity which amounts to  $53.0 \text{ pb}^{-1}$ .

The main source of background to the signal comes from radiative di-muon decays of the  $Z^0$ . Another source for muons are from the decay  $Z^0 \rightarrow \tau^+\tau^-$  where the taus subsequently decay into muons,  $\tau^- \rightarrow \mu^-\bar{\nu}_\mu\nu_\tau$ . This background is suppressed to a few percent due to the muonic branching ratio of the tau and is easily eliminated by requiring no missing energy. The photon deposits its energy in the BGO electromagnetic calorimeter and provided that the cluster fulfills the criteria mentioned in section 6.3.1, it is assumed that this electromagnetic cluster is a photon. The very small possible contamination from the two-photon process  $e^+e^- \rightarrow e(e)\mu\mu$  where only one of the electrons is visible in the detector is negligible. The untagged same process  $e^+e^- \rightarrow (ee)\mu\mu$  where the two electrons are not seen which produces an acollinear pair of muons at large angle is immediately reduced to a negligible level when the presence of an energetic photon is required. Other four fermion processes are removed by requiring the presence of at most two tracks in the tracking chamber. Strictly speaking a few such events can pass our cuts if they occurred when the TEC chamber was not fully efficient, since we have not removed these periods of time. Because of the size of the contamination, it is not necessary to worry about this source when placing a limit on the signal.

### 6.5.1 Muon momentum resolution

To search for the  $\mu^*$  mass resonance peak, the knowledge of the muon momentum resolution function is important. As shown in Section 3.2.4, muons can be identified either in three or two chamber planes.

In the estimation of the signal efficiency, it is compulsory to know the ratio D/T (number of doublet muons/number of triplet muons) in the data. This ratio is underestimated in the Monte-Carlo since this latter contains only geometrical effects.

Listed in Table 6.7 are the number of doublets and triplets for the complete 91-93 data sample and for the non-normalized KORALZ Monte-Carlo.

It is seen that there is a fluctuation in the ratio D/T from year to year and overall there is about 16% more doublets than triplets in the data compared to the Monte-Carlo, but between the 1992 and 1993 running years there was an improvement to about 14%.

The simulated ratio D/T is rescaled to match the one in data and the momenta of the simulated muons are smeared accordingly. This adjustment process is necessary in order to maintain agreement for the energy distributions of the muons, since doublets have a resolution of approximately 21% while triplets have one of  $\approx 2.5\%$  at 45 GeV. See Figures 6-39, 6-40. This adjustment is compulsory since ultimately the invariant mass of the muon-photon pair is calculated and our efficiency for the signal is estimated from such a distribution.

Data 1991					
Doublets	Triplets	Doublets	Triplets	Ratio (D/T)	Ratio (D/T)
$\mu_1$	$\mu_1$	$\mu_2$	$\mu_2$	$\mu_1$	$\mu_2$
151	665	163	653	22.7%	25.0%
Data 1992					
Doublets	Triplets	Doublets	Triplets	Ratio (D/T)	Ratio (D/T)
$\mu_1$	$\mu_1$	$\mu_2$	$\mu_2$	$\mu_1$	$\mu_2$
349	1197	372	1171	29.2%	31.8%
Data 1993					
Doublets	Triplets	Doublets	Triplets	Ratio (D/T)	Ratio (D/T)
$\mu_1$	$\mu_1$	$\mu_2$	$\mu_2$	$\mu_1$	$\mu_2$
300	1269	312	1257	23.6%	24.8%
All Data					
Doublets	Triplets	Doublets	Triplets	Ratio (D/T)	Ratio (D/T)
$\mu_1$	$\mu_1$	$\mu_2$	$\mu_2$	$\mu_1$	$\mu_2$
800	3131	847	3081	25.6%	27.5%
Monte-Carlo					
Doublets	Triplets	Doublets	Triplets	Ratio (D/T)	Ratio (D/T)
$\mu_1$	$\mu_1$	$\mu_2$	$\mu_2$	$\mu_1$	$\mu_2$
1816	18661	2017	18460	9.7%	10.9%

Table 6.7: *The number of doublet and triplet muon tracks for the data sample and the non-normalized Monte-Carlo (the doublet to triplet ratio is the critical value).  $\mu_1, \mu_2$  are the first and second most energetic muons, respectively. On the average it is seen that there are approximately 16% less doublets than triplets compared to the data for the Monte-Carlo which is not inclusive of all time-dependent factors. It is seen that improvement on the D/T ratio was made between 1992-1993 running periods.*

Figure 6-51 shows the difference between the number of doublets and triplets between data and Monte-Carlo events. This and other relevant distributions are shown and explained in the following section.

### 6.5.2 Event selection

The selection of  $\mu^*$  candidates are as follows:

- (1) Two reconstructed muons in the muon chambers, either triplets or doublets;
- (2)  $N_{ASRC} < 16$ ;
- (3) Each muon must be associated with least one Z chamber segment;

In order to reject the four fermion  $e e \mu \mu$  events, we require:

- (4) No more than two good tracks;

These select events with two good muons in the chambers. Figure 6-41 shows the distribution of the total energy in the BGO electromagnetic calorimeter. Only events with at least 5 GeV in the electromagnetic calorimeter are initially selected in order to reduce the background coming from QED radiative di-muon events. The remaining events show the distinctive radiative tail. The distribution of  $\mu^*$  signal Monte-Carlo events are shown in Figure 6-42. The monoenergetic behavior of the signal photons is seen as in the case of the s-channel  $e^*$ . The lighter masses are more heavily boosted yielding a more dispersed spectrum of photon energy. A large proportion of the QED background can be eliminated while maintaining signal selection efficiency with the following condition:

- (5) Total BGO energy at least 10 GeV;

As mentioned, the QED di-muon background also has contributions from tau decays. The total energy deposited in the detector is taken from the sum of the muon momenta and the energy deposited in the BGO calorimeter. This is shown in Figure 6-41. There is the expected peak at the center-of-mass energy with some contamination at lower energy due to tau decays. Since the di-tau events will have missing energy, their contribution can be decreased if there is a requirement on the total energy, or specifically it must be that:

- (6) Total energy seen in the detector is at least 80 GeV;

This value is chosen examining the total energy distribution from the signal events as seen in Figure 6-42.

Figures 6-43 and 6-44 show the energy deposited in the hadron calorimeter, respectively for the background and the signals. To reduce the possibility of a particle escaping the electromagnetic calorimeter and to minimize catastrophic losses of the muon inside the hadron calorimeter that would result in a incorrectly reconstructed muon momentum at the vertex, the following cut is used:

- (7) The energy in the hadron calorimeter is less than 20 GeV;

The data sample still has contamination from cosmics. These events can be suppressed by requiring that the tracks pass close to the interaction point. Cosmics traverse anywhere through the detector fulfilling all other requirements thus far. The requirement of scintillator hits in time with the beam crossing can also reduce cosmic events, but it is sufficient to require a Distance of Closest Approach or DCA from the vertex:

- (8) The DCA of each muon must be less than 20 mm;

It is seen in Figures 6-47 and 6-48 that up to a DCA of 20 mm the data and Monte Carlo are in good agreement; above this point are the extraneous cosmic events. It is noted that in the case of the high mass  $\mu^*$  signal that the second muon will have a large DCA since this muon will have relatively low momenta and consequently suffers from

multiple scattering effects which ultimately results in a backward reconstructed track which appears not to have come from the vertex. This is a loss in signal detection efficiency which is a typical characteristic of all the higher mass  $\mu^*$  signals.

At this point, the data sample is dominated by radiative di-muon events. The re-scaling of the triplet to doublet ratio of the Monte-Carlo is performed. The distribution of the number of p-segments before corrections is shown in Figure 6-51. After correction, the energy distributions are correctly reproduced by the simulation. This can be seen in Figures 6-52 and 6-53 for the triplets and 6-54 and 6-55 for the doublets. All figures show the beam energy divided by the muon momenta since the momentum distribution is Gaussian in  $1/p$  and not  $p$ . For triplets and doublets the most energetic muon momentum is centered at the beam energy however with different resolutions. (Note the different horizontal scales). The second muon exhibits much lower momenta due to the presence of a hard photon.

In order to best separate the QED background from the signal, the difference in the kinematics of the decays is exploited. In radiative di-muon decays of the  $Z^0$ , the muons are essentially back to back because the photon is usually emitted collinearly with the muon. Contrary to this, the photon and muon are emitted back-to-back in the rest frame of a decaying  $\mu^*$ . Even when boosted to the laboratory frame, the muon and photon are well separated. This automatically imposes the muons to be acollinear. Figure 6-56 shows the distribution of the angle in space between the two muons for the data and Monte Carlo. It is seen that for the data the distribution is peaked near  $180^\circ$  while the signal is more homogeneous (Figure 6-57). Thus it is reasonable to keep only the events which satisfy the following:

$$(9) \theta_{\mu(1)\mu(2)} < 140^\circ.$$

A cut is placed at  $140^\circ$  in order to reduce as much as possible the background while maintaining an acceptable efficiency for the signal. After this, no further requirement is necessary on the angle between the photon and closest muon as can be seen in Figures 6-58, 6-59 as this is redundant of the acollinearity requirement.

The invariant mass is calculated similarly as for the excited electron case and is given by Eq. 6.7. Two combinations per event are retained and the result is shown in Figure 6-60 where there are 77 entries in the data while  $81.3 \pm 2.4$  are expected from the sum of the backgrounds. The corresponding distributions for the four signal masses are shown in Figure 6-61 where it is seen that for lower  $\mu^*$  masses there is a better signal detection efficiency.

The efficiencies for the signal detection of  $\mu^*$  events are based on 500 events simulated through the detector and are listed in Table 6.8. After all cuts, all the signal events falling underneath a fitted Gaussian on the mass peak but *above* the peak background are counted.

An example of a  $\mu^*$  candidate is shown in Figure 6-62. The photon energy is 42.9 GeV and there is one triplet and one doublet muon of 32 and 15 GeV momenta, respectively.

$\mu^*$	46 GeV	$23.4 \pm 1.8\%$
$\mu^*$	60 GeV	$31.2 \pm 2.1\%$
$\mu^*$	75 GeV	$31.1 \pm 2.1\%$
$\mu^*$	85 GeV	$10.2 \pm 1.3\%$
KORALZ $\mu^+\mu^-$ Monte-Carlo		$0.10 \pm 0.01\%$
KORALZ $\tau^+\tau^-$ Monte-Carlo		$< 1.2 \times 10^{-3}\%$

Table 6.8: The  $\mu^*$  signal detection efficiencies are based on 500 generated and fully simulated events and the selection efficiencies on the background Monte-Carlo events. All errors are statistical.

### 6.5.3 $e^+e^- \rightarrow \mu\mu\gamma\gamma$

It is interesting to look for a second photon and see if any two invariant mass combinations between muon-photon pairs lie within  $2\sigma$  of each other. In this particular situation only triplets are used, otherwise the invariant mass is not precisely determined. Based on the triplet resolution, a conservative window of 3 GeV is allowed to constitute alike masses, (this value also maintains a consistency with that of the similar  $e^*$  analysis). Figure 6-63 shows the invariant mass distribution of triplet muons with the photons of energy greater than or equal to 5 GeV. There are two entries per event since each photon must be paired with each muon. Figure 6-64 shows the *average* invariant mass for events which lie within 3 GeV of each other. Since no Monte-Carlo is currently available which accurately describes doubly radiative di-muon events, all resulting events must be considered as signal. The important point is that there is no peak in the invariant mass spectrum.

The thirty-two events are taken as signal. Their average invariant mass distribution does not however exhibit a significant peak. In terms of branching ratios, the previous result can be interpreted as a limit at the 95% C.L. assuming a 50% detection efficiency:

$$Br(e^+e^- \rightarrow \mu^*\bar{\mu}^*) \times Br(\mu^* \rightarrow \mu\gamma)^2 < 1.1 \times 10^{-5} \quad (6.10)$$

for  $m_{\mu^*} < 45$  GeV.

In addition, Figure 6-63 shows the distribution of the photon pair invariant mass vs. the muon pair invariant mass. As in the case of the electrons, there is no obvious clustering for any high mass photon regions.

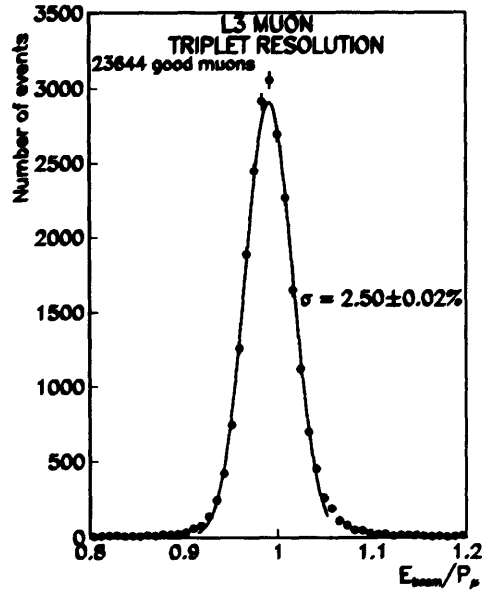


Figure 6-39: *The momentum resolution for triplet di-muons.*

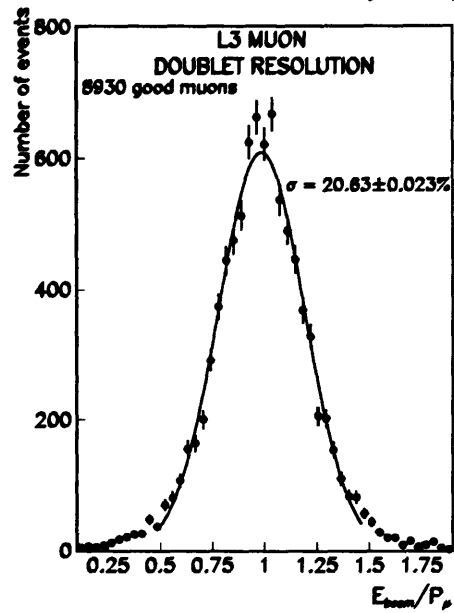


Figure 6-40: *The momentum resolution for doublet di-muons.*

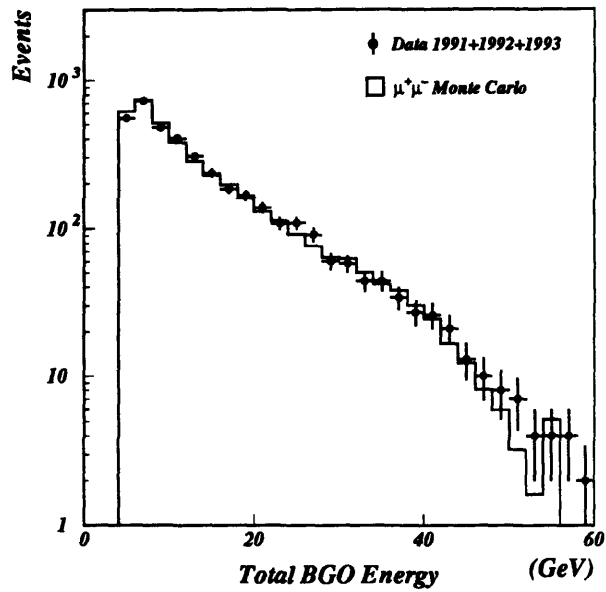


Figure 6-41: *The total energy in the BGO calorimeter.*

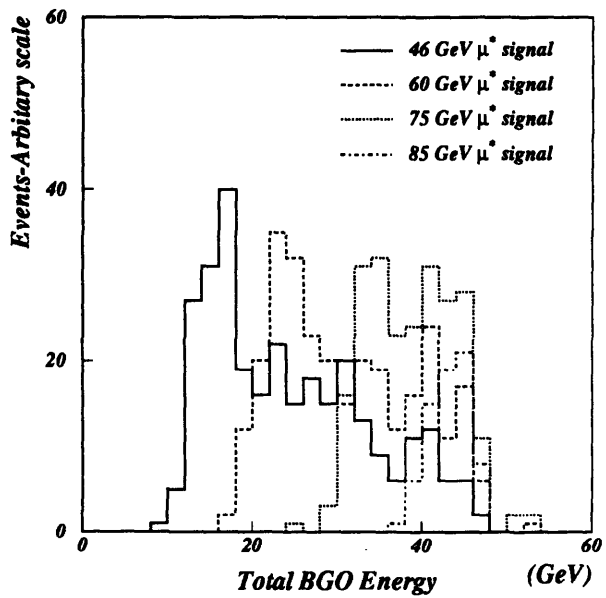


Figure 6-42: *The corresponding distribution for the  $\mu^*$  signals.*

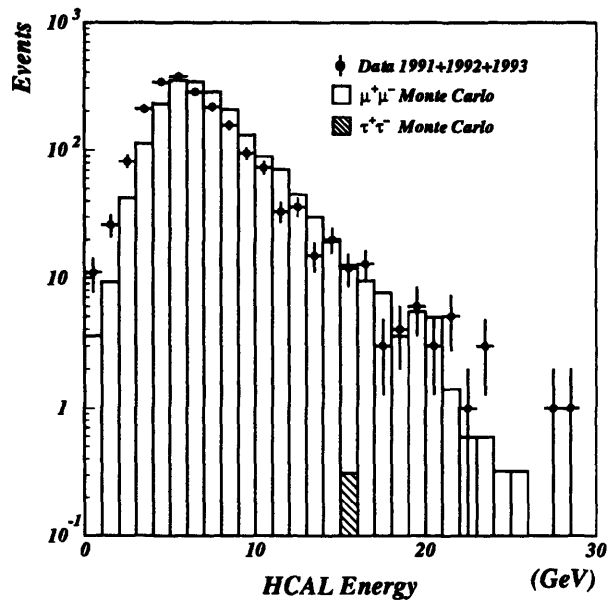


Figure 6-43: The energy deposited in the hadron calorimeter. A cut is placed at 20 GeV.

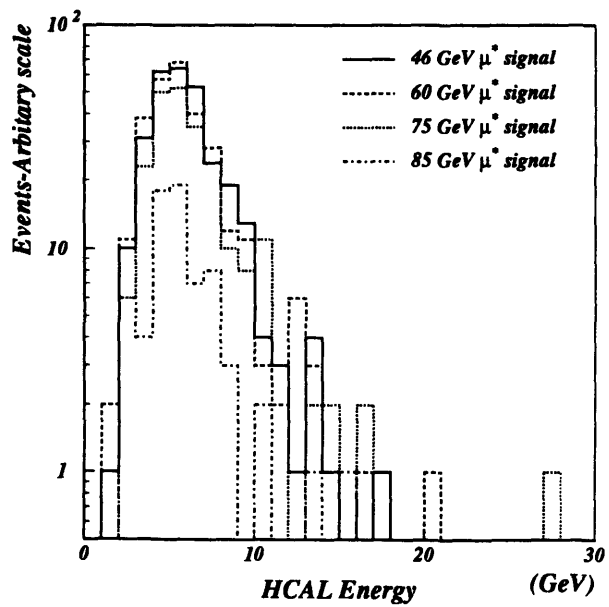


Figure 6-44: The corresponding distribution for the  $\mu^+$  signals.

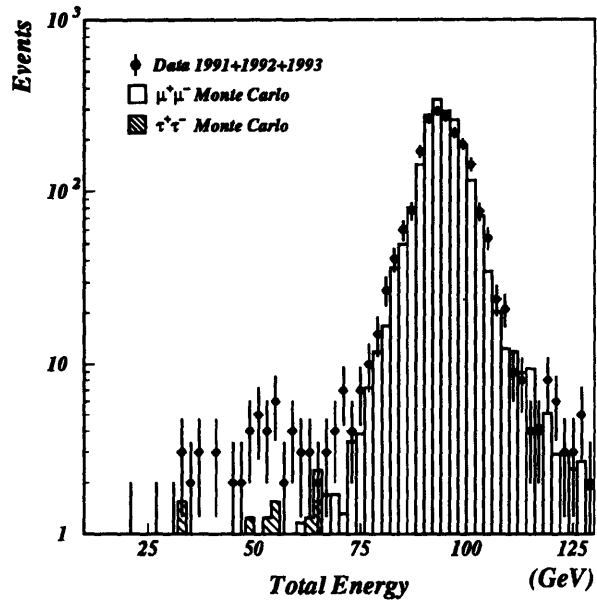


Figure 6-45: *The total energy seen in the muon chambers.*

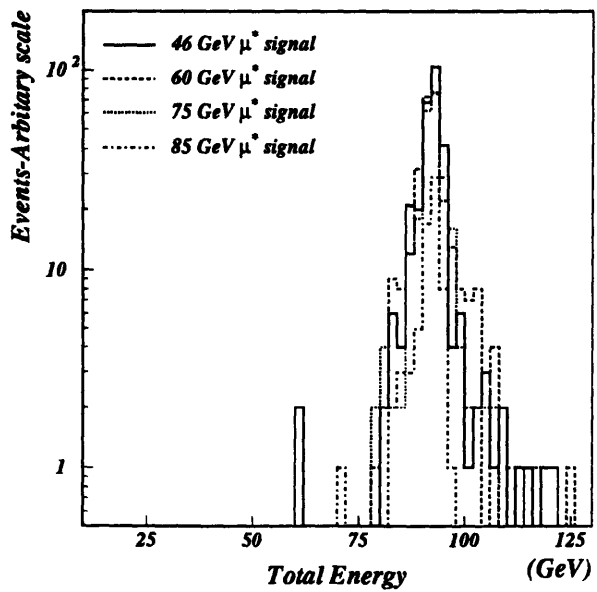


Figure 6-46: *The corresponding distribution for the  $\mu^+$  signals.*

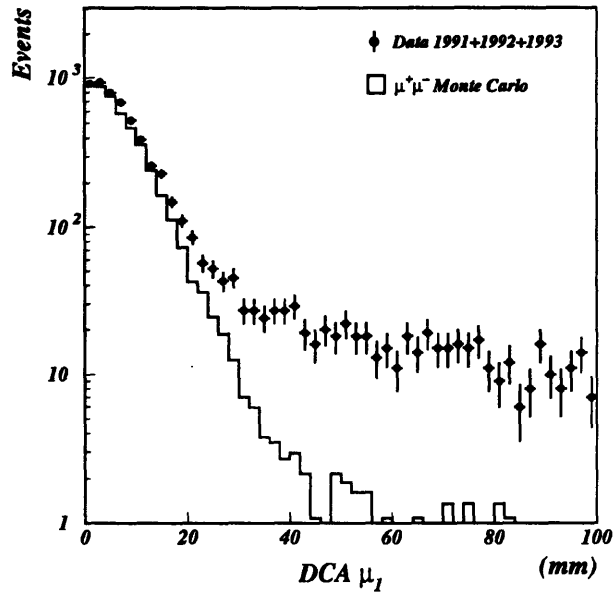


Figure 6-47: *The distance of closest approach for the most energetic muon.*

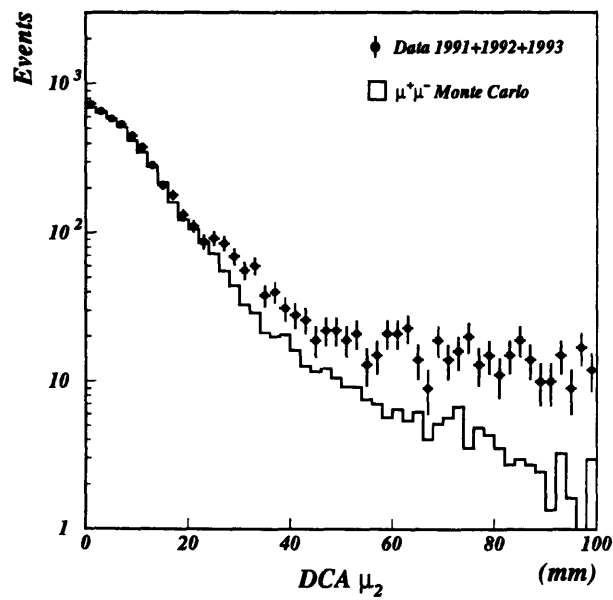


Figure 6-48: *The distance of closest approach for the second most energetic muon.*

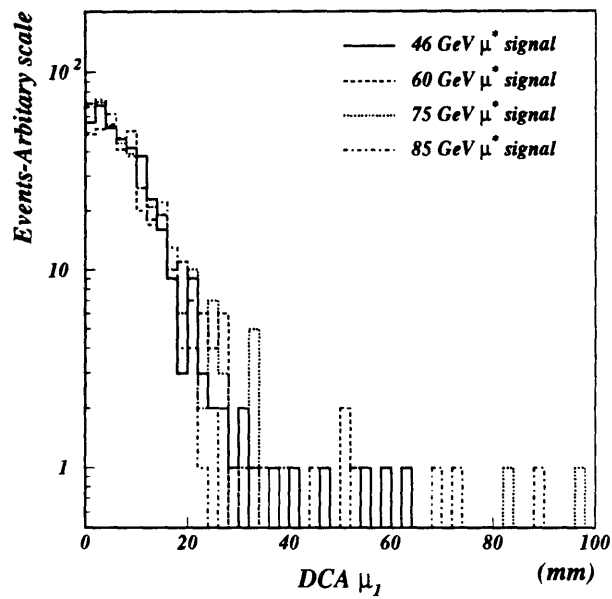


Figure 6-49: The distance of closest approach for the most energetic muon for the  $\mu^*$  signals.

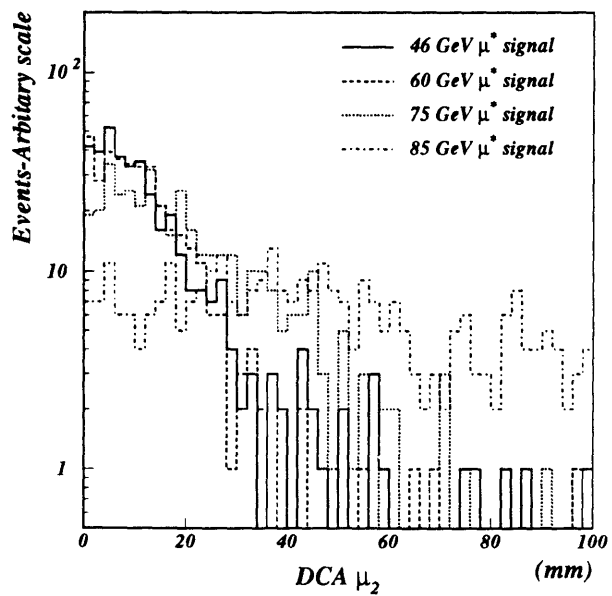


Figure 6-50: The distance of closest approach for the second most energetic muon for the  $\mu^*$  signals.

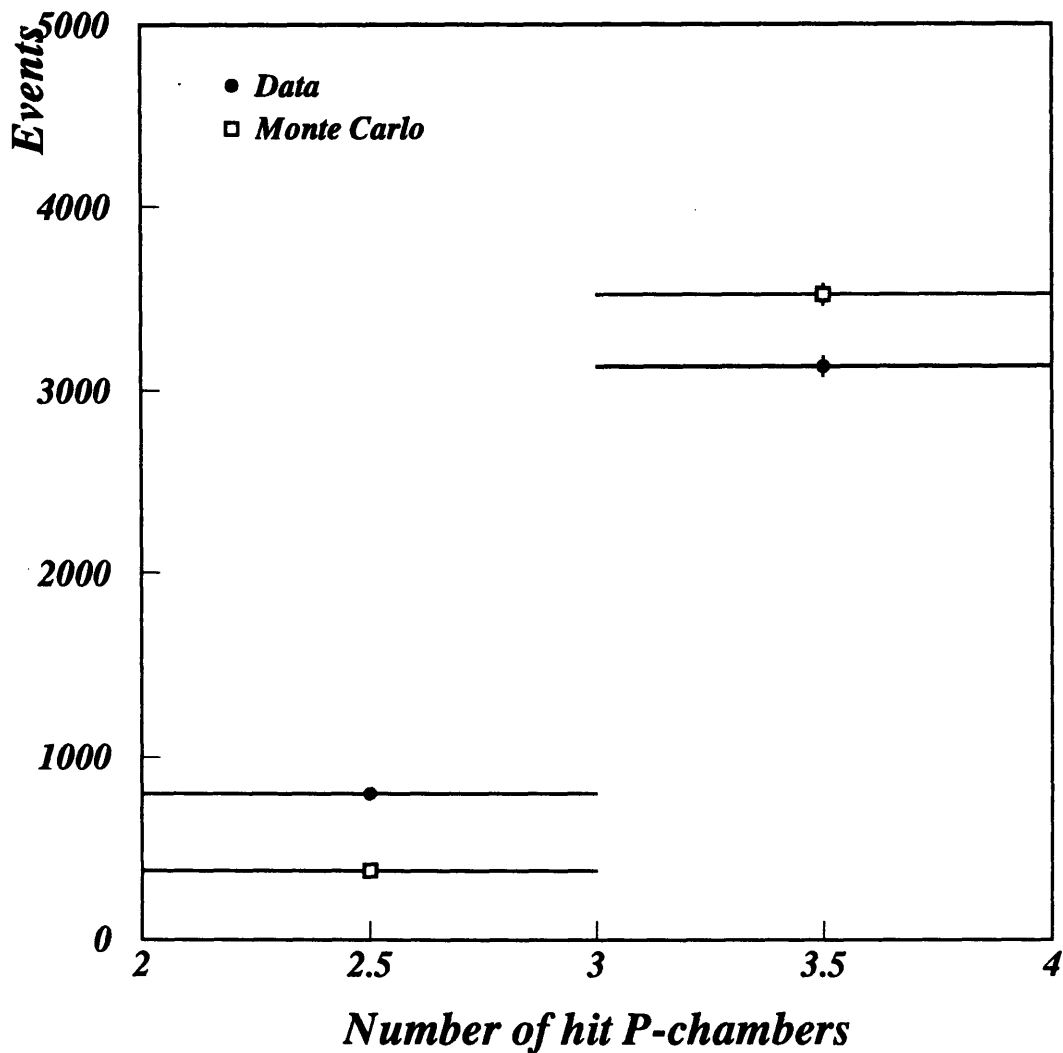


Figure 6-51: The number of triplets vs. doublets compared between Data and Monte-Carlo. In the years 1991-1993 on the average 16% of the triplets must be turned into doublets. The plot is for the most energetic muon (that of the second muon is essentially identical).

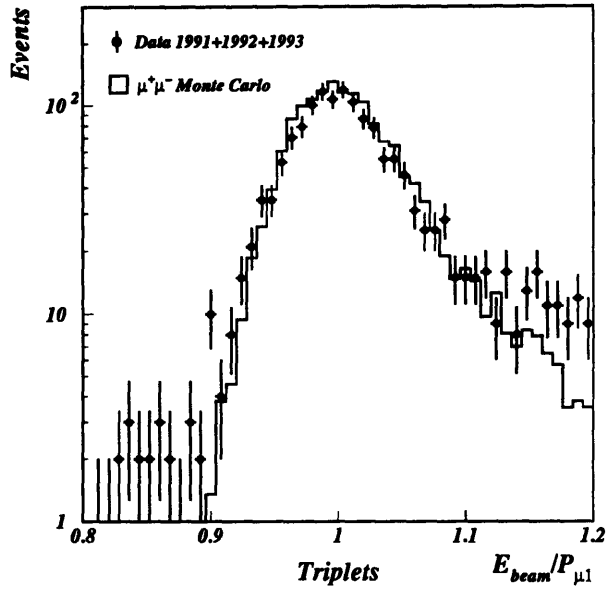


Figure 6-52: *The normalized energy for the most energetic muons which are triplets.*

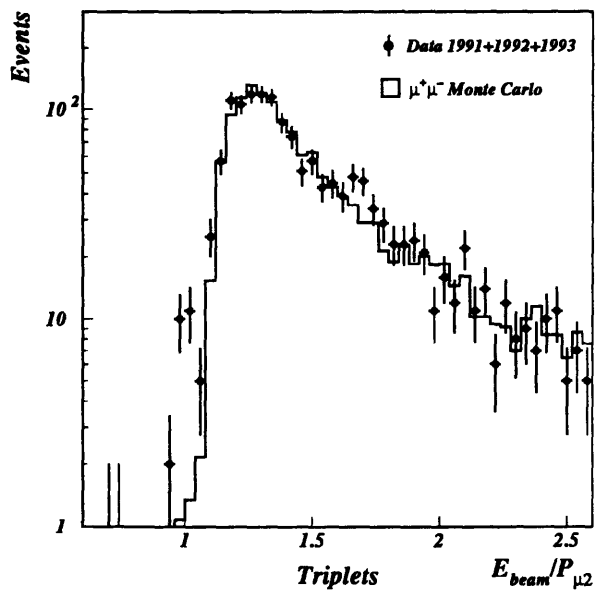


Figure 6-53: *The normalized energy for the second most energetic muons which are triplets.*

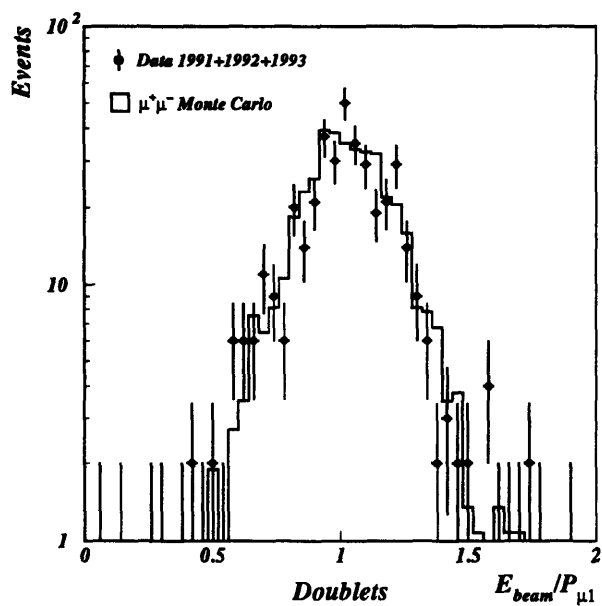


Figure 6-54: *The normalized energy for the most energetic muons which are doublets.*

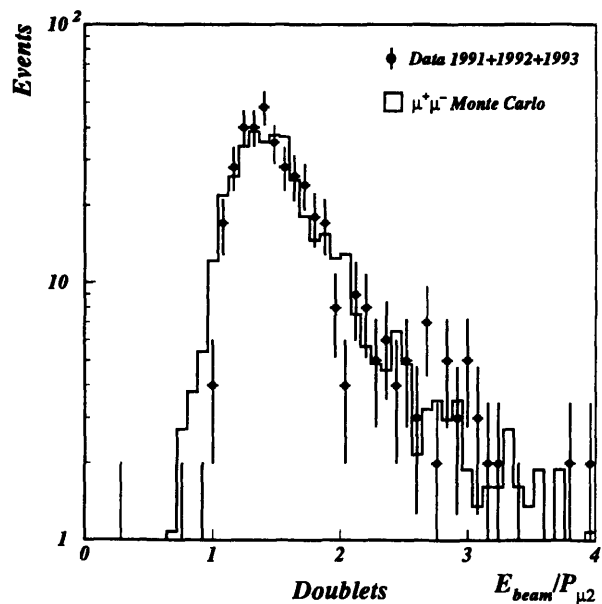


Figure 6-55: *The normalized energy for the second most energetic muons which are doublets.*

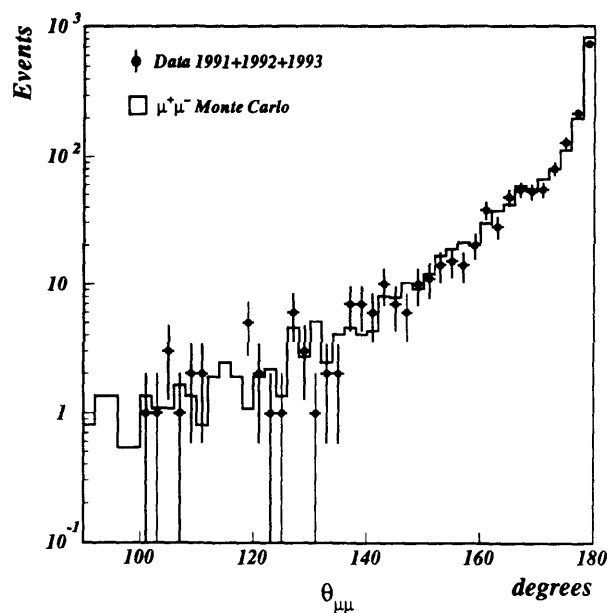


Figure 6-56: The angle in space between the two muons. A cut is placed at  $140^\circ$ .

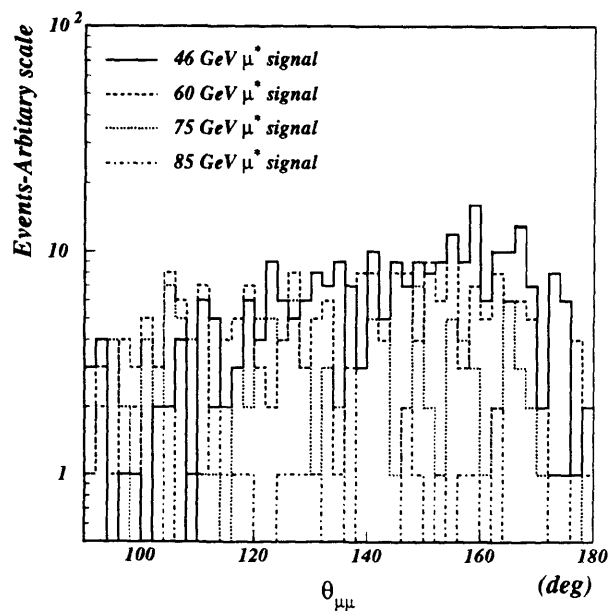


Figure 6-57: The corresponding distribution for the  $\mu^+$  signals.

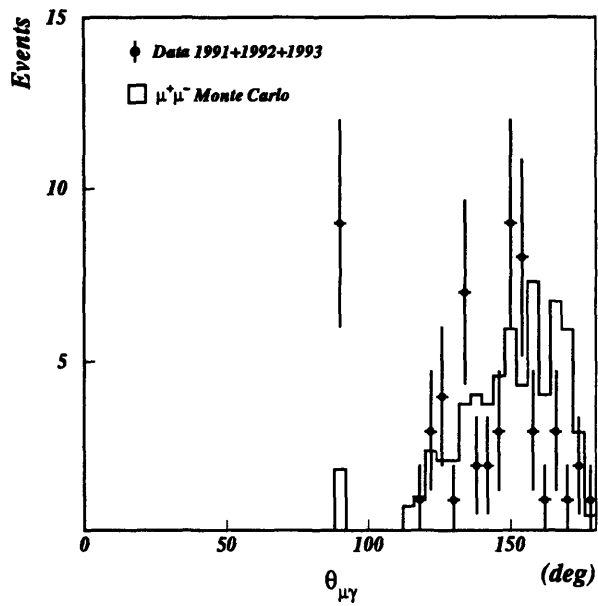


Figure 6-58: *The angle in space between the photon and the closest muon.*

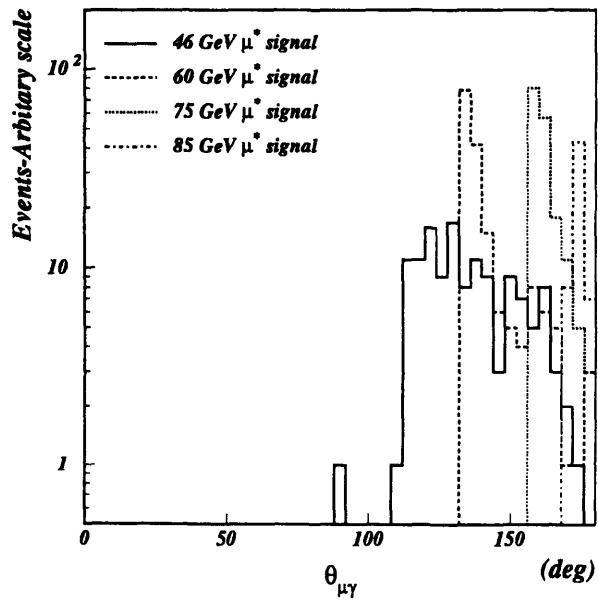


Figure 6-59: *The corresponding distribution for the  $\mu^*$  signals.*

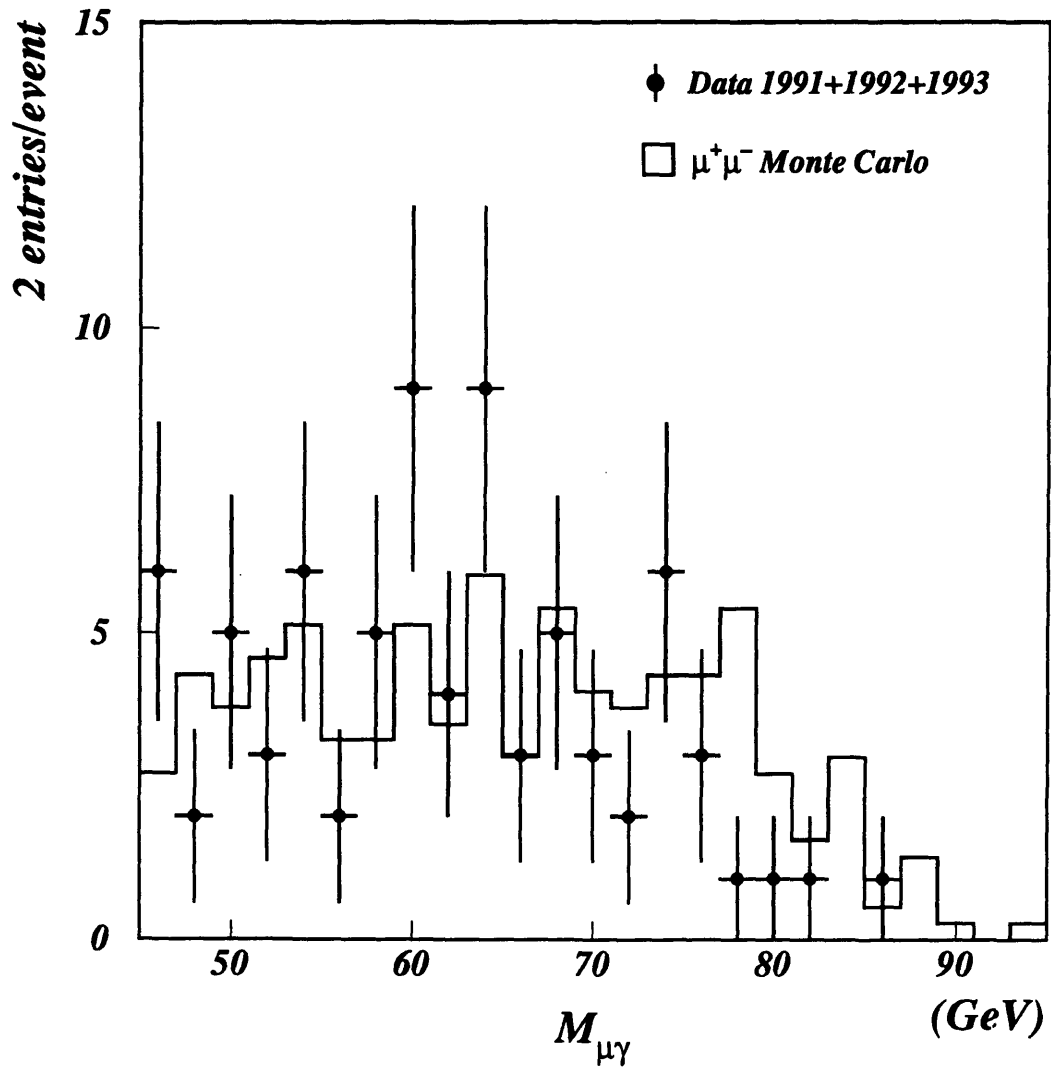


Figure 6-60: The invariant mass for all muon-photon combinations. There are 77 events from the data while the background Monte Carlo predicts  $81.3 \pm 2.4$  events. No evidence for a peak is seen.

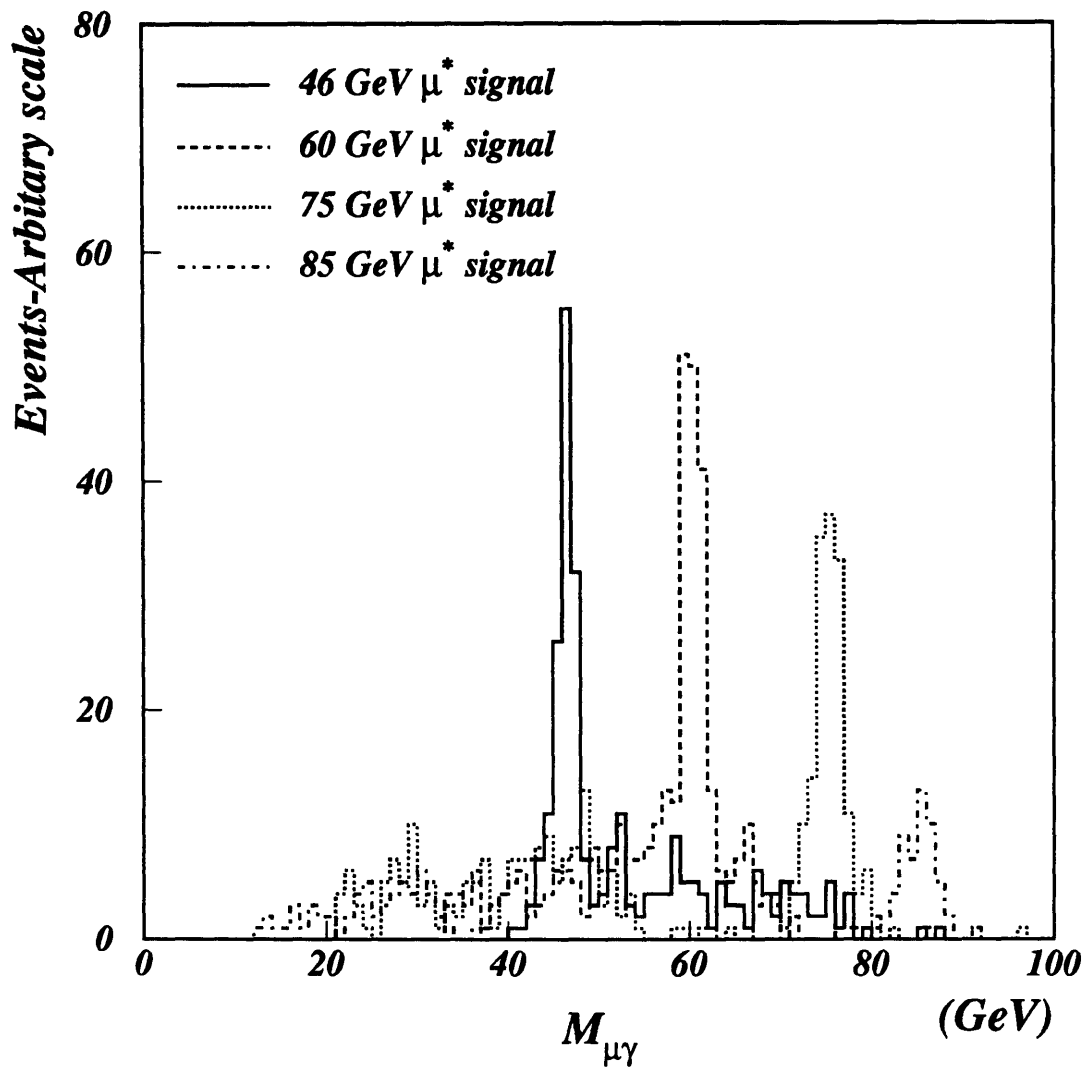


Figure 6-61: *The invariant mass for the four  $\mu^*$  signals. The relative number of remaining events is not related to the cross section but to the efficiency. 500 events were generated for each mass.*

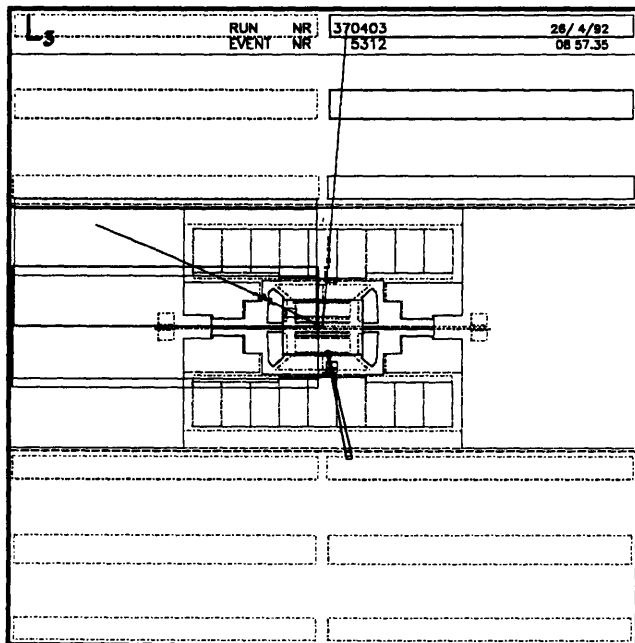
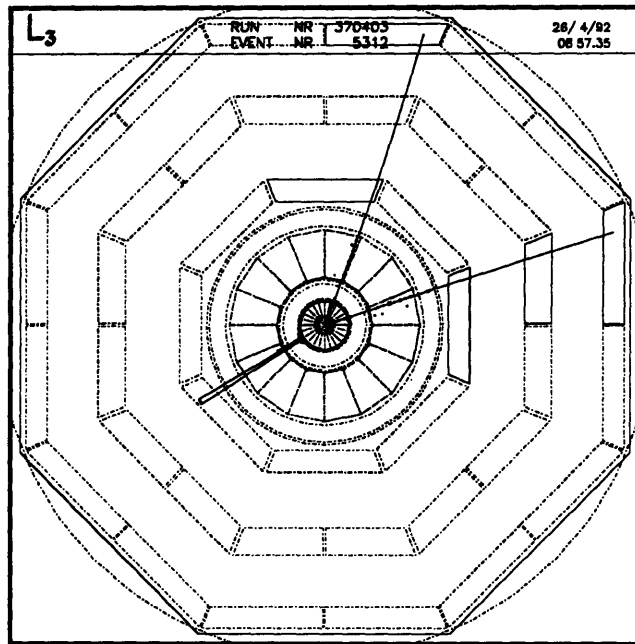


Figure 6-62: An example of a radiative di-muon event from 1992. The photon energy is 42.9 GeV. The triplet and doublet muons have 32 and 15 GeV, respectively.

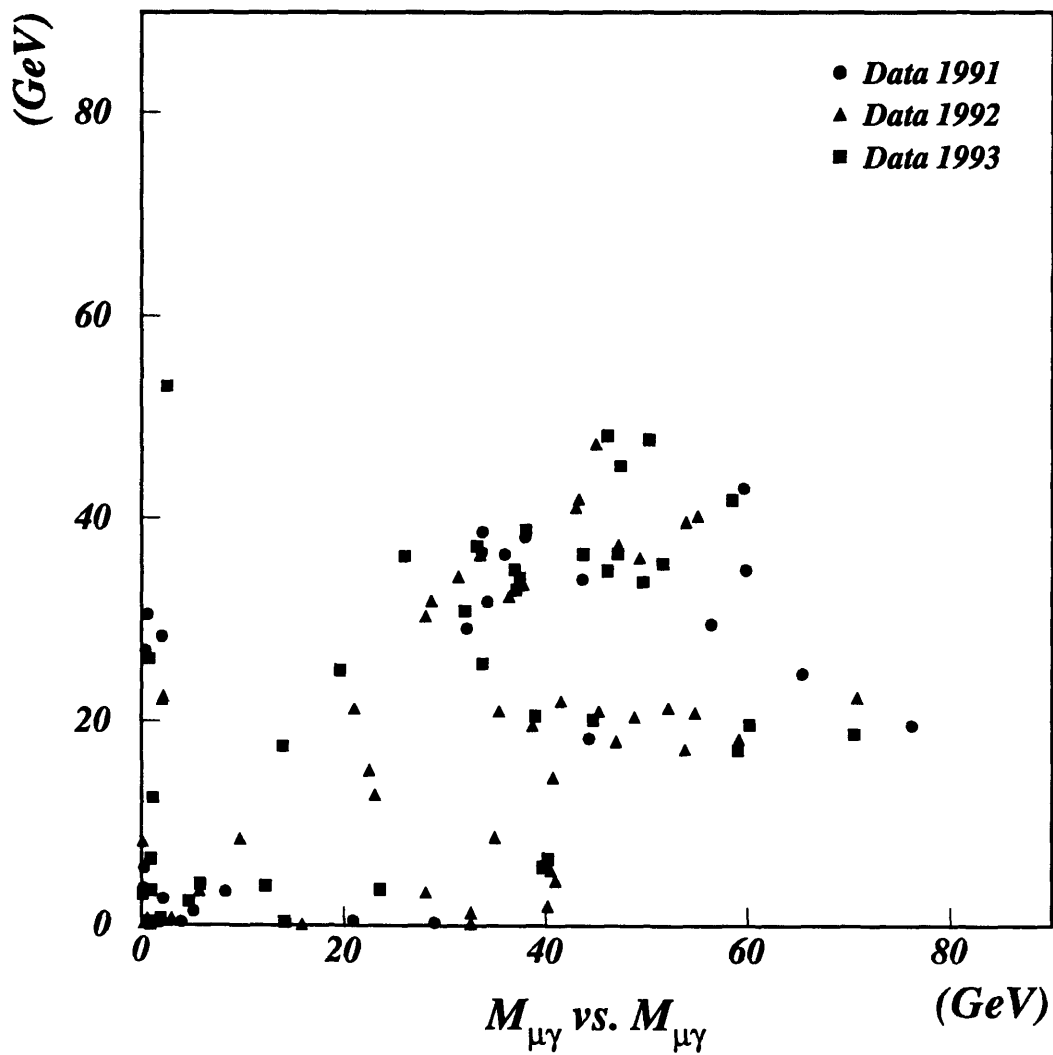


Figure 6-63: The 2-dimensional spectrum of the  $\mu-\gamma$  invariant masses in the context of pair production. Plotted are  $M_{\mu_1\gamma_1}$  vs.  $M_{\mu_2\gamma_2}$  and  $M_{\mu_1\gamma_2}$  vs.  $M_{\mu_2\gamma_1}$  for each event. The average invariant mass of any events lying within 3 GeV of the diagonal are shown in Figure 6-64.

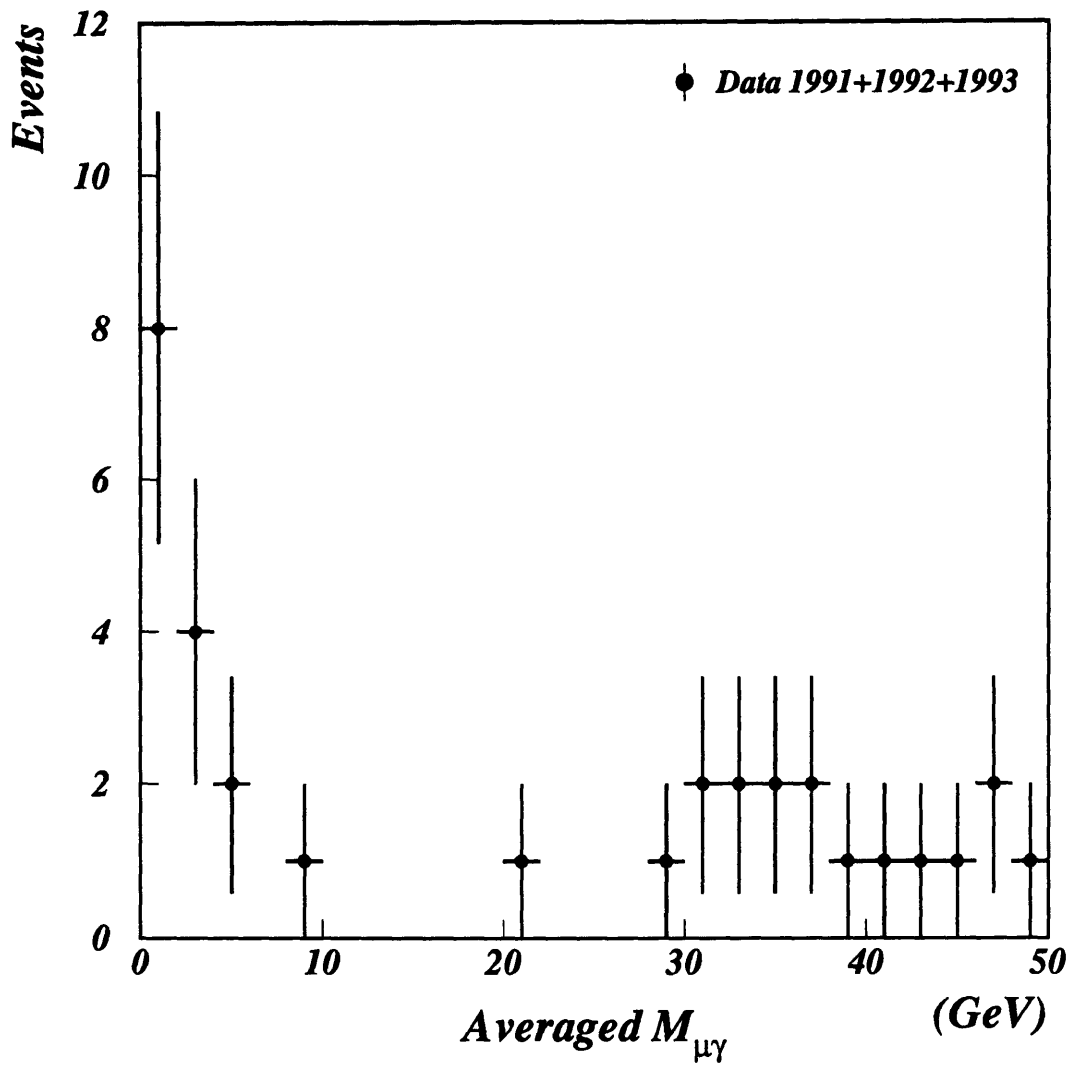


Figure 6-64: The average invariant mass of any pair-produced  $\mu^*$  candidates where the muons have triplet muon tracks. The two invariant masses must lie within  $2\sigma$  of the resolution, which is set at 3 GeV.

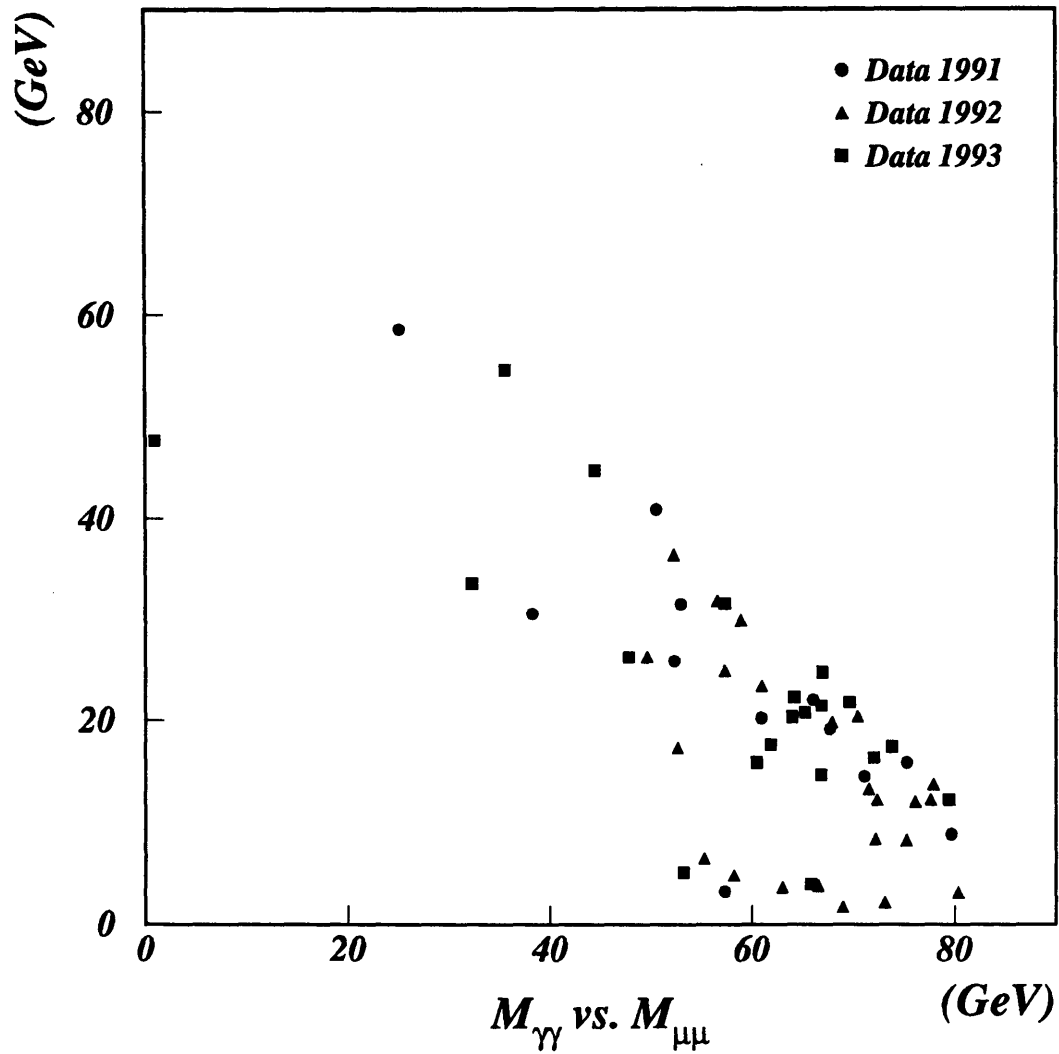


Figure 6-65: *The spectrum of photon-photon invariant mass vs. the muon-muon invariant mass for all events with a second photon of energy greater than or equal to 5 GeV.*

## 6.6 $e^+e^- \rightarrow \tau\tau\gamma$

The search for excited taus requires events selected from the process  $e^+e^- \rightarrow \tau^+\tau^-(\gamma)$ . Tau pairs are identified from all  $Z^0$  decays based on calorimetric quantities within the fiducial volume restricted to the barrel region,  $|\cos \theta| \leq 0.77$ .

The  $c\tau$  of the tau lepton is approximately  $91 \mu\text{m}$ . Even in  $Z^0$  decays, the tau lepton travels on the average approximately 2 mm before decaying. Therefore, it is identified through its decay products. The primary decay modes are as follows:

Decay Mode	Branching ratio (%)
$\tau^- \rightarrow e^- \bar{\nu}_e \nu_\tau$	17.9
$\tau^- \rightarrow \mu^- \bar{\nu}_\mu \nu_\tau$	17.6
$\tau^- \rightarrow \textit{single - prong}$	50.3
$\tau^- \rightarrow \textit{three - prong}$	14.1

The single-prong corresponds to the decay into a single charged hadron together with neutral hadrons, i.e.  $\tau^- \rightarrow \pi^- \nu$ ,  $\tau^- \rightarrow \pi^- \pi^0(\rho) \nu$ , etc. The three-prong decays englobe all decays with three charged hadrons and any neutral hadrons, i.e.  $\tau^- \rightarrow \pi^- \pi^- \pi^+(a1) \nu$ .

The main source of background comes from radiative Bhabha events and from radiative dimuon events. A smaller source of background is produced by hadronic decays of the  $Z^0$  with very low multiplicity. This source is small since it is produced by the lower tail of the fragmentation process. Two photon processes  $e^+e^- \rightarrow (ee)ee$ ,  $e^+e^- \rightarrow (ee)\mu\mu$  and  $e^+e^- \rightarrow (ee)\tau\tau$  are all sources of acollinear leptons with missing energy that are however strongly reduced when the presence of an energetic photon is required. Cosmic ray events are an important source of background that is considered below.

### 6.6.1 Tau identification

The variety of possible decay modes of the tau makes it preferable to rely on an inclusive tau selection than to use a collection of exclusive channels. The dominant decay modes exhibit either one or three tracks, missing energy and can either possess leptons or hadrons. Since the electrons are identified in the electromagnetic calorimeter, the muons in the muon chambers and the hadrons deposit energy in the electromagnetic and hadronic calorimeter, a straightforward particle identification as in the case of di-electrons or di-muons is not possible.

The tau leptons are identified inclusively using a jet algorithm based on the calorimetric and muon chamber information of the detector. The energy of the non-muonic decay of the  $\tau$  is mainly deposited in the electromagnetic calorimeter and in the hadron calorimeter. It is recognized as a narrow jet. The energy deposits are clustered through a selection criterion to form jets. The cluster/jet finding algorithm used is based on the JADE algorithm[44]. The principle for clustering is binary joining in which all initial particles are considered to be an individual cluster and each cluster is examined sequentially; two clusters are joined together if they fall within a distance measure  $y_{ij}$  smaller than a pre-determined value  $y_{cut}$ . The distance measure

$y_{cut}$ (GeV)	Number of jets (%)					
	2	3	4	5	6	7
1	0.4	27.6	43.6	20.4	4.8	1.2
2	2.2	53.8	39.4	2.6	0	0
3	4.8	64.8	28.4	0	0	0
4	7.4	75.8	14.8	0	0	0
5	11.4	78.4	8.2	0	0	0
10	30.4	67.2	0.2	0	0	0

Table 6.9: *The variation on the fraction of events with the given jet number as a function of the invariant mass cut-off labeled  $y_{cut}$ . A value of 2.5 GeV is selected to maximize 3-jet events while minimizing 2-jet events.*

can either be the invariant mass or the transverse momentum relative to an axis. The algorithm implements the invariant mass as the distance measure:

$$y_{ij}^2 = 2E_1E_2(1 - \cos \theta_{ij}) \quad (6.11)$$

where  $y_{ij}$  is the invariant mass.

To select the cutoff  $y_{cut}$  several values were tested on signal Monte-Carlo events in order to ascertain which value would yield the best efficiency for finding three jets, where the photon is considered as a jet. In order to minimize losses due to 2-jet reconstructed events while maximizing the number of 3-jet events, a good choice is  $y_{cut} = 2.5$  GeV. See Table 6.9. The tracks found in the TEC chamber must then be used to identify which of the three jets is most likely to be the photon.

## 6.6.2 Event selection

The search for excited taus requires the presence of an energetic photon with the tau pairs. Before an event is considered to be a tau pair candidate, the following most general conditions must be satisfied:

- (1)  $NASRC < 16$ ;
- (2) Total number of reconstructed tracks  $\leq 10$ ;

The hadronic events are largely reduced by the cluster multiplicity cut. For the events passing these cuts, the jet algorithm is applied. Isolated photons are reconstructed mostly as a separate jet with the choice of  $y_{cut}$ . After jet reconstruction, the photon must be identified within the jets. To best isolate the possible  $\tau^*$  signal, the following kinematical cuts are applied. The total energy distributed in the BGO electromagnetic calorimeter is seen for the data and the three Monte-Carlo backgrounds in Figure 6-66 and for 60 and 80 GeV  $\tau^*$  events in Figure 6-67. The energy is normalized to the center-of-mass energy. In the data the Bhabha peak is seen near 1. The tau events

exhibit less total energy in the BGO because of missing energy and since in many of the decays the energy is distributed in the hadron calorimeter. Di-muon events leave some energy in the BGO, but the magnitude of their contribution is small as the source is the radiated photons since the muons will penetrate the electromagnetic calorimeter. The small rise in the data versus the Monte-Carlo distributions in the normalized region of 0.05 is due to two-photon events.

In order to suppress the large Bhabha background, the following upper limit is required:

- (3) Total normalized energy in the BGO  $< 0.8$ ;

To isolate the signal, the following lower bound is required:

- (4) Total normalized energy in the BGO  $> 0.3$ ;

Next the angle between the two most energetic jets is examined. It is seen in Figure 6-68 that there is a disagreement between data and Monte-Carlo for the events with large acollinearity. To suppress this cosmic contamination, the following requirement is made:

- (5) There must be a scintillator hit within 5 ns of the beam crossing;

The result of this requirement is seen in Figure 6-69. It is seen that the previous excess in the data is eliminated. From the corresponding distribution for the signal which is shown in Figure 6-70, it is decided to suppress the background with a cut on the acollinearity at  $15^\circ$  and  $165^\circ$ .

Before the photon candidate can be chosen, the data sample must meet the following requirements:

- (6) At least 3 jets with an energy of at least 2 GeV;
- (7) Energy of a fourth jet must be less than 5 GeV;
- (8) At least one good electromagnetic cluster;

Distributions of the number of jets and the number of electromagnetic clusters for the data, Monte-Carlo and the signals are shown in Figures 6-71 to 6-74. Events with a fourth jet of energy greater than 5 GeV are discarded to further minimize QED background, where the jet algorithm can often reconstruct more than three jets. The number of tracks is shown in Figures 6-75, 6-76. It is seen that there are events in the data with 0 tracks. This is mainly due to TEC track reconstruction inefficiencies and is explained in more detail in Chapter 7. However, for the purpose of this analysis it is sufficient to place a lower bound at one good track.

Presently, we examine the energy of the most energetic muon as seen in Figure 6-77. It is seen that there is some muon contamination from di-muon events where one muon is lost, and so the following the requirement is placed:

- (9) The most energetic muon must have less than 26 GeV and there must be no more than 1 muon;

An upper limit is placed on the energy deposited in the hadron calorimeter:

- (10) Energy in the HCAL be less than 40 GeV;

This distribution is shown respectively in Figures 6-79, 6-80 for the data and Monte-Carlo and the signals. An upper limit is placed to reject a small part of the background while maintaining good signal detection efficiencies.

In choosing the photon candidate out of the three jets, the electromagnetic cluster-track distances in  $\phi$  are examined. Figures 6-81 through 6-86 show the distributions for this parameter for the three most energetic electromagnetic clusters. In Figure 6-81 the distance between the clusters and track is peaked at 0-0.1 radians, but there is a long tail reaching all the way to  $\pi$  radians. The 60 and 80 GeV signals are seen in Figure 6-82 which indicates that in most of the cases, for the signals the most energetic cluster is the photon. Figures 6-83 and 6-85 possess similar distributions for the data which overall indicates that the tau events may or may not be radiative. The signal distributions shown in Figures 6-84 and 6-85 respectively are the track distance from the second and third most energetic electromagnetic clusters. In the case of the signals, it is seen that there are only a few percentage of events which may have the photon as the second most energetic cluster and the third most energetic cluster is almost always a tau. Upon comparison of these distributions, it is clear that using the third cluster-track distance is a good parameter to isolate the signal from the QED background. Therefore it is required that:

- (11)  $\Delta\phi_3 < 0.3$  radians;

From the remaining events, the photon is chosen to be the jet which has its closest track in  $\phi$  farthest away from the electromagnetic cluster center-of-gravity. The signal Monte-Carlo generator verifies that this method has greater than 99% accuracy for the  $\tau^*$  signals. The photon candidate energy is shown in Figures 6-87 for the data and 6-88 for the signal events. The total visible energy which is comprised of that of the photon, the two tau jets and perhaps a muon is then examined in Figures 6-89,6-90. In order to better isolate the signal, The following is required:

- (12) Energy of the photon candidate be at least 15 GeV;
- (13) Total energy visible in the electromagnetic, hadronic calorimeter and muon chambers  $> 24$  GeV;

After these cuts, the resulting energy distributions for the photon and most energetic and second most energetic jet and total energy are shown in Figures 6-91 through 6-98. This is to verify that the distributions between the Monte-Carlo and the data events are similar for both jets and the photon candidate.

Along with the minimum requirement on the photon energy, the most effective way of isolating the possible  $\tau^*$  signal is with an acollinearity requirement as in the previous cases of the s-channel  $e^*$  and  $\mu^*$  searches. Similarly, we require:

- (14) Angle between the tau jets less than  $140^\circ$ ;

The distributions are shown in Figures 6-99 and 6-100.

After all selection cuts, the invariant mass between each tau jet and photon must be made. However, due to the presence of neutrinos in the final state, the jet energy cannot be directly used. Therefore, it is necessary to rescale the jet energy as is described below.

### 6.6.3 Invariant mass reconstruction

The nature of constructing the invariant mass where a tau is involved is not as direct as in the case of the electrons and muons since the  $\tau$  lepton decays and the neutrinos carry off an unknown amount of energy. However, if one assumes that the direction of flight of the neutrinos is in the direction of the jet, then with the following constraints the invariant mass can be reconstructed:

$$E_\gamma + aE_1 + bE_2 = \sqrt{s} \quad (6.12)$$

$$a\vec{p}_1 + b\vec{p}_2 + \vec{p}_\gamma = \vec{0} \quad (6.13)$$

where Eq. 6.12 is the conservation of energy and Eq. 6.13 is the conservation of momentum.  $E_\gamma$  is the energy of the photon,  $E_1$  is the energy of the most energetic jet,  $E_2$  is the energy of the second jet and  $a, b$  are the scaling factors to account for the missing energy. Solving for  $a$ :

$$a = \frac{\sqrt{s} - E_\gamma - bE_2}{E_1} \quad (6.14)$$

and  $b$  is:

$$b\vec{p}_2 = \vec{0} - \vec{p}_\gamma - a\vec{p}_1 \quad (6.15)$$

after squaring, assuming  $E \approx p$

$$\begin{aligned} b^2 E_2^2 &= (\vec{0} - \vec{p}_\gamma - a\vec{p}_1) \cdot (\vec{0} - \vec{p}_\gamma - a\vec{p}_1) \\ &= E_\gamma^2 + a^2 E_1^2 + 2aE_1 E_\gamma \cos \theta_{\gamma 1} \end{aligned} \quad (6.16)$$

Substituting in  $a$  from Eq. 6.14 and solving for  $b$  one obtains:

$$b^2 = \frac{E_\gamma^2 (1 - \cos \theta_{\gamma 1}) + E_\gamma \sqrt{s} (\cos \theta_{\gamma 1} - 1) + \frac{1}{2}s}{\sqrt{s} E_2 + E_2 E_\gamma (1 + \cos \theta_{\gamma 1})} \quad (6.17)$$

The invariant mass for  $\tau - \gamma$  pairs is:

$$\mathcal{M}_{\tau(1)\gamma} = \sqrt{2E_\gamma a E_{\tau(1)} (1 - \cos \theta_{\tau(1)\gamma})} \quad (6.18)$$

and

$$\mathcal{M}_{\tau(2)\gamma} = \sqrt{2E_\gamma b E_{\tau(2)} (1 - \cos \theta_{\tau(2)\gamma})} \quad (6.19)$$

In this manner, the invariant mass of the photon-tau pairs are constructed and compared with those of all expected background Monte-Carlo. Requiring that the invariant mass be greater than 45 GeV, there remains 147 events in the data while

$\tau^*$	60 GeV	$49.2 \pm 2.2\%$
$\tau^*$	70 GeV	$44.8 \pm 1.6\%$
$\tau^*$	80 GeV	$14.3 \pm 1.6\%$
KORALZ $\tau^+\tau^-$ Monte-Carlo		$0.15 \pm 0.01\%$
KORALZ $\mu^+\mu^-$ Monte-Carlo		$0.01 \pm 3.8 \times 10^{-3}\%$
BABAMC $e^+e^-$ Monte-Carlo		$0.03 \pm 0.01\%$

Table 6.10: The  $\tau^*$  signal detection efficiencies are based on 500 generated and fully simulated events and the selection efficiencies on the background Monte-Carlo events. All errors are statistical.

the total from Monte-Carlo is  $146.9 \pm 3.9$  and the distribution is shown in Figure 6-101.

The  $\tau^*$  signal detection efficiencies are based on 500 events simulated through the detector and are listed in Table 6.10. After all cuts, all the signal events falling underneath a fitted Gaussian on the mass peak but *above* the peak background are counted. Fig. 6-102 shows the corrected and uncorrected invariant masses for a 60 and 80 GeV  $\tau^*$ . The resolution for the 60 GeV signal is  $\sigma = 1.5$  GeV and that of the 80 GeV signal is  $\sigma = 2.2$  GeV.

An example of a  $\tau^*$  candidate is shown in Figure 6-103. The photon energy is 23.6 GeV and there is a three-prong and single-prong decay of the tau. The single prong decay could either be a low-energy charged pion or an electron. The three-prong decay left 24.5 GeV of energy in the hadron calorimeter.

#### 6.6.4 The $\tau$ moments

Due to the short lifetime of the  $\tau$ , its electric dipole and anomalous magnetic moments have not yet been directly measured. However, the previous  $\tau^*$  analysis can be used to indirectly put limits on these values.

As mentioned in Section 2.3.5, an excess in radiative  $\tau$  events where a hard photon is emitted could be attributed to the presence of an anomalous magnetic moment or an electric dipole moment of the  $\tau$ . The partial width of the anomalous production of radiative taus is:

$$\Gamma_{ano} = 0.0282 F_2(0)^2 \quad (6.20)$$

where the values  $M_Z = 91.18$  GeV,  $\sin^2 \theta_W = 0.233$ , and  $\alpha = 1/128$  in Eq. 2.70. Since the tree-level partial width of the  $Z^0$  into particles ' $ff$ ' is given by:

$$\sigma(e^+e^- \rightarrow Z^0 \rightarrow ff) = \frac{12\pi}{M_Z^2} \frac{\Gamma_{e^+e^-} \Gamma_{ff}}{\Gamma_Z^2} \quad (6.21)$$

with the values of  $\Gamma_Z = 2.487$  GeV and  $\frac{\Gamma_{e^+e^-}}{\Gamma_Z} = 3.3$  % we have for the anomalous contribution to the cross section:

$$\sigma_{ano} = .669 F_2(0)^2 \text{ nb} \quad (6.22)$$

Since this value is predicted for the cross section at the  $Z^0$  peak, either the cross section or the luminosity must be rescaled since the  $\tau^*$  analysis was performed with data taken on and around the  $Z^0$  pole.<sup>1</sup> As with the previous analyses, we shall rescale the total luminosities with the hadron lineshape and thus have the resulting effective luminosity of  $\mathcal{L} = 47.2 \text{ pb}^{-1}$  which corresponds to a total integrated luminosity of  $\mathcal{L} = 53.0 \text{ pb}^{-1}$  as was described in Section 6.2. This yields a total number of events possible from the anomalous term:

$$\# \text{Events} = 31,605 F_2(0)^2 \quad (6.23)$$

The results of the  $\tau^*$  analysis can be used since the decay kinematics would be identical to that of a singly produced  $\tau^*$ . In that case, the results were that 147 data events were seen while the total expected from Monte-Carlo was  $146.9 \pm 3.9$ . This of course, is selection-dependent, and the efficiency for signal detection was dependent on its mass. Therefore we will take the conservative estimate of the efficiency to be about 40% since for  $\tau^*$  masses above 80 GeV it was about 50% declining only as  $m_{\tau^*}$  approached  $M_Z$ . So with our results, the 95% C.L. using Poisson statistics gives at most 26 events which could be attributed to an anomalous magnetic coupling. This yields  $26 = (0.4)31,605 F_2(0)^2$  or:

$$F_2(q^2 = 0) \leq 0.05 \quad (6.24)$$

at the 95% C.L.<sup>2</sup> In the context of the electric dipole moment or EDM, the above result can be used with the substitution of:

$$\frac{F_2(0)e\hbar}{2m_\tau c} \rightarrow F_{EDM}(0) \quad (6.25)$$

which yields the result:

$$F_{EDM}(q^2 = 0) \leq 2.6 \times 10^{-16} \text{ e cm} \quad (6.26)$$

Although these limits are far above those of theoretical calculations, this method provides an experimental bound on the anomalous magnetic and electric dipole moments of the  $\tau$  at  $q^2 = 0$ .

---

<sup>1</sup>We note the error in [25] where the authors use the L3 result taken during the 1990 energy scan for a total integrated luminosity of  $2.2 \text{ pb}^{-1}$ . They do not make any adjustment for the data taken off-peak.

<sup>2</sup>For sake of comparison with the previous published limit of [25], if we instead find a value for one standard deviation, then the present result becomes:  $F_2(q^2 = 0) \leq 0.032$

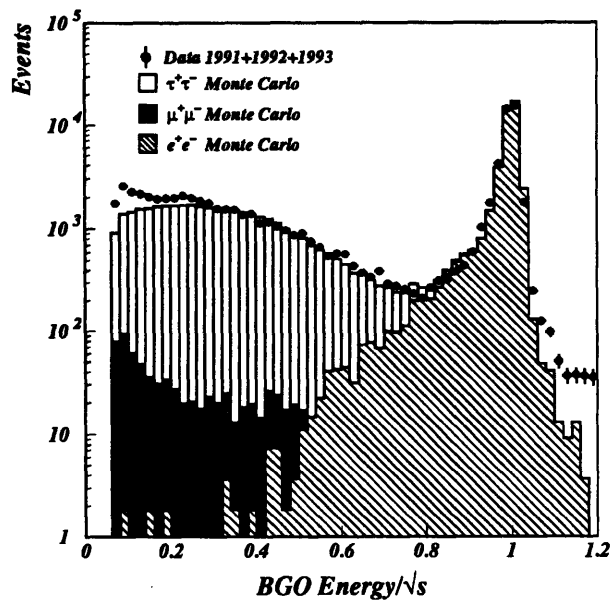


Figure 6-66: The normalized total energy in the electromagnetic calorimeter. Cuts are placed at 0.9 and 0.8.

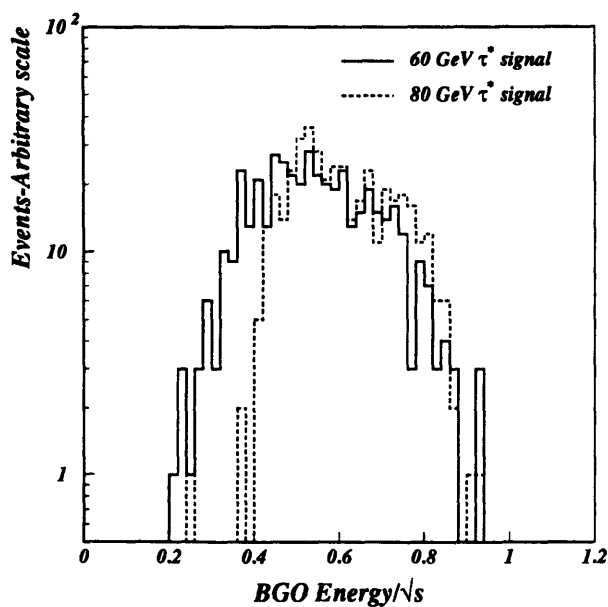


Figure 6-67: The corresponding distribution for the  $\tau^*$  signals.

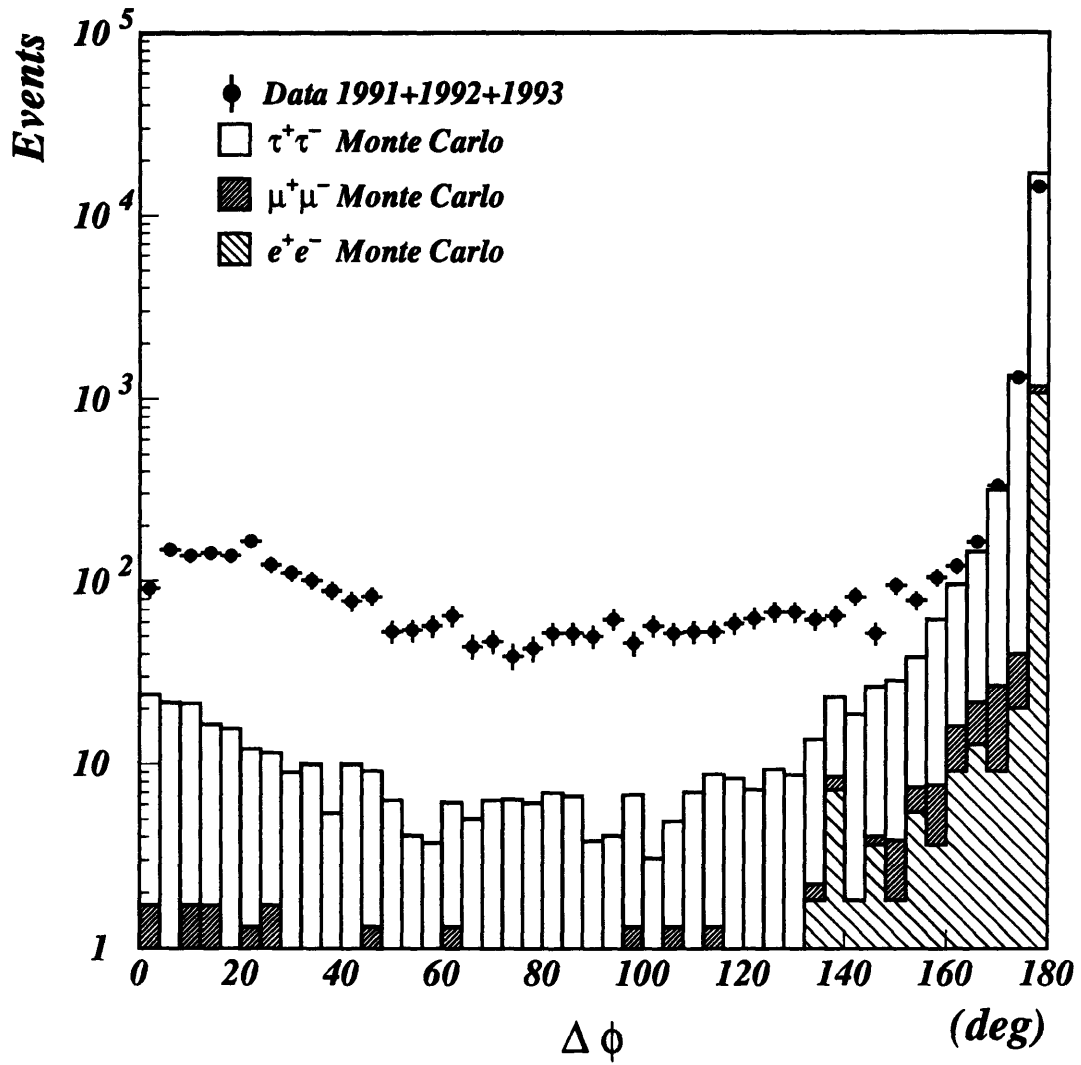


Figure 6-68: The angle between the two most energetic jets in  $\phi$  before any scintillator hit requirements.

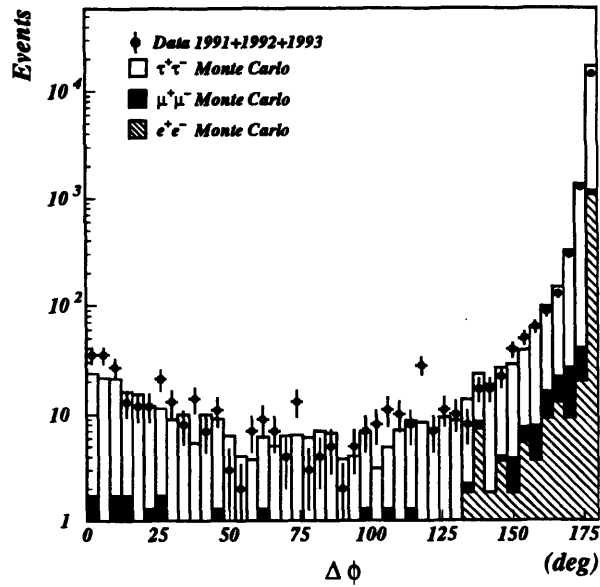


Figure 6-69: The angle between the two most energetic jets in  $\phi$  after requiring at least one scintillator hit with 5 ns of beam crossing. Compare with Fig. 6-68.

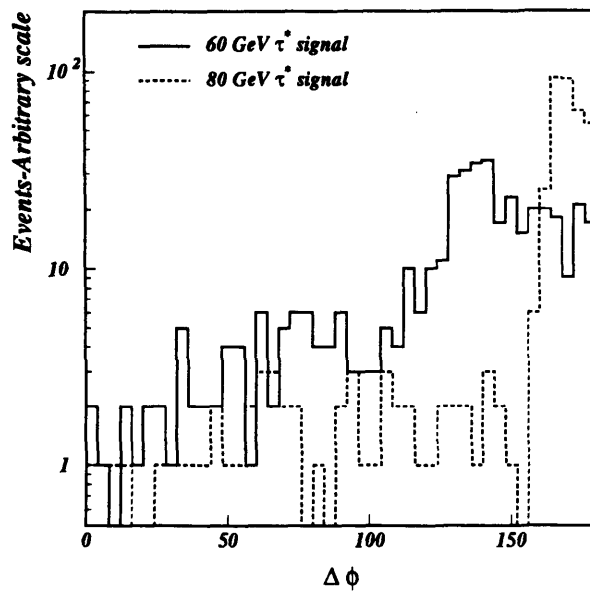


Figure 6-70: The corresponding distribution for the  $\tau^*$  signals.

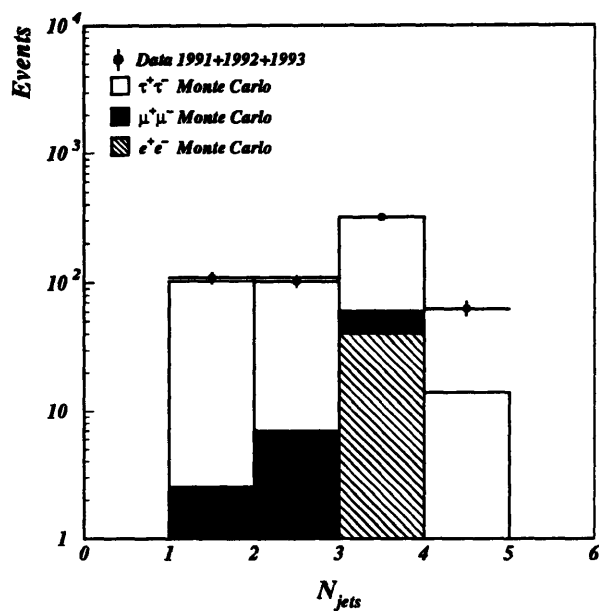


Figure 6-71: The number of jets with at least 2 GeV of energy.

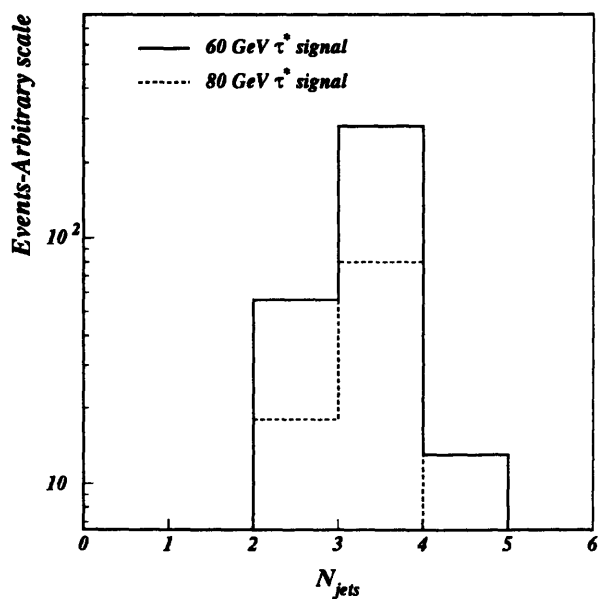


Figure 6-72: The corresponding distribution for the  $\tau^+$  signals. Upon comparison with Figure 6-71 we require two jets.

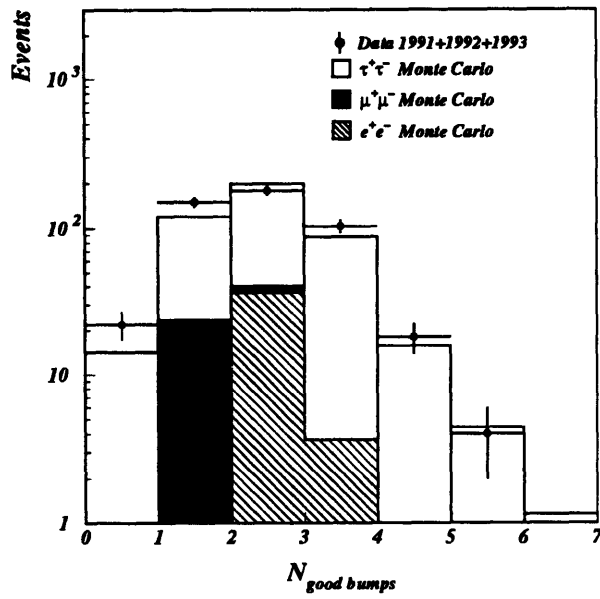


Figure 6-73: The number of good electromagnetic energy clusters.

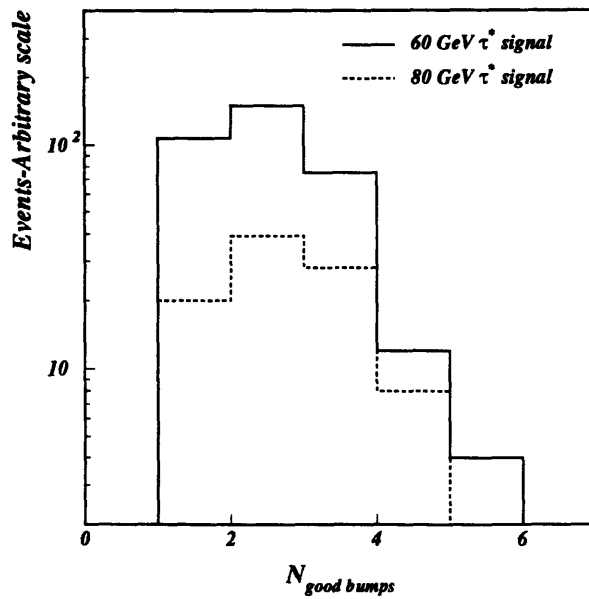


Figure 6-74: The corresponding distribution for the  $\tau^*$  signals. At least one cluster is required.

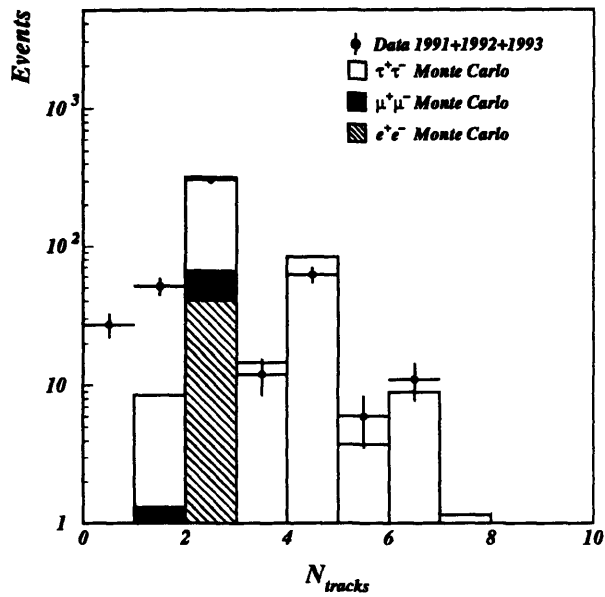


Figure 6-75: The number of good tracks.

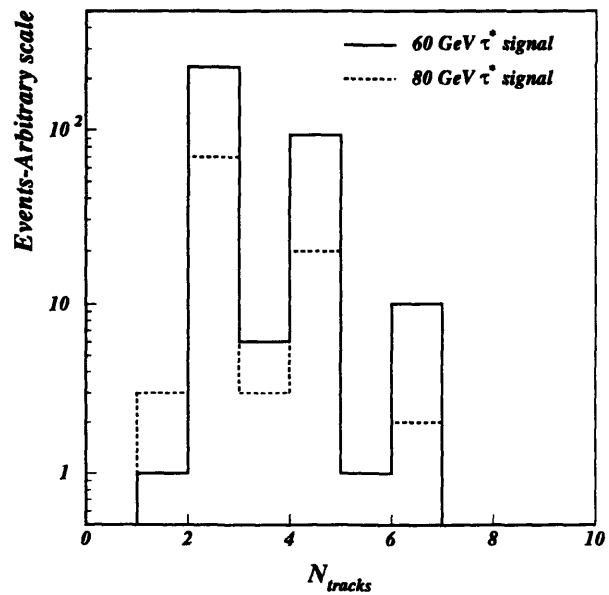


Figure 6-76: The corresponding distribution for the  $\tau^*$  signals. We require at least one track.

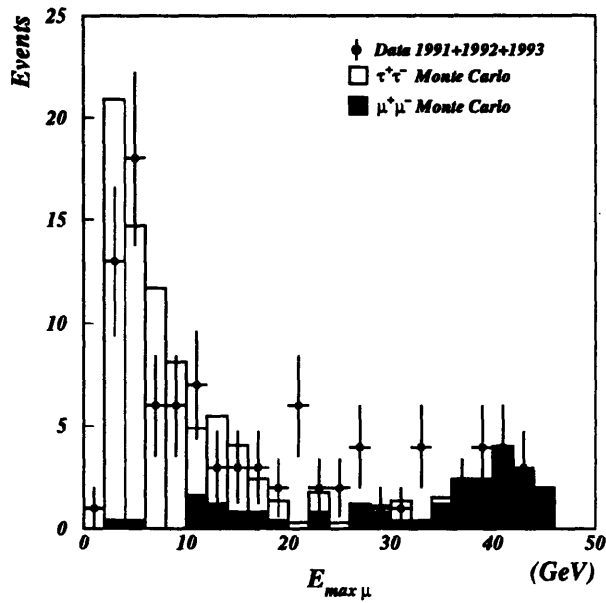


Figure 6-77: The energy of the most energetic muon. A cut is placed at 26 GeV.

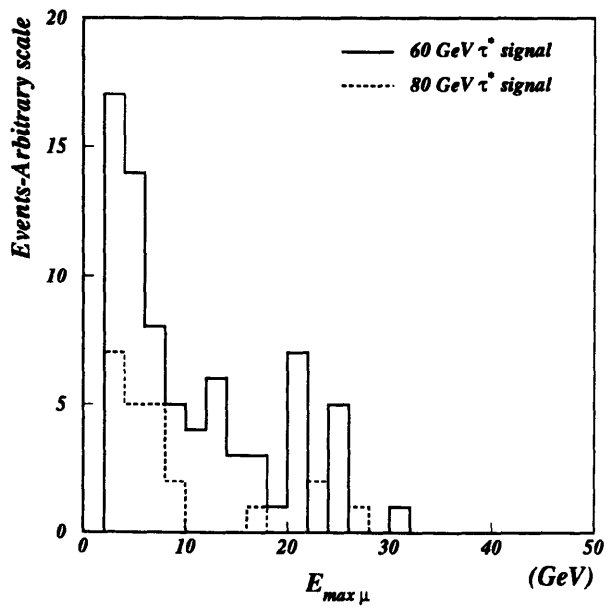


Figure 6-78: The corresponding distribution for the  $\tau^*$  signals.

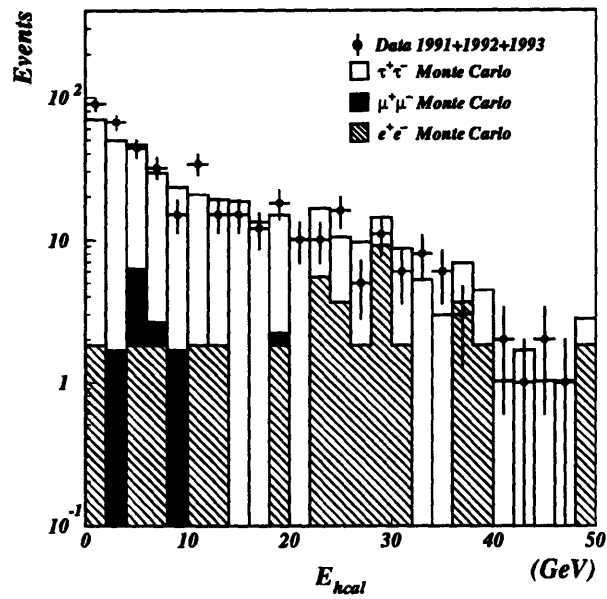


Figure 6-79: The total energy deposited in the hadron calorimeter is shown near the end of the selection cuts.

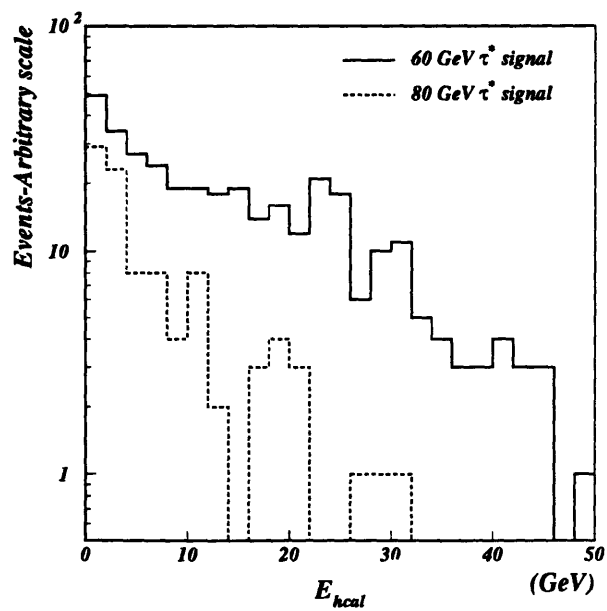


Figure 6-80: The corresponding distribution for the  $\tau^*$  signals.

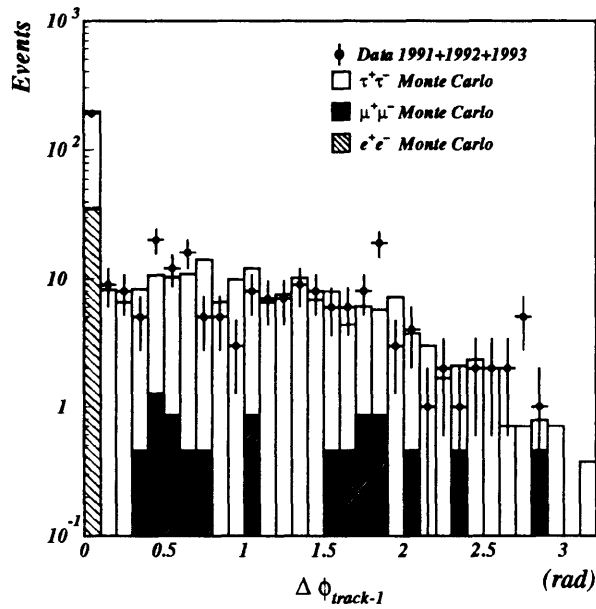


Figure 6-81: The distance in radians from the most electromagnetic cluster to the nearest track.

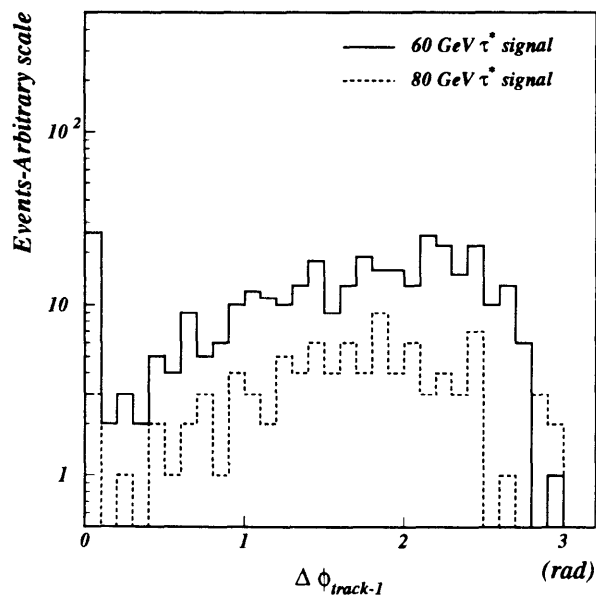


Figure 6-82: The corresponding distribution for the  $\tau^*$  signals.

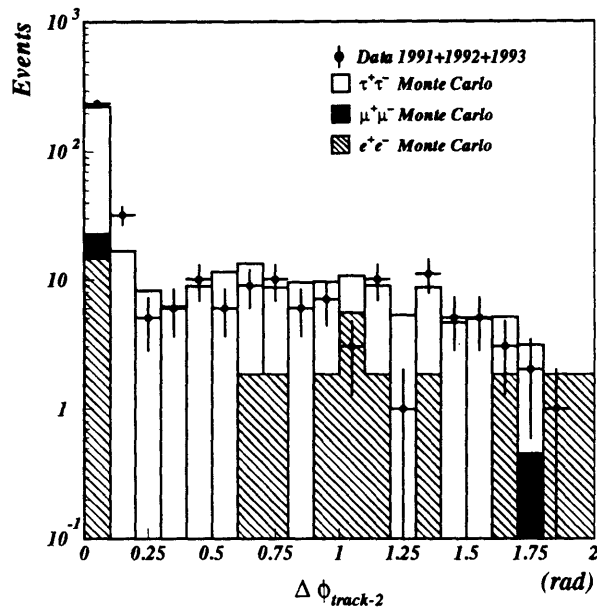


Figure 6-83: The distance in radians from the most second most energetic electromagnetic cluster to the nearest track.

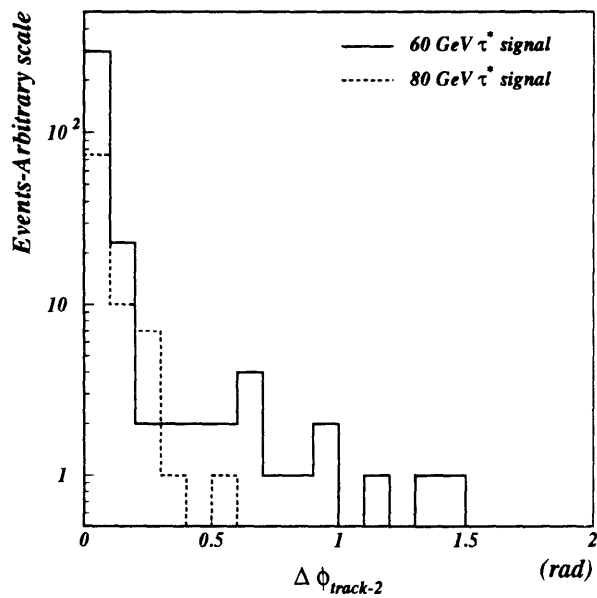


Figure 6-84: The corresponding distribution for the  $\tau^*$  signals.

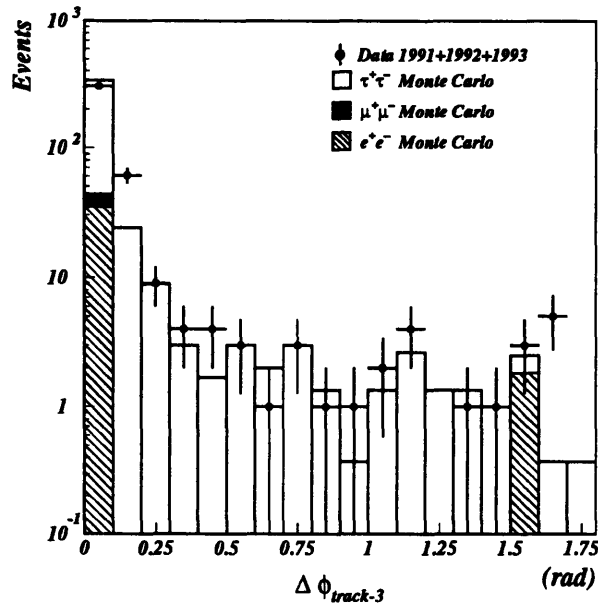


Figure 6-85: The distance in radians from the third most energetic electromagnetic cluster to the nearest track.

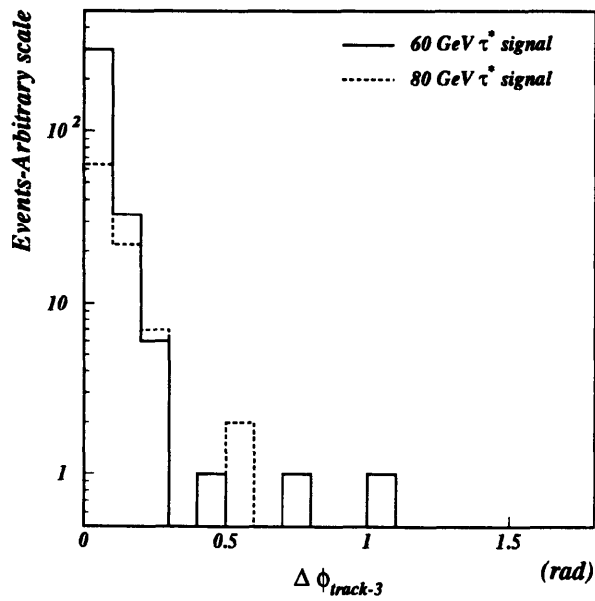


Figure 6-86: The corresponding distribution for the  $\tau^+$  signals. A cut is placed at 0.3.

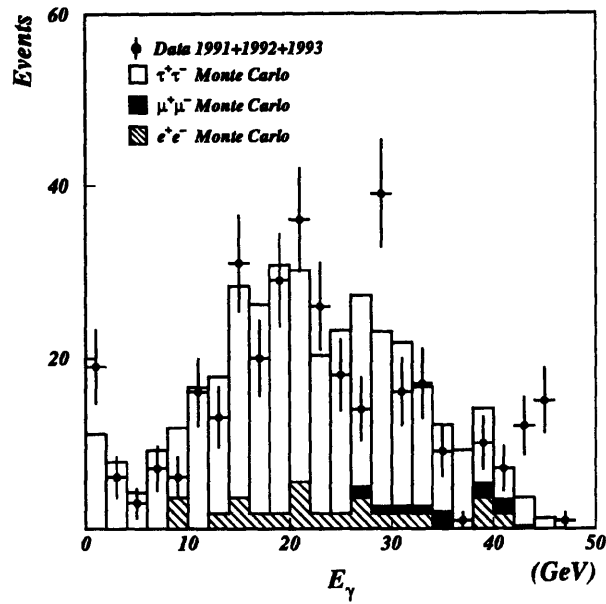


Figure 6-87: The energy of the jet chosen to be the photon. At least 15 GeV of energy will be required.

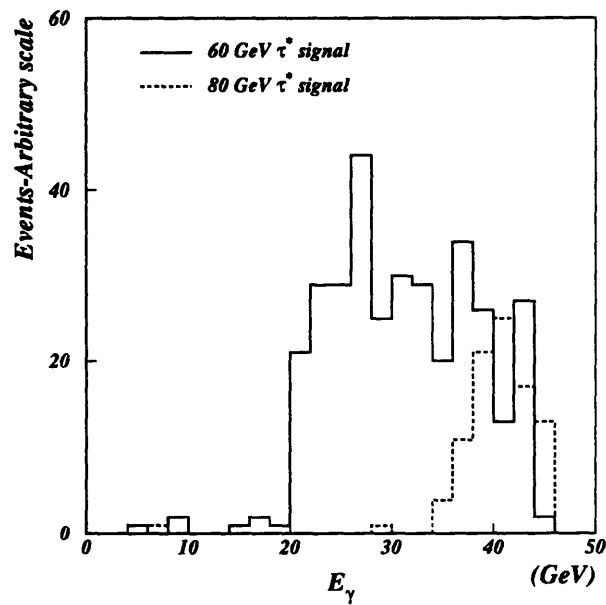


Figure 6-88: The corresponding distribution for the  $\tau^*$  signals.

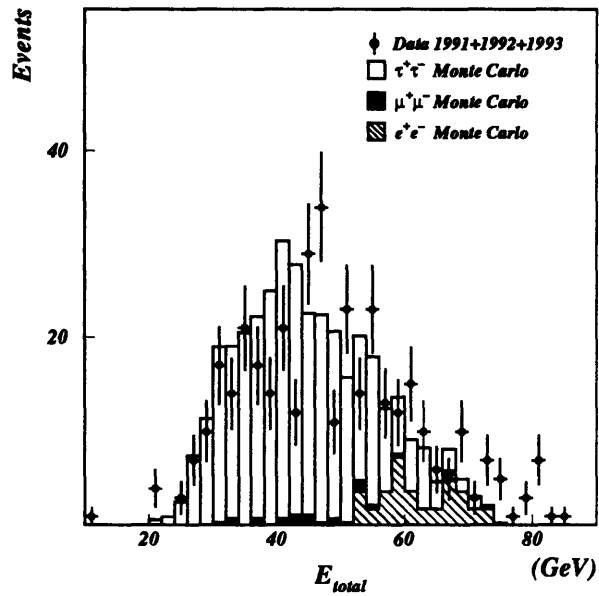


Figure 6-89: The total visible energy in the detector. At least 24 GeV is required.

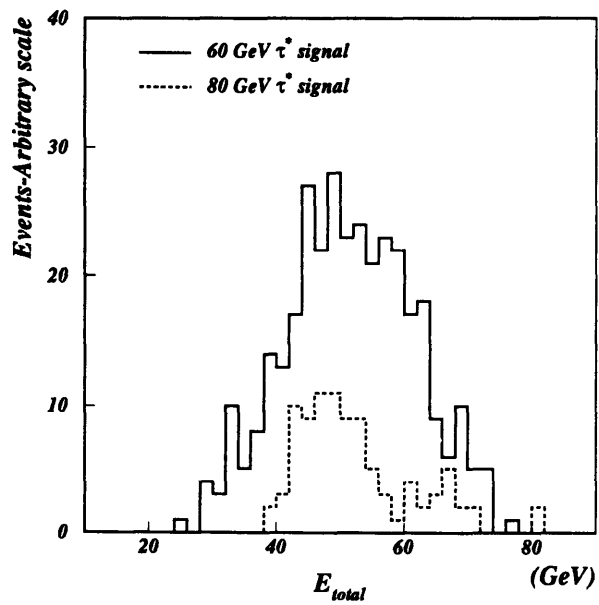


Figure 6-90: The corresponding distribution for the  $\tau^*$  signal.

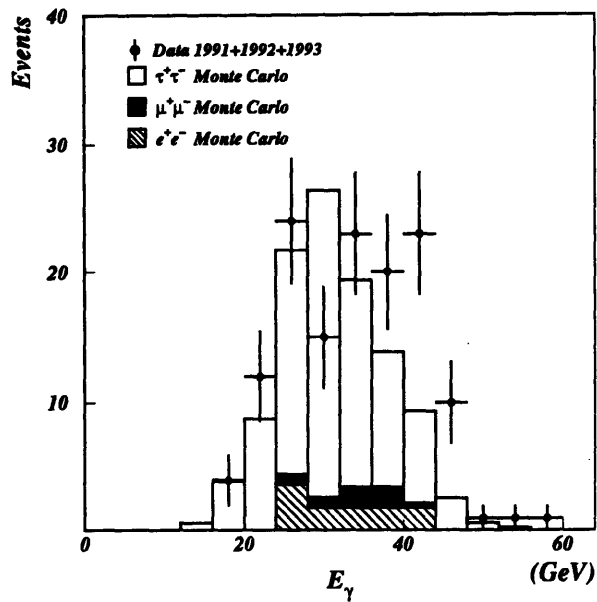


Figure 6-91: *The energy distribution of the photon candidate after cuts on the photon energy and total jet energies. This is to show the agreement between the data and Monte-Carlo for the photon selection process.*

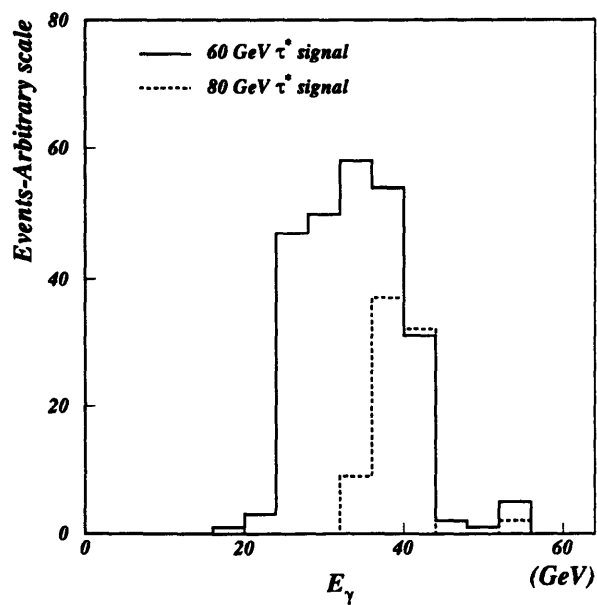


Figure 6-92: *The corresponding distribution for the  $\tau^*$  signals.*

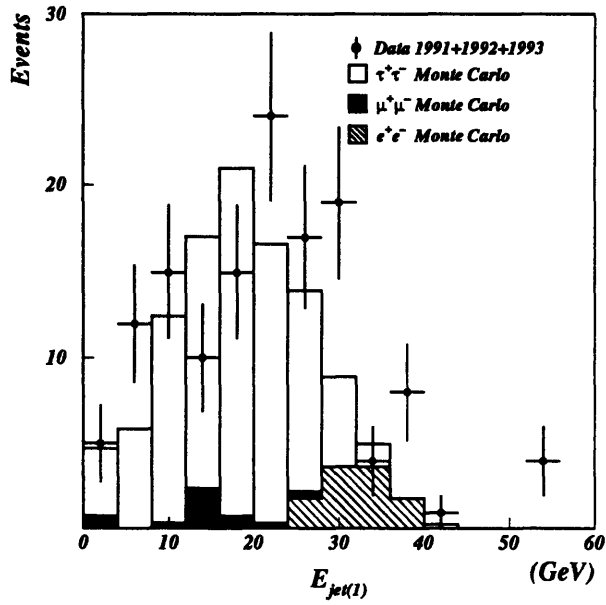


Figure 6-93: *The energy of the jet chosen to be the most energetic tau.*

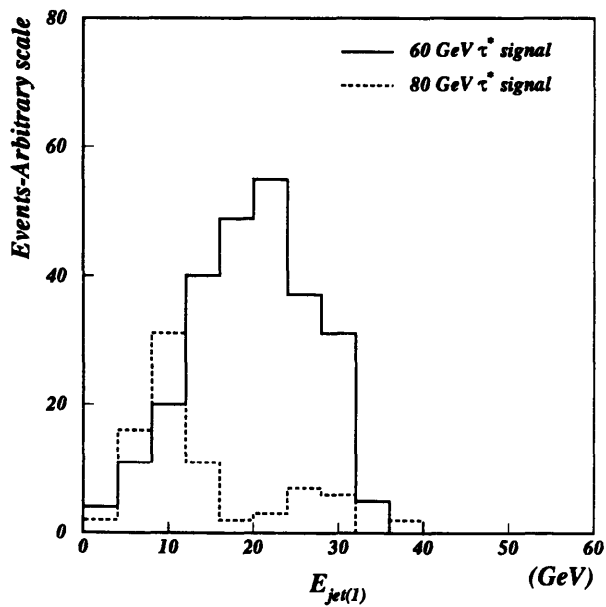


Figure 6-94: *The corresponding distribution for the  $\tau^*$  signals.*

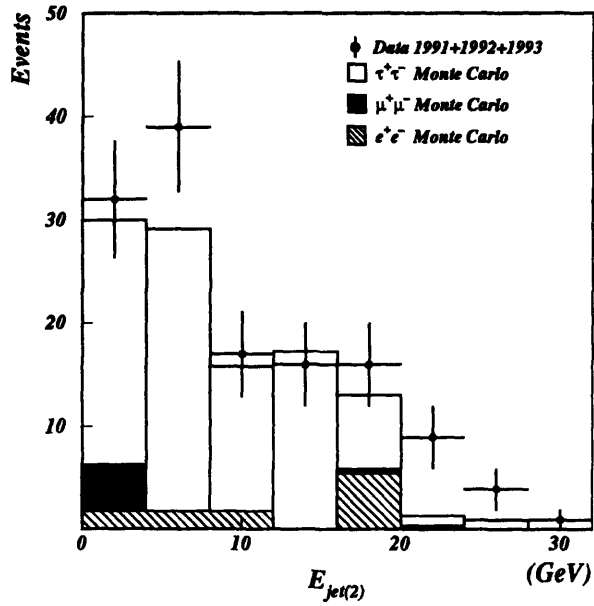


Figure 6-95: The energy of the jet chosen to be the least energetic tau.

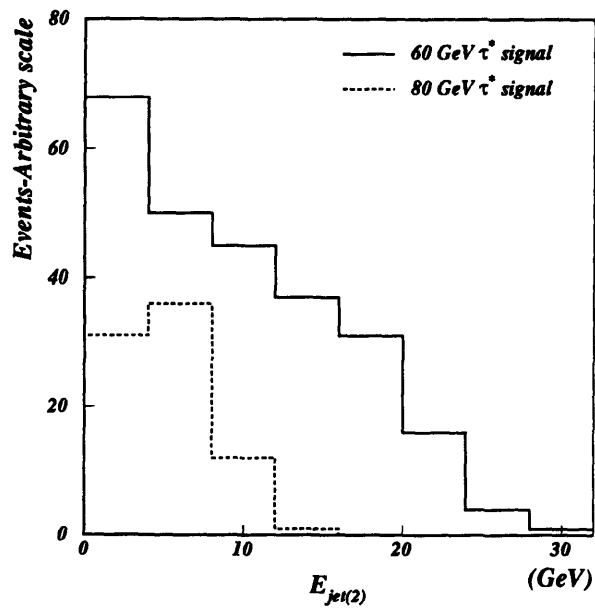


Figure 6-96: The corresponding distribution for the  $\tau^*$  signals.

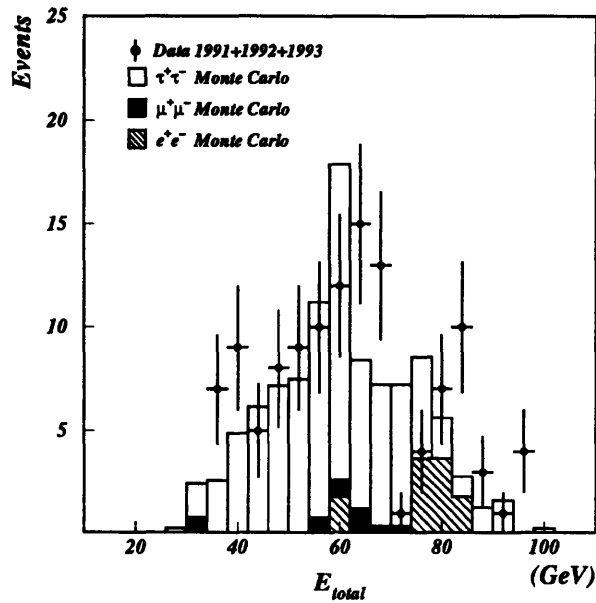


Figure 6-97: The total visible energy in the detector after the requirement of 24 GeV and the presence of at least a 15 GeV photon candidate. This is shown to display the agreement between the data and Monte-Carlo distributions.

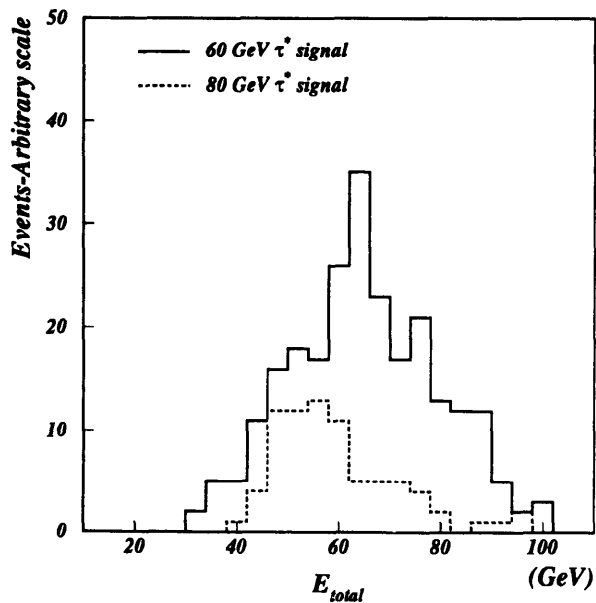


Figure 6-98: The corresponding distribution for the  $\tau^*$  signal.

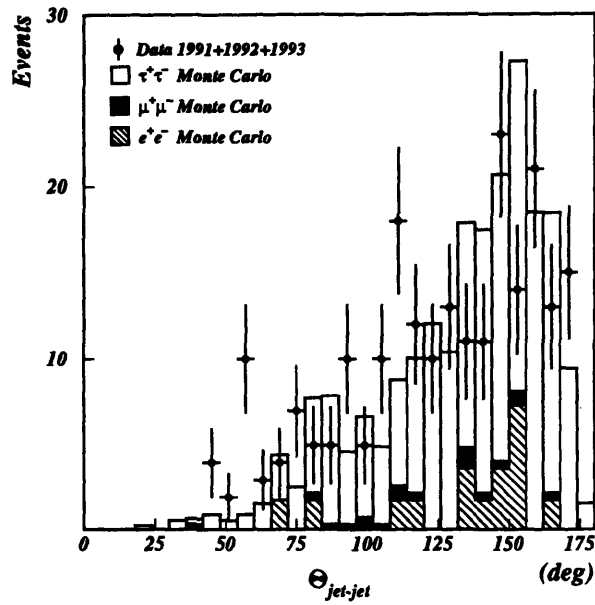


Figure 6-99: The angle in space between the two tau jet candidates. It is required that they be less than  $140^\circ$  apart in order to further reduce the QED background.

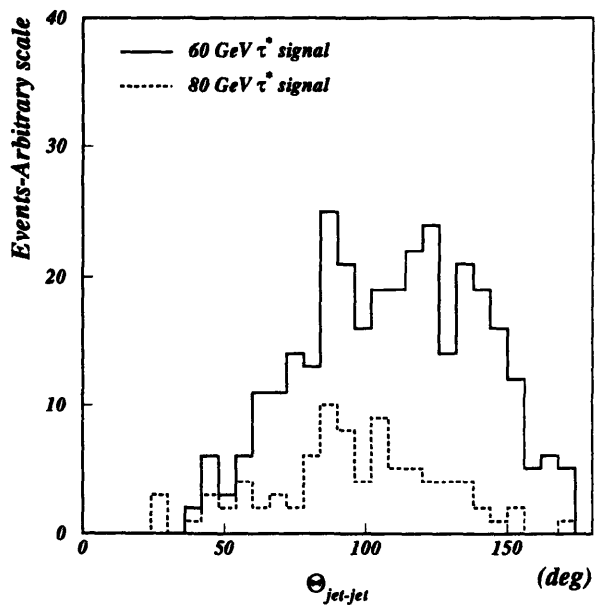


Figure 6-100: The corresponding distribution for the  $\tau^*$  signal. Here the distribution is relatively flat.

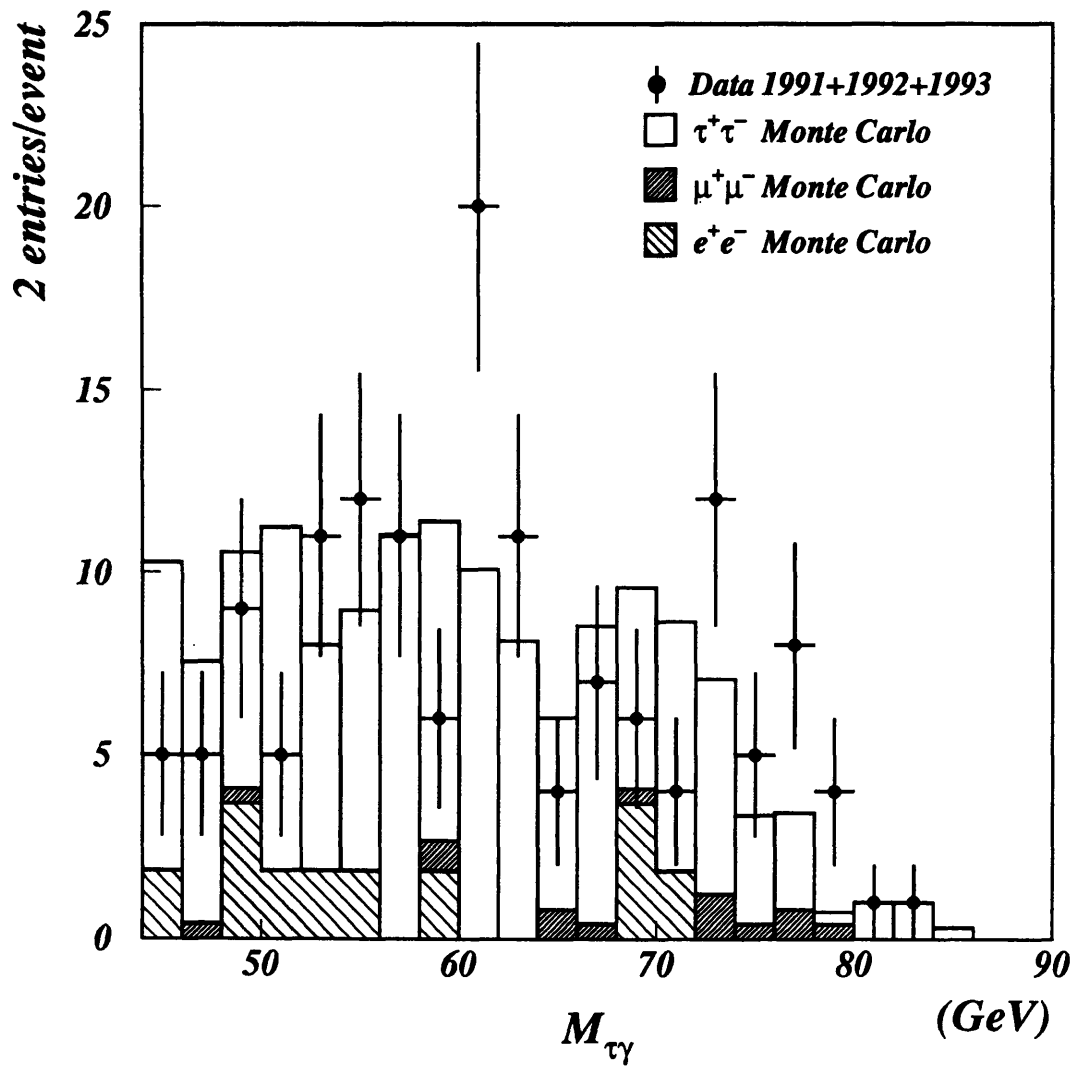


Figure 6-101: The reconstructed  $\tau-\gamma$  invariant mass from radiative di-tau events after rescaling for the neutrino energy loss. After all selection cuts, we have 147 events in Data while  $146.9 \pm 3.9$  in total are expected from the sum of the Monte-Carlo backgrounds.

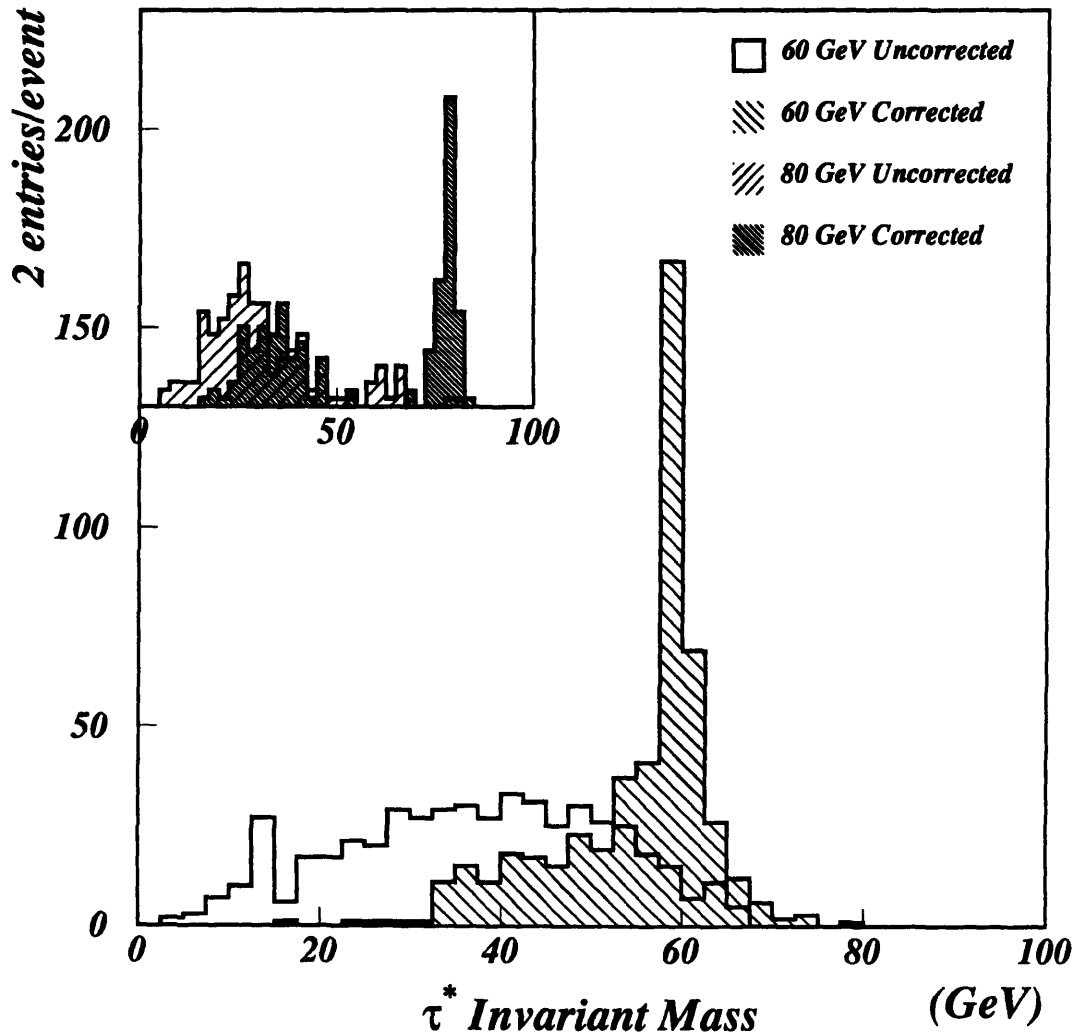


Figure 6-102: The reconstructed invariant mass of a 60 and 80 GeV  $\tau^*$  before and after rescaling for the neutrino energy loss. The rescaled mass resolutions are  $\sigma = 1.5$  and  $2.2$  GeV for the 60 and 80 GeV signals, respectively. The relative number of entries is due to the mass-dependent selection efficiency. For each mass, 500 events were generated and simulated.

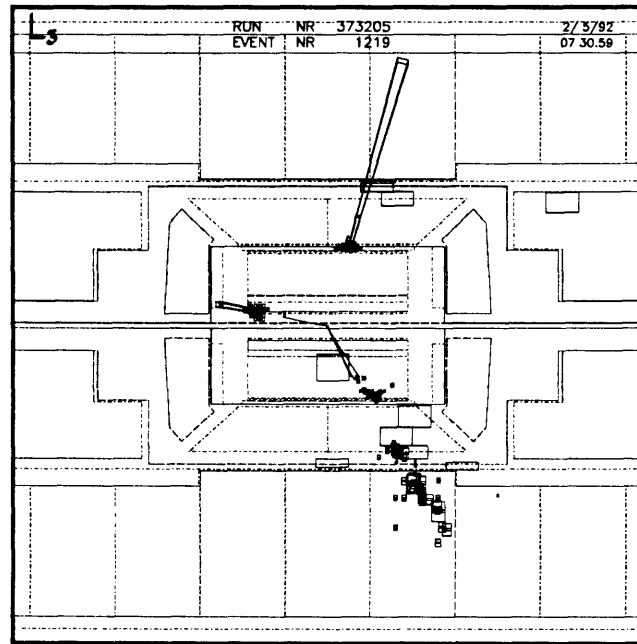
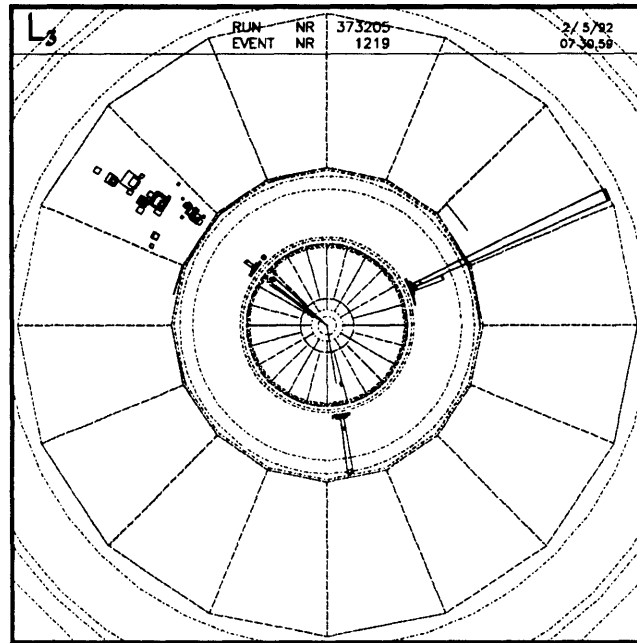


Figure 6-103: An example of a radiative di-tau event from 1992. The photon energy is 23.6 GeV. The single-prong tau decay left 8.2 GeV in the BGO calorimeter, while the three-prong decay left only 1.6 GeV in the BGO but 24.5 GeV in the hadron calorimeter.

## 6.7 Results

The four direct searches for singly produced excited leptons can be interpreted in terms of a limit on the coupling  $\lambda/m_{l^*}$ . A statistical limit, explained below, is placed on singly produced excited leptons as a function of its mass and coupling to the  $Z^0(\gamma)$  for the s(t) channels.

In all of the direct search analyses, all the possible remaining data candidates must be compared with the estimated number of expected events from known background sources. In order to calculate an upper limit on the number  $N$  of signal events, one uses the Poisson distribution.

In the absence of known or estimable backgrounds, the probability to observe the upper limit of  $N$  events for a given true  $\mu$  is at least  $1 - \alpha$  that one will observe  $n_o$  which will result in  $N > \mu$  is given by:

$$1 - \alpha = \sum_{n=n_o+1}^{\infty} \frac{\mu^n e^{-\mu}}{n!} \quad (6.27)$$

In order to improve on this result, the expected background can be statistically subtracted. Let  $n_o$  be the number of events observed, and assume that the mean background value is given by  $\mu_b$  with negligible error, with  $n_b$  denoting the true unknown background value. If  $\mu_s$  is the real unknown mean of the signal, then the confidence limit of  $\alpha$  is found when the value  $N$  is set such that any experiment with  $\mu_s = N$  with the same  $\mu_b$  would observe at most  $n_o$  events and have it be such that  $n_b \leq n_o$ , all with a probability of  $1 - \alpha$ . For any  $N$  and  $\mu_b$ , this probability is given by:

$$1 - \alpha = 1 - \frac{e^{-(\mu_b+N)} \sum_{n=0}^{n_o} \frac{(\mu_b+N)^n}{n!}}{e^{-\mu_b} \sum_{n=0}^{n_o} \frac{(\mu_b)^n}{n!}} \quad (6.28)$$

For all the searches,  $\alpha$  is set at 0.05, and thus all limits are placed at the 95% confidence level.

The cross sections shown in Chapter 2 for the s and t-channels when  $\lambda/m_{l^*} = 1 \text{ TeV}^{-1}$  are used to place exclusion regions as a function of  $\lambda/m_{l^*}$  for the number of excess events which may be attributable to the new physics process. The distributions used to place the limits for the  $e^*$  s-channel,  $e^*$  t-channel,  $\mu^*$  and  $\tau^*$  couplings were given in Figures 6-21, 6-36, 6-60 and 6-101, respectively.

The exclusion regions are shown in Figure 6-104. It is seen that for all cases, the value of  $\lambda/m_{l^*}$  is excluded to approximately  $(10 \text{ TeV})^{-1}$  for masses of  $m_{l^*}$  almost up to the  $Z^0$  mass.

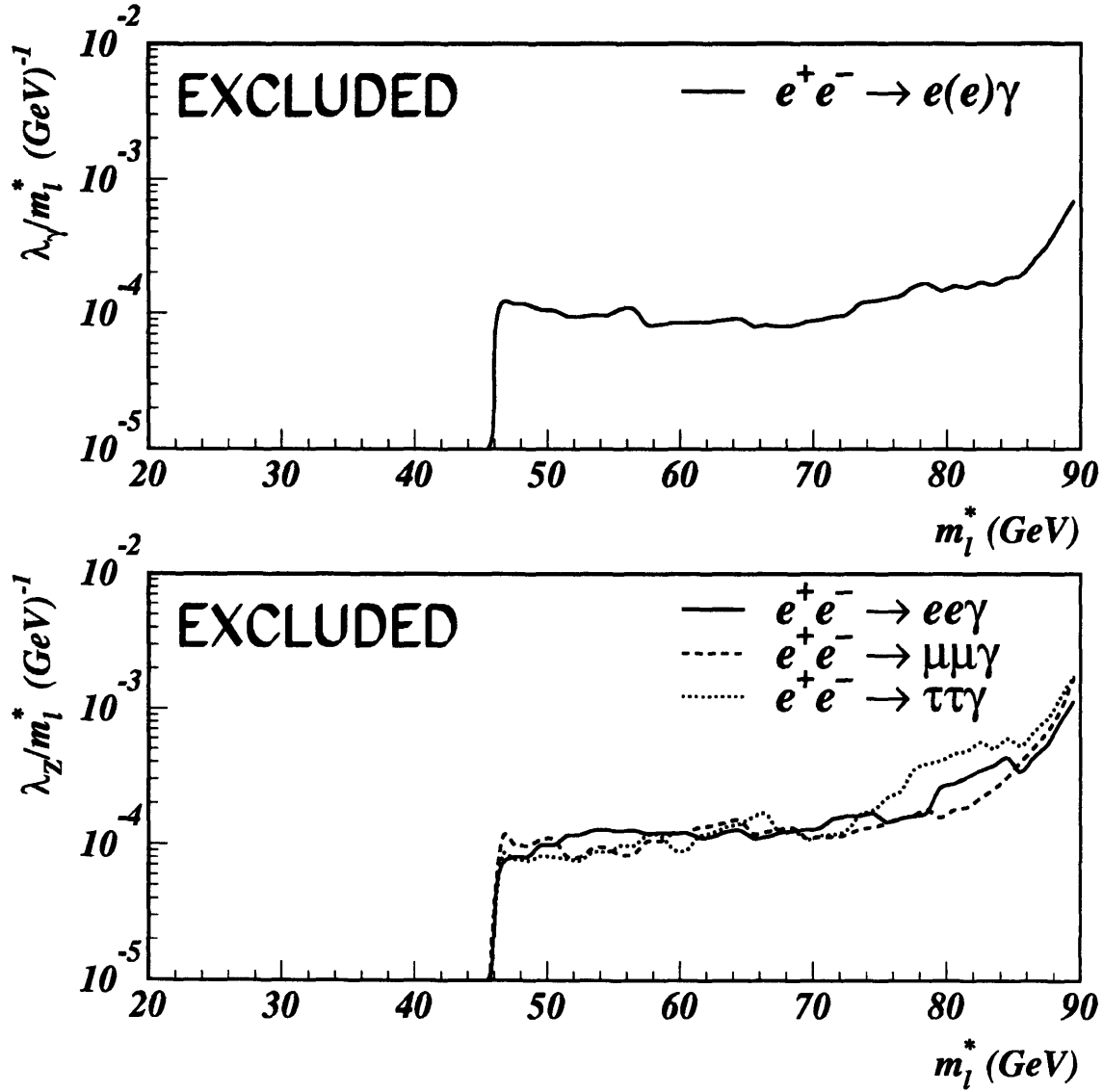


Figure 6-104: The exclusion regions as a function of the coupling and the excited lepton mass at the 95% confidence level. The upper plot shows the  $\lambda_\gamma$  coupling accessible only through the  $t$ -channel process. In the lower plot are the three exclusion regions from the three different  $s$ -channel processes.



# Chapter 7

## Composite Gauge Boson

In the bosonic sector three direct searches which could signal substructure in the  $Z^0$  is performed. First is the ‘gold-plated’ signal of the process  $Z^0 \rightarrow \gamma\gamma\gamma$  which examines the four boson vertex accessible at LEP I. An excess of three photon events would signal  $Z^0$  compositeness. Also searched for is an excess of low-mass region lepton pairs for the electron and muon. Far below the  $Z^0$  peak, an excess of di-leptons could be explained through a  $Z^0\gamma\gamma$  vertex interaction which could only be possible if the charge parity state of the  $Z^0$  could have a  $1^{++}$  component. This latter is only possible in the context of haplons as discussed in Section 2.4.1.

### 7.1 Decay topologies

For the  $Z^0$  compositeness searches, we examine the three photon final state and also the radiative di-muon and di-electron processes in search of lepton-pair invariant masses in excess of Standard Model expectations:

$$e^+e^- \rightarrow Z^0 \rightarrow \gamma\gamma\gamma$$

$$e^+e^- \rightarrow Z^0 \rightarrow \gamma^*\gamma$$

$\hookrightarrow l^+l^-$

### 7.2 $Z^0 \rightarrow \gamma\gamma\gamma$

The present limit on the branching ratio  $\text{Br}(Z^0 \rightarrow \gamma\gamma\gamma)$  is placed based on possibly the simplest model which could describe the  $Z^0\gamma\gamma\gamma$  coupling [34]. The phenomenological process is described by the Lagrangian:

$$\mathcal{L} = \frac{e^3}{\Lambda^4} (Z^{\mu\nu} F_{\mu\nu})(F^{\alpha\beta} F_{\alpha\beta}) \quad (7.1)$$

which yields the decay width:

$$\Gamma(Z \rightarrow 3\gamma) = \frac{2}{9} \alpha^3 M_Z \left( \frac{M_Z^8}{960 \Lambda^8} \right) \quad (7.2)$$

Inserting the matrix elements for this process in a Monte-Carlo program, the average energies and angular separation of the three photons are found to be (photons ordered by energy)

$$\langle E_1 \rangle = 40 \text{ GeV} \quad \langle E_2 \rangle = 31 \text{ GeV} \quad \langle E_3 \rangle = 20 \text{ GeV}$$

$$\langle \theta_{12} \rangle = 150^\circ \quad \langle \theta_{13} \rangle = 130^\circ \quad \langle \theta_{23} \rangle = 80^\circ$$

All the photons are hard and well separated. The kinematical differences between QED and a  $Z^0\gamma\gamma\gamma$  coupling are shown in Figure 7-1 where the Monte-Carlo results from the matrix elements are reproduced. The difference with the QED process are readily noticed. While in QED the most energetic photon is peaked close to the beam energy, the most energetic photon of the signal tends to have lower energy. The difference is more striking for the second photon and is very large for the third photon where the radiative nature of the background is immediately noticeable. The angular separation between the most energetic and the second most energetic photon  $\theta_{12}$  also displays very distinctive features. For the QED background, the two photons are primarily back-to-back while in the signal their opening angle is smaller. From these distributions, it is obvious that the signal can be well separated from the background by appropriate selection cuts based on the kinematics of the photons.

### 7.2.1 Data sample

Only data taken at the  $Z^0$  peak for which the TEC is acceptably functioning (see Section 6.2) is used. According to [34], the signature of the composite  $Z^0$  would be greatly enhanced only on the resonance. The theory does not describe its behavior off-shell, therefore it is incorrect to assume the cross section would scale with the hadronic one. The total luminosity from all data taken on peak from 1991 through 1993 which passes the TEC requirements amounts to  $40.0 \text{ pb}^{-1}$ . In order to increase our total acceptance, we can examine events which are forward-backward in the polar region. However, this is the region of greatest background from Bhabha events. The track reconstruction efficiency as a function of the polar angle must be known in order to determine to what angle the TEC can be relied upon to reject Bhabha events.

### 7.2.2 $e^+e^- \rightarrow e^+e^-\gamma$ background

Particular care must be given to the track reconstruction efficiency when relying on only one out of two sectors to reconstruct tracks, especially in the forward regions. The exact efficiency can be calculated from the event sample which have passed through the TEC acceptability criterion because our data sample contains both the three photon events we are looking for as well as the Bhabha background. The efficiency is found in the following manner:  $N_1$  is defined to be the number of Bhabha events with only one good track,  $N_2$  the number with two good tracks, and  $N_{ee}$  are the total number of Bhabha events, then the single track reconstruction efficiency  $\varepsilon$  is defined by:

$$N_1 = 2N_{ee}\varepsilon(1 - \varepsilon) \tag{7.3}$$

$$N_2 = N_{ee}\epsilon^2 \quad (7.4)$$

where  $\epsilon$  is:

$$\epsilon = \frac{1}{1 + \frac{N_1}{2N_2}} \quad (7.5)$$

which leads to the double track and zero track efficiencies of:

$$\epsilon_2 = \epsilon^2 \quad (7.6)$$

$$\epsilon_0 = (1 - \epsilon)^2 \quad (7.7)$$

assuming uncorrelated events.<sup>1</sup> The single track reconstruction efficiency is calculated in this manner for the data sample inclusive up to polar angle  $\theta_i$  for different  $i$ .

The results for values of  $\theta$  from  $15^\circ$  to  $30^\circ$  is shown in Figure 7-3. It is seen that for all the data taken down to  $30^\circ$  the single track reconstruction efficiency is about 99%. It slowly decreases from this value down to about 98% which corresponds to a polar angle of  $20^\circ$ . If one includes data down to angles below  $20^\circ$ , there is a dramatic loss of efficiency due to the physical decrease in the number of wires in the TEC for these angular regions. Thus the angular cutoff value of  $20^\circ$  is chosen. By taking data down to  $20^\circ$  the acceptance is optimized while minimizing the number of Bhabha events which will leave no tracks in spite of the TEC status.

With a single track efficiency  $\epsilon$  of 98.0%, in 0.04% of the time a Bhabha will leave no tracks and thus pass as a genuine two or three photon event. In order to estimate the magnitude of this Bhabha contamination, a normalized sample of BABAMC Monte-Carlo events are subjected to the three-photon selection cuts (track requirement excepted). It is found that 601 events remain. With the 0 track reconstruction efficiency of 0.04%, this yields only 0.24 events which will infiltrate the final data sample.

It is important to remember that since the efficiency is determined from the same data sample as the analysis itself, the efficiency and numbers found are exact.

### 7.2.3 Event selection

The following selection criteria are used to search for three photon events with the particular characteristics of a composite  $Z^0$ . The main background is the QED process  $e^+e^- \rightarrow \gamma\gamma(\gamma)$  and the small contamination from Bhabhas as previously mentioned are of the order of 0.24 events. Three photon events are selected by the following:

- (1) No tracks;
- (2)  $3 \leq N_{clusters} \leq 8$ ;
- (3) The two most energetic electromagnetic clusters must fall within  $|\cos \theta_1|$  and  $|\cos \theta_2| < 0.94$

---

<sup>1</sup>This latter approximation is valid since the data sample in question is not by nature back-to-back since we are asking for the presence of a hard photon.

In addition, quality cuts described in Section 6.3 are placed on the three most energetic electromagnetic clusters:

- (4)  $\chi^2 < 30$  for those clusters within the barrel region of the electromagnetic calorimeter;
- (5)  $\frac{\Sigma_0}{\Sigma_{25}} > 0.95$  for those clusters within the endcap region of the electromagnetic calorimeter.

Finally, to minimize background from misidentified  $\tau$  events or two-photon physics, the total energy in the BGO calorimeter must fulfill:

- (6) Energy in the BGO  $> 70\%\sqrt{s}$ ;

This selects good three photon events. The energy distributions of the three electromagnetic clusters are shown in Figures 7-4 through 7-6. In the first of these figures is the most energetic cluster. The data shows the expected peak near the beam energy. The signal Monte-Carlo events are arbitrarily normalized and is overlaid to show the difference in the distributions. It is seen that the signal is more evenly distributed than the data and does not exhibit a peak near  $\sqrt{s}/2$ . However, there is still too much overlap to put an energy requirement on the most energetic cluster while maintaining signal detection efficiency. The second most energetic cluster starts to show a difference between data and signal. The data still exhibits a peak near  $\sqrt{s}/2$  while the signal becomes more dispersed toward lower energies. Still no energy requirement is made.

The third most energetic cluster is dramatically different between the data and Monte-Carlo since the QED process exhibits the radiative tail while the average energy of the signal is of the order of 20 GeV. It is also of interest to look at the transverse momentum of the third photon with respect to the thrust axis, where the thrust  $T$  is given by:

$$T = \max \left( \frac{\sum_i |\vec{n} \cdot \vec{p}_i|}{\sum_i |\vec{p}_i|} \right) \quad (7.8)$$

The thrust axis is defined to be in the direction of  $\vec{n}$  for which the thrust is maximal. The distribution of  $p_t$  is shown in Figure 7-7. It is seen that one can distinguish between data and signal with such a parameter. Presently, since a cut on both  $E_3$  and  $p_t$  is redundant, the photon energy as the distinguishing parameter. A good separation between data and signal can be made if the third photon is required to have:

- (7)  $E_3 > 8$  GeV;

In order to further isolate the signal on a kinematical basis, since the composite  $Z^0$  would be expected to decay nearly isotropically in space, it is required that:

- (8)  $\theta_{12} + \theta_{23} + \theta_{13} > 350^\circ$  (planar);
- (9) All clusters are separated by more than  $25^\circ$ .

After all cuts 12 events remain in the data and  $14.8 \pm 0.9$  events are expected from the QED  $\gamma\gamma(\gamma)$  Monte-Carlo. The main parameters of the data are given in Table 7.1 and a scatter plot of the energy vs. the cosine of the polar angle of the third most energetic cluster is shown in Figure 7-8. Also shown in Figure 7-9 are all possible photon pair invariant mass combinations for the final events. No peak is seen.

An example of a three-photon event from 1992 can be seen in Figure 7-10.

## 7.2.4 Branching ratio limit

The efficiency for detecting the signal is determined using the signal Monte-Carlo taken from calculations referenced in [34]. Although this method renders the result somewhat model-dependent, it should be noted that the model taken is the still the most general one which describes a possible  $Z^0\gamma\gamma\gamma$  vertex. The signal detection efficiency is measured from fully simulated three-photon events. It is found that the overall efficiency is  $60.6 \pm 2.15$  %. Therefore we take the conservative value of 58.5%.

Using Poisson statistics, an upper limit on the branching ratio of the process  $Z^0 \rightarrow \gamma\gamma\gamma$  is set at the 95% C.L. :

$$\boxed{\text{Br}(Z^0 \rightarrow \gamma\gamma\gamma) < 7.4 \times 10^{-6}}$$

Since the width of the decay is proportional to  $\Lambda^{-8}$  as given in Eq. 7.2, this result yields a lower limit on the  $Z^0\gamma\gamma\gamma$  contact term interaction strength  $\Lambda$ :

$$\Lambda > 40.0 \text{ GeV} \quad (7.9)$$

## 7.3 $Z^0 \rightarrow \mu^+\mu^-\gamma, e^+e^-\gamma$

As mentioned in Section 2.4.3, the excess of low lepton invariant mass states can signal  $Z^0$  compositeness. The theory is valid for energy regimes much smaller than the  $Z^0$  mass. Nevertheless, it is possible to examine the di-lepton invariant mass spectrum (for electrons and muons) for all radiative di-electron and di-muon events and look for an excess over predicted Standard Model values. The photon spectrum will be hard compared to that of QED events and to place a limit on the branching ratio of  $Z^0$  decays into 'anomalous' di-lepton events, a lower requirement will be placed on the photon energy at 10 GeV.

To select the electron and muon data sample, similar selections are implemented as in the Sections 6.3 and 6.5 for the electrons and muons, respectively. However, no cuts are placed based on  $l^*$  kinematics. The general requirements are:

For the electron spectrum:

- (1) NASRC < 12;
- (2) Exactly two tracks;
- (3) At least three good electromagnetic clusters;

- (4) All three clusters within polar region  $|\cos\theta| < 0.78$ ;
- (5) Energy in the hadron calorimeter  $\leq 10$  GeV;
- (6) Energy of the photon at least 10 GeV.

where the photon is chosen as being the electromagnetic cluster with the track in the  $r - \phi$  plane at the farthest distance.

After these cuts, 703 events remain in data while there are  $859.1 \pm 29.2$  from the background BABAMC Monte-Carlo. The invariant mass distribution of the electron pairs is shown in Figure 7-11.

For the muon spectrum:

- (1) NASRC  $< 16$ ;
- (2) Two good muons, either doublets or triplets;
- (3) Each muon must be associated with at least one Z chamber segment;
- (4) Total energy in the detector at least 80 GeV;
- (5) Energy in the hadron calorimeter not greater than 20 GeV;
- (6) The DCA of each muon  $\leq 20$  mm;
- (7) Energy of the photon at least 10 GeV.

After these cuts, 1998 events remain in the data while the KORALZ Monte-Carlo predicts  $1991.1 \pm 12.1$  events. The resulting invariant mass distribution for the muon pair is shown in Figure 7-12

From the above distributions of the di-lepton invariant masses, Poisson statistics is used for an upper limit on the possible number of excess events above Standard Model predictions. A limit on the branching ratio of  $Z^0 \rightarrow \textit{anomalous } l^+l^-$  is shown in Figure 7-13. It is seen for the mass range pertinent to the compositeness theory, an upper limit on the branching ratio is found to be:

$$\boxed{\text{Br}(Z^0 \rightarrow \gamma^*\gamma \rightarrow l^+l^-) < 10^{-6}}$$

Run	Event	$E_1$	$E_2$	$E_3$	$\theta_{12}$	$\theta_{23}$	$\theta_{13}$	$\theta_1$	$\theta_2$	$\theta_3$	$\phi_1$	$\phi_2$	$\phi_3$
289901	689	40.55	32.96	16.29	158.3	71.2	130.0	105.3	78.4	63.5	50.2	208.2	282.9
307401	3428	37.40	36.37	9.78	169.1	77.0	113.9	26.9	145.2	133.1	152.3	347.0	204.0
338205	3656	44.98	24.48	21.50	168.2	25.8	166.7	109.3	62.0	81.5	175.9	4.5	347.5
424906	171	38.54	34.83	19.51	151.7	92.1	116.4	146.6	60.5	34.6	105.1	297.5	144.4
431302	2121	39.24	35.34	16.11	155.3	89.0	115.9	126.2	69.7	49.0	87.2	245.3	352.7
389301	105	41.58	24.58	23.00	152.0	60.9	147.3	150.7	29.5	52.1	60.8	300.2	203.0
432510	622	45.88	30.35	15.16	167.5	36.4	156.2	85.3	100.3	87.3	227.4	58.7	24.5
467507	4997	41.84	25.84	21.12	151.6	63.2	145.5	132.9	75.3	14.8	216.6	30.7	64.4
481502	1143	39.91	33.70	12.41	171.2	32.2	156.7	136.0	51.3	30.4	196.1	9.1	48.0
493606	2043	34.92	38.08	27.62	125.2	105.8	129.1	34.7	98.6	145.6	290.8	146.9	12.1
495201	4238	44.08	34.12	10.21	170.2	48.6	141.4	25.4	153.6	133.9	238.4	35.7	118.2
502207	51	34.55	23.92	14.56	156.8	112.6	90.8	35.4	124.1	119.2	286.2	90.3	245.4

Table 7.1: The main parameters of the 12 three photon events. The energies are in GeV,  $\theta_{ij}$  are angles in space and all angles are in degrees.

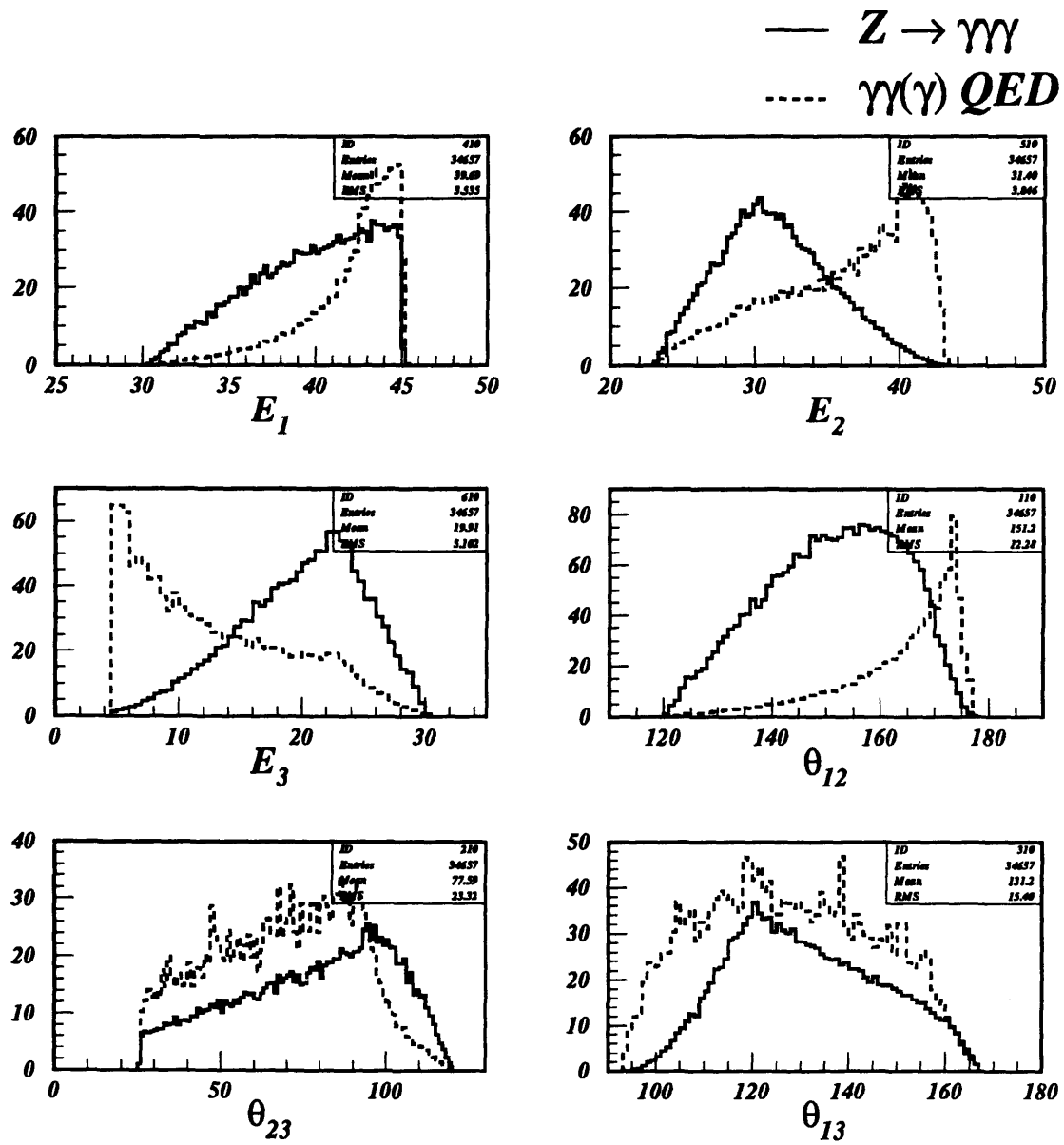


Figure 7-1: Results from the matrix element calculations. The energies are in GeV and the angles are in degrees; the vertical axes are arbitrary.

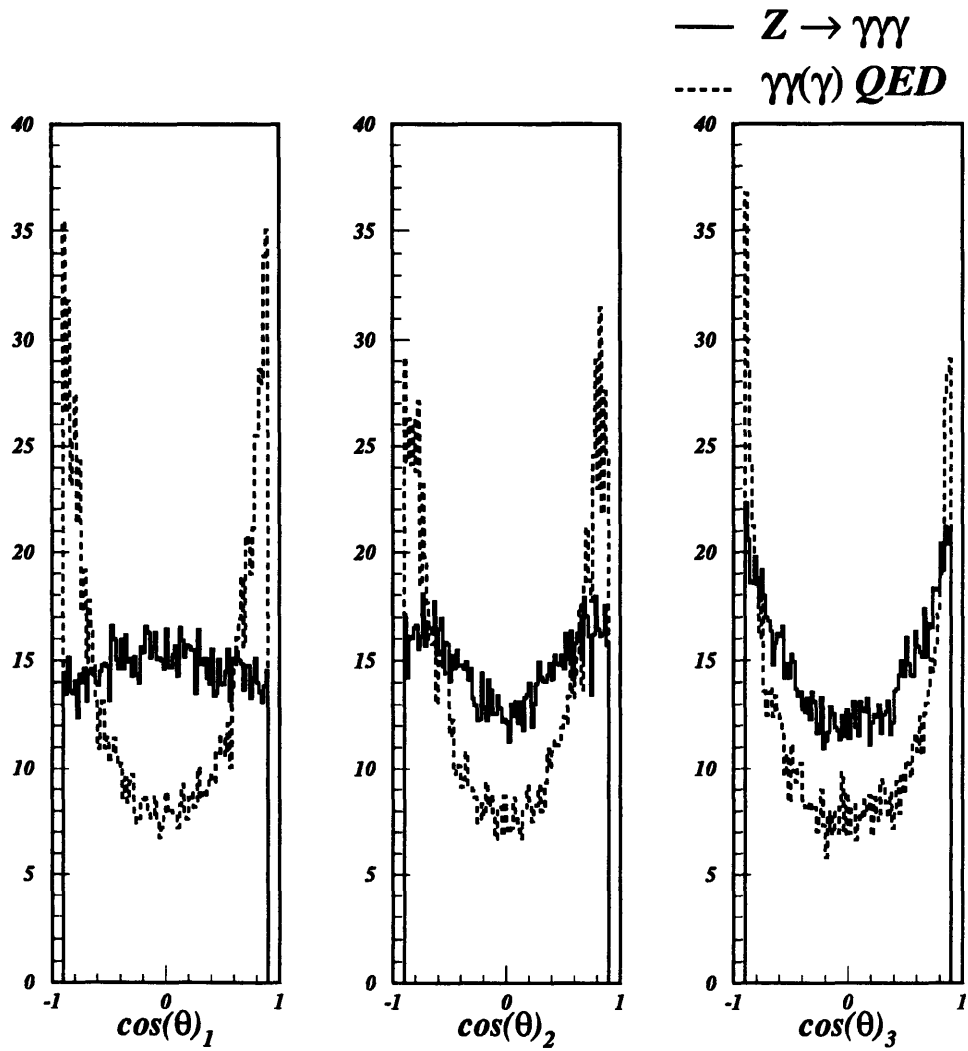


Figure 7-2: Results from the matrix element calculations. The polar angular distributions for the three photons is shown. It is seen that the lesser energetic photons do not possess a flat distribution.

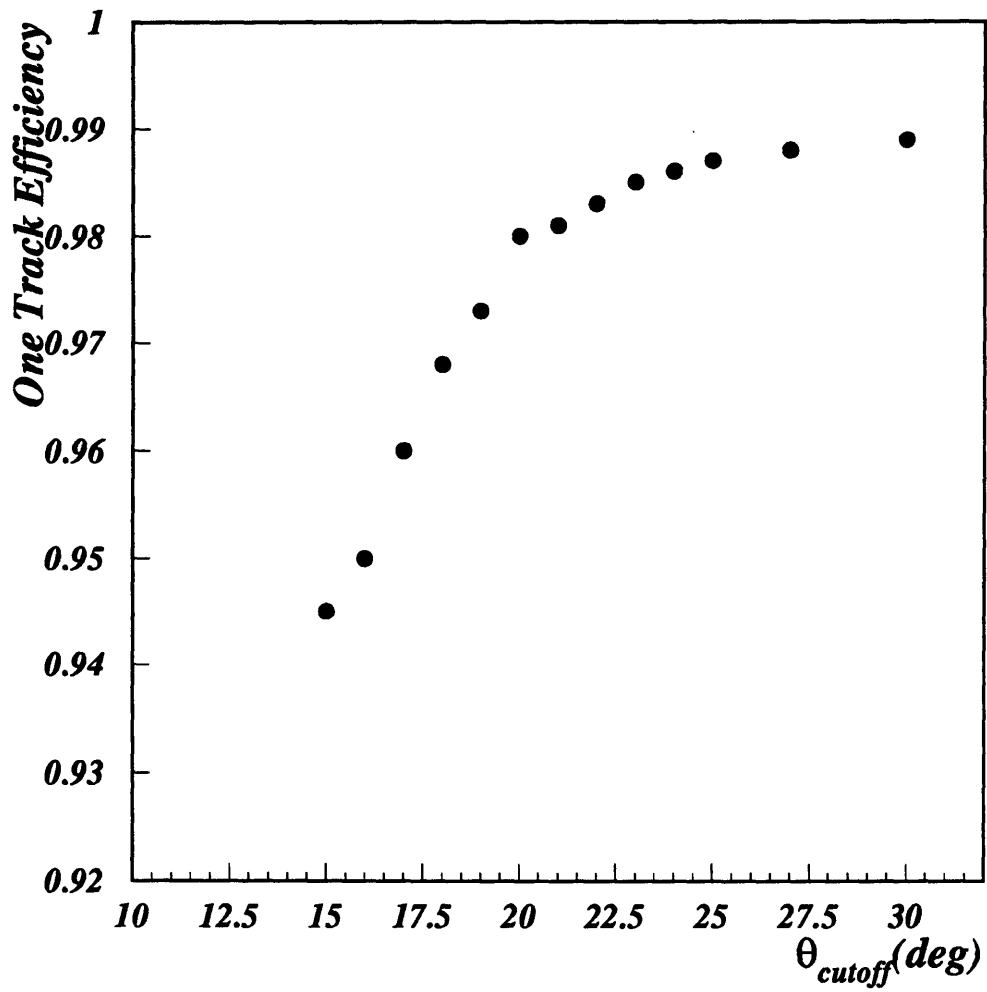


Figure 7-3: *The average efficiency of finding one track as a function of the angular cutoff. This analysis uses data where the two most energetic bumps are above  $20^\circ$ .*

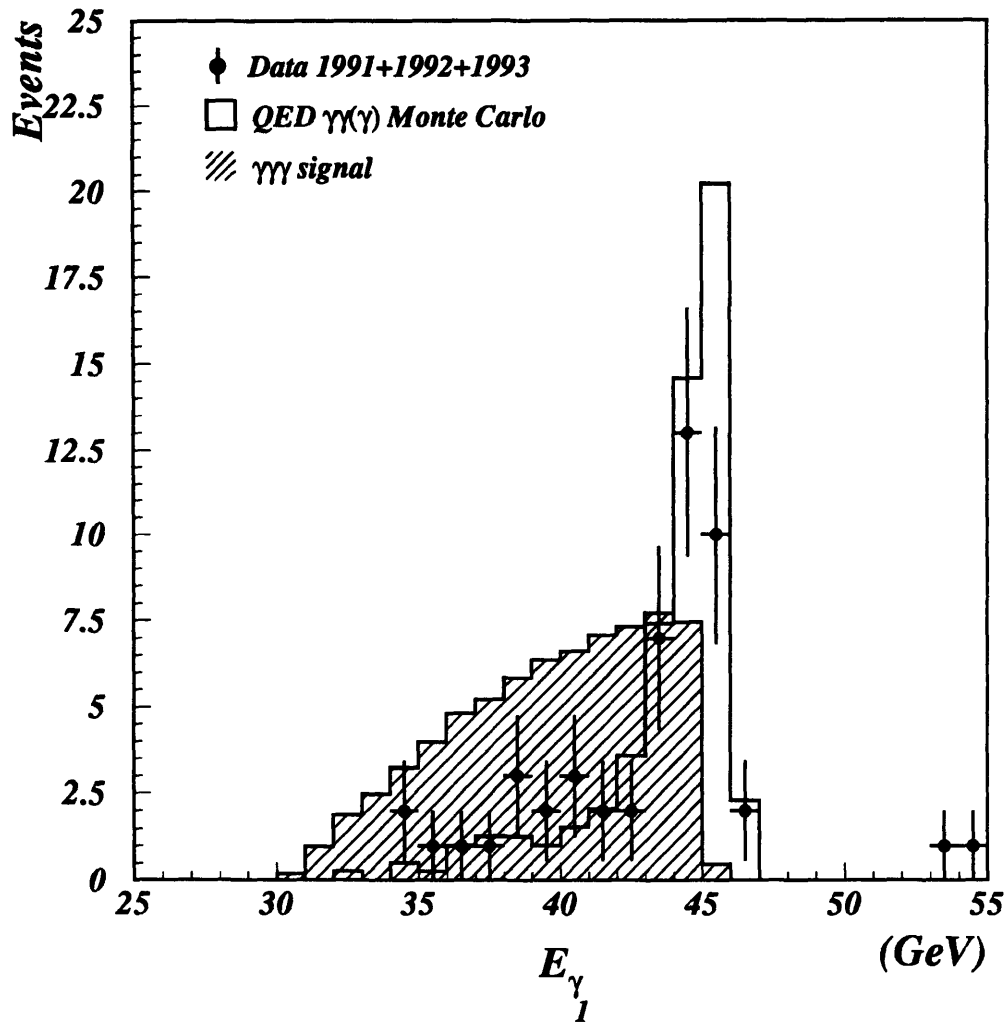


Figure 7-4: The energy of the most energetic photon for the data, the QED Monte-Carlo and the signal (arbitrarily normalized).

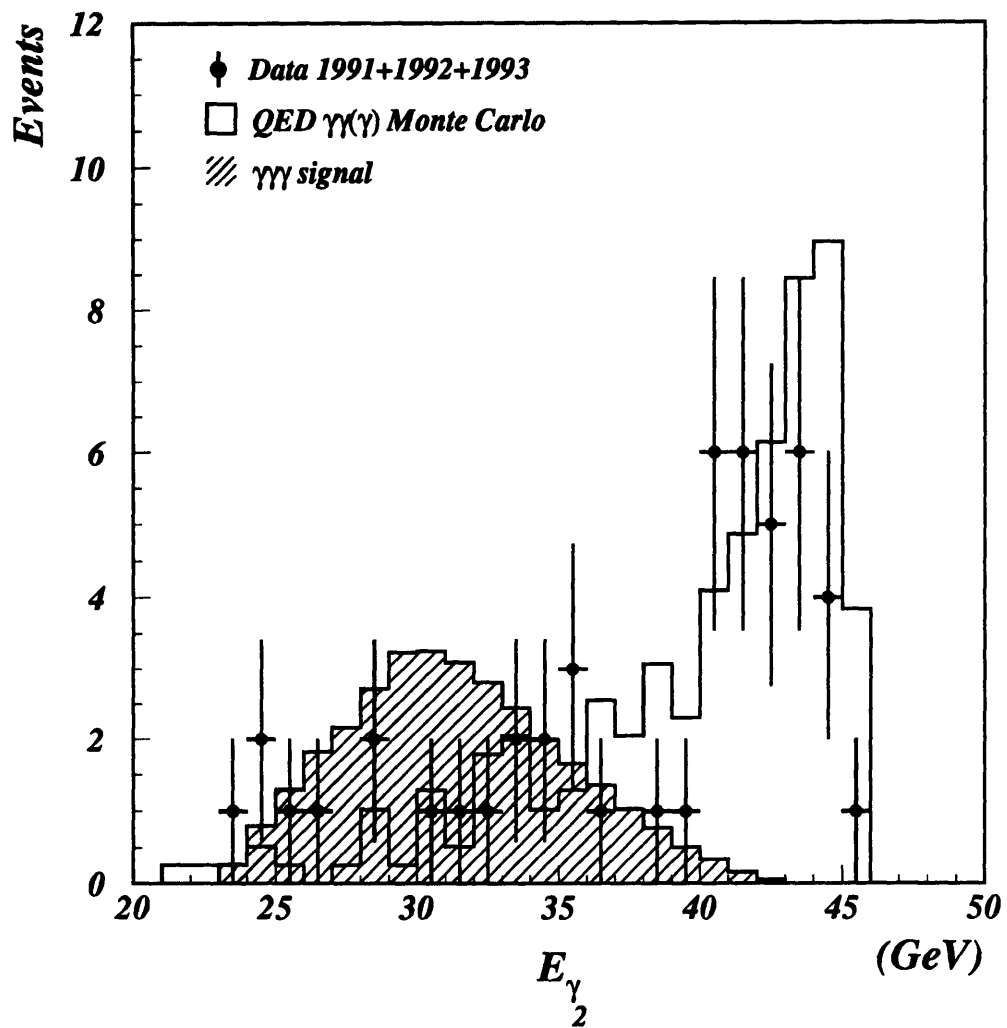


Figure 7-5: The energy of the second most energetic photon for the data, the QED Monte-Carlo and the signal (arbitrarily normalized).

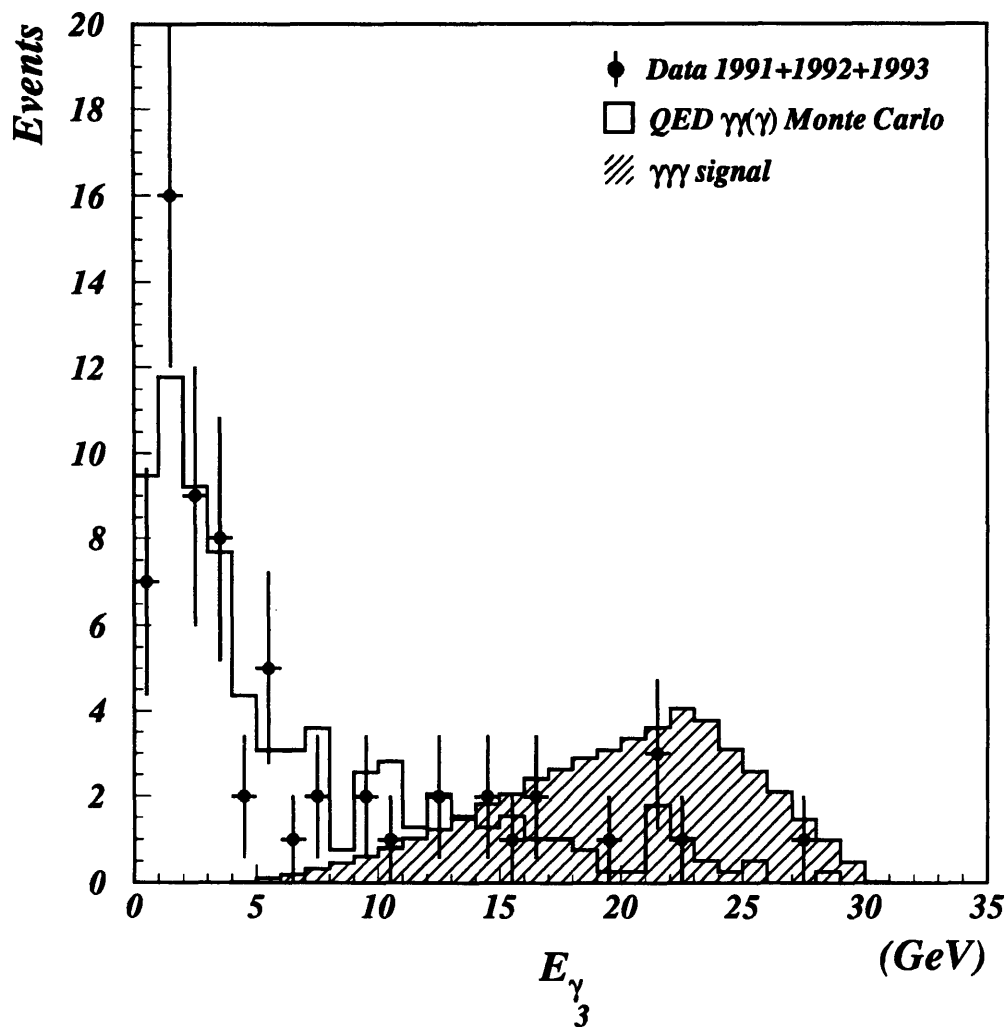


Figure 7-6: The energy of the third most energetic photon for the data, the QED Monte-Carlo and the signal (arbitrarily normalized). After imposing further requirements on the angles, there are 12 events data and  $14.8 \pm 0.9$  predicted from the Monte-Carlo.

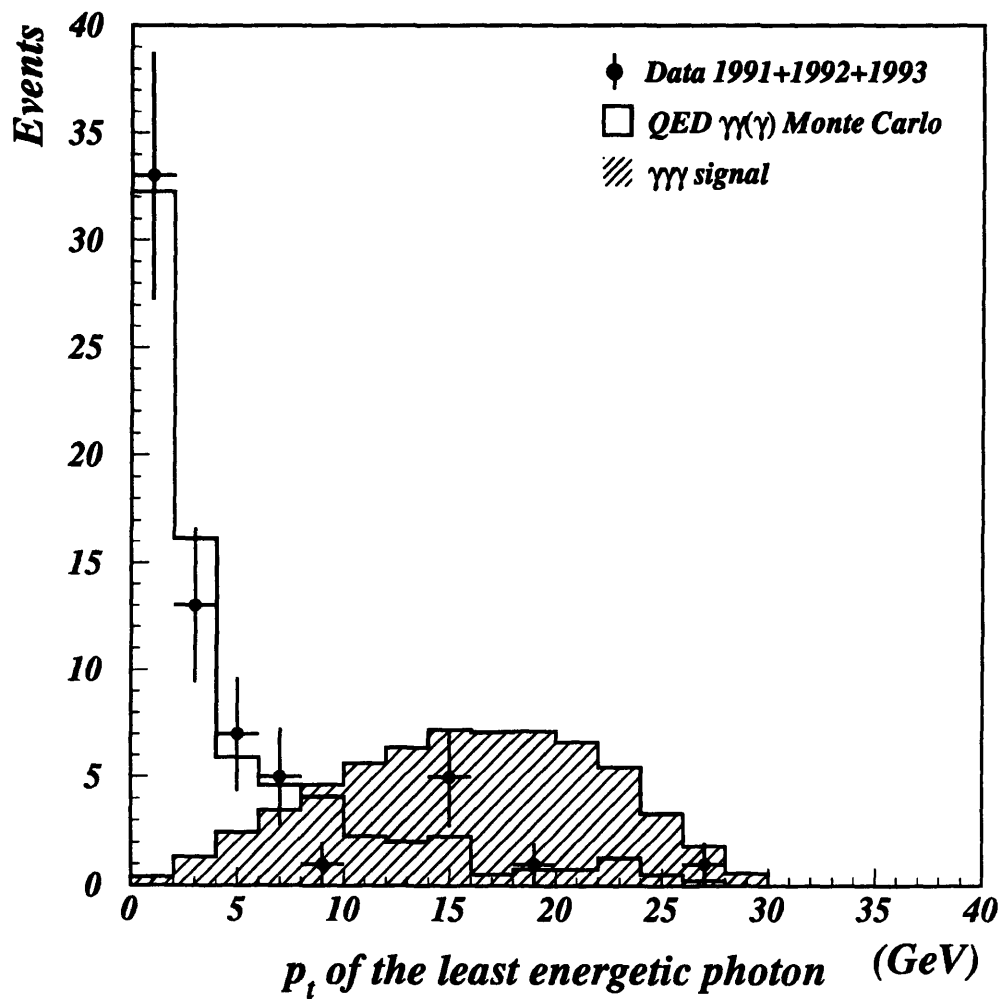


Figure 7-7: The  $p_t$  of the least energetic photon with respect to the thrust axis of the two most energetic photons. The distribution of the  $Z^0 \rightarrow \gamma\gamma\gamma$  is quite distinctive from the QED process. The signal is arbitrarily normalized.

**Data 1991+1992+1993**  
 $e^+e^- \rightarrow \gamma\gamma(\gamma)$

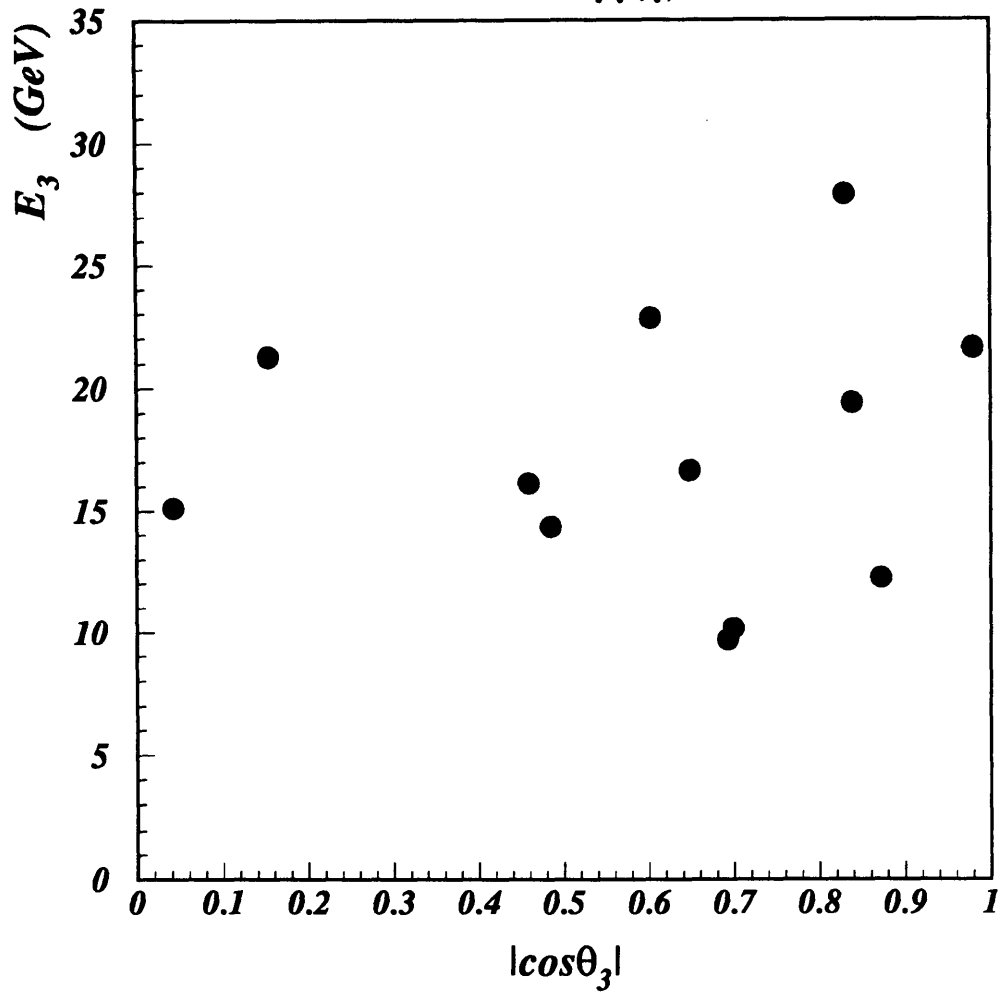


Figure 7-8: *The distribution of the 12 data events. The polar angle of the least energetic photon is plotted as a function of its energy.*

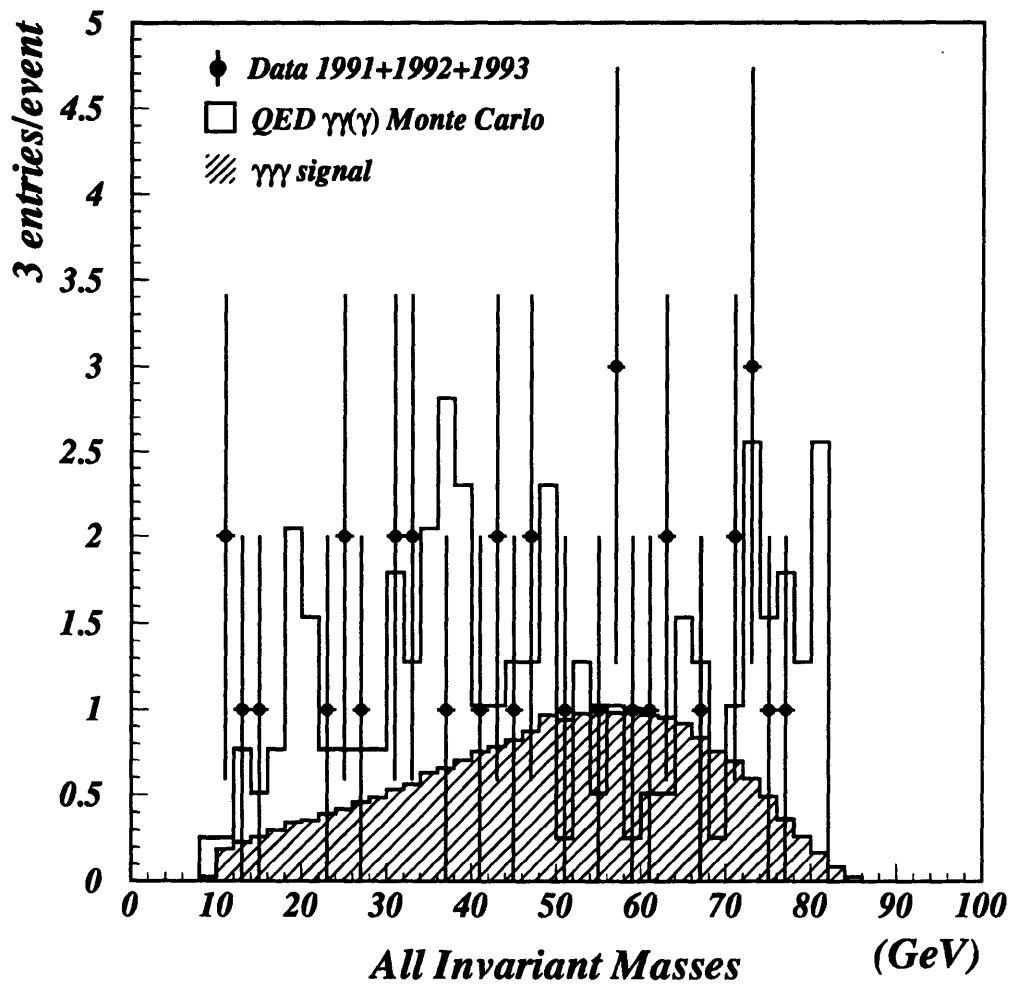


Figure 7-9: The invariant mass distribution of all combinations of photon pairs of the data, Monte-Carlo and the arbitrarily normalized signal.

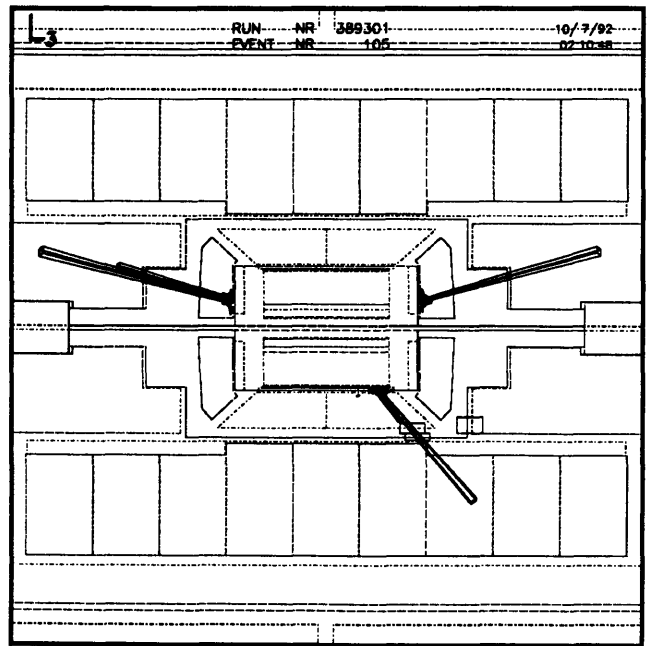
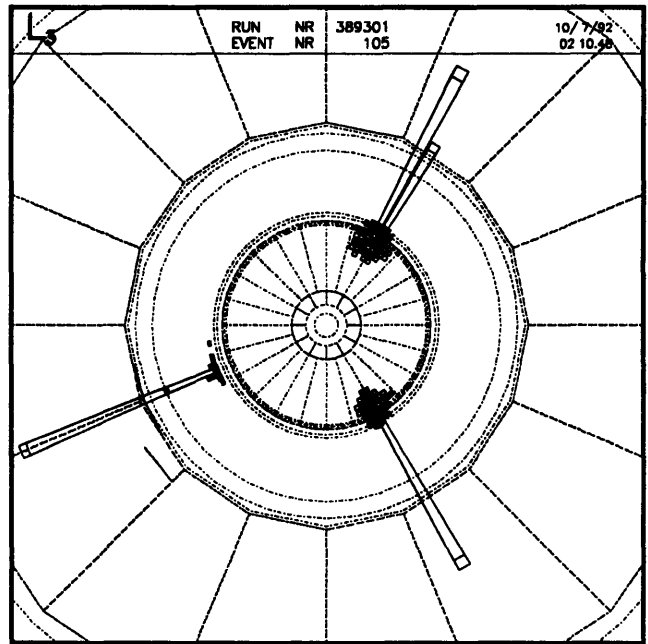


Figure 7-10: An example of a three photon event from 1992.

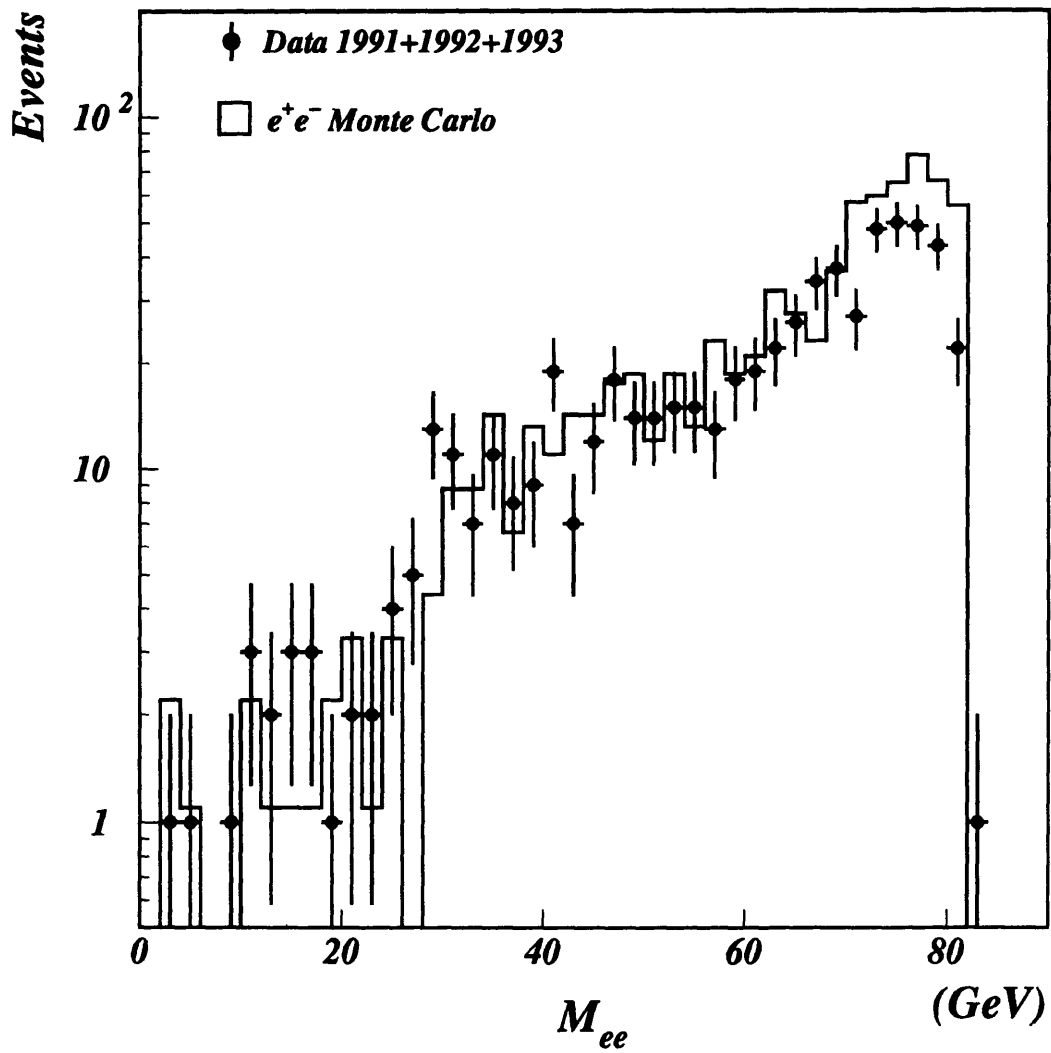


Figure 7-11: *The invariant mass distribution of di-electrons.*

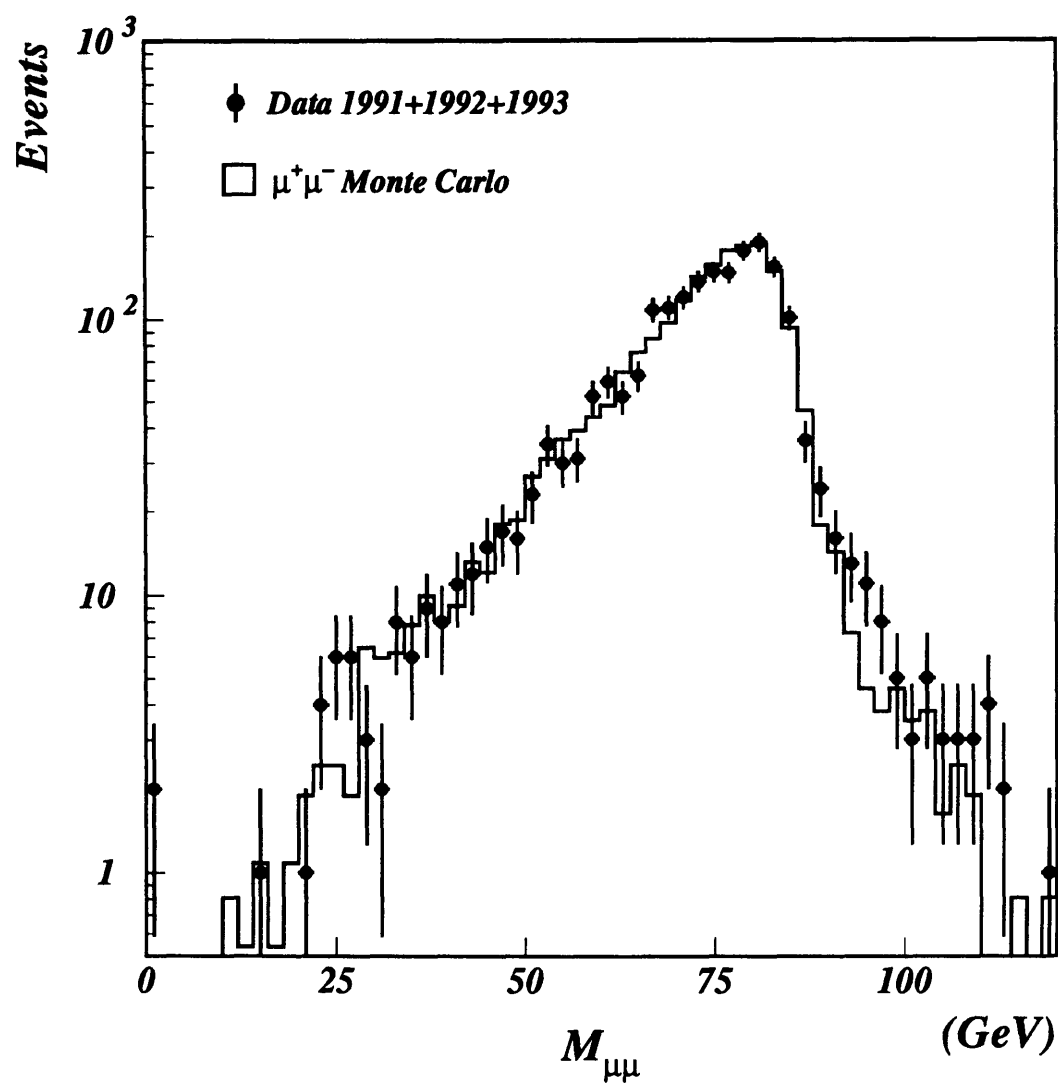


Figure 7-12: *The invariant mass distribution of di-muons.*

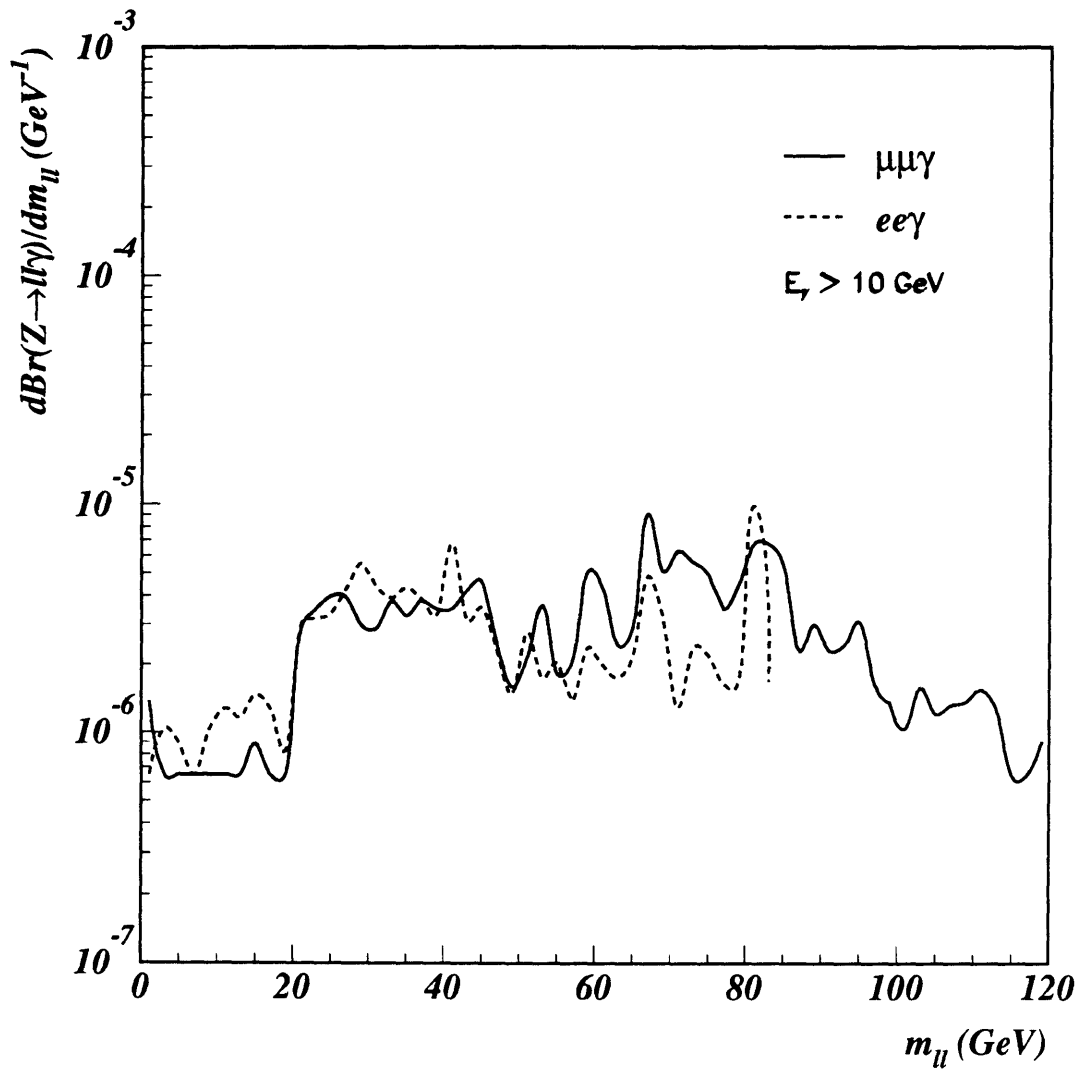


Figure 7-13: The branching ratio of anomalous  $Z^0 \rightarrow l^+l^-\gamma$  events at the 95% confidence level.

# Chapter 8

## Conclusion and Remarks

Presented is a brief overview of the current limits on compositeness from the present work and other analytic techniques from various Collaborations. Stringent limits have been placed in many different searches, and for various physics processes. In closing, future prospects are outlined.

### 8.1 Summary

Included in this work were indirect searches for pair produced excited leptons for both homodoublet and sequential models by examining the allowed width for these decays based on the invisible and total  $Z^0$  widths. The homodoublet leptons were excluded at the 95% C.L. up to the kinematical limit of 45.6 GeV.

Direct searches assuming radiative decay predominance were performed for pair produced excited leptons and muons. No invariant mass peaks were seen. Purely radiative decay branching ratios were placed at:

$$Br(Z^0 \rightarrow e^* \bar{e}^* \rightarrow e\gamma e\gamma) < 4.6 \times 10^{-6} \quad (8.1)$$

and

$$Br(Z^0 \rightarrow \mu^* \bar{\mu}^* \rightarrow \mu\gamma\mu\gamma) < 1.1 \times 10^{-5} \quad (8.2)$$

at the 95% C.L.

Postulating a magnetic transition coupling, singly produced excited leptons have been searched for in the radiative decay mode. The limits on the new coupling  $\lambda_l$  depend on the mass of the hypothetical excited lepton  $l^*$ , and yield the following exclusions at the 95% C.L.:

- $e^*$  s-channel:

for  $m_{e^*} = 45$  GeV:

$$\frac{\lambda_Z}{m_{e^*}} < \frac{1}{11 \text{ TeV}} \quad (8.3)$$

and for  $m_{e^*} = 80$  GeV:

$$\frac{\lambda_Z}{m_{e^*}} < \frac{1}{4 \text{ TeV}} \quad (8.4)$$

- $e^*$  t-channel:

for  $m_{e^*} = 45$  GeV:

$$\frac{\lambda_\gamma}{m_{e^*}} < \frac{1}{6.7 \text{ TeV}} \quad (8.5)$$

and for  $m_{e^*} = 85$  GeV:

$$\frac{\lambda_\gamma}{m_{e^*}} < \frac{1}{5.8 \text{ TeV}} \quad (8.6)$$

- $\mu^*$

for  $m_{\mu^*} = 45$  GeV:

$$\frac{\lambda_Z}{m_{\mu^*}} < \frac{1}{10 \text{ TeV}} \quad (8.7)$$

and for  $m_{\mu^*} = 80$  GeV:

$$\frac{\lambda_Z}{m_{\mu^*}} < \frac{1}{6.7 \text{ TeV}} \quad (8.8)$$

- $\tau^*$

for  $m_{\tau^*} = 45$  GeV:

$$\frac{\lambda_Z}{m_{\tau^*}} < \frac{1}{11 \text{ TeV}} \quad (8.9)$$

and for  $m_{\tau^*} = 80$  GeV:

$$\frac{\lambda_Z}{m_{\tau^*}} < \frac{1}{2.5 \text{ TeV}} \quad (8.10)$$

In the s-channels, for a 90 GeV  $m_{l^*}$ , we have the limit

$$\frac{\lambda_Z}{m_{l^*}} \lesssim \frac{1}{1 \text{ TeV}} \quad (8.11)$$

for  $l = e, \mu,$  and  $\tau$ .

Evidence for  $Z^0$  substructure has been searched for by looking for an excess of three photon final states which are not topologically kinematically compatible with those produced by the purely QED process. A limit has been placed on the branching ratio to be:

$$Br(Z^0 \rightarrow \gamma\gamma\gamma) < 7.4 \times 10^{-6} \quad (8.12)$$

which translates to a four-boson contact term limit on  $\Lambda$  of:

$$\Lambda > 40.0 \text{ GeV} \quad (8.13)$$

at the 95% C.L.

An anomalous production of low mass di-lepton pairs with the presence of a hard photon has been investigated. The decay of the  $Z^0$  into a two photon final state is possible only if it is composite. A limit has been placed at the 95% C.L. for the branching ratio:

$$Br(Z^0 \rightarrow \gamma^*\gamma \rightarrow l^+l^-\gamma) < 10^{-6} \quad (8.14)$$

## 8.2 Other searches for compositeness

Below is a summary of other searches for compositeness led by various collaborations.

### 8.2.1 $e^*$ from $e^+e^- \rightarrow \gamma\gamma(\gamma)$

The existence of the excited state of the electron  $e^*$  can be tested by measuring deviations in the QED process  $e^+e^- \rightarrow \gamma\gamma(\gamma)$ .

The process  $e^+e^- \rightarrow \gamma\gamma$  which proceeds only through the exchange of a virtual electron, is altered when the contribution of the  $e^*$  propagator is included. The total Born level differential cross section can be written as:

$$\left(\frac{d\sigma}{d\Omega}\right)^0 = \sigma(\theta)_{QED}^0 (1 \pm \delta_{new}) \quad (8.15)$$

where

$$\delta_{new} = \frac{s^2}{2} \left(\frac{1}{\Lambda_{\pm}^4}\right) (1 - \cos^2 \theta) \quad (8.16)$$

and  $\Lambda_{\pm}$  are the QED cutoff parameters.

A recent result from the L3 Collaboration is given. The unbinned log-likelihood method is used to place lower limits on the the QED cut-off parameters and the mass of  $e^*$  (see [17] for details). With an integrated luminosity of  $14.2 \text{ pb}^{-1}$ , the results are:

$$\Lambda_+ > 139 \text{ GeV} ; \quad \Lambda_- > 108 \text{ GeV} \quad (8.17)$$

and

$$m_{e^*} > 127 \text{ GeV} \quad (\text{with } \lambda = 1) \quad (8.18)$$

at the 95% C.L.

### 8.2.2 $\nu^*$

The search for an excited neutrino state is held on equal ground with other excited fermion searches. LEP is an ideal place to search for excited neutrinos. The ALEPH Collaboration has a limit derived from the measurement of the total and invisible  $Z^0$  width and they exclude homodoublet neutrinos up to the kinematical limit of 45.5 GeV at the 95% C.L. Since this result is independent of the decay topology, it is inclusive of all  $\nu^*$  decay modes.

For singly produced excited neutrinos, a combined limit from the L3 and ALEPH Collaborations is given. There are two possible dominant decay modes dependent on the couplings. The processes

$$\nu^* \rightarrow eW \quad \text{and} \quad \nu^* \rightarrow \nu\gamma \quad (8.19)$$

have been examined. In neither search were any candidates found with  $E_{\gamma} > 10 \text{ GeV}$ . The combined limit is based on a total integrated luminosity of 8.3 (ALEPH)[51] and

3.8 (L3)[52]  $\text{pb}^{-1}$  and was found from adding the inverse limits in quadrature with the 95% C.L. result:

$$\lambda_{Z\nu^*} < \frac{1}{10 \text{ TeV}} \quad (8.20)$$

for the mass  $m_{\nu^*} \approx 50 \text{ GeV}$  with less stringent limits of

$$\lambda_{Z\nu^*} \lesssim \frac{1}{1 \text{ TeV}} \quad (8.21)$$

for an excited neutrino mass of approximately 80 GeV.

### 8.2.3 $q^*$

The formulation for the existence of excited quarks as an indication of fermion substructure is identical to that of leptons. However, due to the nature of the final state involving the production of jets, the search for excited quarks entail an entirely different analytical approach than the search for excited leptons.

This process has one additional property that excited quarks can decay gluonically. The estimated  $q^*$  branching ratios for  $m_{u^*}, m_{d^*} > M_W, M_Z$  are as follows:

Decay Mode	Br(%)	Decay Mode	Br(%)
$u^* \rightarrow ug$	83	$d^* \rightarrow dg$	83
$u^* \rightarrow u\gamma$	2	$d^* \rightarrow d\gamma$	1
$u^* \rightarrow dW$	11	$d^* \rightarrow uW$	11
$u^* \rightarrow uZ^0$	4	$d^* \rightarrow dZ^0$	5

Searches for an excess of  $q\bar{q}\gamma$  states have been performed at LEP, but the most stringent limits to date come from the CDF Collaboration at Fermilab where  $p\bar{p}$  center-of-mass energies of 1.8 TeV can extend to higher limits. The decay modes examined at CDF are the  $q^*$  decays into  $q\gamma$  and  $qW$ . With some assumptions on the form factors, i.e. that in similar notation with  $\lambda = 1$ , excited quarks are excluded at the 95% C.L. up to masses of 570 GeV.

### 8.2.4 Contact terms

Compositeness would produce new interactions among quarks and leptons. A new interaction at a scale  $\Lambda$  can manifest itself as a perturbation at present energies [53]. The differential cross section of the processes

$$e^+e^- \rightarrow l^+l^- \quad \text{and} \quad e^+e^- \rightarrow \gamma\gamma \quad (8.22)$$

could be affected by contact terms. The new contact Lagrangian among four fermions can be written as:

$$\mathcal{L}_{ffff} = \frac{g^2}{2\Lambda^2} \left[ \eta_{LL} \bar{\psi}_L \gamma_\mu \psi_L \bar{\psi}_L \gamma^\mu \psi_L + \eta_{RR} \bar{\psi}_R \gamma_\mu \psi_R \bar{\psi}_R \gamma^\mu \psi_R + 2\eta_{LR} \bar{\psi}_L \gamma_\mu \psi_L \bar{\psi}_R \gamma^\mu \psi_R \right] \quad (8.23)$$

This Lagrangian is built from fermion currents which preserve chirality. Different models based on different helicities of the currents are denoted by different values of  $\eta$ . The models are as follows:

Model	$\eta_{LL}$	$\eta_{RR}$	$\eta_{LR}$
LL	$\pm 1$	0	0
RR	0	$\pm 1$	0
VV	$\pm 1$	$\pm 1$	$\pm 1$
AA	$\pm 1$	$\pm 1$	$\mp 1$
LR	0	0	$\pm 1$

Two energy scales,  $\Lambda^+$  and  $\Lambda^-$  correspond to the different signs possible for the contact amplitude.

The Collaborations of PEP, PETRA, TRISTAN and ALEPH have searched for the four-fermion contact terms. The combined limits with a normalization of  $g^2/4\pi = 1$  are:

Model	LL		RR		VV		AA		LR	
	$\Lambda^+$	$\Lambda^-$								
$eeee$	1.6	2.2	1.6	2.1	2.8	4.5	3.9	2.8	2.3	3.7
$ee\mu\mu$	2.6	1.9	2.6	1.9	4.1	3.1	4.6	3.8	2.6	2.5
$ee\tau\tau$	1.8	2.3	1.8	2.3	3.9	2.9	2.5	4.0	2.3	1.4
$llll$	3.5	2.8	3.5	2.7	6.0	5.4	5.7	4.4	3.1	4.1

All values are at the 95% C.L. in TeV.

For the two-boson two-fermion interaction, the effective contact Lagrangian is given by:

$$\mathcal{L}_{ff\gamma\gamma} = \frac{2ie^2}{\Lambda^4} F^{\mu\sigma} F_\sigma^\nu \left[ \eta_L \bar{\psi}_L \gamma_\mu \partial_\nu \psi_L + \eta_R \bar{\psi}_R \gamma_\mu \partial_\nu \psi_R \right] \quad (8.24)$$

where  $\eta_L$  and  $\eta_R$  define the chirality of the current. Different models which correspond to the different helicities of the electron current are given by:

Model	$\eta_R$	$\eta_L$
L	0	$\pm 1$
R	$\pm 1$	0
L+R	$\pm 1$	$\pm 1$
L-R	$\pm 1$	$\mp 1$

Two energy scales,  $\Lambda^+$  and  $\Lambda^-$  correspond to the different signs possible for the contact amplitude.

For the two-boson two-fermion terms, results are from the combined limits of ALEPH and TRISTAN:

	L,R		L+R	
	$\Lambda^+$	$\Lambda^-$	$\Lambda^+$	$\Lambda^-$
TRISTAN	96	84	115	101
ALEPH	102	109	121	130
ALEPH+TRISTAN	114	111	135	132

These results are in GeV, at the 95% C.L. Further references can be found in [54].

### 8.2.5 Electric dipole transition of the $Z^0$

If the  $Z^0$  had substructure, one manifestation could be an electric dipole transition of the form (see [55] and references therein):

$$Z^0 \rightarrow Z^* \gamma \quad (8.25)$$

where the  $Z^*$  is off-shell. The cleanest signature is when the virtual  $Z^*$  decays into neutrinos, leaving a hard, single photon. The L3 Collaboration has recently published a limit for the form factor of this transition, defined by:

$$f = \beta \left( \frac{s'}{M_Z^2} - 1 \right) \quad (8.26)$$

where  $s'$  is the squared mass of the  $Z^*$  and  $\beta$  parametrizes the strength of the transition. In the Standard Model  $\beta$  has a value of the order  $10^{-5}$  whereas if the  $Z^0$  is a bound state,  $\beta$  could be several orders larger. A limit is placed on  $\beta$  by examining the single photon spectrum. For a value of  $\beta = 1$  the single photon energy spectrum is greatly enhanced for energies  $E_\gamma > \frac{1}{2}E_{beam}$ , which is in contrast with radiative photons from the Standard Model background  $e^+e^- \rightarrow \nu\bar{\nu}\gamma$  events. The analysis is based on  $11.2 \text{ pb}^{-1}$  of luminosity and the details and selection criteria are given in [56]. The result is:

$$\beta < 0.80 \quad (8.27)$$

at the 95% C.L.

### 8.2.6 Leptoquarks

The similarities between the lepton and quark family structure has given reason to believe that a fundamental interrelation could exist between them, giving rise to particles which could mediate the quark-lepton transitions. These particles are called leptoquarks [57]. They couple to both leptons and quarks and are triplets under  $SU(3)_C$ . Their quantum numbers vary in different models: the spin can be 0, 1, or 2; the charge  $-4/3$ ,  $-1/3$ ,  $+2/3$ , or  $+5/3$ ; isospin 0,  $1/2$  or 1; baryon number  $\pm 1/3$ ; lepton number  $\pm 1$ . From this it is clear that predictions are model-dependent.

The most stringent limits to date come from the H1 and ZEUS Collaborations at HERA, where electrons and protons collide at  $\sqrt{s} = 296 \text{ GeV}$  and thus is an ideal machine to search for such particles. Direct searches were performed for electron + jet or neutrino + jet final states for all combinations of  $SU(2) \times U(1)$  multiplet assignments.

With an integrated luminosity of  $25 \text{ nb}^{-1}$ , leptoquark masses were excluded at the 95% C.L. assuming a normalized coupling of  $g = 0.3$ :

$$M_{LQ} > 145 \text{ to } 192 \text{ GeV} \quad (8.28)$$

for leptoquark production from an electron-quark pair, and

$$M_{LQ} > 98 \text{ to } 121 \text{ GeV} \quad (8.29)$$

for leptoquark production from an electron-anti-quark pair, depending on the specific quantum numbers assigned.

## 8.3 Future prospects

The next substantial step in the search for compositeness will come with the running of LEP 200, where many Standard Model predictions will come to a critical test. Different reactions will shed light on the possibility of fermionic or bosonic substructure. In the following, all numbers quoted are based on the assumed value of the integrated luminosity to be  $500 \text{ pb}^{-1}$  at  $\sqrt{s} = 190 \text{ GeV}$ . For more details see Ref. [58]

In the context of fermion compositeness, various studies will continue to be possible:

- Excited leptons

The direct searches for excited leptons will naturally extend up to the kinematical limits, for both pair produced and singly produced excited leptons. The process  $e^+e^- \rightarrow \gamma\gamma$  will be able to reach about  $m_{e^*} > 260 \text{ GeV}$  when  $\lambda = 1$  or  $m_{e^*} > 3 \text{ TeV}$  when  $g^2 = 4\pi$  ( $e\lambda = g \approx 0.02$ ). The search for an excited neutrino can reach farther than possible before LEP 200 via virtual neutrino exchange in the process  $e^+e^- \rightarrow W^+W^-$ . It will be possible to evaluate the differential cross section for deviations and obtain a sensitivity for  $\nu^*$  masses less than or equal to  $700 \text{ GeV}$  for the coupling  $g^2(c^2 + d^2) = 4\pi$ .

- Contact terms

The study of the four-fermion contact terms will be one of the most powerful methods of putting limits on the compositeness scale  $\Lambda$ . The current limits of a few TeV can be extended into the regions of 4 to 13 TeV with some assumptions on the coupling strengths. These values are dependent on the specific model and beam polarization state. In general the reach will scale with  $\sqrt{s}$  off the  $Z^0$  peak [59].

Contact term studies on the reaction  $e^+e^- \rightarrow W^+W^-$  will provide less stringent bounds on  $\Lambda$ , with a reach of about  $750 \text{ GeV}$ .

In regards to bosonic substructure, the following analysis will provide the most important information:

- Tri-linear couplings

The study of the triple gauge boson vertices  $W^+W^-Z^0$  and  $W^+W^-\gamma$  will be one of the main tasks of LEP 200 analyses. Examination of angular distributions and total cross sections will shed information on possible deviations of tri-linear form factors from their Standard Model predicted values. Any deviations could be interpreted as the effect of anomalous electric dipole and quadrupole moments of the  $W$ . In general, the sensitivity to non-Standard form factors will strongly depend on the correlation of  $\lambda$  and  $\kappa$ . However, in the best case scenario, when they are uncorrelated, a precision of about 10% will be achievable on  $\lambda$  and  $\kappa$ .

For the longer term, the Large Hadron Collider (LHC) at center-of-mass energies of 14-16 TeV will allow the possibility to explore new energy domains. With an

instantaneous luminosity of  $10^{34} \text{ cm}^{-2} \text{ s}^{-1}$ , the event rate for physics processes will be high, however the background will also increase. Thus, the environment is not as ‘clean’ as in  $e^+e^-$  collisions. But on the other hand, hadron collisions have a high discovery potential since their interaction energies have a relatively enormous span.

Among the searches for compositeness possible at the LHC are:

- $q^*$

An analysis of inclusive jet cross sections can study the possibility of quark substructure. Deviations from QCD expectations for high transverse momenta jets can be an effect of composite states. However, this study is sensitive to detector systematics. It has been shown [60] that uncertainties in the resolution, response linearity and overall calorimetric response can fake the presence of a contact interaction  $\Lambda_C$ . With as little as 4% non-linearity in calorimetric response for jets between 500 GeV and 4 TeV, a quark compositeness signal with  $\Lambda_C$  of about 15 TeV will be observed.

- Gauge boson pair production

Gauge boson pair production is an essential test of the tri-linear form factors. As an example, in  $W\gamma$  events, the transverse momentum of the photon is sensitive to anomalous couplings. This process can be studied via leptonic decays of the  $W$ . The main backgrounds come from  $W + jets$ , and  $b\bar{b}, t\bar{t} \rightarrow leptons + jets$ , where a jet is misidentified as a photon. With assumptions on photon rejection, lepton isolation, and other parameters on transverse momenta, the ATLAS Collaboration [60] has predicted that for an integrated luminosity of  $10^5 \text{ pb}^{-1}$ , a significant excess of high  $p_T$  events, approximately 160 over the Standard Model prediction, would be observed for a value of  $\kappa = 1.1$

## 8.4 Concluding remarks

Although the Standard Model remains well confirmed, it is nonetheless imperative to continue searching for deviations in hopes of shedding light into some of its unsolved questions. An attractive solution is the possibility that some of the presently elementary particles are not truly elementary but are tightly bound states of smaller more fundamental particles. One motivation for fermionic compositeness is the potentiality to explain the lepton-quark family spectrum, for which there is no current explanation.

For the gauge bosons, it is possible that massive elementary gauge bosons do not exist in nature and that the  $W$  and  $Z^0$  are made of more fundamental particles, but that the energy scale to show their subconstituents has simply not been reached. Historically, it is an interesting point that not so long ago the pions were the fundamental massive exchange bosons of the nuclear force.

If in the future, signs of compositeness surface, it must be kept in mind that all the above mentioned analyses probe its *presumed manifestations*. It is another matter altogether to prove the existence of composite states via indirect effects on Standard

Model processes. Indeed, short of a  $q^2$  resonance or dependence such as invariant mass peaks or evidence of *deeper* inelastic scattering, much further details would have to be explored before anything certain could be concluded.

Up to present, there seem to be no indications of substructure in fermions or bosons in the available energy regimes. This latter point is all that can truly be ascertained. Therefore it is imperative to continue the search for new particles or evidence of new physics, for if nothing else, it would signal the end of understanding to think that everything is completely understood.



# Appendix A

## Cross-section involving excited leptons $l^*$

In this appendix, the differential cross section for the s-channel and t-channel exchanges involving a single excited lepton are integrated.

The s-channel differential equations (2.59,2.60) can be straightforwardly integrated over t from

$$t_{min} = 0 \quad (A.1)$$

to

$$t_{max} = -s + m_{e^*}^2 \quad (A.2)$$

to find the total cross sections:

$$(\sigma^{l^*l})_{\gamma} = \frac{2\pi\alpha^2\lambda_{\gamma}^l{}^2}{3m_{e^*}^2s^3} (m_{e^*}^2 - s)^2 (2m_{e^*}^2 + s) \quad (A.3)$$

$$(\sigma^{l^*l})_{Z^0} = \frac{4\pi\alpha^2\lambda_Z^l{}^2}{3m_{l^*}^2s|\chi(s)|^2} (A^2 + B^2) (m_{l^*}^2 - s)^2 (2m_{l^*}^2 + s) \quad (A.4)$$

For the t-channel, care must be taken when integrating the terms in powers of  $t^n$ ,  $n < 0$  for which the ordinary leptons masses must be kept to avoid divergences. The momentum transferred squared  $t$  is:

$$t = \frac{1}{2} \left( -s + m_{e^*}^2 + 3m_e^2 + \cos\theta \frac{\sqrt{(-4m_e^2 + s)(-4m_{e^*}^2m_e^2 + (s - (m_{e^*}^2 + m_e^2))^2)}}{\sqrt{s}} \right) \quad (A.5)$$

where  $\theta$  is the scattering angle of the outgoing excited lepton. For the upper bound of the integration, the ordinary electron mass,  $m_e$ , in the radical is neglected which simplifies greatly the expression of  $t_{max}$ . The integration bounds are:

$$t_{min} = t(\cos\theta = 1), \quad t_{max} = -s + m_{e^*}^2 \quad (A.6)$$

The indefinite integral is:

$$\int \frac{d\sigma}{dt} dt \propto \frac{1}{m_{e^*}^2s^2} \left[ \frac{2m_{e^*}^4m_e^2}{t} + t(m_{e^*}^2 - 2s) + \ln(t) (-m_{e^*}^4 + 2m_{e^*}^2s - 2s^2) + \right]$$

$$\left. \frac{2 \left( m_e^2 t - st - \frac{t^2}{2} \right) + \frac{m_e^2 t^2 - st^2 - 2t^3}{3} + m_e^2 t (-m_e^2 + s)}{s} \right] \quad (\text{A.7})$$

In this expression, the terms sensitive to the electron mass are the  $\ln$  and the  $2m_e^4 m_e^2/t$  parts. When calculating the lower limit, the electron mass in all the other terms can be set to zero yielding:

$$\int \frac{d\sigma}{dt} \Big|_{t=t_{min}} \propto \frac{1}{m_e^2 s^2} \left\{ - \left[ \ln(t_{min}) (-m_e^4 + 2m_e^2 s - 2s^2) \right] + \frac{4m_e^4 m_e^2}{-s + m_e^2 + 3m_e^2 + \sqrt{(-4m_e^2 + s) (-4m_e^2 m_e^2 + (s - (m_e^2 + m_e^2))^2)}} \right\} \quad (\text{A.8})$$

The second term of this expression tends zero nicely when  $m_e \rightarrow 0$  and is therefore neglected. Its value is much smaller than the  $\ln$  term. The total cross section is then:

$$\begin{aligned} (\sigma^{e^+e})_\gamma &= \frac{2\pi\alpha^2\lambda_\gamma^2}{3m_e^2 s^3} \left( 3s \ln \left[ \frac{t_{min}}{m_e^2 - s} \right] (-m_e^4 + 2m_e^2 s - 2s^2) \right. \\ &\quad \left. - (m_e^2 - s) (2m_e^4 - 7m_e^2 s + 8s^2) \right) \end{aligned} \quad (\text{A.9})$$

# Appendix B

## Decay width and lifetime of the $l^*$

In this appendix, the branching ratio of the radiative decay  $l^* \rightarrow l\gamma$  is calculated.

The matrix element for an  $l^*$  decay into a lepton and photon is taken from the effective Lagrangian 2.33:

$$\mathcal{M} = \frac{e\lambda}{2m_{l^*}} \left[ \bar{u}(p_2) \sigma^{\mu\nu} (1 - \gamma^5) q_\nu \epsilon_\mu^* u(p_1) \right] \quad (\text{B.1})$$

where  $p_1$  is the four-momentum of the  $l^*$ ,  $p_2$  is that of the ordinary lepton and  $q$  is the four-momentum of the photon. Eq. B.1 can be written as:

$$\mathcal{M} = \frac{ie\lambda}{4m_{l^*}} \left[ \bar{u}(p_2) (\gamma^\mu \gamma^\nu - \gamma^\nu \gamma^\mu) (1 - \gamma^5) q_\nu \epsilon_\mu^* u(p_1) \right] \quad (\text{B.2})$$

Then  $\mathcal{M}\mathcal{M}^*$  becomes, summing over outgoing spins and averaging over incoming spins:

$$\begin{aligned} \frac{1}{2} \sum_{\text{spins}} \mathcal{M}\mathcal{M}^* &= -\frac{1}{2} \left( \frac{e\lambda}{4m_{l^*}} \right)^2 q_\nu q_\mu \epsilon_\mu^* \epsilon_\beta \times \\ & \quad \text{Tr} \left[ \not{p}_2 (\gamma^\mu \gamma^\nu - \gamma^\nu \gamma^\mu) (1 - \gamma^5) \not{p}_1 (\gamma^\alpha \gamma^\beta - \gamma^\beta \gamma^\alpha) (1 - \gamma^5) \right] \end{aligned} \quad (\text{B.3})$$

By expansion and using the relations  $\gamma^5 \gamma^\mu = \gamma^\mu \gamma^5$  and  $(\gamma^5)^2 = 1$ , the  $q_\nu q_\mu$  times the trace term becomes:

$$\begin{aligned} & \left[ 2 \text{Tr} \left( \not{p}_2 \gamma^\mu \not{q} \not{p}_1 \not{q} \gamma^\beta \right) - 2 \text{Tr} \left( \not{p}_2 \not{q} \gamma^\mu \not{p}_1 \not{q} \gamma^\beta \right) \right. \\ & \left. - 2 \text{Tr} \left( \not{p}_2 \gamma^\mu \not{q} \not{p}_1 \gamma^\beta \not{q} \right) + 2 \text{Tr} \left( \not{p}_2 \not{q} \gamma^\mu \not{p}_1 \gamma^\beta \not{q} \right) \right] \end{aligned} \quad (\text{B.4})$$

Using the Dirac matrices algebra  $\gamma^\mu \gamma^\nu + \gamma^\nu \gamma^\mu = 2g^{\mu\nu}$ , Eq. B.4 becomes:

$$\begin{aligned} & 3 \times 16 (p_1 \cdot q) \left[ p_2^\beta q^\mu + p_2^\mu q^\beta - (p_2 \cdot q) g^{\mu\beta} \right] + 16 (p_2 \cdot q) \left[ p_1^\beta q^\mu + p_1^\mu q^\beta - (p_1 \cdot q) g^{\mu\beta} \right] \\ & - 16 q^\beta \left[ (p_1 \cdot q) p_2^\mu - (p_2 \cdot q) p_1^\mu + (p_1 \cdot p_2) q^\mu \right] - 16 q^\mu \left[ (p_1 \cdot q) p_2^\beta - (p_2 \cdot q) p_1^\beta + (p_1 \cdot p_2) q^\beta \right] \end{aligned} \quad (\text{B.5})$$

Now we absorb the photon polarization vectors  $\epsilon_\mu \epsilon_\beta$  into the trace terms using the relation:

$$\sum_{\text{spin}} \epsilon_\mu^* \epsilon_\beta = -g_{\mu\beta} + \frac{q_\mu q_\beta}{\xi^2} \quad (\text{B.6})$$

where  $\xi^2$  is the mass of the photon. In the case of the photon final state  $q^2 = 0$  and Eq. B.3 becomes:

$$|\mathcal{M}|^2 = \left( \frac{e\lambda}{4m_{l^*}} \right)^2 [32(p_1 \cdot q)(p_2 \cdot q)] \quad (\text{B.7})$$

One can obtain the decay width  $\Gamma(l^* \rightarrow l\gamma)$  from the squared matrix element Eq. B.7:

$$d\Gamma = \frac{1}{4m_{l^*}} |\mathcal{M}|^2 \frac{d^3p_2 d^3p_3}{(2\pi)^3 2E_2 (2\pi)^3 2E_3} (2\pi)^4 \delta^4(p_1 - p_2 - p_3) \quad (\text{B.8})$$

For the integration, we choose the rest frame of the  $l^*$  thus we have for the four-vectors:

$$p_1 = (m_{l^*}, \vec{0}) \quad p_2 = (E_2, \vec{p}_2) \quad (\text{B.9})$$

and Eq. B.8 becomes:

$$d\Gamma = \frac{1}{8m_{l^*}} \frac{1}{(2\pi)^2} \left( \frac{e\lambda}{4m_{l^*}} \right)^2 32 [m_{l^*}^3 E_2 - m_{l^*}^2 E_2^2] \frac{1}{E_2 E_3} \delta(m_{l^*} - E_2 - E_3) \delta^3(-\vec{p}_2 - \vec{p}_3) \quad (\text{B.10})$$

Integrating, neglecting the mass of the ordinary lepton, one obtains:

$$\Gamma(l^* \rightarrow l\gamma) = \frac{\alpha}{4} \left( \frac{\lambda}{m_{l^*}} \right)^2 m_{l^*}^3 \quad (\text{B.11})$$

where  $\alpha = e^2/4\pi$ . The decay width can be used to estimate the mean free path  $L$  of the  $l^*$ ,  $L = \gamma\beta c\tau$ , where  $\gamma$  is the Lorentz boost,  $\beta c$  is the velocity of the  $l^*$  and  $\tau$  is the lifetime and  $\gamma = E/m$ ,  $\beta = p/E$  where  $p = (M_{Z^0}^2 - m_{l^*}^2) / (2M_{Z^0})$ . For an example, we choose a 45 GeV  $l^*$  which would have the lifetime

$$\tau \approx \frac{8 \times 10^{-24}}{\lambda^2} \text{ s} \quad (\text{B.12})$$

and a momentum of 34.5 GeV. This yields a mean free path of:

$$L = \frac{2 \times 10^{-13} \text{ cm}}{\lambda^2} \quad (\text{B.13})$$

For our region of interest of  $\lambda/m_{l^*} \approx 10^{-4} \text{ GeV}^{-1}$ , the mean free path is:

$$L \approx 10^{-8} \text{ cm} \quad (\text{B.14})$$

For higher masses, the mean free path is even shorter. Thus for all masses, the excited leptons decay extremely close to the interaction point.

# Bibliography

- [1] P. T. Matthews, A. Salam, *Rev. Mod. Phys.* **23** (1951) 311.
- [2] J. Hamilton, W. S. Woolcock, *Rev. Mod. Phys.* **35** (1963) 737.
- [3] G. F. Chew, *et al.*, *Phys. Rev.* **106** (1957) 1337.
- [4] F. E. Low, *Phys. Rev.* **96** (1954) 1427.
- [5] M. Gell-Mann, M. L. Goldberger, *Phys. Rev.* **96** (1954) 1433.
- [6] J. Steinberger, *Phys. Rev.* **76** (1949) 1180.
- [7] S. L. Glashow, *Nucl. Phys.* **22** (1961) 579;  
S. Weinberg, *Phys. Rev. Lett.* **19** (1967) 1264;  
A. Salam, Elementary Particle Theory,  
Ed. Svartholm, Stockholm, "Almqvist and Wiksell" (1968) 367.
- [8] R. P. Feynman, *Rev. Mod. Phys.* **20** (1948) 367; *Phys. Rev.* **74** (1948) 939,  
1430; *Phys. Rev.* **76** (1949) 749, 769; *Phys. Rev.* **80** (1950) 440;  
S. Tomonaga, *Prog. Theor. Phys.* **1** (1946) 27;  
F. J. Dyson, *Phys. Rev.* **75** (1949) 468, 1736.
- [9] F. E. Low, *Phys. Rev. Lett.* **14** (1965) 238.
- [10] C. N. Yang, R. L. Mills, *Phys. Rev.* **96** (1954) 191.
- [11] J. Goldstone, *Nuovo Cimento* **19** (1961) 154;  
J. Goldstone, A. Salam, S. Weinberg, *Phys. Rev.* **127** (1962) 965.
- [12] P. W. Higgs, *Phys. Lett.* **12** (1964) 132; *Phys. Rev. Lett.* **13** (1964) 508; *Phys. Rev.* **145** (1966) 1156;  
F. Englert, R. Brout, *Phys. Rev. Lett.* **13** (1964) 321.
- [13] E. W. N. Glover, J. J. van der Bij 'Bhabha Scattering', Z Physics at LEP 1,  
CERN 89-08 Vol. 1 (1989). Editors G. Altarelli, R. Kleiss and C. Verzegnassi.
- [14] R. Cahn, *Phys. Rev.* **D36** (1987) 2666; E. A. Kuradev, *Sov. J. Nucl. Phys.* **41**  
(1989) 466.
- [15] M. Baillargeon, F. Boudjema, UdeM-LPN-TH-30 (1991).

- [16] E. W. N. Glover, J. J. van der Bij 'Rare  $Z^0$  Decays', Z Physics at LEP 1, CERN 89-08 Vol. 2 (1989). Editors G. Altarelli, R. Kleiss and C. Verzegnassi.
- [17] O. Adriani *et al.*, Phys. Lett. **B288** (1992) 404.
- [18] J. Kühn, P. M. Zerwas, Phys. Lett. **B147** (1984) 189.
- [19] J. Bjorken, S. Drell, Relativistic Quantum Mechanics, McGraw-Hill Pub. Co., New York, 1964.
- [20] "Review of Particle Properties", Phys. Rev. D **45** (1992).
- [21] F. M. Renard, Phys. Lett. **B116** (1982) 264.
- [22] K. Hagiwara *et al.*, Z. Phys. **C29** (1985) 115.
- [23] See for example M. Peskin, Proceedings from 'Tenth International Symposium on Lepton-Photon Interactions at High-Energies', Bonn, FRG, August 1981.
- [24] F. Boudjema, DESY preprint 92-116 (1992).
- [25] J. A. Grifols, A. Méndez, Phys. Lett. **B255** (1991) 611.
- [26] UA1 Collaboration, G. Arnison *et al.*, Phys. Lett. **B122** (1983) 103; Phys. Lett. **B126** (1983) 398;  
UA2 Collaboration, P. Bagnaia *et al.*, Phys. Lett. **B129** (1983) 130;  
UA2 Collaboration, R. Ansari *et al.*, Phys. Lett. **B186** (1987) 440.
- [27] The LEP Collaborations ALEPH, DELPHI, L3, OPAL and The LEP Electroweak Working Group, CERN PPE/93-157 (1993).
- [28] UA2 Collaboration, Alitti *et al.*, CERN-PPE/91-216 (1991).
- [29] H. Fritzsch, CERN-TH-3219 (1981);  
H. Fritzsch, G. Mandelbaum, Phys. Lett. **B109** (1982) 224;  
H. Fritzsch, G. Mandelbaum, Phys. Lett. **B102** (1981) 319.
- [30] L. F. Abbott, E. Farhi, Phys. Lett. **B101** (1981) 69.
- [31] F. Boudjema, N. Dombey, Z. Phys. **C35** (1987) 499.
- [32] R. Kögerler, *et al.*, CERN-TH- 3231 (1982);  
H. Fritzsh, *et al.*, Phys. Lett. **B114** (1982) 157;  
B. Schrempp, *et al.*, DESY preprint 84-055 (1984).
- [33] F. M. Renard, Phys. Lett. **B116**(1982) 269.
- [34] F. Boudjema, F. M. Renard "Compositeness" in Ref. [16].  
F. Boudjema "The Composites In Question", PITHA-91/7 May 1991.  
M. Baillargeon, F. Boudjema "New Physics Through Final State Photons", ENSLAPP-A-365192 January 1992.

- [35] LEP Design Report, Vol. I-II, CERN-LEP/84-01, June 1984;  
I. Wilson, H. Henke, "The LEP Main Ring Accelerating Structure", CERN 89-09 (1989);  
R. Bailey *et al.*, "LEP Energy Calibration", CERN SL/90-95 (1990).
- [36] L. Aranaudon *et al.*, "The Energy Calibration of LEP in 1991", CERN PPE/92-125 (1992).
- [37] L3 Collaboration, B. Adeva *et al.*, NIM A **289** (1990) 35, and references therein;  
L3 Technical Proposal to CERN-LEPC May 1983.
- [38] J. A. Bakken *et al.*, NIM A **280** (1989) 25.
- [39] O. Adriani *et al.*, NIM A **302** (1991) 53.
- [40] F. James, 'Monte Carlo Theory and Practice', Rep. Prog. Phys. **43** (1980) 1145.
- [41] R. Kleiss, F. A. Berends, W. Hollik, BABAMC, Nucl. Phys. **B228** (1983) 535.
- [42] D. Karlen, Nucl. Phys. **B289** (1987) 23.
- [43] S. Jadach, W. Hollik, R. Stuart, B. F. L. Ward, Z. Was *et al.*, KORALZ 4.0.
- [44] T. Sjöstrand and M. Bengtsson, JETSET, Comput. Phys. Commun. **43** (1987) 367;  
T. Sjöstrand, Z Physics at LEP 1, CERN 89-08 Vol. 3 (1989). Editors G. Altarelli, R. Kleiss and C. Verzegnassi.
- [45] F. A. Berends, R. Kleiss, GGG, Nucl. Phys. **B186** (1981) 22.
- [46] R. Brun *et al.*, "GEANT 3", CERN DD/EE/84-1 (Revised) September 1987.
- [47] H. Fesefeldt, RWTH Aachen Report PITHA 85/02 (1985).
- [48] A. Rubbia, Proceedings from 'Neutral Currents Twenty Years Later', Paris, France, July 1993. "Search for New Physics at LEP".
- [49] A. Rubbia, Diplôme de l'Université de Genève Département de Physique Nucléaire et Corpusculaire, July 1990. Unpublished.
- [50] A. Rubbia, Ph.D. Thesis, Massachusetts Institute of Technology, June 1993. Unpublished.
- [51] The ALEPH Collaboration, D. Decamp *et al.*, CERN-PPE/91-149 (1991).
- [52] The L3 Collaboration, B. Adeva *et al.*, Phys. Lett. **B252** (1990) 525.
- [53] E. Eichten, *et al.*, Phys. Rev. Lett. **50** (1983) 811.

- [54] M. Bardadin-Otwinowska, Proceedings to the 'Trieste Workshop on the Search for New Elementary Particles: Status and Prospects', Trieste, Italy, May 1992. "Compositeness at LEP".
- [55] A. Barroso *et al.*, Phys. Lett. **B196** (1987) 547.
- [56] The L3 Collaboration, O. Adriani *et al.*, CERN-PPE/92-185 (1992).
- [57] B. Schrempp, *et al.*, Phys. Lett. **B153** (1985) 101.
- [58] D. Treille, *et al.*, Proceedings from 'ECFA Workshop on LEP 200', Aachen, Germany, Sept.-Oct. 1986. "Compositeness at LEP II".
- [59] F. Schrempp, *et al.*, Max-Planck-Inst. Munich preprint MPI-PAE/PTh 69/86 (1986).
- [60] The ATLAS Letter of Intent, CERN/LHCC 92-3 LHCC/I1, 1992.